

# Commissioning of the KATRIN Raman system and durability studies of optical coatings in glove box and tritium atmospheres

Zur Erlangung des akademischen Grades eines  
DOKTORS DER NATURWISSENSCHAFTEN  
von der Fakultät für Physik des  
Karlsruher Instituts für Technologie

genehmigte  
DISSERTATION  
von

Diplom-Physiker  
**Sebastian Fischer**  
aus Schwäbisch Hall

Referent: Prof. Dr. Guido Drexlin  
Institut für Experimentelle Kernphysik  
Karlsruher Institut für Technologie

Korreferent: Prof. Dr. Helmut H. Telle  
Department of Physics  
Swansea University (Wales)

Tag der mündlichen Prüfung: 11. Juli 2014



# Abstract

Neutrinos are the most abundant massive elementary particles in the universe and they play a key role in cosmology and in particle physics. They have influenced the formation of large scale structure in the early universe and they yield insight into physics beyond the standard model. Neutrino flavour oscillation experiments have proven that neutrinos must have a mass of at least  $0.05 \text{ eV}/c^2$  while experiments based on tritium  $\beta$ -decay set an upper limit of about  $2 \text{ eV}/c^2$  (95% C.L.). An improved constraint or even an accurate determination of the neutrino mass would trigger significant progress in particle physics and cosmology.

The aim of the Karlsruhe Tritium Neutrino (KATRIN) experiment is a neutrino mass measurement with a sensitivity of  $0.2 \text{ eV}/c^2$  (90% C.L.) by the investigation of the endpoint region of the tritium  $\beta$ -spectrum. Molecular tritium with an isotopic purity of  $\geq 95\%$  is injected into the Windowless Gaseous Tritium Source (WGTS) of KATRIN. In order to reach the design sensitivity of KATRIN, the isotopic purity has to be monitored continuously (every  $\leq 250 \text{ s}$  using real-time data analysis) on the  $10^{-3}$  level over the complete KATRIN measurement time of about three years. Therefore, prototypes of a custom-made Raman spectroscopy system have been developed and it was demonstrated that this technique is capable to monitor relative variations of the isotopic purity on the  $10^{-3}$  level under the relevant conditions.

The aim of this work was to design, to construct and to commission the Raman system that is actually used for KATRIN and to optimise the system with respect to two aspects: achieving the best metrological performance (quantified by the level of detection and the precision), and simultaneously ensuring the reliable and stable operation of the system over the projected operating time of several years. Furthermore, a software for the automated acquisition and quantitative analysis of Raman spectra had to be developed.

Based on the layout of the prototype systems, several improvements were implemented into the KATRIN Raman system which resulted in the stabilisation of the optical layout and of the laser beam parameters and increased the effective laser power.

The KATRIN Raman system has been tested under realistic conditions, i.e. with circulating highly purified tritium gas (200 mbar total pressure, isotopic purity  $\geq 90\%$ ). A relative precision of  $0.34 \cdot 10^{-3}$  was achieved for the monitoring of the  $T_2$  content (188 mbar partial pressure) using 29.5 s acquisition time. The precision requirement of KATRIN was thus clearly fulfilled, even at much shorter acquisition times than initially requested by the KATRIN experiment. A level of detection of  $4.8 \cdot 10^{-3}$  mbar was achieved corresponding to an improvement by a factor of five with respect to the most sensitive prototype system until then. These results demonstrate the success of the implemented optimisations in the KATRIN Raman system.

---

The software package LARASoft was developed which enables the automated acquisition and the quantitative analysis of Raman spectra. For the first time, it is possible that trained but non-expert personnel can perform quantitative compositional gas analyses of tritium gas mixtures. Additionally, all relevant hardware parameters are continuously evaluated to judge the status of the system and to warn the operators in case of a malfunction.

The central optical component of the KATRIN Raman system is the sample cell which is equipped with optical windows and is located inside a glove box for radiation safety. The anti-reflection coatings on these windows have to withstand intense laser irradiation, environmental influences, and physical and radio-chemical processes due to  $\beta$ -radiation over the course of months and years. A severe coating damage of the tritium facing side of the sample cell windows was experienced before the beginning of this work. This clearly demonstrated that this issue must not be underestimated. The formation of corrosive hydrofluoride species was identified as presumable cause of the coating damage. The replacement of a single component in the gas circulation system was sufficient to prevent similar damage in the future.

A variety of harmful effects on optical coatings in glove box and tritium gas atmosphere have been studied and evaluated with respect to their relevance. Coatings manufactured by electron-beam deposited are in general more susceptible to environmental effects (variation of pressure, oxygen concentration, humidity) than dense coatings. This generic statement was also found to be valid for effects due to the radioactive tritium gas. Electron beam deposited coating samples showed clear indications for coating alterations after already about 10 days of exposure to tritium gas while still no indications were found on samples of ion assisted deposition, magnetron sputtered, and ion beam sputtering coatings even after 39 days. Therefore, electron-beam deposited coatings should, in contrast to the current situation, not be used in glove box and tritium atmospheres. A batch of the optical windows of the sample cell have therefore been coated with anti-reflection coating based on magnetron sputtering. These windows will be tested under realistic conditions soon. It is expected that the new coating type will further improve the long-term performance of the optical components and hence reduce their failure probability during long-term operation.

Valuable information for the operation of the system were gained within this work. These allowed to define the operation parameters and the required tests and maintenance works which are necessary to ensure that the required metrological performance is continuously achieved. Based on the results of this work, the acquisition time of the system can be reduced to 20 s while still reliably fulfilling the  $10^{-3}$  precision requirement which allows to monitor even short-term fluctuations of the gas composition in the WGTS. This was initially not requested by the KATRIN experiment and therefore opens from the perspective of the Raman system the possibility to further improve the neutrino mass sensitivity.

In conclusion, Raman spectroscopy is not only a technique that can in principle be applied for quantitative gas compositional analysis but it has become a reliable and powerful method that can be routinely employed in KATRIN, even by non-expert personnel. This is an important step on the track towards the neutrino mass measurement with the KATRIN experiment.

# Zusammenfassung

Neutrinos sind die am häufigsten vorkommenden massebehafteten Elementarteilchen im Universum und spielen dabei eine Schlüsselrolle in der Kosmologie und in der Teilchenphysik: Sie haben die Strukturbildung im frühen Universum beeinflusst und geben einen Einblick in die Physik jenseits des Standardmodells. Experimente zur Untersuchung von Neutrino-Flavour-Oszillationen konnten zeigen, dass Neutrinos eine Masse von mindestens  $0,05 \text{ eV}/c^2$  besitzen. Experimente basierend auf der Untersuchung des Tritium- $\beta$ -Zerfalls ergaben eine Obergrenze von  $2 \text{ eV}/c^2$  (95% Vertrauensintervall). Eine weitere Einschränkung oder eine tatsächliche Bestimmung der Neutrinomasse würde zu einem signifikanten Fortschritt in der Teilchenphysik und in der Kosmologie führen.

Das Ziel des Karlsruhe Tritium Neutrino (KATRIN) Experiments ist die Messung der Neutrinomasse mit einer Sensitivität von  $0,2 \text{ eV}/c^2$  (90% Vertrauensintervall) durch die genaue Vermessung der Endpunktregion des Tritium- $\beta$ -Spektrums. Dabei wird molekulares Tritium mit einer Isotopenreinheit von  $\geq 95\%$  in die fensterlose gasförmige Tritiumquelle von KATRIN eingespeist. Um die geplante Sensitivität von KATRIN zu erreichen, muss die Isotopenreinheit kontinuierlich (alle  $\leq 250 \text{ s}$  mit sofortiger Datenanalyse) und mit einer relativen Präzision von  $10^{-3}$  während der gesamten Messzeit von drei Jahren überwacht werden. Dazu wurde ein auf Ramanspektroskopie basierendes Verfahren entwickelt. Mit Prototypsystemen konnte gezeigt werden, dass diese Methode in der Lage ist, relative Schwankungen der Isotopenreinheit im  $10^{-3}$  Bereich unter den geforderten Bedingungen nachzuweisen.

Das Ziel dieser Arbeit war das tatsächlich in KATRIN verwendete Ramansystem zu entwerfen, aufzubauen und in Betrieb zu nehmen, sowie es hinsichtlich zweier Aspekte zu optimieren: Optimierung der messtechnischen Leistung, d.h. der Nachweisgrenze und der Präzision, sowie die Gewährleistung des verlässlichen und stabilen Betriebs über Jahre hinweg. Zusätzlich sollte eine Software zur automatisierten Aufnahme und quantitativen Analyse von Ramanspektren entwickelt werden.

Ausgehend vom Aufbau der Prototypen wurden im KATRIN Ramansystem weitere Verbesserungen implementiert, die zur Stabilisierung des Strahlengangs und der Eigenschaften des Laserstrahls, sowie zur Erhöhung der effektiven Laserleistung führten.

Das KATRIN Ramansystem wurde unter realistischen Bedingungen getestet, d.h. mit zirkulierendem hochreinen Tritiumgas (200 mbar Gesamtdruck,  $\geq 90\%$  Isotopenreinheit). Eine relative Präzision von  $0,34 \cdot 10^{-3}$  wurde für die Überwachung der  $T_2$ -Konzentration bei einer Messzeit von 295 s erreicht (188 mbar  $T_2$  Partialdruck). Die von KATRIN geforderte relative Präzision wurde folglich erfüllt, sogar bei deutlich geringeren Messzeiten als gefordert. Gleichzeitig wurde eine Nachweisgrenze von  $4,8 \cdot 10^{-3}$  mbar erreicht, was einer Verbesserung um einen Faktor fünf gegenüber des bis dato sensitivsten Prototyps entspricht. Diese Ergebnisse belegen den Erfolg der implementierten Verbesserungen.

---

Das im Rahmen dieser Arbeit entwickelte Programm LARASoft ermöglicht die vollständig automatisierte Aufnahme und Analyse von Ramanspektren. Daher ist es erstmalig möglich, dass geschultes, jedoch nicht auf Ramanspektroskopie spezialisiertes, Personal quantitative Gasanalysen von Tritiumgasmischungen in nahezu Echtzeit durchführen können. Die Software überwacht außerdem den Zustand des Ramansystems und warnt die Betreiber im Falle einer Fehlfunktion.

Die zentrale optische Komponente des KATRIN Ramansystems ist die Probenzelle, die mit optischen Fenstern ausgestattet ist und sich aus Gründen des Strahlenschutzes innerhalb einer Handschuhbox befindet. Die Antireflexbeschichtungen auf diesen Fenstern müssen über Monate oder Jahre hinweg intensiver Laserbestrahlung, Umwelteinflüssen, sowie durch  $\beta$ -Strahlung ausgelösten physikalischen und radio-chemischen Prozessen standhalten. Eine vor Beginn dieser Arbeit aufgetretene massive Beschädigung der dem Tritiumgas zugewandten Seite der Fenster der Probenzelle zeigt, dass dieser Aspekt nicht unterschätzt werden darf. Als vermutliche Ursache für die Beschädigung wurde die Bildung von korrosiven Fluorwasserstoffverbindungen identifiziert. Durch den Austausch einer einzigen Komponente im Gaszirkulationssystem konnten weitere vergleichbare Beschädigungen verhindert werden.

Weitere schädliche Einflüsse auf optische Beschichtungen, die durch den Betrieb innerhalb von Handschuhboxen und Tritiumgasumgebung hervorgerufen werden können, wurden untersucht und bezüglich ihrer Relevanz bewertet. Poröse Beschichtungen, die auf der thermischen Verdampfung des Beschichtungsmaterials basieren, sind im allgemeinen anfälliger gegenüber Umwelteinflüssen (Veränderung von Druck, Sauerstoffkonzentration und Luftfeuchtigkeit) als Beschichtungen mit größerer Packungsdichte. Diese allgemeine Aussage wurde auch für den Einfluss von Tritiumgas bestätigt. Thermisch aufgedampfte Beschichtungen zeigten bereits nach ca. zehn Tagen Kontakt mit Tritiumgas Anzeichen einer Veränderung, während Beschichtungen, die auf ionenstrahlgestützter Deposition, Magnetron- und Ionenstrahlputtern basieren, selbst nach 39 Tagen noch keine Auffälligkeiten aufwiesen. Daher sollten im Gegensatz zur derzeitigen Praxis thermisch aufgedampfte Beschichtungen nicht in Handschuhboxen und tritiumführenden Anlagen verwendet werden. Mittels Magnetronputtern beschichtete Fenster wurden für die Probenzelle gefertigt und werden in naher Zukunft unter realistischen Bedingungen getestet.

Es wurden im Rahmen dieser Arbeit wertvolle Erfahrungen für den Betrieb des Ramansystems gewonnen. Diese erlauben, die Betriebsparameter des KATRIN Ramansystems und die zur dauerhaften Wahrung seiner messtechnischen Leistungsfähigkeit notwendigen Wartungen und Kontrollen festzulegen. Das System kann mit einer Messzeit von 20 s betrieben werden und gleichzeitig die geforderte Präzision von  $10^{-3}$  erreichen, was die Überwachung von kurzzeitigen Schwankungen der Gaszusammensetzung erlaubt. Da dies über die ursprünglichen gestellten Anforderungen hinausgeht, ist aus Sicht des KATRIN Ramansystems eine weitere Sensitivitätssteigerung von KATRIN möglich.

Ramanspektroskopie ist heute nicht mehr nur eine Technik, die grundsätzlich in der Lage ist quantitative Gasanalysen von Tritiumgasgemischen durchzuführen, sondern vielmehr ein verlässliches und leistungsfähiges Hilfsmittel, das standardmäßig beim KATRIN Experiment eingesetzt werden kann. Damit ist ein wichtiger Schritt auf dem Weg zur Neutronenmassenmessung mit dem KATRIN Experiment vollzogen.

# Contents

<b>List of Figures</b>	<b>xi</b>
<b>List of Tables</b>	<b>xv</b>
<b>Introduction</b>	<b>1</b>
<b>1. Neutrino physics</b>	<b>3</b>
1.1. Postulation, discovery and properties of neutrinos . . . . .	3
1.2. Neutrino oscillations . . . . .	5
1.3. Theoretical models of neutrino masses . . . . .	12
1.4. Impact of neutrino masses on cosmology . . . . .	14
1.5. Methods of neutrino mass measurement . . . . .	15
1.5.1. Indirect measures . . . . .	16
1.5.2. Direct methods . . . . .	19
<b>2. The KATRIN Experiment</b>	<b>25</b>
2.1. Working principle . . . . .	25
2.1.1. Physical principles of the tritium $\beta$ -spectrum . . . . .	25
2.1.2. Concept of the Windowless Gaseous Tritium Source (WGTS) . . . . .	28
2.1.3. Concept of the MAC-E filter . . . . .	29
2.2. Experimental overview . . . . .	31
2.2.1. WGTS cryostat and Inner Loop . . . . .	32
2.2.2. Calibration and monitoring section . . . . .	34
2.2.3. Transport section . . . . .	34
2.2.4. Spectrometer and detector section . . . . .	35
2.3. Neutrino mass sensitivity and WGTS-related systematic effects . . . . .	35
2.4. Monitoring of the source gas composition using Raman spectroscopy . . . . .	39
2.5. Objectives of this work . . . . .	40
<b>3. Quantitative Raman spectroscopy of hydrogen isotopologues</b>	<b>43</b>
3.1. Rotational-vibrational excitations of diatomic molecules . . . . .	45
3.1.1. Semi-classical model of rotational-vibrational excitations . . . . .	45
3.1.2. Selection rules and calculation of Raman line positions . . . . .	49
3.2. Raman line intensities . . . . .	51
3.3. Quantitative analysis of Raman spectra of hydrogen isotopologues . . . . .	56
<b>4. The KATRIN Raman system LARA3: Setup and commissioning</b>	<b>63</b>
4.1. Experience from preceding Raman system prototypes . . . . .	63
4.2. Experimental setup of LARA3 . . . . .	65
4.2.1. LARA3 <i>pre</i> : A pre-stage of the KATRIN Raman system . . . . .	66

4.2.2.	Excitation beam path and laser . . . . .	66
4.2.3.	Raman sample cell (LARA cell) . . . . .	71
4.2.4.	Light collection and analysis system . . . . .	73
4.2.5.	Monitoring systems and auxiliary equipment . . . . .	75
4.3.	Overview and objectives of LARA3 commissioning . . . . .	81
4.4.	Commissioning of LARA3 <i>pre</i> with static gas mixtures . . . . .	81
4.4.1.	LARA3 <i>pre</i> run 1: Characterisation of light collection system and double pass configuration . . . . .	82
4.4.2.	LARA3 <i>pre</i> run 2: Long-term test and monitoring of system performance . . . . .	88
4.5.	Characterisation of the Finesse laser . . . . .	96
4.6.	Commissioning of LARA3 at the LOOPINO facility . . . . .	100
4.6.1.	The tritium circulation test loop LOOPINO . . . . .	101
4.6.2.	Monitoring of a circulating tritium gas mixture (run C148) . . . . .	104
4.6.3.	Status of optical components after run C148 . . . . .	112
4.7.	Evaluation of the results with respect to KATRIN . . . . .	115
<b>5.</b>	<b>Durability of optical coatings in tritium and glove box environments</b>	<b>119</b>
5.1.	Introduction to optical coatings . . . . .	120
5.1.1.	Working principles of optical multilayer coatings . . . . .	120
5.1.2.	Manufacturing methods of optical coatings . . . . .	122
5.2.	Coatings employed in the KATRIN Raman system and coating issues encountered . . . . .	123
5.3.	Harmful effects on coatings in glove box and tritium environments . . . . .	127
5.3.1.	Radiation-induced densification . . . . .	127
5.3.2.	Vacuum, hydrogen, and water moisture-related effects . . . . .	131
5.3.3.	Laser-induced contamination . . . . .	131
5.3.4.	Formation of tritiated hydrogen fluoride species . . . . .	133
5.3.5.	Conclusions . . . . .	137
5.4.	Durability test of optical coatings in highly purified tritium gas . . . . .	138
5.4.1.	Description of coating samples . . . . .	139
5.4.2.	Experimental setup . . . . .	139
5.4.3.	Inspection of already damaged LARA cell windows . . . . .	143
5.4.4.	Tritium exposure of samples and status of samples . . . . .	143
5.4.5.	Discussion of results . . . . .	148
5.5.	Improved coating scheme for LARA cell and glove box windows . . . . .	148
5.6.	Conclusions . . . . .	150
<b>6.</b>	<b>Software for the operation of the KATRIN Raman system</b>	<b>153</b>
6.1.	Requirements for the LARA software package . . . . .	153
6.2.	Existing software for the operation of Raman systems and data analysis . . . . .	155
6.2.1.	Data acquisition software . . . . .	155
6.2.2.	Data analysis software . . . . .	156
6.2.3.	Suitability of existing software for the operation of the KATRIN Raman system . . . . .	156

6.3. LARASoft: Software for the automated operation of the KATRIN Raman system . . . . .	156
6.3.1. General software control . . . . .	156
6.3.2. Selection and configuration of sensors and devices . . . . .	157
6.3.3. System status monitoring . . . . .	157
6.3.4. Configuration of data analysis procedures . . . . .	157
6.3.5. Real-time view of Raman spectrum and gas composition . . . . .	163
6.3.6. Raw CCD image and focus mode . . . . .	163
6.3.7. Storage of settings in measurement templates . . . . .	166
6.3.8. Connection of LARASoft to the KATRIN data acquisition and management framework . . . . .	166
6.4. Evaluation of software performance with respect to KATRIN . . . . .	166
<b>7. Recommendations for the operation of the KATRIN Raman system</b>	<b>171</b>
7.1. Experimental aspects . . . . .	171
7.2. Data acquisition and analysis settings . . . . .	172
7.3. Parameters to be monitored in particular during the operation of the KATRIN Raman system . . . . .	175
7.4. Maintenance of the LARA system between two neutrino mass measurement runs . . . . .	175
<b>8. Summary and outlook</b>	<b>179</b>
<b>A. Proposed system for simple and reliable wavelength calibration</b>	<b>183</b>
<b>B. Procedures and SpecTools settings for analysis of Raman data</b>	<b>189</b>
B.1. LARA3 <i>pre</i> run 1 . . . . .	189
B.2. LARA3 <i>pre</i> run 2 . . . . .	190
B.2.1. Pre-processing and generation of necessary correction files . . . . .	190
B.2.2. SpecTool analysis of Raman spectra in batch mode of SpecTools . . . . .	191
B.3. LARA3 run C148 . . . . .	192
<b>C. Calculation of beam sizes and power densities for Gaussian beams</b>	<b>195</b>
<b>D. Details on optical coatings employed in this work</b>	<b>197</b>
D.1. Coating samples in durability test . . . . .	197
D.2. Reflectance plots of improved coatings for LARA cell windows . . . . .	200
<b>Publications</b>	<b>203</b>
<b>Index</b>	<b>204</b>
<b>Bibliography</b>	<b>207</b>



# List of Figures

1.1.	Example for $\nu_e \rightarrow \nu_\mu$ neutrino oscillations for $(\sin^2(2\theta) = 0.2)$ . . . . .	8
1.2.	Simulation of baryon density distribution in the universe as function of the sum of neutrino masses . . . . .	14
1.3.	Neutrino mass scenarios and relation to density parameter $\Omega$ . . . . .	16
1.4.	Neutrinoless double $\beta$ -decay. . . . .	18
1.5.	Single $\beta$ -decay . . . . .	21
1.6.	Results of previous neutrino mass experiments using tritium $\beta$ -decay . . . . .	22
2.1.	Tritium $\beta$ -spectrum for zero and non-zero neutrino mass . . . . .	27
2.2.	Schematic drawing of the Windowless Gaseous Tritium Source . . . . .	28
2.3.	Principle of the MAC-E filter . . . . .	30
2.4.	CAD drawing of the KATRIN experiment . . . . .	31
2.5.	Picture of WGTS source tube during manufacturing and schematic diagram of two phase neon cooling system . . . . .	32
2.6.	Schematic flow diagram of Inner Loop . . . . .	33
2.7.	Final states distribution of daughter molecules . . . . .	38
2.8.	Schematic drawing of a Raman spectroscopy system and exemplary Raman spectrum . . . . .	40
3.1.	Quantum mechanical picture of Raman scattering . . . . .	43
3.2.	Impact of vibrational nuclear potential on Raman spectrum . . . . .	48
3.3.	Generic Raman spectrum of a diatomic molecule . . . . .	52
3.4.	Definition of scattering angles $\varphi, \theta$ . . . . .	54
3.5.	Raman spectrum of T <sub>2</sub> , DT mixture . . . . .	56
3.6.	Raman spectrum of all hydrogen isotopologues . . . . .	57
3.7.	Data flow diagram of SpecTools . . . . .	61
4.1.	Degradation of anti-reflection coated optical windows after contact with highly purified tritium gas . . . . .	65
4.2.	Layout of optical beam path of LARA3 <sub>pre</sub> and LARA3 . . . . .	67
4.3.	Working principle of an optical isolator . . . . .	69
4.4.	Raman sample cell (LARA cell) with tapped holes . . . . .	72
4.5.	Fibre bundle . . . . .	74
4.6.	Top view of the KATRIN Raman system . . . . .	80
4.7.	Chromatic aberration in light collection system . . . . .	83
4.8.	Raman spectrum of H <sub>2</sub> , HD, D <sub>2</sub> gas sample . . . . .	84
4.9.	Chromatic aberration in single pass configuration . . . . .	85
4.10.	Chromatic aberration in double pass configuration . . . . .	87

4.11. Comparison of rel. Raman intensities measured in single pass (SP) and double pass (DP) configuration . . . . .	88
4.12. Temperature in the laser enclosure, beam power, and beam position during LARA3pre run 2 . . . . .	90
4.13. Raman spectrum and dark spectrum from LARA3pre run 2 . . . . .	91
4.14. Example spectrum of LARA3pre run 2 with fitted branches and lines . . . . .	93
4.15. Relative Raman intensities of LARA3pre run 2 . . . . .	95
4.16. LARA3pre run 2: Histograms of residuals of linear fit of $I_{rel}$ . . . . .	96
4.17. Layout of beam path for test of Finesse laser . . . . .	97
4.18. Parameters of Finesse laser for different water chiller temperature set points	98
4.19. Finesse laser parameters for 24°C water chiller temperature set point . . . . .	99
4.20. LOOPINO flow diagram . . . . .	102
4.21. The 'Appendix'. A hardware interface for Raman measurements with LARA cells inside the glove box . . . . .	102
4.22. Dismantled regulation valve VAI83406 of LOOPINO . . . . .	104
4.23. Averaged Raman spectra at time $t = 0.5 - 1.5$ h and $t = 113.5 - 114.5$ h of run C148 . . . . .	106
4.24. Relative Raman intensities measured in run C148 . . . . .	108
4.25. Histogram of residuals of $I_{rel}$ of LARA3 run C148 . . . . .	108
4.26. Laser and sensor data of run C148 . . . . .	110
4.27. Spots on selected optics after run C148 . . . . .	112
4.28. Damaged LARA cell window $L_1$ after run C148 . . . . .	113
5.1. Estimation of reflection losses for the case of uncoated windows . . . . .	119
5.2. Snell's law and multiple reflections in a thin layer . . . . .	121
5.3. Schematic drawing of microscopic structure of amorphous $SiO_2$ . . . . .	127
5.4. Effect of $\pm 1\%$ refractive index variation of the first coating layer on the reflectance $R$ of the AR coating . . . . .	129
5.5. Removal of laser-induced contamination on a LARA cell window by UV irradiation . . . . .	133
5.6. Determination of vacuum laser wavelength . . . . .	136
5.7. Raman spectrum with calculated HF, DT, TF line positions . . . . .	137
5.8. Coating samples IV1, IV2, IV3, IV4, and the uncoated substrate IV6 (from left to right) inside sample holder before exposure to tritium . . . . .	140
5.9. Holding structure and vessel for tritium exposure . . . . .	141
5.10. Microscope images of damaged AR coatings on LARA cell windows . . . . .	144
5.11. Microscopy images of coating samples after tritium exposure . . . . .	147
5.12. New coating scheme for LARA cell and Appendix windows . . . . .	149
5.13. Raman and laser window after magnetron sputtering . . . . .	150
6.1. 'Main' tab of LARASoft . . . . .	158
6.2. 'Sensors and devices' tab of LARASoft . . . . .	159
6.3. Schematic drawing of algorithm for evaluation of a sensor values . . . . .	159
6.4. 'LARA status monitoring' tab of LARASoft . . . . .	160
6.5. 'Data processing of individual spectra' tab of LARASoft . . . . .	161
6.6. 'Live view' tab of LARASoft . . . . .	164
6.7. 'Alignment' tab of LARASoft . . . . .	165

---

6.8. Schematic overview of the continuous data acquisition and analysis . . . .	167
A.1. CAD visualisation of proposed system for wavelength calibration of the HTS spectrometer . . . . .	183
A.2. Overview drawing of system for wavelength calibration . . . . .	185
A.3. Drawing of the fibre mount with collimation lens . . . . .	186
A.4. Drawing of the flip mount . . . . .	187
C.1. Beam waist of a Gaussian beam at the focus point . . . . .	195
D.1. Transmittance plots of coating samples 1 (IAD) and 2 (MS) . . . . .	198
D.2. Transmittance plots of coating samples 3 (IBS) and 4 (EBD) . . . . .	199
D.3. Reflectance plots of broadband AR coating of LARA cell Raman windows based on magnetron sputtering and electron beam deposition . . . . .	201
D.4. Reflectance plots of 532 nm AR coating of LARA cell laser windows based on magnetron sputtering . . . . .	202



# List of Tables

1.1.	Leptons in the standard model . . . . .	5
1.2.	Best fit results for neutrino oscillation parameters . . . . .	12
1.3.	Recent limits on $T_{1/2}$ and $m_{\beta\beta}$ from $0\nu\beta\beta$ experiments . . . . .	19
3.1.	Energy conversion coefficients . . . . .	44
3.2.	Rotational, vibrational and electrical excitation energies of $H_2$ and $T_2$ .	45
3.3.	Definition of branches based on selection rules. . . . .	51
3.4.	Influence of $J''$ on nuclear weight $g_N$ . . . . .	54
4.1.	Parameters of lasers and water chillers . . . . .	71
4.2.	LARA cell parameters . . . . .	73
4.3.	LARA3 sensors and hardware parameters . . . . .	78
4.4.	Overview of LARA3 <i>pre</i> runs . . . . .	82
4.5.	Attribution of atomic emission lines observed in LARA3 <i>pre</i> run 2 . . . . .	92
4.6.	Achieved relative precision in LARA3 <i>pre</i> run 2 . . . . .	94
4.7.	Statistical analysis of laser parameters for 24°C temperature set point of water chiller . . . . .	100
4.8.	Overview of LARA3 operation at LOOPINO (run C148) and details on windows of LARA cell . . . . .	105
4.9.	Achieved relative precision in LARA3 run C148 . . . . .	109
4.10.	Chronological overview of LARA cell pressure , LOOPINO operation conditions, and performed actions . . . . .	111
4.11.	Calculated laser power density at various positions in the LARA3 setup and comparison to laser induced damage threshold (LIDT) . . . . .	114
5.1.	Comparison of selected physical vapour deposition coating manufacturing techniques . . . . .	124
5.2.	Optical coatings on selected transparent components in the Raman system	125
5.3.	List of experienced optical coating damages at TLK . . . . .	126
5.4.	Influence of a +1% variation of the refractive index in the first coating layer on the relative Raman intensities . . . . .	130
5.5.	Raman line positions and Raman shifts from literature . . . . .	135
5.6.	Calculated Raman shifts of HF, DF, and TF . . . . .	136
5.7.	Details on coating types in durability test . . . . .	140
5.8.	Overview of actions performed during durability test . . . . .	145
6.1.	Example for labelling of analysis results . . . . .	167
7.1.	Example specification of parameter ranges for the grading of the system status . . . . .	174

A.1. Main components of the proposed wavelength calibration system . . . . .	184
C.1. Calculated laser power density at various positions in the LARA3 setup .	196
D.1. Details on the materials and structure of the coating samples . . . . .	197

# Introduction

Neutrinos are elementary particles and part of the standard model of particle physics which describes the fundamental properties and interactions of matter. Neutrinos are massless particles in the basic form of the standard model as they do not couple to the vacuum expectation value of the Higgs field [Zub11]. However, the discovery of neutrino oscillations has proven that neutrinos must have mass by the measurement of non-zero values for differences of the mass squares  $\Delta m_{ij}^2 = m_i^2 - m_j^2$  between the mass eigenstates (e.g. [Ber13a] and references therein). Experiments aiming at the measurement of the absolute value of the neutrino mass have not yet been sensitive enough and hence only resulted in an upper limit of about 2 eV/c<sup>2</sup> (95% C.L.) [Kra05, Lob03, Ase11]. Although this limit is considered as a great success in experimental physics, the result is not yet sufficient to trigger progress in particle physics and cosmology. So is the knowledge of the absolute value of the neutrino mass crucial to further scrutinise theoretical models which aim for an explanation of neutrino masses [Zub11]. The accurate measurement of the neutrino mass will also help in the context of cosmology where the neutrino mass is one of the parameters that influenced the structure formation in the early universe [Aba11]. Here, an independent laboratory measurement of the neutrino mass would clarify the role of neutrinos as hot dark matter and would help to decrease the number of fit parameters in the cosmological models and hence reduce their complexity .

The aim of the Karlsruhe Tritium Neutrino experiment (KATRIN) [KAT05] is the model-independent measurement of the neutrino mass by the investigation of the endpoint region of the tritium  $\beta$ -spectrum. The KATRIN experiment is designed to discover a neutrino mass of 350 meV/c<sup>2</sup> with 5 $\sigma$  significance and to be able to set an upper limit of 200 meV/c<sup>2</sup> (90% C.L.) in case no neutrino mass can be detected. KATRIN will therefore probe the neutrino mass parameter space in a region relevant for cosmology and particle physics [Dre13]. KATRIN uses a Windowless Gaseous Tritium Source (WGTS) which combines a high source activity (10<sup>11</sup> Bq) with low systematic uncertainties. It is essential for the minimisation of the systematic uncertainties in KATRIN to operate the WGTS with highly purified tritium gas (95% isotopic purity). Additionally, changes of the gas composition have to be detected and taken into account when determining the neutrino mass from the tritium  $\beta$ -spectrum [Bab12]. For this purpose, a system is required that monitors the source gas composition automatically, continuously (every < 250 s), and precisely (monitoring of the isotopic purity with a relative precision < 10<sup>-3</sup>). These metrological requirements have to be reliably fulfilled over the course of about 5 years of KATRIN operation while keeping the need for maintenance as low as possible.

Raman spectroscopy is the method of choice for the compositional analysis of the tritium gas in the WGTS since all hydrogen isotopologues (T<sub>2</sub>, DT, D<sub>2</sub>, HT, HD, H<sub>2</sub>) cannot only be identified but also quantified [Stu10a]. Within the joint R&D work at Swansea University and Tritium Laboratory Karlsruhe (KIT) in the past years, three prototypes

of Raman spectroscopy systems have been built, tested, and operated. It could be shown that Raman spectroscopy is able to meet the requirements specified by the KATRIN experiment [Sch11c, Fis11, Sch13d].

However, the task remains to actually design, construct and commission the Raman system for KATRIN which has to be optimised with respect to two aspects. On the one hand, the experience gained from the prototype systems and additional ideas should be exploited to maximise the metrological performance of the system. On the other hand, special care has to be taken to ensure the reliable and stable operation of the system over the complete operation time. The general objective of this work therefore is to accomplish this task and reach such a state of maturity for the KATRIN Raman system, that it can be reliably and effectively operated in the KATRIN experiment.

Three subtasks are of particular relevance in this work:

1. Design, setup and commissioning of the KATRIN Raman system with the aim to maximise the metrological performance.
2. Investigation and elimination of detrimental processes affecting the stability of the system during long-term operation. Particular emphasise is thereby placed on the anti-reflection coatings of the optical components that are operated under special atmospheric conditions, e.g. in glove boxes filled with nitrogen gas, or are even in direct contact with the radioactive tritium gas.
3. Development of an operation software for the KATRIN Raman system that features the automated acquisition and quantitative analysis of Raman spectra but also monitors the status of the laser system during unattended long-term operation.

The thesis is structured as follows: Neutrinos, their relevance for particle physics and cosmology, and the available techniques for neutrino mass measurements are introduced in chapter 1. The KATRIN experiment and the necessity of a Raman system in KATRIN are presented in chapter 2. At the end of this chapter, also the objectives of this work are further refined. The theoretical foundations of quantitative Raman spectroscopy are summarised in chapter 3. The design and commissioning of the KATRIN Raman system is discussed in chapter 4. The durability of optical coatings in tritium or glove box atmosphere is subject of chapter 5. The operation software for the KATRIN Raman system is presented in chapter 6. Chapter 7 gives an overview of recommendations for the operation of the KATRIN Raman system. The work is concluded by a summary and outlook in chapter 8.

# 1. Neutrino physics

Since its onset with  $\beta$ -decay studies in 1914, neutrino physics has been a rich source of puzzles and surprises as a result of the peculiar properties and interactions of this elementary particle. It took about 40 years from the observation of the first indirect indications for the existence of neutrinos in 1914 [Cha14] to the actual discovery of neutrinos in 1953 [Rei56]. Since then, neutrino physics has continuously gained pace and nowadays is a very vivid field of research and it has stimulated significant progress in nuclear and (astro)particle physics, and in cosmology.

Neutrinos are elementary particles, electrically neutral and take part only in the weak interaction which makes them hard to detect and study. Neutrinos have spin  $\frac{1}{2}$  and a tiny but non-zero rest mass (less than  $1/250000$  of the electron rest mass).

Many of the initially puzzling features in neutrino physics have been explained but even a century after the onset of neutrino and weak interaction physics, fundamental questions remain:

- How do neutrinos behave under CP transformations?
- Are neutrinos of Dirac or Majorana type and what is their mass?
- How are neutrino masses generated and why are they so small in comparison to the other elementary particles?
- How did neutrinos influence the formation of large scale structure in the early universe?

This chapter will give an overview of neutrinos and selected neutrino properties (section 1.1 and 1.2). Special emphasise will be put on the the theoretical foundation of neutrino masses (section 1.3), the impact of neutrinos on cosmology (section 1.4), and on experimental methods for the measurement of neutrino masses (section 1.5).

## 1.1. Postulation, discovery and properties of neutrinos

Neutrino physics can be traced back to 1914 when J. Chadwick discovered a continuous electron spectrum in the  $\beta$ -decay of  $^{214}\text{Pb}$  and  $^{214}\text{Bi}$  [Cha14]. Discrete spectra had been observed before in the two-body  $\alpha$ - and  $\gamma$ -decays and a likewise behaviour had been expected for  $\beta$ -decay. The continuous spectrum was confirmed in two additional experiments [Ell27, Mei30] and hence was in conflict to the principle of energy conservation in a nuclear decay. In order to avoid abandoning the energy conservation, W. Pauli in his classical letter proposed an additional, undetectable spin- $\frac{1}{2}$  particle to participate

in the interaction [Pau30]. The postulation of a new particle (nowadays known as the 'neutrino') formed the basis for today's understanding of  $\beta$ -decay

$$(Z, A) \rightarrow (Z + 1, A) + e^- + \bar{\nu}_e \quad (1.1)$$

where the mother nucleus (atomic number  $Z$ , mass number  $A$ ) transforms into a daughter nucleus (atomic number  $Z + 1$ , mass number  $A$ ) under the emission of an electron  $e$  and an electron anti-neutrino  $\bar{\nu}_e$ <sup>1</sup>. The undetected neutrino carries away missing energy and angular momentum which explains the continuous energy spectrum in the, now, three-body decay. Pauli also realised that neutrinos must have a 'small' mass and can only interact weakly with matter [Pau30]. The understanding of  $\beta$ -decay was significantly improved shortly thereafter based on the theoretical description by E. Fermi [Fer34] which is still being valid today as the low-energy limit of weak interactions and also used in KATRIN for the description of the  $\beta$ -spectrum (section 2.1).

In 1956, the first neutrino was detected by F. Reines and C. L. Cowan using a nuclear fission reactor as an intense source of electron anti-neutrinos  $\bar{\nu}_e$  [Rei56]. They utilised the 'classical' inverse  $\beta$ -decay reaction

$$\bar{\nu}_e + p \rightarrow n + e^+ \quad (1.2)$$

in a water target with dissolved  $\text{CdCl}_2$ . The tank was equipped with liquid scintillator detectors. The positron  $e^+$  was detected by the two 511 keV electrons stemming from its annihilation and the neutron  $n$  by the delayed gammas from the  $^{113}\text{Cd}(n,\gamma)^{114}\text{Cd}$  capture reaction. The experimentally measured cross section of  $(11 \pm 2.6) \cdot 10^{-44}\text{cm}^2$  was in agreement with theoretical predictions [Rei59].

After the discovery of electron (anti-)neutrinos, the two other neutrino flavour states coupling to muon  $\mu$  and tau  $\tau$  leptons were subsequently discovered at particle accelerators: the muon neutrino  $\nu_\mu$  in 1962 by the AGS neutrino experiment [Dan62] and the tau neutrino  $\nu_\tau$  in 2000 by the DONUT experiment [Kod01]. A fourth generation (flavour) of neutrinos with  $m_\nu \lesssim 104 \text{ GeV}/c^2$  was not found at the  $e^+e^-$  collider LEP at CERN where also the total number  $N_\nu = 2.92 \pm 0.05$  of 'light' neutrino generations ( $m_\nu < 45 \text{ GeV}/c^2$ ) was determined from the decay width of the Z boson [ALE06].

Neutrinos are fermions (spin  $\frac{1}{2}$ ) and belong to the group of leptons in the standard model (table 1.1) which only interact via the weak interaction. The weak interaction maximally violates parity, i.e. only left-handed neutrinos and right-handed anti-neutrinos take part in the weak interaction. This is a consequence of the V-A theory of the weak interaction [Sch95]. It will be shown in section 1.3 that right-handed neutrinos and left-handed anti-neutrinos would be needed to generate neutrino masses via Yukawa couplings, i.e. in the same fashion as for the other fermions in the standard model [Zub11]. Since such types of (anti-)neutrinos have not yet been discovered, neutrinos were considered massless in the basic form of the standard model.

---

<sup>1</sup>on the quark level, this corresponds to a down-quark decaying into an up-quark while interacting with a W boson which couples to an electron and an anti-neutrino.

**Table 1.1.: Leptons in the standard model.** Leptons and their anti-particles are subdivided into three generations (also called 'flavours').

	Generations			Electric Charge	Spin	Interactions
	1	2	3			
Particles	$\nu_e$	$\nu_\mu$	$\nu_\tau$	0	1/2	Weak
	$e^-$	$\mu^-$	$\tau^-$	$- e $	1/2	Weak, electromagnetic
Anti-particles	$\bar{\nu}_e$	$\bar{\nu}_\mu$	$\bar{\nu}_\tau$	0	1/2	Weak
	$e^+$	$\mu^+$	$\tau^+$	$+ e $	1/2	Weak, electromagnetic

## 1.2. Neutrino oscillations

The properties of neutrinos have been studied in great detail over the past five decades. Of special importance were the large number of neutrino oscillation experiments in which flavour changing processes of neutrinos were observed. These experiments have yielded clear experimental proof that neutrinos must possess a non-zero mass. However, this type of experiment is not able to directly measure the neutrino mass but can assess only the difference of the mass squares of the mass eigenstates. Therefore, complementary experiments aiming for the measurement of the absolute mass scale of neutrinos are of vital importance. This section will give an overview of neutrino oscillation experiments and their implications for our understanding of neutrino properties.

### Solar neutrino problem

The study of neutrino oscillations was triggered by the so-called 'solar neutrino problem' which refers to a discrepancy between the expected and the measured flux of solar neutrinos on earth. The sun is an intense source of neutrinos as a result of the large number of nuclear fusion processes of hydrogen to helium in the dominant pp cycle [Zub11]



For the following historical discussion, the most relevant neutrino production process in the sun is the decay of  ${}^8\text{B} \rightarrow {}^4\text{He} + {}^4\text{He} + e^+ + \nu_e$ . Although the flux rate of  ${}^8\text{B}$  neutrinos is a factor  $10^4$  smaller than for pp neutrinos,  ${}^8\text{B}$  neutrinos are much easier to detect due to their larger energy of  $E_{\nu, {}^8\text{B}} < 15 \text{ MeV}$  ( $E_{\nu, \text{pp}} < 0.42 \text{ MeV}$ ) [Zub11, Bah05]. Predictions for the neutrino flux on earth stemming from the fusion reactions in the sun existed already in the 1960s [Bah64] when the first experiment for the measurement of solar neutrinos was proposed by R. Davis [Dav64]. The experiment was setup in the Homestake mine and consisted of a large detector of liquid perchloroethylene  $\text{C}_2\text{Cl}_4$ . The flux of electron neutrinos was measured by the reaction  $\nu_e + {}^{37}\text{Cl} \rightleftharpoons {}^{37}\text{Ar} + e^-$  and the subsequent detection of single argon atoms in a radio-chemical synthesis [Dav68]. The actual experimental results for the measured electron neutrino flux, however, were a factor of seven smaller than the theoretical expectations [Dav68] which became a significant open issue in astrophysics and particle physics and was dubbed the 'solar neutrino problem'.

Much later, these pioneering experimental results were verified by other radio chemical experiments, namely by GALLEX [GAL99], SAGE [SAG02], and GNO [GNO05] and by the water Cerenkov detector Kamiokande and Super-Kamiokande [Sup98a].

### Neutrino oscillations

At the same time as the onset of the solar neutrino experiments, Pontecorvo and Gribov proposed that transitions ('oscillation') between the neutrino flavours can occur [Pon67, Pon68, Gri69]. Based on this assumption, a fraction of the electron neutrinos emitted in the sun could have been oscillated into other types of neutrinos while travelling to earth. As the detection mechanism is solely sensitive to electron neutrinos, a reduced flux rate would then be detected in comparison to the initial flux which would explain the solar neutrino problem. As will be shown later in this section, compelling evidence for neutrino oscillations has been found since 1998 not only for solar neutrinos but also for neutrinos from other sources like nuclear fission reactors, particle accelerators and from atmospheric neutrinos. Therefore, neutrino oscillations nowadays are a well-established fact. The current understanding of neutrino oscillations is based on the ground-laying work of Pontecorvo [Pon68] and Maki, Nakagawa and Sakata [Mak62] and will be briefly outlined.

Neutrinos are produced in weak interactions and hence are represented by a weak eigenstate  $|\nu_\alpha\rangle$  where  $\alpha = e, \mu, \tau$  stands for one of the lepton flavours. Neutrinos with non-zero masses and corresponding mass eigenstates  $|\nu_i\rangle$  do not necessarily have to be identical to the flavour eigenstates. The flavour eigenstates thus can be written according to

$$|\nu_\alpha\rangle = \sum_i U_{\alpha i} |\nu_i\rangle \quad (1.4)$$

$$|\nu_i\rangle = \sum_{\alpha=e,\mu,\tau} U_{\alpha i}^* |\nu_\alpha\rangle \quad (1.5)$$

as linear superposition of the mass eigenstates and vice versa [Zub11].  $U_{\alpha i}$  thereby is an element of the unitary Pontecorvo-Maki-Nakagawa-Sakata (PMNS) matrix which connects the flavour bases with the bases of the mass eigenstates. A parametrisation of the PMNS matrix  $U$  in the standard case of three flavour and mass eigenstates, is a  $3 \times 3$  matrix [Ber13a]

$$U = \begin{pmatrix} c_{12}c_{13} & s_{12}c_{13} & s_{13}e^{-i\delta} \\ -s_{12}c_{23} - c_{12}s_{23}s_{13}e^{i\delta} & c_{12}c_{23} - s_{12}s_{23}s_{13}e^{i\delta} & s_{23}c_{13} \\ s_{12}s_{23} - c_{12}c_{23}s_{13}e^{i\delta} & -c_{12}s_{23} - s_{12}c_{23}s_{13}e^{i\delta} & c_{23}c_{13} \end{pmatrix} \times \begin{pmatrix} 1 & 0 & 0 \\ 0 & e^{i\frac{\alpha_{23}}{e}} & 0 \\ 0 & 0 & e^{i\frac{\alpha_{31}}{e}} \end{pmatrix} \quad (1.6)$$

where  $s_{ij} = \sin \theta_{ij}$  and  $c_{ij} = \cos \theta_{ij}$ . The parameters  $\theta_{12}$ ,  $\theta_{13}$ , and  $\theta_{23}$  are the mixing angles,  $\delta$  a CP<sup>2</sup> violating Dirac phase [Ber13a]. If neutrinos are Majorana particles, additional phases  $\alpha_{21}$  and  $\alpha_{31}$  appear, which however are inaccessible in oscillation studies.

---

<sup>2</sup>CP-symmetry is the invariance of physical processes under the charge conjugation (C) and parity (P) transformations.

The three-flavour form of  $U$  nowadays is used to interpret neutrino oscillation data (when neglecting potential sterile neutrinos). However, for the sake of simplicity and clarity and due to the observation that oscillation scales of solar and atmospheric neutrinos are separated by more than one order of magnitude, the following discussion will be restricted to the case of two flavours and mass eigenstates and, correspondingly, the absence of CP violation. Under these assumptions, eq (1.6) reduces to a  $2 \times 2$  matrix and eq. (1.4) can be written as

$$\begin{pmatrix} \nu_e \\ \nu_\mu \end{pmatrix} = \begin{pmatrix} \cos \theta & \sin \theta \\ -\sin \theta & \cos \theta \end{pmatrix} \begin{pmatrix} \nu_1 \\ \nu_2 \end{pmatrix} \quad (1.7)$$

with a single mixing angle  $\theta$ . Each of the two mass eigenstates  $|\nu_i\rangle$  has a well-defined mass  $m_i$ . Based upon this formalism, predictions for different experimental scenarios can be made. The probability for a neutrino of flavour  $\alpha$  and energy  $E$  to be detected as a neutrino of flavour  $\beta \neq \alpha$  after propagating a distance ('baseline')  $L$  through vacuum is given by [Zub11]

$$P(\nu_\alpha \rightarrow \nu_\beta) = \sin^2(2\theta) \sin^2\left(\frac{\Delta m^2 L}{4\hbar c E}\right) \geq 0. \quad (1.8)$$

The mixing angle  $\theta$  determines the maximum value of  $P(\nu_e \rightarrow \nu_\mu)$  while the difference of the mass squares  $\Delta m^2 = m_2^2 - m_1^2$  defines the frequency of the oscillation. The energy dependence in (1.8) originates from the time evolution of the mass eigenstates while propagating. The probability that a neutrino of flavour  $\alpha$  is also detected as neutrino of flavour  $\alpha$  is accordingly given by

$$P(\nu_\alpha \rightarrow \nu_\alpha) = 1 - P(\nu_\alpha \rightarrow \nu_\beta) \leq 1. \quad (1.9)$$

Experiments measuring  $P(\nu_\alpha \rightarrow \nu_\beta)$  with  $\alpha \neq \beta$  are called appearance experiments because they search for neutrinos belonging to a new flavour which was initially not present. When measuring  $P(\nu_\alpha \rightarrow \nu_\alpha)$ , experiments are called disappearance experiments since they measure a reduction ('disappearance') of the neutrino flux due to oscillations into another flavour. Examples for both types of experiments are shown in figure 1.1. The characteristic quantity is the oscillation length [Zub11]

$$L_0 = 4\pi\hbar c \frac{E}{\Delta m^2} = 2.48 \text{ m} \cdot \frac{E/\text{MeV}}{\Delta m^2/\text{eV}^2} \quad (1.10)$$

which depends on neutrino energy  $E$  and on  $\Delta m^2$ . Experiments are typically designed such that the neutrino flux rate is measured close to the oscillation length where the oscillation effect is the strongest and hence the best experimental sensitivity is achieved. For reactor neutrinos ( $E \approx 1-8$  MeV [Mül11]) and a value  $\Delta m^2 = 2 \cdot 10^{-3}$  eV<sup>2</sup> [Ber12] the oscillation length is about  $L_0 \approx (1-10)$  km. For neutrinos from accelerators ( $E \approx 1$  GeV [Abe14a], same value for  $\Delta m^2$ ),  $L_0 \approx 10^3$  km is significantly larger and hence more difficult to realise.

Generally speaking, a neutrino oscillation experiment measures the variation of the neutrino flux rate relative to the initial flux rate at the position of the neutrino production.

The solar neutrino problem was caused by the, at that time, missing independence evidence of the accuracy of the calculations of the neutrino production rates in the sun. Although the neutrino flux predictions for stars, nuclear reactors and accelerators have improved, they are still a significant source for systematic uncertainties (e.g. for nuclear fission reactors [Mül11]). Modern neutrino oscillation experiments therefore aim for a measurement of the oscillation parameters (mixing angle and  $\Delta m^2$ ) which is mostly independent of the initial neutrino flux. Principally, this can be achieved in three ways which ideally are combined in a single experiment:

- If a neutrino detector is located at a fixed position where the (dis)appearance probability  $P$  changes significantly with neutrino energy, an oscillation pattern (figure 1.1) can actually be measured. This requires a sufficiently good energy resolution for the neutrino detector and the exact knowledge of the shape of the 'un-oscillated' spectrum (including the influence of the detector response). An impressive example was published by the KamLAND experiment for electron anti-neutrinos from nuclear fission reactors [Abe08]. Complementary, as in the case of atmospheric neutrinos, the source-detector baseline can be varied to obtain ideal conditions [Hos06].
- The neutrino flux of a source is measured by two (or more), ideally identical detectors at different baselines. The first detector is placed close enough to the source so that oscillations have not yet significantly affected the neutrino flux. The second detector is placed at a baseline where the oscillation effect is large. By measuring the ratio of the neutrino fluxes, the oscillation parameters can be determined. This 'near-far' technique is often employed in experiments using accelerators [Abe11c, Mic08] or nuclear fission reactors [An14, Ahn12].
- Assuming a constant neutrino energy, a spatial variation of the number of detected neutrinos can be detected if the oscillation length is small in comparison to the size of the neutrino detector, i.e. the oscillation probability changes significantly within

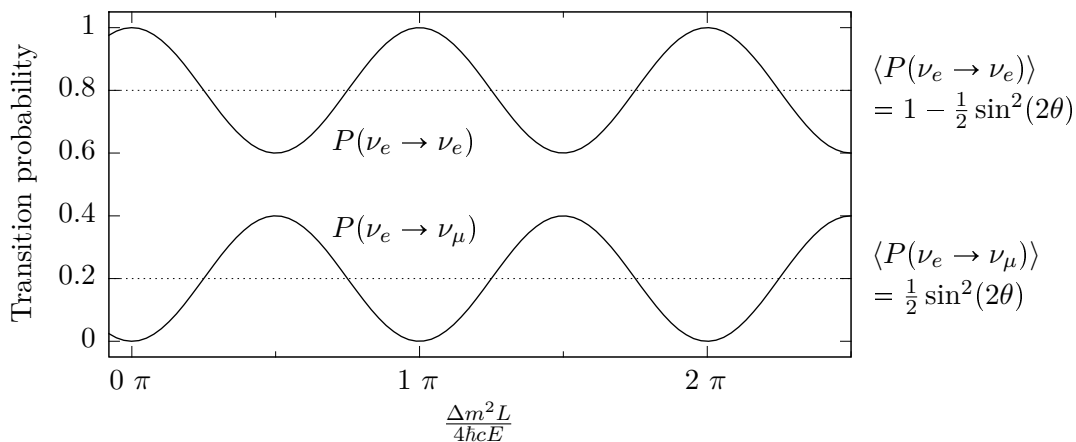


**Figure 1.1.: Example for  $\nu_e \rightarrow \nu_\mu$  neutrino oscillations ( $\sin^2(2\theta) = 0.2$ ).** The oscillation effect reaches its first maximum at  $\frac{E}{L} = \frac{\Delta m^2}{4\pi\hbar c}$ . *Upper curve:* Disappearance experiment. *Lower curve:* Appearance experiment.

the detector. Obviously, a sufficiently good spatial detector resolution is necessary and a broad neutrino energy distribution will cause a smearing of the pattern. This technique will potentially be used in the search for sterile neutrinos [Aba12].

The PMNS matrix has been probed by various experiments in the past years. The experiments were sensitive on different parameters of the PMNS matrix depending on the neutrino source (and hence energy) and the experimentally realised baseline. Significant progress in the understanding of the PMNS matrix was made by combining results from different experiments in the full three flavour treatment of neutrino oscillations. Here, only a brief overview of selected results will be given.

### Solar neutrinos

As discussed before, solar neutrinos were already studied in the 1970s by radio-chemical experiments which led to the solar neutrino problem. The commissioning of the water Cerenkov detector Kamiokande and later of its larger successor Super-Kamiokande allowed to measure the flux rate of solar neutrinos for the first time in real-time and to resolve the direction of the incident neutrino [Hir90, Hir91, Kam96, Sup98a]. The neutrino detection is based on neutrino-electron scattering

$$\nu_\alpha + e^- \rightarrow \nu_\alpha + e^- \quad (1.11)$$

which in principle is sensitive to all neutrino flavours  $\alpha = e, \mu, \tau$  but dominated by electron neutrinos [Zub11]. The electrons are accelerated above the speed of light in water and hence emit Cerenkov light which is detected by photo multiplier tubes. Kamiokande and Super-Kamiokande measured consistent  ${}^8\text{B}$  neutrino fluxes [Abe11b] which were about a factor of two smaller than the predictions of the standard solar model [Bah01].

The solar neutrino problem was solved in 2001 when the Sudbury Neutrino Observatory (SNO) measured the total  ${}^8\text{B}$  neutrino flux rate, i.e. the flux rate of  $\nu_e$ ,  $\nu_\mu$ , and  $\nu_\tau$ . The SNO detector was also making use of the Cerenkov effect but employed 1000 tons of heavy water ( $\text{D}_2\text{O}$ ), and in a specific phase 2 tons of dissolved salt ( $\text{NaCl}$ ), as detector material [SNO01]. This allowed for the observation of two additional detection channels

$$\nu_e + \text{d} \rightarrow e^- + \text{p} + \text{p} \quad (\text{CC}) \quad (1.12)$$

$$\nu_\alpha + \text{d} \rightarrow \nu_\alpha + \text{p} + \text{n} \quad (\text{NC}) \quad (1.13)$$

besides the electron neutrino dominated elastic scattering (ES; eq. (1.11)) [Aha13]. While the charged current (CC) reaction is only sensitive to electron neutrinos, the neutral current (NC) reaction is equally sensitive to all flavours. The NC channel for the first time allowed one to measure the total  ${}^8\text{B}$  neutrino flux and comparison to the other flavour-selective channels to discriminate between the  $\nu_e$  and ( $\nu_\mu, \nu_\tau$ ) contributions. The total neutrino flux rate was found to be  $(5.44 \pm 0.99) \cdot 10^6 \text{ cm}^{-2} \text{ s}^{-1}$  [SNO01] and hence in good agreement with the predictions from the standard solar models [Bah01, Bru98, Bru99]. The neutrino flux rate in the ES channel was consistent with results from Super-Kamiokande and the flux rate in the CC channel (solely sensitive on  $\nu_e$ ) was one third of the total flux [SNO01]. This showed that the solar neutrino problem was caused by the significant non-electron neutrino components in the  ${}^8\text{B}$  neutrino flux which stem from

neutrino oscillations. The results of all SNO measurement phases are summarised in [Aha13] and yield the following oscillation parameters

$$\Delta m_{21}^2 = (5.6_{-1.4}^{+1.9}) \cdot 10^{-5} \text{ eV}^2 \quad (1.14)$$

$$\tan^2 \theta_{12} = 0.427_{-0.029}^{+0.033} \quad (1.15)$$

For completeness, it should be noted that solar neutrinos are also studied by the Borexino experiment [Bel12]. Borexino detected solar neutrinos from the pep reaction for the first time [Bel12] and further demonstrated the reduction of the survival probability of high-energetic electron neutrinos to be due to the Mikheyev–Smirnov–Wolfenstein (MSW) effect [Bel10, Mik85, Wol78].

### Atmospheric neutrinos

Cosmic rays impinging on the the upper atmosphere produce mesons which can subsequently decay into muons and neutrinos [Zub11]. As can be seen in the example of pion decay

$$\begin{aligned} \pi^+ &\rightarrow \mu^+ + \nu_\mu \\ &\hookrightarrow e^+ + \nu_e + \bar{\nu}_\mu, \end{aligned} \quad (1.16)$$

roughly a value of about 2 is expected for the flavour ratio  $R = (\nu_\mu + \bar{\nu}_\mu)/(\nu_e + \bar{\nu}_e)$  between muon (anti-)neutrinos and electron (anti-)neutrinos [Hir88] flux rates. Atmospheric neutrinos have energies in the GeV range and propagate at variable baseline  $L$  depending on their point of production. If produced in the atmosphere directly above the neutrino detector,  $L \approx 10$  km is realised but if produced in the atmosphere at the opposite side of the earth, the baseline is enlarged to  $L \approx 10^4$  km [Zub11]. This allows one to probe the oscillation probability  $P$  as a function of  $L/E$  when measuring the ratio  $R$  as a function of the neutrino direction (zenith angle) in the experiment. First indications for oscillations of atmospheric muon neutrinos were already found in 1994 by the Kamiokande experiment [Fuk94], which was followed by a definite evidence for  $\nu_\mu \rightarrow \nu_\alpha$  oscillations in 1998 by the Super-Kamiokande experiment [Sup98b]. Recent results for the oscillation parameters are [Abe11a]

$$1.2 \cdot 10^{-3} \text{ eV}^2 \leq |\Delta m_{23}^2| \leq 4 \cdot 10^{-3} \text{ eV}^2 \text{ (90\% C.L.)} \quad (1.17)$$

$$0.78 \leq \sin^2 2\theta_{23} \text{ (90\% C.L.)} \quad (1.18)$$

which indicate a significantly larger mass splitting  $\Delta m^2$  than for solar neutrinos. However, the sign of  $\Delta m_{23}^2$  is currently not yet determined.

### Accelerator neutrinos

Neutrino beams are produced in particle accelerators by irradiating a target (e.g. graphite or aluminium) with a proton beam. The pions produced in the interaction are sign selected for a specific charge ( $\pi^+$  or  $\pi^-$ ) and collimated. When decaying, they produce a beam of muon (anti-)neutrinos with energies up to a few hundred GeV [Zub11]. Special experimental measures are taken to reduce to electron neutrino 'contamination' of the beam to the few-percentage range and to decrease the energy spread of the neutrinos

[And98, Abe11c, Ahn01]. A near and far detector concept (far baseline between 250-300 km [Ahn01, Abe11c] and about 730 km [MIN11, Acq06]) is typically realised. The appearance channel  $\nu_\mu \rightarrow \nu_e$  allows one to measure  $\theta_{13}$  and the CP violating phase  $\delta$  (eq.(1.6)) while the disappearance channel  $\nu_\mu \rightarrow \nu_\mu$  is sensitive on  $\Delta m_{32}^2$  and  $\theta_{23}$  [Zub11]. The T2K experiment reported an accurate measurement of  $\theta_{23}$  [Abe14b]

$$|\Delta m_{31}^2| > 0 : \quad \sin^2(2\theta_{23}) = 0.514_{-0.056}^{+0.055} \quad \Delta m_{32}^2 = (2.51 \pm 0.10) \cdot 10^{-3} \text{ eV}^2/c^4 \quad (1.19)$$

$$|\Delta m_{31}^2| < 0 : \quad \sin^2(2\theta_{23}) = 0.511 \pm 0.055 \quad \Delta m_{32}^2 = (2.48 \pm 0.10) \cdot 10^{-3} \text{ eV}^2/c^4 \quad (1.20)$$

which takes into account that the sign of  $|\Delta m_{31}^2|$  is not yet known. The measurement of the CP violating phase  $\delta$  is not yet possible but experiments start to disfavour certain values of  $\delta$  [Abe14a]. A definite measurement of  $\delta$  will only be possible with future long baseline neutrino oscillation experiments [Ada13, Rub13].

The OPERA experiment [Acq06] provided experimental information on  $\nu_\mu \rightarrow \nu_\tau$  oscillations. Based on the observation of three tau neutrino events, the hypothesis of no oscillations can be currently excluded with  $3.4\sigma$  confidence [Aga14]. Detection of a fourth tau neutrino was reported recently [OPE14].

### Reactor neutrinos

Nuclear fission reactors are intense sources for electron anti-neutrinos ( $E_\nu \leq 8$  MeV) which stem from a cascade of thousands of  $\beta$ -decays of the fission products of  $^{235}\text{U}$ ,  $^{238}\text{U}$ ,  $^{239}\text{Pu}$ , and  $^{241}\text{Pu}$  [Zub11]. The experiments Daya Bay [An12, An13, An14], Reno [Ahn12, Kim14] and Double Chooz [Abe12, Dou12] recently measured  $\theta_{13}$ , the smallest of all mixing angles. The results are consistent and hence combined by [Ber12] to a best fit value of

$$\sin^2 2\theta_{13} = 0.095 \pm 0.010. \quad (1.21)$$

A recalculation of neutrino flux predictions of nuclear reactors [Men11] has re-ignited the discussion about the potential existence of an additional generation of 'sterile' neutrinos [Aba12]. These hypothetical particles are dubbed 'sterile' as they do not interact via the left-handed weak interaction. Their existence can only be detected by mixing effects, such as in oscillation experiments where a fraction of 'active' neutrinos oscillates into the sterile state and hence reduces the number of observed neutrinos in the experiment. The subject of sterile neutrinos is an open issue at the time of writing. A variety of experimental efforts [Aba12], also within KATRIN [For11, Ste13], are ongoing to verify or disprove the hypothesis.

### Summary

To fully exploit the results of all experiments, global analyses in the three neutrino framework (e.g. [GG12, For12a, Fog13, Ber12]) have to be performed. Table 1.2 lists the best fit results for the oscillation parameters from [Ber12]. Currently, neither the sign of  $\Delta m_{23}^2$  nor the mass of the lightest mass eigenstate is known. This leads to three possible scenarios for the mass eigenstates.

- 'Normal' hierarchy  $\left( \Delta m_{23}^2 > 0, m_1 \ll \sqrt{\Delta m_{12}^2} \right) : m_1 \ll m_2 < m_3.$

**Table 1.2.: Best fit results for neutrino oscillation parameters.** Source [Ber12].

Parameter	Unit	Best fit value ( $\pm 1\sigma$ )
$\Delta m_{21}^2$	eV <sup>2</sup>	$(7.50 \pm 0.20) \cdot 10^{-5}$
$ \Delta m_{23}^2 $	eV <sup>2</sup>	$(2.32^{+0.12}_{-0.08}) \cdot 10^{-3}$
$\sin^2(2\theta_{12})$		$0.857 \pm 0.024$
$\sin^2(2\theta_{23})$		$> 0.95$ (90% C.L.)
$\sin^2(2\theta_{13})$		$0.095 \pm 0.010$

- 'Inverted' hierarchy ( $\Delta m_{23}^2 < 0, m_3 \ll \sqrt{|\Delta m_{23}^2|}$ ) :  $m_3 \ll m_1 < m_2$ .
- 'Quasi-degenerate' scenario ( $m_i \ll \sqrt{|\Delta m_{23}^2|}$ ) :  $m_1 \approx m_2 \approx m_3$ .

In the first two cases, the mass of the lightest mass eigenstate is small in comparison to the lower mass splitting, i.e. there are three distinct neutrino masses. In the third case (quasi-degenerate), the mass of the lightest mass eigenstate is so large that the masses can be approximated by a single neutrino mass. Future experiments based on neutrinos from accelerators [Pat13, Ada13, Rub13], reactors [Zha08, Zha09, Li14], and the atmosphere [Aar14] will be sensitive on the mass hierarchy. However, it is essential to measure the absolute scale of neutrino masses, a task which cannot be accessed via oscillation experiments.

### 1.3. Theoretical models of neutrino masses

Neutrino oscillations have proven that there are at least two neutrino mass eigenstates with non-zero mass. The question therefore arises how non-zero neutrino masses are theoretically explained. This section discusses different theoretical models for the generation of neutrino masses.

Charged fermions gain mass in the standard model via the spontaneous symmetry breaking and the Higgs mechanism [Hig64, Kib67]. The doublet of scalar Higgs fields obtains a non-zero vacuum expectation value which couples to a doublet of left-handed and a singlet of right-handed fermions [Zub11]. This coupling is called Yukawa coupling and creates a term in the Lagrangian which, in case for the electron, is [Zub11]

$$\mathcal{L}_{\text{Yuk}} = -\frac{c_e v}{\sqrt{2}} (\bar{e}_R e_L + \bar{e}_L e_R) \quad (1.22)$$

$$= -\frac{c_e v}{\sqrt{2}} \bar{e} e \quad (1.23)$$

$$= -m_e \bar{e} e. \quad (1.24)$$

$c_e$  is a coupling constant and  $v$  the vacuum expectation value of the Higgs field.  $e$  is the Spinor of the electron and  $\bar{e}$  the adjoint spinor. The indices  $L, R$  indicate if the neutrino

is left- or right-handed. In eq. (1.24), the electron mass  $m_e$  was introduced. Neutrinos are massless in the standard model because no right-handed neutrino singlet state exists in the V-A theory [Sch95].

### Extension of the standard model by right-handed neutrinos

The standard model can be extended by introducing right-handed neutrino singlet states. Hence a Yukawa coupling also becomes possible for neutrinos and a so-called 'Dirac mass term', similar to eq.(1.23), is added to the Lagrangian. However, to explain the smallness of the neutrino masses in comparison to other fermions (e.g.  $m_e/m_\nu > 2.6 \cdot 10^5$  for  $m_\nu < 2$  eV), a tiny coupling constant  $c_\nu$  has to be introduced. Although this scenario seems possible, such a small coupling constant is often regarded as 'unnatural'.

### Majorana mass term and seesaw mechanism

Also so-called Majorana mass terms can be introduced in the Lagrangian yielding a total mass term of [Sch97]

$$\mathcal{L} = -\frac{1}{2} \left[ \begin{pmatrix} \bar{\nu}_L & \bar{N}_L^c \end{pmatrix} \begin{pmatrix} m_L & m_D \\ m_D & m_R \end{pmatrix} \begin{pmatrix} \nu_R^c \\ N_R \end{pmatrix} + \text{h.c.} \right] \quad (1.25)$$

$N$  stands for a heavy and sterile, i.e. not weakly interacting, neutrino. The indices  $L, R$  indicate if the neutrino is either left- or right-handed. The superscript  $c$  labels the charge conjugate state, i.e. an anti-neutrino, and h.c. stands for the hermitian conjugate expression. The mass matrix consists of one Dirac mass  $m_D$  and two Majorana masses  $m_L$  and  $m_R$ . The mass eigenstates are acquired by diagonalising the mass matrix. This corresponds to a transformation from the flavour bases to the bases of the mass eigenstates. Three specific cases will be discussed:

- For  $m_L = m_R = 0$ , the mass eigenstates have the mass  $m = m_D$ , i.e. the Dirac mass term is realised.
- For  $m_L = 0$  and  $m_R \gg m_D$ , two distinct mass eigenstates are found

$$m_1 = \frac{m_D^2}{m_R} \ll m_D \quad (1.26)$$

$$m_2 = m_R \left( 1 + \frac{m_D^2}{m_R^2} \right) \approx m_R. \quad (1.27)$$

The condition  $m_R \gg m_D$  makes  $m_1$  small, i.e.  $m_1 \ll m_D$ . The actual magnitude of  $m_1$  depends on the choice which mass scale is used for  $m_D$  (e.g. charged lepton masses or quark masses [Zub11]) and obviously on  $m_R$ . The second mass eigenstate  $m_2 \approx m_R$  is heavy and for most models out of range for experiments. This model is called type I seesaw mechanism [GM79, Yan79, Moh80, Moh81] and elegantly explains the smallness of neutrino masses.

If neutrinos are of Majorana type, also lepton number violating processes are possible [Zub11]. This is relevant for the neutrinoless double  $\beta$ -decay that will be discussed further below in this chapter.

- If  $m_R \gg m_D$  and  $m_L \neq 0$  but  $m_L \ll m_R$ , a second contribution to the neutrino mass is added due to a coupling to the Higgs field [Zub11]. This can lead to almost degenerate, i.e. approximately identical, neutrino masses. This model is called type II seesaw.

### Neutrino masses due to supersymmetry and Higgs triplets

Models going even further beyond the standard model allow for other ways of neutrino mass generation. As an example, R-parity violating supersymmetric models can be mentioned [Hir04]. Also the introduction of a Higgs triplet in addition to the Higgs doublet allows to generate neutrino mass [Zub11].

## 1.4. Impact of neutrino masses on cosmology

According to the 'Big Bang' model, the universe was formed in a hot dense state and since then has been expanding and simultaneously cooling down [Per09]. The universe is isotropic and on large scales ( $> 100 \text{ Mpc} = 3.1 \cdot 10^{18} \text{ m}$ ) homogeneous [Zub11]. However, existing density inhomogeneities (e.g. galaxy clusters) at the present epoch were presumably caused by quantum fluctuations in the early universe which were amplified during the inflationary stage of the universe and then subsequently grew by gravitational clustering [Per09]. In the early universe, neutrinos were free-streaming relativistic particles and hence caused a damping of the gravitational clustering. The effect was most significant on small scales and the strength did depend on the total neutrino mass  $m_{\text{tot}} = \sum_i m_i$  [Per09]. An example of this effect is shown in figure 1.2 where a section of the universe was simulated for different values of  $m_{\text{tot}}$ .

Apart from their impact on the formation of large-scale structure, neutrinos also contribute to the overall matter and energy content of the universe. The evolution of the universe is determined by the Friedmann equations which connect the energy contributions of radiation, matter and dark energy to the geometry of the universe [Per09]. The universe is observed to be flat, i.e. it has a Euclidean geometry, in this case the critical

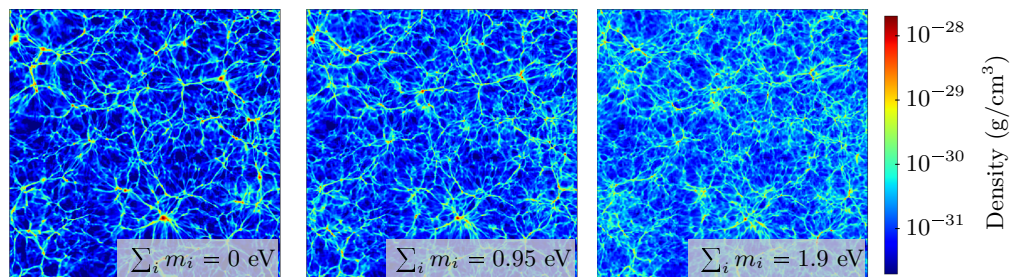


**Figure 1.2.: Simulation of baryon density distribution in the universe as function of the sum of neutrino masses.** An increasing neutrino mass reduces the maximum density, i.e. massive neutrinos smear out small scale structure. Each slice is  $200h^{-1}\text{Mpc}$  wide. Image adopted from [Aga10].

energy density is [Zub11]

$$\varrho_{\text{crit}} = \frac{3H_0^2}{\pi G}. \quad (1.28)$$

Here,  $H_0$  is the Hubble parameter (first measured in 1929 [Hub29]), and  $G$  the gravitational constant. The energy density  $\varrho_x$  of a certain contribution  $x$  is typically expressed by the density parameter

$$\Omega_x = \frac{\varrho_x}{\varrho_{\text{crit}}} \quad (1.29)$$

i.e. relative to the critical energy density.

Neutrinos contribute to the energy density as 'hot' dark matter because they do not take part in the electromagnetic interaction (dark) and they were relativistic (hot) when decoupling from the thermal equilibrium in the early universe [Per09]. The density parameter of neutrinos with masses in the range between  $5 \cdot 10^{-4}$  eV and 1 MeV can be parametrised by [Ber13b]

$$\Omega_\nu h^2 \approx \frac{\sum_i m_i c^2}{93 \text{ eV}} \quad (1.30)$$

using the total neutrino mass and the dimensionless Hubble parameter

$$h = \frac{H_0}{100} \cdot \frac{\text{s Mpc}}{\text{km}} \approx 0.68 \quad (1.31)$$

where  $H_0$  was taken from [PC14a]. Eq. (1.30) is also visualised in figure 1.3 for the normal and inverted hierarchy and the quasi-degenerate scenario.

As neutrino masses currently are open parameters in cosmological models, a laboratory measurement of neutrino masses would reduce the number of open parameters and hence increase the confidence of parameters deduced from them.

## 1.5. Methods of neutrino mass measurement

This section gives an overview of methods for neutrino mass determination. It has to be pointed out early on that not all methods have the same observable, i.e. different 'kinds' of neutrino mass are determined. This has to be taken into account when comparing and combining results. The methods will be split into direct and indirect methods:

- Direct methods are based purely on kinematics and hence on the conservation of momentum and the validity of the energy-momentum relation

$$E^2 = p^2 c^2 + m^2 c^4 \quad (1.32)$$

where  $E$  is the particle energy,  $p$  the momentum,  $m$  the rest mass, and  $c$  the speed of light. Such methods are mostly model-free, i.e. they do not rely on additional assumptions. The time-of-flight measurement of cosmic neutrinos and the single  $\beta$ -decay will be discussed as examples of direct methods.

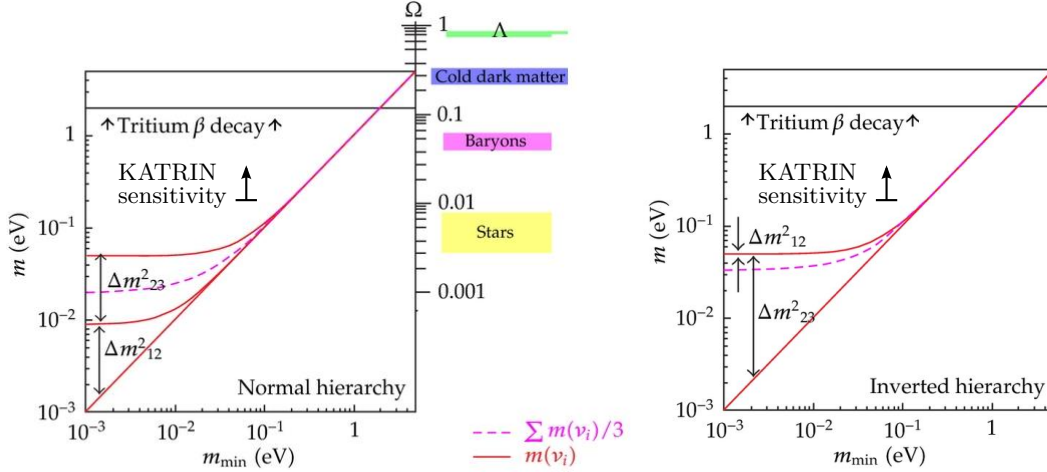


**Figure 1.3.:** Neutrino mass scenarios and relation to energy density parameter  $\Omega$ . The mass eigenvalues and a third of the total neutrino mass are plotted as a function of the smallest mass eigenvalue. The density parameter  $\Omega_\nu$ , calculated according to eq.(1.30), is shown as a second vertical axis for comparison. The ranges of the other energy contributions (stars, baryons, cold dark matter, dark energy  $\Lambda$ ) are indicated. The current laboratory limit on the neutrino mass  $m < 2$  eV (95% C.L.) [Kra05, Ase11, Ber12] corresponds to a density parameter of  $\Omega_\nu < 0.12$  [Dre13]. Image adopted from [Dre13].

- Indirect methods do not only rely on fundamental assumptions on intrinsic neutrino properties but they typically rely also on a sophisticated model to extract the neutrino mass from a physical process. This makes the determination of the neutrino mass more susceptible to systematic and model-dependent uncertainties. Nevertheless, indirect methods allow one to probe aspects of neutrino physics which cannot be accessed by direct methods (e.g. verification of the Majorana nature of the neutrino) and they are valuable cross-checks for direct methods. The deduction of the neutrino mass from cosmological observations and the neutrinoless double  $\beta$ -decay will be discussed as representatives of indirect methods.

### 1.5.1. Indirect measures

#### Deduction from astrophysical observations

As discussed in section 1.4, the neutrino mass plays a distinct role in the evolution of the universe. This can be employed to deduce the total neutrino mass  $m_{\text{tot}} = \sum_i m_i$  from astrophysical and cosmological observations:

- Observations of large-scale structure, i.e. the distribution of galaxy clusters (e.g. by the Sloan Digital Sky Survey (SDSS) [Ahn14]).
- Study of the cosmic microwave background (CMB) [Pen65], e.g. by the WMAP [Ben13] and Planck [PC14a] satellites and the South Pole Telescope [Sch11a] and the Atacama Cosmology Telescope [Sie13].

The total neutrino mass  $m_{\text{tot}}$  typically is determined by fitting a large number of parameters to the different data sets. The Planck collaboration has recently released an analysis which results in upper limits in the range

$$m_{\text{tot}} = \sum_i m_i < 0.23 - 1.08 \text{ eV}/c^2 \quad (95\% \text{ C.L.}) \quad (1.33)$$

depending on the considered data sets [PC14b]. The cosmological constraints on  $m_{\text{tot}}$  seem to be more sensitive than laboratory measurements of the neutrino mass. However, the limits from cosmological observations are prone to systematic uncertainties and therefore must be verified by independent measurements. Ideally, a future determination of the neutrino mass by a laboratory measurement would allow one to fix the neutrino mass as input to cosmological models and hence reduce the complexity of the analysis of cosmological and astrophysical data.

### Investigation of neutrinoless double $\beta$ -decay

Double  $\beta$ -decay

$$(Z, A) \rightarrow (Z + 2, A) + 2e^- + 2\bar{\nu}_e \quad (2\nu\beta\beta) \quad (1.34)$$

is a rare process which can be considered as two simultaneous  $\beta$ -decays within one nucleus with atomic number  $Z$  and mass number  $A$  [Goe35]. The symbol  $2\nu\beta\beta$  is used to denote this process since two electrons ( $\beta\beta$ ) and two anti-neutrinos ( $2\nu$ ) are emitted due to the conversion of the neutrons (down quarks) into protons (up quarks). The energy spectrum of the total electron energy  $E = E_{e1} + E_{e2}$  (with  $E_{ei}$  being the energy of the electron  $i$ ) is continuous due to the accompanying neutrino emission. The  $2\nu\beta\beta$  process is only relevant for even-even<sup>3</sup> nuclei which for energetic reasons cannot decay via single  $\beta$ -decay. This is the case if the mass  $m(Z, A)$  of the mother nucleus is smaller than the mass of the single  $\beta$ -decay daughter nucleus, i.e.  $m(Z, A) < m(Z + 1, A)$ , and if simultaneously  $m(Z, A) > m(Z + 2, A)$  is fulfilled [Zub11]. Albeit a low probability due to its nature as a second-order weak interaction,  $2\nu\beta\beta$  has been observed for different isotopes, e.g. for  $^{136}\text{Xe}$  (half-life  $T_{1/2} \approx 2 \cdot 10^{21}$  yr) [Alb14b],  $^{76}\text{Ge}$  ( $T_{1/2} \approx 1.8 \cdot 10^{21}$  yr) [GER13] and for  $^{100}\text{Mo}$  ( $T_{1/2} \approx 7 \cdot 10^{17}$  yr) and other isotopes in the NEMO-3 experiment [Fla11, Bar11].

Far more interesting would be the observation of a neutrinoless double  $\beta$ -decay

$$(Z, A) \rightarrow (Z + 2, A) + 2e^- \quad (0\nu\beta\beta) \quad (1.35)$$

process. Here, a virtual Majorana neutrino is exchanged in the nucleus instead of the emission of two anti-neutrinos (figure 1.4, left). This process can only occur if two conditions are fulfilled:

- The neutrino is of Majorana nature, i.e. its own anti-particle. This is necessary as the Majorana neutrino is emitted as an 'anti'-neutrino in one  $\beta$ -decay and absorbed as a neutrino in the second  $\beta$ -decay.

<sup>3</sup>Nuclei with an even number of protons and neutrons are called even-even nuclei. Such nuclei have a large binding energy due to the pairing term in the Bethe-Weizsäcker mass formula [Wei35] and are hence very stable.

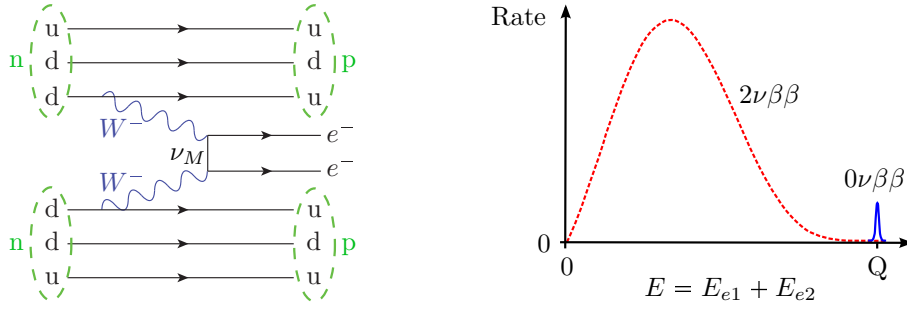


**Figure 1.4.: Neutrinoless double  $\beta$ -decay.** *Left:* Feynman diagram. The process requires an exchange of a virtual massive Majorana neutrino  $\nu_M$  which performs a spin-flip between emission and absorption. *Right:* Spectrum of total electron energy ( $E_{e1}$  and  $E_{e2}$  is the energy of the electron 1 and 2, respectively). The spectrum is continuous in case of  $2\nu\beta\beta$ . For  $0\nu\beta\beta$ , only a mono-energetic line at the Q-value of the decay is observed. The intensity of the  $0\nu\beta\beta$  peak is artificially increased for the purpose of illustration.

- The Majorana neutrino has a non-zero rest mass which enables the required 'spin-flip' between emission (right-handed 'anti'-neutrino) and absorption (left-handed neutrino). The larger the mass of the neutrino for a fixed neutrino energy, the more probable is the 'spin-flip'. Hence, the neutrino mass will be related to the half-life  $T_{1/2}$  of the process.

The observable of  $0\nu\beta\beta$  is a mono-energetic line at the Q-value of the decay in the total electron energy spectrum (figure 1.4, right). This is a distinct feature in contrast to the continuous spectrum of  $2\nu\beta\beta$ . The half-life of the process is given by [Zub11]

$$T_{1/2} = \left( G^{0\nu}(Q, Z) |M_{\text{nuc}}|^2 \left( \frac{m_{\beta\beta}}{m_e} \right)^2 \right)^{-1} \quad (1.36)$$

where  $G^{0\nu}(Q, Z)$  is a phase space factor (function of the Q-value of the decay and the atomic number  $Z$  of the nucleus),  $M_{\text{nuc}}$  the nuclear matrix element,  $m_e$  the electron mass and  $m_{\beta\beta}$  the so-called Majorana mass. The Majorana mass

$$m_{\beta\beta} = \left| \sum_i U_{ei} m_i \right|, \quad (1.37)$$

is a coherent superposition of the neutrino mass eigenvalues  $m_i$ , weighted by the complex matrix elements  $U_{ei}$  of the PKMS matrix. Due to the complex  $U_{ei}$  factors,  $m_{\beta\beta}$  can become very small, or even vanish in the specific case of the normal hierarchy [Wei13b]. In order to determine  $m_{\beta\beta}$  from the measured half-life, nuclear matrix elements have to be calculated. This calculation is a dominant source of systematic uncertainty [Zub11].

A wide variety of isotopes is being used by different experiments (selection shown in table 1.3) but no clear evidence for the existence of neutrinoless double  $\beta$ -decay has yet been found. In 2001, a claim for the observation of neutrinoless double  $\beta$ -decay in  $^{76}\text{Ge}$  was published [KK01] and later refined [KK04, Kla06]. Since then, this claim has been controversially discussed in the community but recent experiments start to exclude the

**Table 1.3.: Recent limits on  $T_{1/2}$  and  $m_{\beta\beta}$  from  $0\nu\beta\beta$  experiments.**

Experiment	Status	Isotope	Limits (90% C.L.)		Reference
			$T_{1/2} >$ ( $10^{25}$ yr)	$m_{\beta\beta} <$ (meV)	
NEMO-3	finished	$^{100}\text{Mo}$	0.11	300-900	[NEM13]
GERDA	running	$^{76}\text{Ge}$	2.1	200-400 <sup>†</sup>	[Ago13]
EXO-200	running	$^{136}\text{Xe}$	1.1	190-450	[Alb14a]
KamLAND-Zen	running	$^{136}\text{Xe}$	1.9	120-250	[Kam13]

<sup>†</sup> Based on combined analysis with other  $^{76}\text{Ge}$  data.

claim [Kam13, Ago13, Dev13]. Therefore, up to now, only upper limits for the Majorana mass

$$m_{\beta\beta} < 900 \text{ meV} \quad (90\% \text{ C.L.}) \quad (1.38)$$

can be given (based on table 1.3). It has to be stressed at this point, that this limit cannot be easily compared to neutrino mass limits deduced from single  $\beta$ -decay which will also be discussed in this chapter. This is due to the generic types of neutrino mass the experiments are sensitive to. Therefore, both types of experiments are complementary and give different insights into the neutrino mass.

## 1.5.2. Direct methods

### Supernova time-of-flight measurements

Stars gain energy via the nuclear fusion reactions of light into heavier elements which allows to generate elements up to  $^{56}\text{Fe}$  [Per09]. If the core of the star reaches the Chandrasekhar limit (about 1.4 solar masses), it cannot further obtain nuclear fusion energy and sustain the gravitational pressure, it starts to contract ('core collapse') and afterwards explodes [Per09]. Neutrinos of all types are produced during such a core-collapse supernova via two generic processes:

$$p + e^- \rightarrow n + \nu_e \quad (\text{Neutronisation}), \quad (1.39)$$

$$e^+ + e^- \rightarrow \nu_\alpha + \bar{\nu}_\alpha \quad \alpha = e, \mu, \tau \quad (\text{Thermalisation}). \quad (1.40)$$

The neutronisation process occurs at the scale of milliseconds while the core of the progenitor star is being compressed after the termination of the fusion process while the thermalisation process takes place over about 10 s when the neutrinos of all flavours are slowly diffusing through the dense nuclear material (mean free path is reduced to about 1 m [Sch97]).

On 23 February 1987, the type IIa supernova SN1987A was observed in the Large Magelanic Cloud [Wes87]. Neutrinos from the supernova were detected by the Kamiokande

(12 neutrinos within 13 s,  $E_\nu \leq 35$  MeV) [Hir87] and the IMD (8 neutrinos within 6 s,  $E_\nu \leq 40$  MeV) [Bio87, Bra88] detectors.

Since massive neutrinos propagate with a velocity  $v < c$  depending on their mass  $m_\nu$  and energy  $E_\nu$  and owing to the long baseline between the supernova and the earth ( $L = 1.6 \cdot 10^5$  light years [Sch97]), the detected supernova neutrinos can be used to deduce information on the neutrino mass. The difference  $\Delta t$  of the arrival times of two neutrinos with a common mass  $m_\nu$  but different energies  $E_{\nu 1}$  and  $E_{\nu 2} > E_{\nu 1}$  is given by [Zub11]

$$\Delta t = \Delta t_0 + \frac{Lm_\nu^2}{2c} \left( \frac{1}{E_{\nu 2}^2} - \frac{1}{E_{\nu 1}^2} \right) \quad (1.41)$$

where  $\Delta t_0$  is the time difference of the neutrino emission in the supernova. Assuming  $\Delta t_0 = 0$ , a limit of  $m_\nu < 30$  eV can be deduced from the SN987A neutrinos [Zub11, Sch97]. A refined analysis, also taking into account neutrino emission models, reduced the limit to  $m < 5.7$  eV (95% C.L.) [Lor02] although some model dependence is introduced. Nevertheless, the time-of-flight measurement of supernova neutrinos is still counted as a direct method.

### Investigation of weak decays

At present, the study of weak decays is the most sensitive method to determine the neutrino mass in a direct, model-independent way. Three types of weak decays

$$(Z, A) \rightarrow (Z + 1, A) + \bar{\nu}_e + e^+ \quad \beta^- \text{ - decay} \quad (1.42)$$

$$(Z, A) \rightarrow (Z - 1, A) + \nu_e + e^- \quad \beta^+ \text{ - decay} \quad (1.43)$$

$$e^- + (Z, A) \rightarrow (Z - 1, A) + \nu_e \quad \text{Electron capture} \quad (1.44)$$

generally exist. The most relevant process for neutrino mass determination currently is the  $\beta^-$ -decay, but also experiments based on electron capture do exist. The observable in a  $\beta$ -decay experiment is an 'average electron neutrino mass square' [Ott08, Dre13]

$$m^2(\nu_e) = \sum_i |U_{ei}|^2 m_i^2 \quad (1.45)$$

which differs from the neutrino mass determined in neutrinoless double  $\beta$ -decay in that no cancellations can occur. The decay energy (Q-value) of the  $\beta^-$ -decay is given by the mass difference of the neutral mother and daughter atoms [Zub11]

$$Q = (m(Z, A) - m(Z + 1, A)) c^2 \quad (1.46)$$

In the following, this work will focus on  $\beta^-$ -decay (figure 1.5, left) and the minus superscript will be omitted. If other types of weak decays are discussed, they will explicitly be mentioned. In case of a vanishing neutrino mass and if there are no excitations of the daughter nucleus (or molecule), the so-called endpoint energy  $E_0$  is given by

$$E_0 = Q - E_{\text{rec}} \quad (1.47)$$

where  $E_{\text{rec}}$  is the kinetic energy related to the recoil of the daughter nucleus [Ott08]. These quantities will be of relevance in section 2.1 where the energy spectrum of the

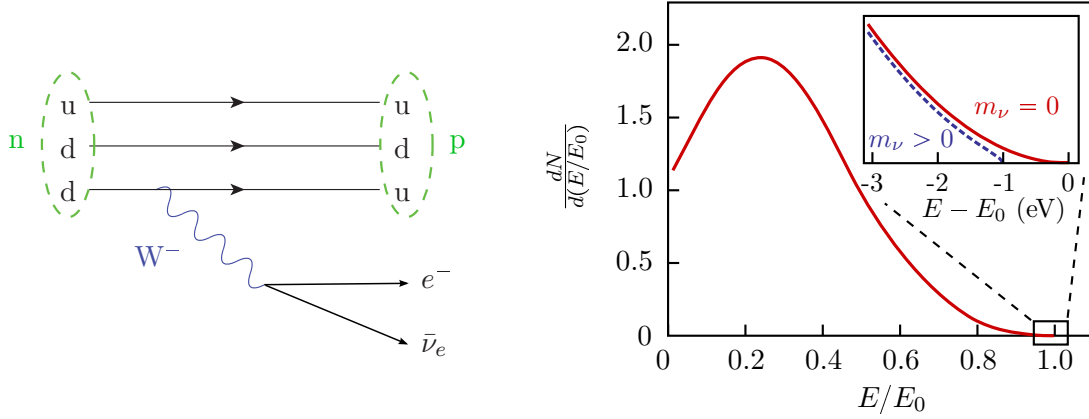


**Figure 1.5.: Single  $\beta$ -decay.** *Left:* Feynman diagram of single  $\beta$ -decay. *Right:* A non-zero neutrino mass  $m_\nu = \sum_i |U_{ei}|^2 m_i^2$  influences the shape of the spectrum only close to the endpoint  $E_0$ . Figure adopted from [Sch13b].

$\beta$ -decay is calculated. A generic electron energy spectrum of  $\beta$ -decay is shown in figure 1.5 where the effect of a non-zero neutrino mass becomes apparent only close to the endpoint  $E_0$ . An experiment aiming for the measurement of the neutrino mass therefore must precisely determine the shape of the spectrum in this region. The hydrogen isotope tritium  ${}^3\text{H}$  (in the following denoted by the symbol T for the sake of simplicity) is the best suited isotope for the neutrino mass measurement because of several reasons [Ott08, Zub11, Wei13]:

- Tritium has a low Q-value of about 18.6 keV which is beneficial for the count rate near the endpoint.
- Tritium  $\beta$ -decay is a super-allowed decay with a short half-life of about 12.3 years. Therefore, only a small amount of tritium is needed to achieve a sufficiently high activity. In addition, the nuclear matrix element of this decay is energy independent which simplifies the analysis of  $\beta$ -spectra (see next chapter).
- Tritium has an atomic number  $Z = 1$  and hence a very simple electronic shell. This minimises the Coulomb interaction between the emitted electron and the nucleus and allows for a detailed theoretical calculation of the process.
- Tritium appears in nature typically in its molecular form  $\text{T}_2$  whose simple structure allows for the quantitative calculation of the excited final states of the daughter molecule ( ${}^3\text{HeT}$ )<sup>+</sup>.

Tritium has been used in many neutrino mass experiments in the past (see figure 1.6). Also the currently most stringent upper limit on the neutrino mass of about  $m(\nu_e) < 2 \text{ eV}/c^2$  (95% C.L.) [Kra05, Ase11, Ber12] was determined from tritium  $\beta$ -decay. Significant improvement was achieved in the 1990s by the introduction of electrostatic spectrometers of the MAC-E type (discussed in section 2.1.3). This type of spectrometer also is employed in the KATRIN experiment [KAT05] which is the next-generation neutrino mass experiment.

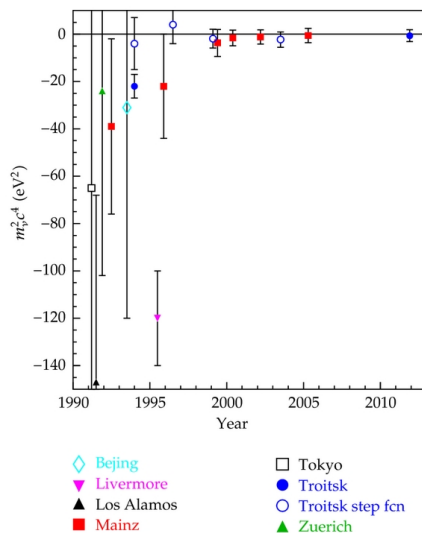


**Figure 1.6.: Results of previous neutrino mass experiments using tritium  $\beta$ -decay.** The experiments in Los Alamos, Zürich, Tokyo, Beijing, and Livermore [Rob91, Hol92, Kaw91, Che95, Sto95] were performed with magnetic spectrometers and the experiments in Troitsk and Mainz with electrostatic spectrometers [Wei99, Kra05, Bel95, Lob99, Ase11]. More information on tritium based neutrino mass measurements can e.g. be found in [Dre13, Ott08]. Figure from [Dre13].

An alternative concept for the measurement of the tritium  $\beta$ -spectrum is currently being investigated by the Project 8 collaboration [Mon09, For12b, Pro12]. Strong magnetic fields will be used to generate synchrotron radiation in the radio-frequency range from tritium  $\beta$ -electrons. The detection of the synchrotron radiation will be used to determine the tritium  $\beta$ -spectrum. The current aim of the collaboration is to demonstrate the feasibility of this detection technique.

Another technique for neutrino mass measurements is based on low temperature micro-calorimeters [Gat01, Boo96] which contain the isotope of interest. This allows one to measure, apart from the neutrino energy, the total decay energy including nuclear recoil and excited final states of the daughter nuclei. Depending on the employed detector technique, the deposited energy is measured by a change of the resistance [Vac08], a change of magnetisation [Gas09, Ran12], or via a temperature rise [KB08]. Similar to tritium  $\beta$ -decay, only a small fraction of the decays contains sufficient information on the neutrino mass. However, as all decays are measured, countermeasures against pile-up of low-energetic events have to be implemented. This is achieved by a segmentation of the detector to reduce the activity, and hence the count rate, per detector [Dre13].

The electron capture reaction of the isotope  $^{187}\text{Re}$  has been used in micro-calorimeters to determine the neutrino mass. The Q-value of  $^{187}\text{Re}$  is 2.47 keV. Compared to tritium, the low Q-value enhances the relative fraction of decays in the energy region of interest by a factor of about 350 [Wei13b], however the decay rate scales as  $E_0^5$ , counteracting this. Upper limits on  $m(\nu_e)$  have been achieved by the MANU ( $m(\nu_e) < 26$  eV (95% C.L.) [Gat01]) and MIBETA experiments ( $m(\nu_e) < 15$  eV (90% C.L.) [Sis04]). Since then, the

experimental efforts were targeted to improve the detector energy resolution down to the eV range and to reduce the response time of the detector to limit signal pile-up [Dre13]. However due to technical reasons, current R&D efforts focus on the isotope  $^{163}\text{Ho}$  which has a Q-value similar to that of  $^{187}\text{Re}$ . Also for this isotope, different detector techniques [Fle09, Gas09, Gom13] and  $^{163}\text{Ho}$  production methods [Eng13] are being investigated. A  $^{163}\text{Ho}$  spectrum was measured for the first time by calorimetry [Ran12]. The aim of a neutrino mass sensitivity in the eV, or even sub-eV, range remains challenging due to different experimental aspects such as energy resolution, pile-up, background level, and mass production of detectors. However, significant progress has been made in the past years. Therefore, the calorimetry approach based on cryogenic detectors might eventually become another method for neutrino mass measurements.

At the current stage, the most sensitive and advanced experiment for direct neutrino mass measurements is the Karlsruhe Tritium Neutrino (KATRIN) experiment. Based on tritium  $\beta$ -decay and the MAC-E spectrometer technique, it is a direct successor of the Mainz and Troitsk experiments. As this work is performed within the context of the KATRIN experiment the experiment is described in detail in the next chapter.



## 2. The KATRIN Experiment

The Karlsruhe Tritium Neutrino Experiment (KATRIN) is the next-generation neutrino mass experiment currently being constructed and commissioned at the Karlsruhe Institute of Technology (Karlsruhe, Germany). It is designed for a  $5\sigma$  discovery potential of  $350 \text{ meV}/c^2$  and will be able to set an exclusion limit (90% C.L.) of  $200 \text{ meV}/c^2$  on the neutrino mass in case of a result compatible with zero.

In this chapter the KATRIN experiment and the objectives of this thesis are described. The general physical principles of tritium  $\beta$ -decay, the concept of the Windowless Gaseous Tritium Source, and the electrostatic spectrometer are discussed in section 2.1. The tasks of the individual subsystems of KATRIN will be briefly summarised in section 2.2. Section 2.3 summarises the systematic and statistical uncertainties of the neutrino mass measurement. A set of systematic uncertainties is connected with the purity of the tritium gas which is used in KATRIN. The concept for the measurement of the gas composition using Raman spectroscopy is introduced in section 2.4, before the objectives of this work are given in section 2.5.

[KAT05] and [Dre13, Wei03, Ott08] are used as general reference for the information in this chapter and therefore will only be explicitly referenced when specific information (e.g. numbers and equations) are given.

### 2.1. Working principle

#### 2.1.1. Physical principles of the tritium $\beta$ -spectrum

The neutrino mass measurement by KATRIN is based on the  $\beta$ -decay of the super-heavy hydrogen isotope tritium (atomic number  $Z = 1$ , mass number  $A = 3$ )



where a helium ion, an electron and an electron anti-neutrino are formed. Using Fermi's golden rule [Fer34], the decay rate  $\frac{d^2N}{dt dE}$  can be expressed as a function of the kinetic energy  $E$  of the  $\beta$ -electron by

$$\begin{aligned} \frac{d^2N}{dt dE} = & C \cdot F(E, Z + 1) \cdot \sqrt{(E^2 + m_e^2)^2 - m_e^2 c^4} \cdot (E + m_e c^2) \\ & \cdot (E_0 - E) \cdot \sqrt{(E_0 - E)^2 - m_\nu^2 c^4} \cdot \Theta(E_0 - E - m_\nu c^2) \end{aligned} \quad (2.2)$$

where  $F(E, Z+1)$  is the Fermi function,  $m_e$  the electron mass,  $m_\nu$  the neutrino mass,  $c$  the speed of light, and  $E_0 \approx 18.6 \text{ keV}$  the so-called endpoint energy, i.e.  $E$  for the case that

a massless neutrino is produced at rest. The Heaviside step function  $\Theta(E_0 - E - m_\nu c^2)$  ensures the conservation of energy. The Fermi function takes into account the interaction of the outgoing electron with the helium nucleus [Hol92]. The constant

$$C = \frac{G_f^2}{2\pi^3 \hbar^7 c^5} \cos^2 \theta_c |M_{\text{nuc}}|^2 \quad (2.3)$$

contains the Fermi constant  $G_f$ , the reduced Plank constant  $\hbar$ , the Cabbibo angle  $\theta_c$  and the nuclear matrix element  $M_{\text{nuc}}$  which is constant due to the super-allowed nature of the tritium  $\beta$ -decay.

Eq. (2.2) is valid for a tritium  $\beta$ -decay with only one type of neutrino flavour present in the final state and if excited states of the other decay products are neglected. Certainly, this has to be treated as a first approximation only, since there are three neutrino mass states available as shown in the previous chapter, and since tritium occurs in nature in molecular form and therefore electronic and rotational-vibration excited states of the daughter molecule ( ${}^3\text{HeT}$ )<sup>+</sup> have to be considered. Therefore, eq. (2.2) has to be summed over the mass eigenstates  $m_i$  (summation index  $i$ ) and weighted by the squares of the corresponding PMNS matrix elements  $|U_{ei}^2|$  to consider the probability that a certain mass eigenstate is produced after the decay. An electronic or rotational-vibrational excitation  $j$  of the daughter molecule will reduce the endpoint energy by its excitation energy  $V_j$ , i.e. the endpoint energy  $E_0$  in eq. (2.2) has to be replaced by  $E_j = E_0 - V_j$ . As present experiments are not sensitive to the excited states of the daughter molecule, eq. (2.2) also has to be summed over all possible excited states  $j$  which are weighted by the probability  $P_j$  that this state is actually populated. Applying both corrections, eq. (2.2) becomes

$$\begin{aligned} \frac{d^2 N}{dt dE} = & C \cdot F(E, Z + 1) \cdot \sqrt{(E^2 + m_e^2)^2 - m_e^2 c^4} \cdot (E + m_e c^2) \\ & \cdot \left( \sum_{i,j} |U_{ei}^2| \cdot P_j \cdot (E_j - E) \cdot \sqrt{(E_j - E)^2 - m_{\nu_i}^2 c^4} \cdot \Theta(E_j - E - m_{\nu_i} c^2) \right) \end{aligned} \quad (2.4)$$

Nevertheless, as even the  $\Delta m_{23}$  mass splitting [Ber12]

$$\left| \sqrt{\Delta m_{23}^2} \right| \approx 0.04 \text{ eV} \quad (2.5)$$

is small in comparison to the resolution of modern spectrometers for tritium  $\beta$ -spectroscopy (0.93 eV in case of KATRIN), the contributions from the individual mass eigenstates cannot be resolved in the spectrum. When introducing an average 'electron' neutrino mass square

$$m(\nu_e)^2 = \sum_i |U_{ei}^2| m(\nu_i)^2 \quad (2.6)$$

eq. (2.4) is simplified to

$$\begin{aligned} \frac{d^2 N}{dt dE} = & C \cdot F(E, Z + 1) \cdot \sqrt{(E^2 + m_e^2)^2 - m_e^2 c^4} \cdot (E + m_e c^2) \\ & \cdot \left( \sum_j |U_{ei}^2| \cdot P_j \cdot (E_j - E) \cdot \sqrt{(E_j - E)^2 - m(\nu_e)^2 c^4} \cdot \Theta(E_j - E - m_{\nu_i} c^2) \right) \end{aligned} \quad (2.7)$$

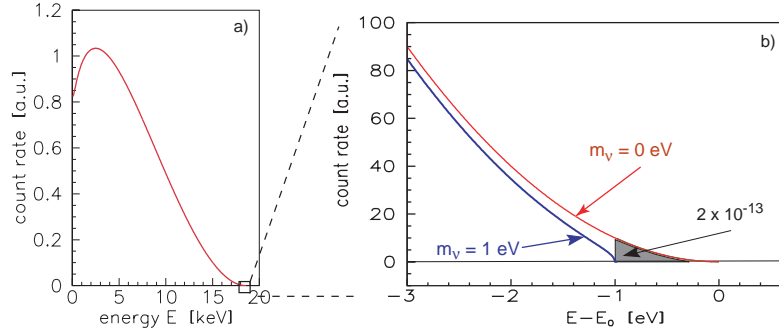


**Figure 2.1.:** Tritium  $\beta$ -spectrum for zero and non-zero neutrino mass. *Left:* Full  $\beta$ -spectrum. *Right:*  $\beta$ -spectrum in the last 3 eV below the endpoint. A non-zero neutrino mass (here exemplary shown for  $m_\nu = 1$  eV) has an influence on the spectrum only close to the endpoint. The grey area represents only a fraction of  $2 \cdot 10^{-13}$  of the overall spectrum demonstrating the low count rate close to the endpoint. Image from [KAT05].

by removing the summation over the parameter  $i$  and replacing the neutrino mass in the square root by the newly defined average one.

The effect of a non-zero neutrino mass on the  $\beta$ -spectrum is significant only close to the endpoint where  $E \approx E_j$  and hence  $m(\nu_e)^2 c^4$  becomes significant in the square root in eq. (2.7) (illustrated in figure 2.1). This was already realised by Fermi in 1934 when he also concluded from the visual analysis of the experimental data that the neutrino mass must be 'small' [Fer34]. Since the neutrino mass square is the actual observable in eq. (2.7), an improvement of the neutrino mass sensitivity by a factor of ten can only be achieved by a reduction of the experimental uncertainties by two orders of magnitude.

Three general prerequisites for a successful neutrino mass measurement can be deduced from this discussion of the tritium  $\beta$ -spectrum:

- An intense  $\beta$ -electron source with an activity of about  $10^{11}$  Bq is necessary to achieve a sufficiently high count rate in the energy interval of interest (approximately  $E_0 - 30$  eV to  $E_0 + 5$  eV).
- An electro-static spectrometer with an energy resolution in the sub-eV range at about 18.6 keV electron energy is needed to resolve the distortion of the  $\beta$ -spectrum which is caused by the neutrino mass.
- Systematic effects which alter the energy of the  $\beta$ -electrons have to be minimised, characterised, and finally accounted for in the data analysis

Two experimental techniques are employed in KATRIN to fulfil these prerequisites: The Windowless Gaseous Tritium Source for the generation of  $\beta$ -electrons and the MAC-E filter for the energy analysis of these. These are briefly introduced in the following sections 2.1.2 and 2.1.3.

### 2.1.2. Concept of the Windowless Gaseous Tritium Source (WGTS)

The currently most sophisticated concept to achieve a high-intensity source of tritium  $\beta$ -electrons with small systematic uncertainties is the so-called Windowless Gaseous Tritium Source (WGTS). This type of tritium source was pioneered in the LANL neutrino mass experiment [Wil87, Rob91] and further developed in the Troitsk neutrino mass experiment [Bel95]. The working principle of the WGTS is illustrated in figure 2.2.

The key feature of the WGTS is that a gas column is used as  $\beta$ -electron source. Within the WGTS the ideal case of completely undisturbed tritium molecules is much better resembled than in solid sources which also have been used in the past [Kra05]. The absence of 'windows', i.e. physical barriers between the source and the spectrometer section, is crucial to exclude distorting energy loss of the  $\beta$ -electrons. The number of tritium atoms inside the WGTS is given by

$$N_T = \rho d \cdot A \cdot \epsilon_T \quad (2.8)$$

where  $\rho d$  is the column density, i.e. the areal density of atoms in the source with respect to the cross-sectional area of the source tube.  $A$  is the cross section of the source tube and  $\epsilon_T$  the isotopic purity, i.e. the ratio of tritium atoms in the source to the total number of atoms. A value of  $\rho d = 5 \cdot 10^{17} \text{ cm}^{-2}$  has been chosen to balance two contrary interests: A maximisation of the activity to increase the count rate and a minimisation of the gas density to reduce the energy loss of  $\beta$ -electrons due to scattering off gas molecules inside the source [KAT05, Bab12]. The activity of the WGTS at this column density will be

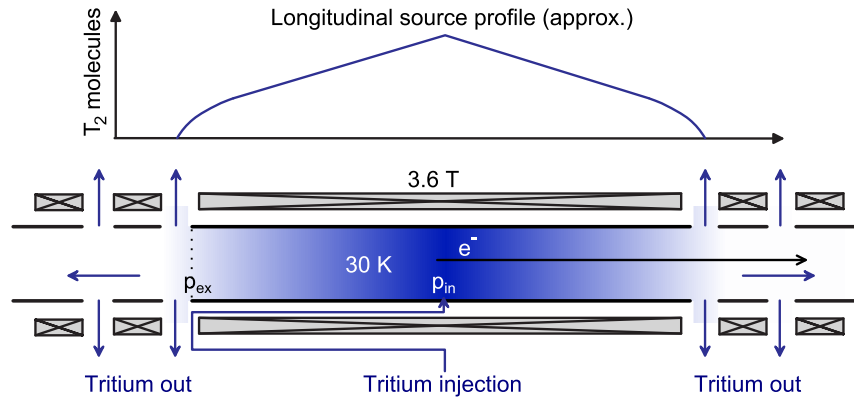


**Figure 2.2.: Schematic drawing of the Windowless Gaseous Tritium Source.**

Molecular tritium gas is injected in the middle of the source tube (10 m length, 9 cm diameter,  $p_{\text{in}} \approx 10^{-3}$  mbar), streams freely towards both ends of the source tube where it is pumped of and recirculated. By stabilising the injection and pumping rate, a gas column with inhomogeneous ( $p_{\text{ex}} \approx 0.05 p_{\text{in}}$ ) but stable density profile is formed. The source tube is cooled to about 30 K to reduce its conductivity and hence increase the source activity. A superconducting solenoid (3.6 T magnetic field strength) is used to magnetically guide the  $\beta$ -electrons towards the spectrometer which is located at one side of the beam tube. No 'window' separates the source tube from the spectrometer, i.e. the spectrometer is kept tritium-free only by pumping at the end of the source tube. The  $\beta$ -electrons are not affected by the pumping due to the magnetic guidance. Image from [Bab12].

$10^{11}$  Bq. As will be shown in section 2.3, the column density is an essential parameter with respect to systematic and statistical uncertainties. In consequence, the column density has to be stabilised to the  $10^{-3}$  level in order to achieve the design sensitivity of  $200 \text{ meV}/c^2$  (90% C.L.). This is accomplished by stabilising the key parameters of the WGTS on the  $10^{-3}$  level, namely

- the source tube temperature of about 30 K absolute temperature,
- the tritium injection rate of  $1.853 \text{ mbar } \ell/\text{s}$ , and
- the pumping rate at the ends of the source tube.

It is intended to operate the WGTS with an isotopic purity  $\varepsilon_T \geq 0.95$  to achieve a high specific activity of the source while keeping the column density and hence the scattering of  $\beta$ -electrons at a moderate level. In order to continuously achieve such a high isotopic purity, it will be necessary to regularly replace a fraction of the gas by high-purity tritium gas. The technical realisation of this procedure is described in section 2.2.1. Based on the experience at the Tritium Laboratory Karlsruhe, an isotopic composition of about  $\geq 90\%$   $T_2$ ,  $\leq 10\%$   $DT$  with traces of  $HT$ ,  $D_2$ ,  $H_2$ , and tritiated methane species is expected for the tritium gas mixture in the WGTS. The gas composition is another key aspect of systematic uncertainties in KATRIN as the different hydrogen isotopologues ( $T_2$ ,  $DT$ ,  $D_2$ ,  $HT$ ,  $HD$ , and  $H_2$ ) differ not only in their mass and hence recoil energy, but also in their rotation-vibration states of the daughter molecule after tritium  $\beta$ -decay. The control of systematic effects which are related to the gas composition is the fundamental motivation for the commissioning of the Raman system in this work. More details on these effects are given in section 2.3. Further information on the physics of the WGTS and the instrumentation to control and monitor its key parameters can be found in [Bab12].

### 2.1.3. Concept of the MAC-E filter

The KATRIN experiment uses a so-called MAC-E filter<sup>1</sup> for energy analysis of tritium  $\beta$ -electrons. This type of spectrometer was first presented in [Kru83] and has also been used in the Mainz and Troitsk neutrino mass experiments [Kra05, Lob03, Ase11]. The key advantage of this filter for electron spectroscopy is that a high energy resolution (in case of KATRIN  $\Delta E = 0.93 \text{ eV}$  at  $18.6 \text{ keV}$ ) can be achieved while maintaining a large acceptance angle for the incident  $\beta$ -electrons. This is essential because of the isotropic emission of  $\beta$ -electrons in the WGTS and the simultaneous need to maximise the count rate.

A MAC-E filter acts as an electrostatic high pass filter, i.e. it transmits electrons with kinetic energies above a certain threshold  $|eU|$ , where  $e$  is the elementary charge and  $U$  the voltage of the electrostatic retarding potential. By measuring the rate of transmitted electrons as a function of the retardation voltage  $U$ , the integrated  $\beta$ -spectrum

$$\dot{N}_{\text{int}}(eU) = N_T \int_{E=eU} \frac{d^2 N}{dt dE} dE \quad (2.9)$$

<sup>1</sup>Magnetic adiabatic collimation combined with an electrostatic filter

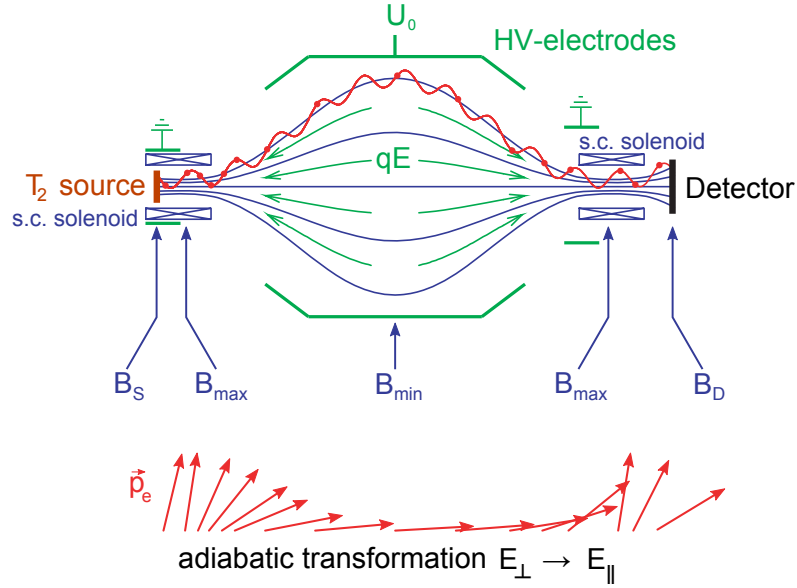


**Figure 2.3.: Principle of the MAC-E filter.** Two superconducting solenoids form an inhomogeneous magnetic field ( $B_{\max} = 20000 B_{\min}$ ) inside a vacuum tank (not shown).  $\beta$ -electrons are emitted isotropically from the tritium source and follow the magnetic field lines on spiral trajectories due to their cyclotron motion. The electrostatic retardation potential is formed by ring electrodes and reaches its maximum in the centre of the vessel where the magnetic field strength is minimal ( $B_{\min}$ ). Due to the gradual decrease of the magnetic field strength, the kinetic energy  $E_{\perp}$  stored in the cyclotron motion of the electrons is transferred into the longitudinal motion of the electrons while running against the electrostatic retardation potential (also illustrated by the gradual flip of the momentum vector  $\vec{p}_e$  shown below). Adiabaticity, i.e. the conservation of energy, is ensured in this process by a careful design of the electromagnetic fields which conserve the magnetic moment  $\mu = E_{\perp}/B$  of the electrons (see e.g. [Val09, Wan13]). Electrons that are able to pass the electrostatic potential maximum, are re-accelerated to their initial energy and guided on the detector for counting. Image according to [KAT05].

can be determined<sup>2</sup>.  $N_T$  is the number of tritium atoms in the source (eq. (2.8)) and  $\frac{d^2 N}{dt dE}$  the tritium  $\beta$ -spectrum from eq. (2.7).

The electrostatic retardation potential is sensitive only to the kinetic energy which is related to the electron motion (anti-)parallel to the electric field lines. Accordingly, electrons which are emitted at finite angle relative to the electric field lines may not be able to pass the retardation potential although their total kinetic energy is larger than the chosen energy threshold  $|eU|$ . In order to counteract this effect, the isotropically emitted  $\beta$ -electrons are collimated to a broad but parallel beam while running against the electrostatic retarding potential (figure 2.3). This reduces the fraction of the kinetic energy which remains in the motion transversal to the electric field lines.

The magnetic field strength  $B$  cannot be reduced to zero in the MAC-E filter and hence

<sup>2</sup>An ideal MAC-E filter was assumed (perfect energy resolution, no background) and no interactions of the  $\beta$ -electrons with the gas column are taken into account. For a full treatment see e.g. [Mer12].

a small fraction  $\Delta E$  of the total kinetic energy  $E$

$$\frac{\Delta E}{E} = \frac{B_{\min}}{B_{\max}} \quad (2.10)$$

remains in the transversal motion.  $\Delta E$  hence determines the 'energy resolution' of the filter, i.e. the additional kinetic energy the  $\beta$ -electrons need at most to pass the electrostatic barrier. A ratio of  $B_{\max} = 20000 B_{\min}$  is realised in KATRIN which yields to an energy resolution of 0.93 eV for  $\beta$ -electrons with  $E = 18.6$  keV.

## 2.2. Experimental overview

An overview of the experimental setup of the KATRIN experiment is shown in figure 2.4. The source tube inside the WGTS cryostat is connected to the vacuum vessel of the MAC-E filter ('main spectrometer') by the differential and cryogenic pumping sections and the pre-spectrometer. Before the subsystems are individually discussed, three general statements about the experiment are made:

- All subcomponents of KATRIN are linked to form a continuous beam line from the calibration and monitoring system to the detector system. Superconducting magnets are located along the beam line to connect the source tube with the detector surface. The  $\beta$ -electrons are guided by magnetic field lines all along the about 70 m long beam line.
- The energy analysis is done in two steps by the pre- and main spectrometers which are both of MAC-E type. The pre-spectrometer offers the option to be operated at

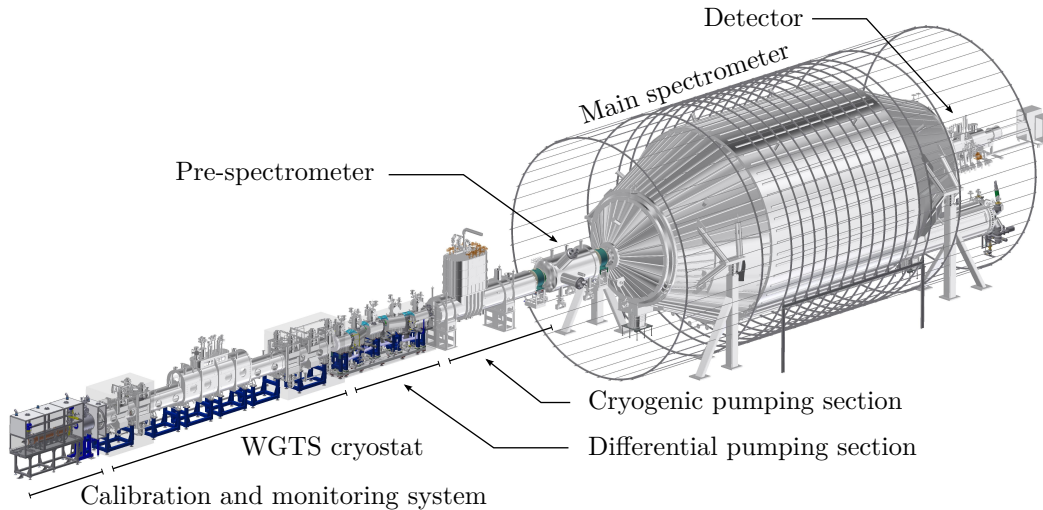


**Figure 2.4.: CAD drawing of the KATRIN experiment.** Both pre- and main spectrometer are based on the MAC-E filter principle. The components with labels below belong to the 'source and transport section', the components with labels above to the 'spectrometer and detector section'. Not shown: Inner loop for tritium in the WGTS source tube and the monitor spectrometer for high voltage monitoring.

fixed retarding potential and to reject all  $\beta$ -electrons which have a kinetic energy of less than about 18.3 keV. The main spectrometer is used to actually measure the integrated  $\beta$ -spectrum near the endpoint by scanning of the retardation potential.

- The tritium flow rate is reduced by 14 orders of magnitude at the entrance of the pre-spectrometer by the subsequent pumping stages in the WGTS and the differential and cryogenic pumping sections. This ensures that the spectrometers are kept tritium-free and hence at low background despite the absence of physical barriers in the source tube and despite the large pressure difference between the WGTS source tube ( $p \approx 10^{-3}$  mbar) and the vacuum vessels of the spectrometers ( $p = 10^{-11}$  mbar in the main spectrometer)

### 2.2.1. WGTS cryostat and Inner Loop

The WGTS cryostat stabilises the source tube temperature to better than 30 mK at about 30 K absolute temperature using a novel two phase neon cooling system (figure 2.5). The WGTS cryostat has been tested at the Tritium Laboratory Karlsruhe in a pre-configuration (WGTS demonstrator) in which the superconducting magnets were replaced by dummy cold masses. A superior temperature stability of 1.5 mK/h was achieved but the required temperature homogeneity along the beam tube axis was not yet fully achieved [Gro13]. The WGTS cryostat is currently being finalised by installation of the superconducting magnets and all other cryostat components. Within the scope of these works, also changes of the cryogenic system are incorporated to reduce the spacial temperature inhomogeneity to the required level of  $\pm 30$  mK over the full length of the 10 m source tube.

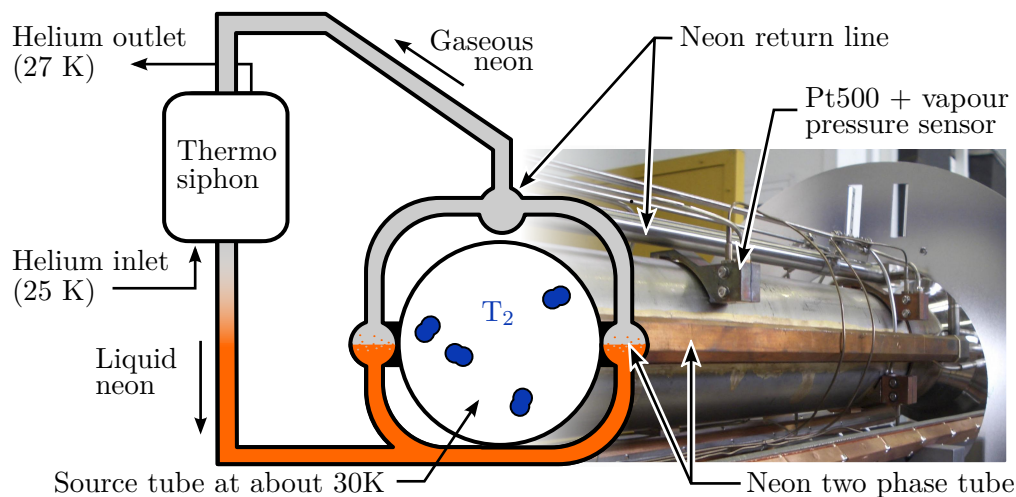


**Figure 2.5.:** Picture of WGTS source tube during manufacturing and schematic diagram of two phase neon cooling system. The WGTS source tube is temperature stabilised by boiling neon inside the two phase tubes at both sides. The neon is re-condensed in a custom-made heat exchanger ('Thermo siphon') which is cooled by helium gas [Gro09]. The source tube temperature is measured by platinum resistance thermometers (Pt500) which are in situ calibrated by vapour pressure sensors [Gro11].

The task of the Inner Loop is to stabilise the gas injection rate of 1.853 mbar  $\ell/s$  into the WGTS source tube to better than 0.1% and to keep the isotopic purity  $\varepsilon_T$  above 95% [KAT05]. Gas which was pumped out at both ends of the source tube is purified and then re-injected (figure 2.6). The pumping rate at both ends of the beam tube is given by the rotation frequency of the turbo molecular pumps and is typically stable to  $10^{-4}$  [Bab12]. The stability of the gas injection rate hence is determined by the pressure stability inside the pressure controlled buffer vessel. The Inner Loop will be operated with a tritium throughput of 40 g/day which requires a closed tritium cycle and a laboratory with the capability to operate tritium experiments with inventories in the gram-scale.

The Tritium Laboratory Karlsruhe (TLK) has a license to handle 40 g of tritium and an extensive experience in the design and operation of tritium experiments [Bor11]. The complete infrastructure of the TLK is needed to maintain the gas circulation in the Inner Loop: The impurities which are separated from the gas stream by the permeator in the Inner Loop are sent to the CAPER facility of TLK [Bor05] where the gas stream is separated in two streams: A stream of hydrogen isotopologues ( $T_2$ ,  $DT$ ,  $D_2$ ,  $HT$ ,

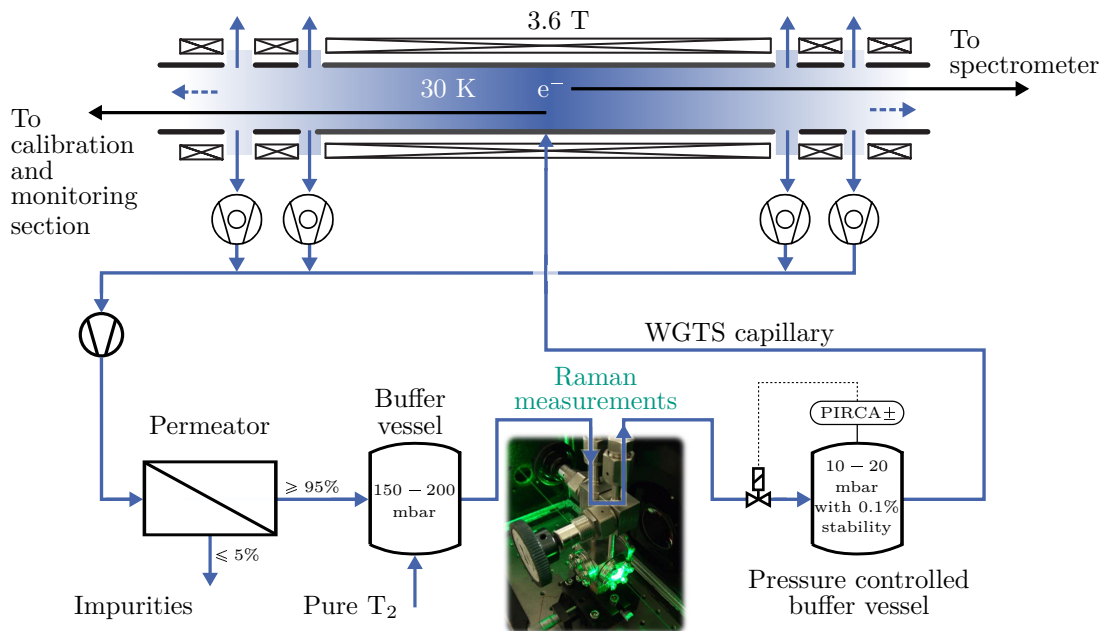


**Figure 2.6.: Schematic flow diagram of Inner Loop.** Most of the tritium gas in the WGTS source tube is pumped off by turbo-molecular pumps, afterwards purified by a palladium membrane filter ('permeator'), and finally re-injected into the source tube. The permeator can only be passed by hydrogen isotopes and hence separates impurities (typically  $^3\text{He}$  and tritiated methane species). The automatic regulation valve in front of the pressure controlled buffer vessel stabilises the pressure inside the buffer vessel and hence the gas injection rate into the source tube on the 0.1% level. Highly purified tritium gas (purity  $\geq 95\%$ ) can be fed into the Inner Loop to keep the isotopic purity  $\varepsilon_T$  of the gas above 95%. A Raman measurement system is located between the two buffer vessels and continuously measures the gas composition in-line. The WGTS capillary is an about 10 m long tube and connects the components inside the glove box (permeator, buffer vessels, Raman measurement cell) with the WGTS cryostat.

HD, H<sub>2</sub>) and a stream of de-tritiated, i.e. tritium-depleted, methane species, helium, nitrogen. The latter is sent to the central tritium retention system for further tritium depletion and controlled discharge [Dör05]. The former is sent to the isotope separation system where the tritium is purified to up to 98% by displacement gas chromatography [Dör02, Doe08]. The purified tritium gas can be re-injected into the Inner Loop to maintain the isotopic purity above 95%. The gas streams from both pumping sections of KATRIN (section 2.2.3) are processed similarly. The availability of the tritium processing infrastructure of the Tritium Laboratory Karlsruhe is therefore an essential cornerstone for the KATRIN experiment.

The Inner Loop was not yet operated with tritium to simplify the pending connection of the WGTS cryostat but it has been tested with nitrogen and deuterium gas. In these tests, a bypass tube with identical gas dynamical properties as the WGTS capillary was used as place holder. The pressure fluctuations were more than one order of magnitude smaller than the maximal tolerable 0.1% level, even under unrealistically large temperature cycling of the beam tube replacement [Pri10a, Stu10b, Bor14]. This demonstrated the stable tritium circulation characteristics in the Inner Loop.

The gas composition and hence the isotopic purity is determined by a Raman measurement system which is operated in an 'in-line' mode, i.e. the complete gas stream has to pass through the Raman sample cell before entering the pressure controlled buffer vessel. The pressure inside the Raman sample cell is about 150-200 mbar depending on the amount of gas in the Inner Loop and the chosen pressure set point inside the pressure controlled buffer vessel. The Raman measurement system is the central component in this work. The basics of the Raman measurement will be introduced in section 2.4. The theoretical foundations of Raman spectroscopy are presented in detail in chapter 3 before the experimental setup and the commissioning of the system are discussed in the subsequent chapters.

### 2.2.2. Calibration and monitoring section

The calibration and monitoring section (CMS) in general has three tasks: (i) The so-called rear-wall of the calibration and monitoring section defines the electric plasma potential relative to the high voltage in the spectrometer [Bab12]. (ii) A gold layer on the rear wall is used to generate X-rays due to the  $\beta$ -electrons impinging on the surface. The X-rays are detected by a silicon drift diode and are used as a precise measure of the  $\beta$ -activity in the source [Röll11, Roe12, Pri13]. (iii) An angle and energy selective electron gun [Val11] is used to probe the column density in the WGTS via the inelastic scattering of electrons and to measure the electro-optic transmission properties of the complete KATRIN beam line. The CMS is currently in the design and construction phase.

### 2.2.3. Transport section

The transport section consists of two subsystems, namely the differential pumping section (DPS) and the cryogenic pumping section (CPS). Both systems are connected in series

(order: WGTS-DPS-CPS) and have the task to reduce the tritium flow rate to a level of  $10^{-14}$  in comparison to the inlet rate at the centre of the WGTS source tube. Tritium molecules which reach the pre- and main spectrometers of KATRIN otherwise would produce background events which disturb the measurement of the  $\beta$ -spectrum near the endpoint [Kos12, Mer12]. Differential, i.e. mechanical, pumping is employed in the DPS while the CPS is a cryogenic pump where the residual tritium molecules are trapped on the about 3 K cold surface of the beam tube [Gil10]. In addition to the tritium flow rate reduction, the transport section also adiabatically guides the  $\beta$ -electrons from the WGTS to the spectrometers along magnetic field lines. The DPS has been successfully commissioned in 2012 [Kos12, Luk12] but a failure of an electric diode in the superconducting magnet was experienced. Due to technical reasons a repair of the system was not possible and hence a new system is currently under construction. The CPS is currently in the final stage of construction.

#### 2.2.4. Spectrometer and detector section

The pre- and the main spectrometer are based on the MAC-E filter principle and are employed for the energy analysis of the  $\beta$ -electrons. The pre-spectrometer offers the option to be operated at a retarding potential of about 18.3 keV to reject all  $\beta$ -electrons that do not contain any information on the neutrino mass. The main spectrometer has an energy resolution of 0.93 eV at 18.6 keV electron energy and was commissioned in 2013 to study the rate of background events in the spectrometer and to measure its transmission properties using a electron gun as reference source. The detector section counts  $\beta$ -electrons which have sufficient energy to pass the electrostatic barrier in the main spectrometer. The detector system was simultaneously commissioned to the main spectrometer. Details on the combined commissioning can be found in [Sch14b, Lei14] and references therein.

In addition to the pre- and main spectrometers, a third spectrometer based on the MAC-E principle is used in KATRIN to monitor the stability of the high voltage using monoenergetic conversion electrons from  $^{93\text{m}}\text{Kr}$  as a natural reference standard [Sle13].

### 2.3. Neutrino mass sensitivity and WGTS-related systematic effects

It is anticipated to reach comparable levels of systematic and statistical uncertainties for the determination of  $m_\nu^2$  ( $\sigma_{\text{sys}} = 0.017 \text{ eV}^2/c^4$  and  $\sigma_{\text{stat}} = 0.018 \text{ eV}^2/c^4$ ) after three years of effective measurement duration. When adding both quadratically, a total uncertainty of

$$\sigma_{\text{tot}} = \sqrt{\sigma_{\text{sys}}^2 + \sigma_{\text{stat}}^2} \approx 0.025 \text{ eV}^2/c^4 \quad (2.11)$$

is obtained. Accordingly, a neutrino mass of

$$\begin{aligned} m_\nu &= \sqrt{5 \cdot \sigma_{\text{tot}}} \\ &\approx 350 \text{ meV}/c^2 \end{aligned} \quad (2.12)$$

can be detected by KATRIN with  $5\sigma$  significance. In case the measurement result is consistent with zero, an upper limit of

$$m_\nu \leq \sqrt{1.64 \cdot \sigma_{\text{tot}}} \quad (2.13)$$

$$\approx 200 \text{ meV}/c^2 \text{ (90\% C.L.)} \quad (2.14)$$

can be set by KATRIN [KAT05]. This would still correspond to an improvement of the limit on the neutrino mass by one order of magnitude in comparison to the present limit of about  $2 \text{ eV}/c^2$  [Kra05, Ase11, Ber12].

The minimisation and control of the systematic uncertainties is absolutely essential to achieve the projected sensitivity of KATRIN. The maximum tolerable systematic uncertainty of  $\sigma_{\text{sys}} = 0.017 \text{ eV}^2/c^4$  is based on the premise that there are at most five dominating effects which individually contribute to no more than  $7.5 \cdot 10^{-3} \text{ eV}/c^2$  [KAT05]. Two parameters of the WGTS are closely linked to systematic uncertainties in the neutrino mass measurement, namely the column density  $\varrho d$  and the gas composition. Both parameters will be discussed in the following sections.

### Systematic uncertainty related to the column density $\varrho d$

The column density is the areal density of atoms in the source with respect to the cross-section of the source tube and hence a measure for the opaqueness of the gas column. At first glance,  $\varrho d$  appears to be a proportionality factor in eq. (2.8) and hence should not influence the shape of the spectrum but only the overall count rate. In consequence, the absolute value of  $\varrho d$  would not be of interest as long as activity fluctuations of the source during one scan of the  $\beta$ -spectrum are monitored and taken into account. But the absolute value of  $\varrho d$  does affect the shape of the  $\beta$ -spectrum due to inelastic scattering of  $\beta$ -electrons off the gas molecules in the WGTS. For the nominal value of  $\varrho d = 5 \cdot 10^{17} \text{ molecules}/\text{cm}^2$ , only 41.3% of the  $\beta$ -electrons are expected to leave the source without any scattering while 29.3% and 16.7% have experienced one or two scattering processes, respectively [Bab12]. The accurate knowledge of the scattering probabilities and the associated energy loss of the  $\beta$ -electrons is essential for the neutrino mass measurement. These scattering probabilities will therefore be measured once in an extensive calibration run using the electron beam of the CMS (section 2.2.2).

After this initial measurement, it is sufficient to measure the column density to determine the scattering probabilities using a gas dynamical model of the WGTS [Kae12, Hoe12]. About every 2 hours, an electron beam of the CMS is used to determine the column density by measuring the rate of electrons from the electron gun reaching the detector as a function of the retardation potential of the spectrometer [KAT05]. During the actual neutrino mass measurements between two electron gun measurements, only relative changes of the column density will be indirectly monitored: The activity  $N_T$  of the source will be measured by the X-ray detector system in the CMS (section 2.2.2), and the isotopic purity  $\varepsilon_T$  will be monitored by the Raman measurement system in the Inner Loop. Using both measurements, the deviation of the column density from the previously measured value can be determined via eq. (2.8).

In order to keep the systematic uncertainty on  $m_\nu^2$  due to an unaccounted variation of the column density below the aforementioned limit of  $7.5 \cdot 10^{-3} \text{ eV}/c^2$ , the Raman and

X-ray monitoring systems have to be able to detect  $10^{-3}$  variations of the source activity and the isotopic purity, respectively [Bab12].

### Systematic uncertainties related to the gas composition

Also the gas composition itself, i.e. the absolute values of the molar fractions of the gas constituents, is relevant for the systematic uncertainties in the WGTS due to four effects which are briefly outlined.

1. Recoil effect

The daughter molecule ( $\text{HeT}^+$  in case of  $\text{T}_2$  and  $\text{HeD}^+/\text{HeH}^+$  in case of the isotopologues DT/HT) experiences a recoil due to the emission of the  $\beta$ -electron which will manifest itself as a reduction of the endpoint energy. For electron energies  $E$  close to the endpoint, the recoil energy

$$E_{\text{rec}} \approx E \cdot \frac{m_e}{m_{\text{mol}}} \quad (2.15)$$

solely depends on the ratio of the electron mass  $m_e$  and the mass of the daughter molecule  $m_{\text{mol}}$  [KAT05]. The large relative mass differences of the hydrogen isotopologues will therefore be directly propagated to the recoil energy. As a consequence, the tritium  $\beta$ -spectrum measured in KATRIN will actually be a superposition of  $\beta$ -spectra with different endpoint energies where weighting factors of the individual spectra have to be introduced based on the concentration values of the individual hydrogen isotopologues.

2. Doppler effect

The molecules in the WGTS are not at rest but exhibit a thermal motion and a global bulk velocity due to the diffusion towards both ends of the source tube. This causes a Doppler shift of the  $\beta$ -electron energy. In a non-relativistic approximation the Doppler shift of an  $\beta$ -electron with kinetic energy near the endpoint is given by [KAT05]

$$\Delta E \approx m \cdot v_e \cdot v_{\text{mol}} \quad (2.16)$$

where  $m$  and  $v_e$  are the the mass and the velocity of the  $\beta$ -electron and  $v_{\text{mol}}$  is the velocity component of the decaying molecule in the direction of the emitted electron. A Doppler shift of  $\Delta E \approx 130$  meV is found for  $\text{T}_2$  which demonstrates the significant size of this effect with respect to the projected neutrino mass sensitivity of KATRIN [Bab12]. For other molecules,  $v_{\text{mol}}$  and hence also  $\Delta E$  will vary accordingly due to the large relative mass differences of the hydrogen isotopologues.

3. Elastic  $e^-$  -  $\text{T}_2$  scattering

In addition to the inelastic scattering already mentioned before, also elastic scattering of the  $\beta$ -electrons is possible. In this scattering process, the  $\beta$ -electron (energy  $E$ , mass  $m_e$ ) loses the energy

$$\Delta E = 2 \frac{m_e}{m_{\text{mol}}} E (1 - \cos \theta_s) \quad (2.17)$$

depending on the mass of the molecule  $m_{\text{mol}}$  and the polar scattering angle  $\theta_s$ . Typically, small scattering angles  $\theta_s \approx 3^\circ$  are realised and hence the energy loss for

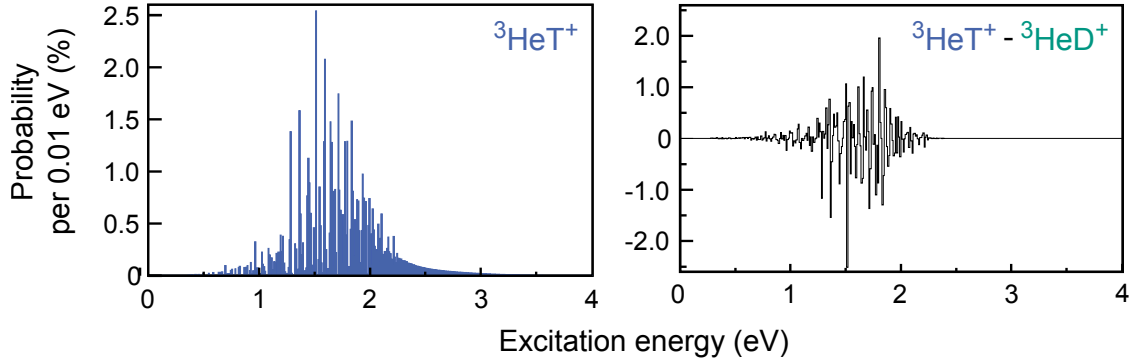


**Figure 2.7.: Final states distribution of daughter molecules.** *Left:* Final states distribution of  $({}^3\text{HeT})^+$  showing rotational and vibrational excitations. *Right:* Difference of final states distributions of  $({}^3\text{HeT})^+$  and  $({}^3\text{HeD})^+$ . The nuclear recoil energy is already accounted for in both plots. Source: Plots from [Sch13b] based on data from [Dos06].

$T_2$  is of the order of 16 meV. Similar to the recoil of the daughter molecule, the large relative mass differences of the hydrogen isotopologues manifests itself in a typical molecular-specific energy loss due to elastic scattering.

#### 4. Final states distribution

The final states of the daughter molecules have been introduced in eq. (2.4) to take into account the molecular excitation energy which reduces the endpoint energy in the  $\beta$ -spectrum. The lowest electronic excitation of  $({}^3\text{HeT})^+$  is at about 27 eV [Sae00] but the rotational and vibrational excitation levels are on average at an energy of about 1.89 eV for  $({}^3\text{HeT})^+$  (figure 2.7 left; [Dos06]) and hence can be excited by the nuclear recoil. The distribution of final states deviates between the individual isotopologues due to the difference in reduced mass of the molecule (figure 2.7 right). KATRIN will determine the neutrino mass from the spectrum in the interval  $E_0 - 30$  eV to  $E_0$ , and hence will only be marginally affected by electronic excitations. The rotational and vibrational final states, however, will be the ultimate accuracy limit for neutrino mass measurements using molecular tritium since the energy interval cannot be arbitrarily small due to the vanishing count rate near the endpoint.

These effects are considered in the gas dynamical model of the WGTS [Kae12, Hoe12] which will be used to analyse the acquired tritium  $\beta$ -spectra. The model, however, can only be applied when the gas composition is determined by an external measurement and hence is available as an input parameter. The necessary accuracy of the gas composition measurement depends on two aspects, (i) the maximum tolerable systematic uncertainty caused by the accuracy of the gas composition measurement and (ii) the gas composition. Before discussing the first point, a short example is given to illustrate the second aspect: If the tritium gas is perfectly pure ( $\varepsilon_T = 1$ ), the accuracy of the gas composition measurement is not relevant as only tritium will be detected. The larger the concentrations of admixtures of other hydrogen isotopologues are, the more stringent becomes the accuracy requirement for the system. This is of benefit for the Raman measurement system in KATRIN as the projected tritium purity of  $\varepsilon_T = 0.95$  is still close to the ideal

case of pure tritium gas.

The required accuracy of the gas composition was determined within the scope of previous research efforts [Sch13b, Sch12a]. The maximum tolerable systematic uncertainty due to the measurement accuracy of the gas composition was set to  $6 \cdot 10^{-3} \text{ eV}^2/c^4$  which corresponds to the uncertainty of the theoretical description of the final states [KAT05]. The accuracy of the gas composition measurement is determined from the uncertainty of the calibration factors which are needed to convert Raman intensities into molar fractions, i.e. concentration values (to be discussed in 3.3). Owing to the high isotopic purity of the tritium gas in the Inner Loop a relative uncertainty of about 50% on the calibration factors would still be sufficient to fulfil the requirement [Sch12a] for KATRIN. Nevertheless it is meaningful to apply a more stringent requirement of a relative uncertainty of only 10% on the calibration factors to anticipate potential future improvements of the theoretical description of the final state distributions. It was shown in [Sch13b] that the relative calibration uncertainty of the KATRIN Raman system is 2-3% and hence clearly satisfies the requested accuracy.

## 2.4. Monitoring of the source gas composition using Raman spectroscopy

This section gives a brief overview of the application of Raman spectroscopy in KATRIN to motivate the objectives of this work which are outlined in the next section.

Raman spectroscopy is an optical method based on the Raman scattering of laser light off a sample, here the gas molecules (figure 2.8, left). Within Raman scattering, the molecules make a transition between excited states that causes the wavelength of the scattered light to shift. The observable in a Raman measurement is the intensity of the scattered light as a function of 'Raman shift' which is a measure of the energy difference between the molecular excitation levels. The large relative mass differences of the hydrogen isotopes is associated with a significant variation of the molecular energy levels between the hydrogen isotopologues and accordingly of their Raman shifts. This allows one to identify the individual hydrogen isotopologues in a Raman spectrum (figure 2.8, right). For quantitative gas analysis, the intensity of the scattered light is accurately determined at specific Raman shifts.

Raman spectroscopy is used in KATRIN for the analysis of the WGTS source gas because of three general benefits:

- All gas species which are of primary interest for KATRIN (hydrogen isotopologues, tritiated methane species) can be detected simultaneously [Stu10a].
- Raman spectroscopy is a contact-free method, i.e. no sample-taking is necessary. This avoids handling of radioactive samples which potentially have to be disposed of after analysis [Dem12].
- Only optical access to the tritium gas is necessary for Raman analysis. This can be realised by installing a sample cell equipped with windows into the Inner Loop.

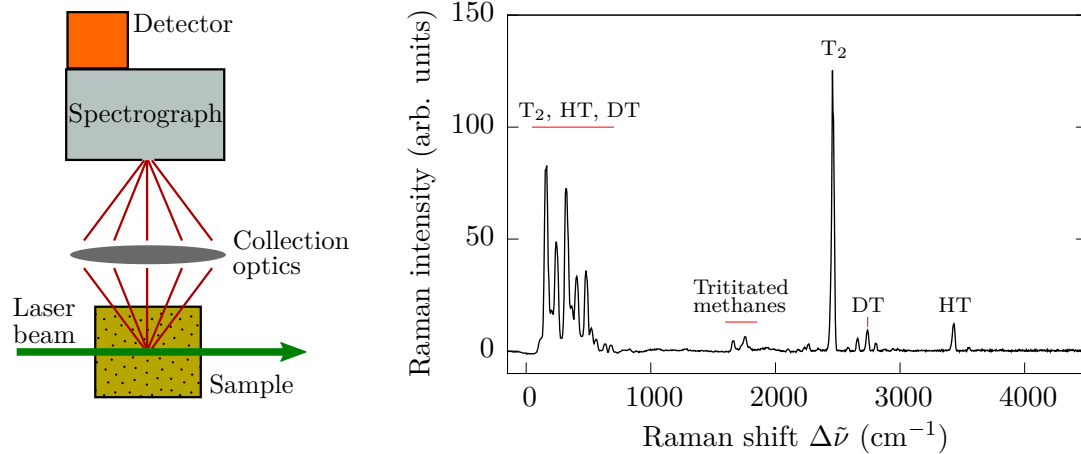


**Figure 2.8.: Schematic drawing of a Raman spectroscopy system and exemplary Raman spectrum.** *Left:* Sketch of a Raman spectroscopy system. A laser beam scatters off the gas molecules in the sample. The scattered light is collected and analysed using a spectrograph and a light detector. *Right:* Exemplary Raman spectrum of a typical tritium gas sample (T<sub>2</sub>, HT, DT and tritiated methane species). The Raman shift of the observed peaks in the spectrum allows to identify individual molecular species. The structure of Raman spectra of diatomic molecules will be discussed in chapter 3.

## 2.5. Objectives of this work

The general suitability of Raman spectroscopy for the precise and accurate compositional analysis of tritium gas mixtures has already been demonstrated in previous studies at TLK: It was shown in [Stu10a] that all hydrogen isotopologues can be detected simultaneously. The monitoring of the gas composition of a circulating gas mixture under conditions similar to those in the Inner Loop was demonstrated in [Stu10b, Fis11]. Within these measurements, the  $10^{-3}$  relative precision requirement was fulfilled for the first time by continuous Raman measurements with 250 s acquisition time. A concept for the accurate calibration of the Raman systems was developed and successfully tested in research [Sch13b] conducted in parallel to the present work.

Therefore, at first glance it might seem that no further R&D efforts are necessary for the application of Raman spectroscopy in KATRIN since the general suitability of this technique was proven. But it has to be kept in mind that the projected operation time of the KATRIN Raman system is three net years distributed over the course of 5 calendar years. Hence, it is essential that the system achieves its metrological performance (accuracy, precision and sensitivity) continuously and reliably over the complete operation time. This is a challenging task which requires an elaborate design of the optical setup and the consideration of physical but also technical constraints which otherwise could limit the performance of the system during long-term operation or even cause its failure. Examples for such effects were experienced in the past, namely the laser pointing and power instabilities that limited the metrological performance of the prototype systems [Fis10, Stu10b] and the severe damage of the anti-reflection coatings on the sample cell windows after about three months of exposure to highly purified tritium gas

[Stu10b, Fis11].

The main objectives of this work therefore are (i) to setup and to commission the KATRIN Raman system such that the best metrological performance but also sufficient reliability is achieved and (ii) to reach a maturity level that it is ready for the operation by non-expert personnel in the KATRIN experiment.

This work focusses in particular on three tasks which are essential to achieve the aforementioned goal:

### **Setup and commissioning of the KATRIN Raman system LARA3**

Design and construction of the KATRIN Raman system using the expertise and experience gained from the prototype systems that were built and operated at the Tritium Laboratory Karlsruhe and Swansea University. Improvement of the metrological performance by increase of the effective laser power in the sample cell and by stabilisation of the laser properties. Optimisation of the optical beam path to improve the reproducibility of the beam alignment which is necessary for a reliable long-term operation. Commissioning of the KATRIN Raman system and determination of the minimum acquisition to reliably fulfil the 0.1% relative precision requirement of KATRIN.

### **Study of durability of optical coatings in long-term operation with tritium**

Identification and elimination of the cause for the damage of the anti-reflection coatings which was experienced after exposure to highly purified tritium gas. Investigation of harmful effects on optical coatings when being operated inside glove boxes or even in contact with tritium gas. Evaluation if these effects are of relevance for the operation of the KATRIN Raman system and which potential countermeasures can be taken. Search for optical coatings that can be reliably used in tritium gas atmosphere.

### **Development of operation software for the KATRIN Raman system**

The operation software for the KATRIN Raman system does not only have to acquire Raman spectra but should also automatically perform a complete quantitative analysis as near as possible to real-time. In addition routines must be implemented to autonomously monitor the status of the KATRIN Raman system during the mostly unattended and autonomous operation of the system.

These tasks are also reproduced in the structuring of this work. The theoretical fundamentals for the quantitative Raman spectroscopy of hydrogen isotopologues are described in chapter 3. The setup and commissioning of the KATRIN Raman system is subject of chapter 4. Chapter 5 focuses on the durability of optical coatings in tritium and glove box environments. The development of LARAsoft, the operation software for the KATRIN Raman system, is presented in chapter 6. Chapter 7 summarises lessons learnt from this and other works which are important for the operation and maintenance of the KATRIN Raman system during neutrino mass measurements. The results of this work are summarised in chapter 8.



### 3. Quantitative Raman spectroscopy of hydrogen isotopologues

The Raman effect describes the inelastic scattering of photons from molecules which was predicted in 1923 by Adolf Smekal [Sme23] and discovered by Chandrasekhara Venkata Raman and Kariamanickam Srinivasa Krishnan in 1928 [Ram28]. C. V. Raman subsequently received the Nobel Prize in 1930 for this discovery [Ram13]. Due to the inelastic scattering, energy is transferred between the photon and molecule which changes its excitation state (figure 3.1). Energies are in molecular spectroscopy, for historical and practical reasons, commonly expressed in wavenumbers  $\tilde{\nu}$  through division by Plank's constant  $h$  and the speed of light  $c$ . Thus, wavenumbers are also the inverse of the wavelength  $\lambda$  of light, i.e.

$$\tilde{\nu} = \frac{E}{hc} = \frac{1}{\lambda}, \quad [\tilde{\nu}] = \text{cm}^{-1}. \quad (3.1)$$

As the molecular states are quantised, only discrete amounts of energy are transferred between photon and molecule during Raman scattering. The Raman shift

$$\Delta\tilde{\nu} = \frac{1}{hc}(E_f - E_i) \quad (3.2)$$

corresponds to the difference of the initial and final molecular energy states  $E_i$  and  $E_f$  respectively, but also connects the wavelength  $\lambda_i$  of the incident light with the wavelength  $\lambda_f$  of the Raman scattered light by

$$\Delta\tilde{\nu} = \frac{1}{\lambda_f} - \frac{1}{\lambda_i}. \quad (3.3)$$

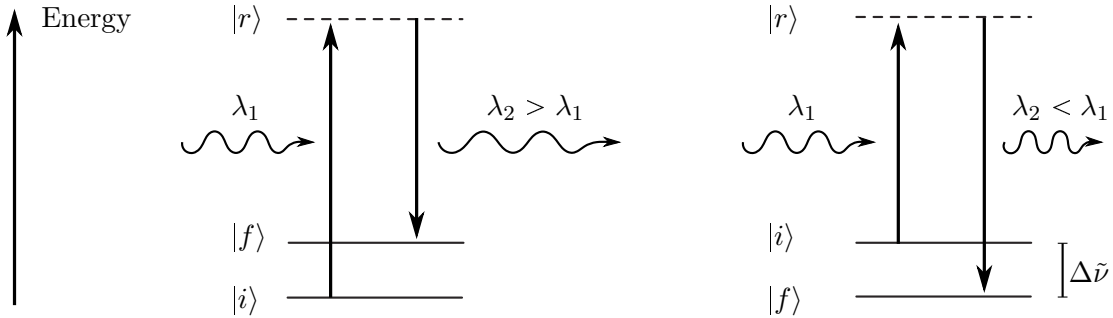


**Figure 3.1.: Quantum mechanical picture of Raman scattering.** The initial state  $|i\rangle$  and the final state  $|f\rangle$  have different energy levels  $E_i = \langle i|E|i\rangle$  and  $E_f = \langle f|E|f\rangle$ . The Raman shift  $\Delta\tilde{\nu} = E_f - E_i$  is indicated. *Left:* Stokes Raman scattering.  $E_i < E_f$ . *Right:* Anti-Stokes Raman scattering. The molecule is in an excited state before scattering and  $E_i > E_f$ . In both types of scattering a virtual state  $|r\rangle$  is involved. (Figure according to [Lon02]).

**Table 3.1.: Energy conversion coefficients.** For details see main text.

	J	eV	cm <sup>-1</sup>	K
1 Joule (J) $\hat{=}$	1	$6.24 \cdot 10^{18}$	$5.03 \cdot 10^{22}$	$7.24 \cdot 10^{22}$
1 eV $\hat{=}$	$1.60 \cdot 10^{-19}$	1	$8.07 \cdot 10^3$	$1.16 \cdot 10^4$
1 cm <sup>-1</sup> $\hat{=}$	$1.99 \cdot 10^{-23}$	$1.24 \cdot 10^{-4}$	1	1.44
1 K $\hat{=}$	$1.38 \cdot 10^{-23}$	$8.62 \cdot 10^{-5}$	$6.95 \cdot 10^{-1}$	1

Besides wavenumbers also other expressions of energy are used in molecular spectroscopy: When estimating the thermal excitation of molecules, the conversion into temperature according to  $T = E/k_B$ , where  $k_B$  is the Boltzmann constant, is used. The energy unit electronvolt (eV) is also of relevance, e.g. when assessing the impact of molecular excitations on the tritium  $\beta$ -spectrum. In this thesis, energies will typically be given in wavenumbers. The conversion coefficients between the different representations are given in table 3.1.

The large relative mass difference of the hydrogen isotopes (hydrogen  $m_{1H} = 1$  atomic unit, tritium  $m_T = 3$  atomic units) causes distinct shifts of the molecular energy levels and consequently results in a unique set of Raman shifts for each hydrogen isotopologue ( $H_2$ , HD, HT,  $D_2$ , DT,  $T_2$ ). Each Raman shift manifests itself as a line in the spectrum of the scattered light when irradiating a sample with monochromatic (laser) light. Due to the simple structure of diatomic molecules their Raman spectra cannot only be qualitatively but also quantitatively evaluated. As it will be shown in this chapter, this makes an accurate compositional monitoring of the KATRIN source gas possible.

It should be noted that this work makes use of the spontaneous vibrational-rotational Raman effect, therefore other Raman techniques, e.g. resonance, stimulated or surface-enhanced Raman spectroscopy, are not covered here. Further information on these techniques can be found in extensive literature on laser spectroscopy, e.g. in [Lon02, Dem08].

This chapter gives an overview of rotational-vibrational excitations of diatomic molecules with the aim to calculate the Raman shifts of hydrogen isotopologues and other relevant diatomic molecules (section 3.1). Afterwards the theoretical principles of Raman line intensity calculations will be introduced (section 3.2) which are necessary for the accurate calculation of Raman spectra. The chapter concludes with a description (section 3.3) of how the acquired Raman spectra are quantitatively evaluated and how this can be utilised for an accurate gas composition monitoring of the KATRIN source gas.

### 3.1. Rotational-vibrational excitations of diatomic molecules

Three types of excited states of hydrogen isotopologues will need to be considered: Rotational, vibrational, and electronic excitations. Only the first two types can be excited by light in the visible range or thermally at room temperature (table 3.2) and are therefore of relevance for this work. Electronic excitations will be omitted in the following and it will be assumed that the molecule is in the electronic ground state. Rotational and vibrational excitations of diatomic molecules can be treated semi-classically to explain the principle structure of molecular excitation levels and hence Raman spectra. Semi-classically means that the states of the molecule are quantised but the electromagnetic field of the incident and scattered light is treated classically. Based on this approach, a set of phenomenological molecular constants (e.g.  $\omega_e$ ,  $x_e\omega_e$ ,  $B_\nu$ ,  $D_\nu$ ) will be introduced to characterise the vibrational and rotational behaviour of diatomic molecules. However, a full quantum mechanical treatment of the molecular Schrödinger equation is necessary for an accurate calculation of molecular energy levels and the deduction of the phenomenological molecular constants from ab-initio. As this work will follow the phenomenological approach, the reader is referred to [Dem06, Mül98, Sch87] for further details for the quantum mechanical treatment.

#### 3.1.1. Semi-classical model of rotational-vibrational excitations

The semi-classical model of rotational-vibrational states of a diatomic molecule is based on the Schrödinger equation in the Born-Oppenheimer approximation. In this approximation the wave function of the molecule can be written as a product of an electronic and a nuclear wave function which are both independent of each other, i.e. electronic and nuclear motions are decoupled (details in [Bor27] and appendix VIII in [Bor66]).

**Table 3.2.: Rotational, vibrational and electronic excitation energies of H<sub>2</sub> and T<sub>2</sub>.** These energies, expressed in term values, wavelength equivalent ( $\lambda = hc/E$ ) and temperature ( $T$ ), are necessary to excite a molecule from the ground state into the corresponding first excited state. Visible light ( $400 \text{ nm} \leq \lambda \leq 750 \text{ nm}$ ) can excite molecular rotations and vibrations but no electronic excitations. Thermal excitation of vibrational states at room temperature ( $T = 300 \text{ K}$ ) is negligible. Data based on [Sch87, Her79].

	Rotational		Vibrational		Electronic	
	H <sub>2</sub>	T <sub>2</sub>	H <sub>2</sub>	T <sub>2</sub>	H <sub>2</sub>	T <sub>2</sub>
$E/hc$ (cm <sup>-1</sup> )	350	120	4150	2450	91700	91696
$\lambda$ (nm)	28570	83300	2410	4080	109.05	109.07
T (K)	510	175	5930	3490	132048	132042

The Schrödinger equation which determines the nuclear wave function is given by

$$\left[ \frac{-\hbar^2}{2\mu} \nabla^2 + E_n^{(0)}(\mathbf{R}) \right] \chi_m(\mathbf{R}) = E_m \chi_m(\mathbf{R}) \quad (3.4)$$

where  $\mu = M_1 M_2 / (M_1 + M_2)$  is the reduced mass of the molecule,  $\nabla$  the Nabla operator,  $E_n^{(0)}(\mathbf{R})$  the nuclear potential for a given inter-nuclear distance vector  $\mathbf{R} = \mathbf{R}_1 - \mathbf{R}_2$ ,  $E_m$  the energy eigenvalue and  $\chi_m(\mathbf{R})$  the nuclear wave function of  $m$ -th rotational-vibrational state [Dem05]. Molecular vibrations and rotations are both described by corresponding terms in the nuclear potential as it will be shown in the following.

### Rigid Rotator model

The simplest model of a rotating diatomic molecule is the so-called rigid rotator, i.e. assuming that the nuclei are connected by a massless rod at a fixed equilibrium distance  $R_e$  and the molecule rotates around its centre of mass. Solving eq. (3.4) under these assumptions yields the rotational energy eigenvalues

$$F_{\text{rot}}(J) = \frac{J(J+1)\hbar}{4\pi c\mu R_e^2} \quad (3.5)$$

with the rotational quantum number  $J = 0, 1, 2, \dots$  [Dem05]. The Raman shift of an exemplary transition between states that deviate in  $J$  by 2 units is

$$\Delta\tilde{\nu} = F_{\text{rot}}(J+2) - F_{\text{rot}}(J) = 5B_e(J+1) \quad \text{with} \quad B_e = \frac{\hbar}{4\pi c\mu R_e^2} \quad (3.6)$$

where constant  $B_e$  has been introduced. The Raman lines of all  $J \rightarrow J+2$  rotational transitions should hence be equally spaced in the Raman spectrum with an inter-line spacing of  $5B_e$ .

### Centrifugal distortion of molecular rotation

The rigid rotator model is not yet sufficient to describe all experimental rotational spectra since the inter-nuclear distance vector  $\mathbf{R}$  is not a constant but increases with increasing rotational quantum number. This can be described by a centrifugal force according to Hook's law where the stiffness of the inter-nuclear connection is characterised by the spring constant  $k$ . Hence, the nuclear potential in eq. (3.4) is extended by a spring potential  $E_{\text{spring}}(\mathbf{R}) = 1/2k(|\mathbf{R}| - R_e)^2$  with  $||\mathbf{R}| - R_e| \ll R_e$ . In a Taylor expansion for small displacements [Dem05], the rotational energy eigenvalues can be given as

$$F_{\text{rot}}(J) = B_e J(J+1) - D_e J^2(J+1)^2 + H_e J^3(J+1)^3 + \dots \quad (3.7)$$

with the additional centrifugal constants

$$D_e = \frac{\hbar^3}{4\pi k c \mu^2 R_e^6}, \quad H_e = \frac{3\hbar^5}{4\pi k^2 c \mu^3 R_e^{10}}. \quad (3.8)$$

This parametrisation of rotational energy levels allows for the calculation of Raman shifts when taking the higher order corrections for larger  $J$  values into account. In this

work, corrections up to the third order, i.e. the  $H_e$ , term, are typically sufficient. The exemplary rotational transition with  $\Delta J = 2$  now results in a Raman shift

$$\begin{aligned}\Delta\tilde{\nu}(J) &= F_{\text{rot}}(J+2) - F_{\text{rot}}(J) \\ &= B_e(4J+6) - D_e(8J^3 + 36J^2 + 60J + 36) \\ &\quad + H_e(12J^5 + 90J^4 + 304J^3 + 558J^2 + 540J + 216)\end{aligned}\quad (3.9)$$

which is non-linear in  $J$ . Hence, such Raman lines are not equally spaced with a fixed inter-line spacing as in eq. (3.6) but the inter-line spacing decreases with increasing  $J$  as typically  $D_e \gg H_e$ .

### Harmonic vibration

The most basic model of molecular vibrations is the harmonic oscillator that assumes a linear restoring force  $F = -k(|\mathbf{R}| - R_e)$  for small elongations from the equilibrium inter-nuclear distance  $R_e$ . Accordingly, the already introduced quadratic spring potential

$$E_{\text{vib}}(|\mathbf{R}|) = \frac{1}{2}k(|\mathbf{R}| - R_e)^2 \quad (3.10)$$

is used for the nuclear potential in eq. (3.4). Solving such a Schrödinger equation yields for the vibrational energy levels  $G(v)$

$$G(v) = \omega_e \left( v + \frac{1}{2} \right) \quad \text{with} \quad \omega_e = \frac{1}{2\pi c} \sqrt{\frac{k}{\mu}}, \quad [\omega_e] = \text{cm}^{-1} \quad (3.11)$$

where  $v = 0, 1, 2, \dots$  is the vibrational quantum number [Dem05]. Vibrational transitions with  $\Delta v = 1$  hence have a Raman shift  $\Delta\tilde{\nu} = \omega_e$  which is independent of  $v$ . Accordingly, all transitions with  $\Delta v = 1$  contribute to a single line in the Raman spectrum.

### Anharmonic vibrations

The harmonic oscillator is only a valid model for small elongations around  $R_e$ , i.e. small values of  $v$ , as it e.g. predicts  $E(v) \rightarrow \infty$  for  $v \rightarrow \infty$  and hence does not take into account that the molecule breaks apart when reaching the finite molecular binding energy  $E_b$ . A widely used model potential to take into account anharmonicity is the Morse potential [Mor29]

$$E_{\text{vib}}(|\mathbf{R}|) = E_b \left[ 1 - e^{-a(|\mathbf{R}| - R_e)} \right]^2 \quad (3.12)$$

with the molecule specific constants  $E_b$ ,  $a$ , and  $R_e$  is a better approximation of the molecular potential (figure 3.2 left) and additionally allows for an analytical calculation of term values when solving the Schrödinger equation [Dem05]:

$$\begin{aligned}G_{\text{vib}}(\nu) &= \frac{E_{\text{vib}}(\nu)}{hc} = \omega_e \left( \nu + \frac{1}{2} \right) - \omega_e x_e \left( \nu + \frac{1}{2} \right)^2 \\ \text{with} \quad \omega_e &= \frac{\omega_0}{2\pi c}, \quad \omega_e x_e = \frac{\omega_0^2}{16\pi c^2 E_b}, \quad \omega_0 = a \sqrt{\frac{2E_b}{\mu}}.\end{aligned}\quad (3.13)$$

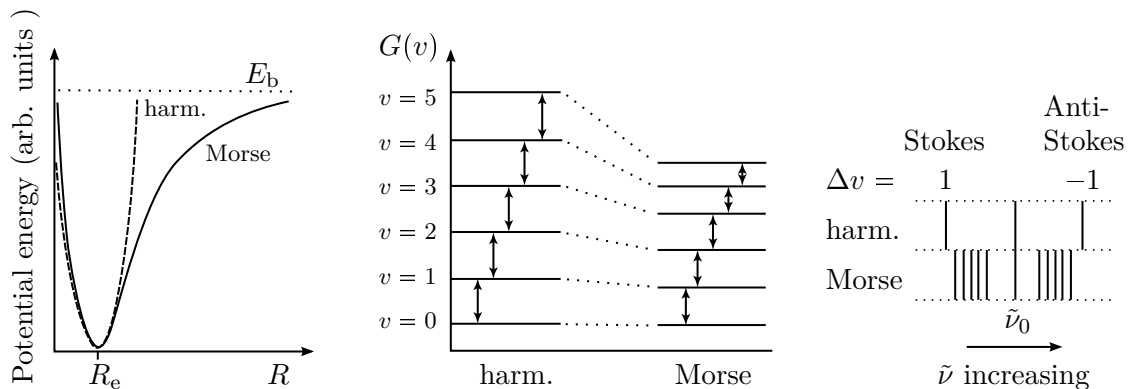


**Figure 3.2.: Impact of vibrational nuclear potential on Raman spectrum.** *Left:* Harmonic (dashed line) and Morse (solid line) nuclear potential as function of internuclear distance  $R$ . Both potentials have their minimum at the equilibrium distance  $R_e$ . The Morse potential does not exceed the binding energy  $E_b$ . *Middle:* Term scheme for both potentials. The energy levels are equidistant for the harmonic potential while the distances between neighbouring Morse energy levels decrease with increasing  $v$ . *Right:* Raman spectrum. The harmonic potential produces only one Stokes and Anti-Stokes line each around the laser line at  $\tilde{\nu}_0$ . The anharmonic Morse potential generates many lines due to the non-equidistant spacing of the energy levels. The Raman line splitting is exaggerated for demonstration purposes. Drawings based on [Lon02].

Due to the anharmonicity, the Raman shifts for  $\Delta v = 1$

$$\Delta\tilde{\nu}(v) = G_{\text{vib}}(v+1) - G_{\text{vib}}(v) = \omega_e - \omega_e x_e \left( 2v + \frac{7}{4} \right) \quad (3.14)$$

are not constant any more but depend on  $v$ . As a consequence each transition with  $\Delta v = 1$  appears as an individual line in the Raman spectrum (figure 3.2), when being measured with sufficient spectral resolution. As the Morse potential is in some cases still not sufficiently accurate to describe high resolution molecular spectra, the  $(v+1/2)$  power series in eq. (3.13) can be extended beyond the second order for an improved agreement between experimental data and model.

### Combined treatment of molecular rotation and vibration

Rotational and vibrational motion in a molecule can not be treated as being completely decoupled from each other, i.e. the influence of one excitation type onto the other has to be taken into account. As the vibrational excitations are by two to three orders of magnitude more energetic than the rotational ones (table 3.2) [Dem05], the common way is to treat the rotational constants in eq. (3.7) as dependent on the vibrational quantum number  $v$ :  $B_e \rightarrow B(v)$  and accordingly for  $D_e$  and  $H_e$ . Explicit formulas for  $B(v)$ ,  $D(v)$  and  $H(v)$  can be given in case of the Morse potential [Dem06]. The generic approach for arbitrary potentials again is a phenomenological power series to reproduce

the  $v$  dependence of the rotational constants:

$$B(v) = B_e - \alpha_e \left( v + \frac{1}{2} \right) + \gamma_e \left( v + \frac{1}{2} \right)^2 + \dots \quad (3.15)$$

$$D(v) = D_e - \beta_e \left( v + \frac{1}{2} \right) + \delta_e \left( v + \frac{1}{2} \right)^2 + \dots \quad (3.16)$$

and accordingly for  $H(v)$  where  $\alpha_e$ ,  $\gamma_e$ ,  $\beta_e$ ,  $\delta_e$ , etc. are molecular specific constants. This now allows writing down a generic expression for the term values  $T(v, J)$  of a rotating diatomic molecule with arbitrary vibrational potential:

$$\begin{aligned} T(v, J) = & \omega_e \left( v + \frac{1}{2} \right) - \omega_e x_e \left( v + \frac{1}{2} \right)^2 \\ & + \omega_e y_e \left( v + \frac{1}{2} \right)^3 + \omega_e z_e \left( v + \frac{1}{2} \right)^4 \dots \\ & + B(v)J(J+1) - D(v)J(J+1)^2 + H(v)J(J+1)^3 \dots \end{aligned} \quad (3.17)$$

This parametrisation will be used in section 5.3.4 to calculate Raman line positions of hydrogen fluoride and its deuterated and tritiated forms (HF, DF, TF).

### 3.1.2. Selection rules and calculation of Raman line positions

After finding a generic expression of the term values of diatomic molecules (eq. (3.17)), the next step is to specify selection rules, i.e. to state which transitions between the ro-vibrational states are quantum mechanically allowed for Raman scattering. In this context one has to address the principles of energy and angular momentum conservation.

In infra-red (IR) absorption spectroscopy, the incident photon can only be absorbed by the molecule if the photon energy  $h\nu$  corresponds to the energy difference  $\Delta E$  between two molecular states, i.e. if  $\Delta E = h\nu$ . The Hamiltonian describing such a process is

$$H = -\vec{p} \cdot \vec{\mathcal{E}} \quad (3.18)$$

which stands for the electric field (strength)  $\vec{\mathcal{E}}$  coupling to the permanent dipole moment  $\vec{p}$  of the molecule. Accordingly, only molecules with a permanent dipole moment can absorb and emit light. In case of light scattering from molecules, the situation is different as neither the condition  $\Delta E = h\nu$  has to be fulfilled nor a permanent dipole moment has to exist: The incident light polarises the molecule and generates a linear induced electric dipole moment

$$\vec{p}_{\text{ind}} = \alpha \cdot \vec{\mathcal{E}} \quad (3.19)$$

(in addition to the potentially existing permanent one) which again interacts with the electric field (eq. (3.18)). The second order polarisability tensor  $\alpha$  is a molecular-specific constant and determines the molecular susceptibility to electronic polarisation along arbitrary directions.

Following closely reference [Lon02], the necessary condition for a Raman-active molecule will now be deduced in a classical treatment. Considering a molecule that does not rotate but is free to vibrate around its equilibrium position one can do a Taylor expansion of  $\alpha$  with respect to the normal coordinates of vibration  $Q_k$ . Each component  $\alpha_{\rho\sigma}$  can be expressed as

$$\alpha_{\rho\sigma} = (\alpha_{\rho\sigma})_0 + \sum_k \left( \frac{\partial \alpha_{\rho\sigma}}{\partial Q_k} \right)_0 Q_k + \frac{1}{2} \sum_{k,l} \left( \frac{\partial^2 \alpha_{\rho\sigma}}{\partial Q_k \partial Q_l} \right)_0 Q_k Q_l + \dots \quad (3.20)$$

where the subscript '0' indicates that the expressions are evaluated at the equilibrium position. Neglecting second and higher order terms and introducing the equilibrium and derived polarisability tensors  $\alpha_0$  and  $\alpha'_k$ , respectively, reduces eq. (3.20) to

$$\alpha_k \approx \alpha_0 + \alpha'_k Q_k \quad \text{with} \quad (\alpha'_{\rho\sigma})_k = \left( \frac{\partial \alpha_{\rho\sigma}}{\partial Q_k} \right)_0. \quad (3.21)$$

Assuming that the molecule is harmonically vibrating in its  $k$ -th normal coordinate, i.e.  $Q_k = Q_{k0} \cos(\omega_k t + \delta_k)$ , results in a time dependent polarisability tensor

$$\alpha_k \approx \alpha_0 + \alpha'_k Q_{k0} \cos(\omega_k t + \delta_k). \quad (3.22)$$

If the molecule is irradiated with light of frequency  $\omega_{\text{ext}}$  and hence exposed to an electric field  $\vec{\mathcal{E}} = \vec{\mathcal{E}}_0 \cos(\omega_{\text{ext}} t)$ , the linear induced electric dipole moment is according to eq. (3.19) and eq. (3.22)

$$\vec{p}_{\text{ind}} = \alpha_0 \vec{\mathcal{E}}_0 \cos(\omega_{\text{ext}} t) + \alpha'_k \vec{\mathcal{E}}_0 Q_{k0} \cos(\omega_k t + \delta) \cos(\omega_{\text{ext}} t). \quad (3.23)$$

Using the trigonometric identity  $\cos A \cos B = \frac{1}{2} (\cos(A+B) + \cos(A-B))$ , the expression can be rearranged to

$$\vec{p}_{\text{ind}} = \underbrace{\alpha_0 \vec{\mathcal{E}}_0}_{\vec{p}_{\text{Ray}}} \cos(\omega_{\text{ext}} t) + \frac{1}{2} \underbrace{\alpha'_k Q_{k0} \vec{\mathcal{E}}_0}_{\vec{p}_{\text{Ram}}} [\cos((\omega_{\text{ext}} + \omega_k)t + \delta) + \cos((\omega_{\text{ext}} - \omega_k)t + \delta)]. \quad (3.24)$$

Thus, the molecule exhibits three linear induced dipole moments which have different frequencies, namely a dipole moment of frequency  $\omega_{\text{ext}}$  which is responsible for Rayleigh scattering, the Stokes Raman moment of frequency  $(\omega_{\text{ext}} - \omega_k)$ , and the Anti-Stokes Raman moment of frequency  $(\omega_{\text{ext}} + \omega_k)$ . The Raman-related dipole moments only contribute if at least one component of the derived polarisability tensor  $\alpha'_k$  is non-zero

$$(\alpha'_{\rho\sigma})_k = \left( \frac{\partial \alpha_{\rho\sigma}}{\partial Q_k} \right)_0 \neq 0. \quad (3.25)$$

In summary, this means that Raman scattering is only possible if the polarisability of the molecule changes due to the molecular excitation. This is in contrast to Rayleigh scattering where it is sufficient that the molecule is polarisable at all at the equilibrium position. Although this statement was deduced in a classical approximation, it is in principle also valid in the quantum mechanical context when replacing the polarisability tensor by the transition polarisability operator whose expectation value  $\langle f | \alpha | i \rangle$  has to be

**Table 3.3.: Definition of branches based on selection rules.** The branch nomenclature follows the PhD thesis of Richard Lewis [Lew07], a former member of the KATRIN laser Raman group. In general,  $\Delta\tilde{\nu}_{\text{vib}} \gg \Delta\tilde{\nu}_{\text{rot}}$ , i.e. the  $O_1$  and  $S_1$  branches closely surround the  $Q_1$  branch which is well separated from the  $O_0$ ,  $Q_0$  and  $S_0$  branches. Stokes Raman with  $\Delta\nu > 1$  are not listed as they are not of relevance for this work.

$\Delta\nu$	$\Delta J$	Branch name	Raman shift $\Delta\tilde{\nu}$	Scattering type
0	-2	$O_0$	$-\Delta\tilde{\nu}_{\text{rot}}$	Anti-Stokes scattering
0	0	$Q_0$	0	Rayleigh scattering
0	2	$S_0$	$\Delta\tilde{\nu}_{\text{rot}}$	Stokes Raman scattering
1	-2	$O_1$	$\Delta\tilde{\nu}_{\text{vib}} - \Delta\tilde{\nu}_{\text{rot}}$	
1	0	$Q_1$	$\Delta\tilde{\nu}_{\text{vib}}$	
1	2	$S_1$	$\Delta\tilde{\nu}_{\text{vib}} + \Delta\tilde{\nu}_{\text{rot}}$	

evaluated with respect to the initial and final molecular wave functions  $|i\rangle$  and  $|f\rangle$ . The selection rules of Raman scattering emerge from the calculation of these transition matrix elements and hence depend on the molecular wave functions. The wave functions again depend on the chosen molecular vibrational and rotational potential in the Schrödinger equation (eq. (3.4)).

The selection rule of pure rotational Raman transitions ( $\Delta v = 0$ ) is  $\Delta J = 0$  or  $\pm 2$ . For rotational-vibrational transitions  $\Delta v = 1$  has to be fulfilled in addition (details in [Lon02], chapter 6). The  $\Delta v$  selection rule is exact in case of the harmonic oscillator potential. If anharmonicities are included, so-called overtone-transitions with  $\Delta v = 2, 3, \dots$  are also allowed but with very reduced probability [Dem06]. Based on these selection rules, transitions with common  $\Delta J$ ,  $\Delta v$  are grouped into individual branches (table 3.3). Within each branch, the Raman lines are ordered according to the rotational quantum number  $J''$  of lower molecular state. For the scope of this work, the molecules can be assumed to be in the vibrational ground state before scattering due to the large vibrational excitation energies (table 3.2) and the restriction to room temperature. Hence, every line in a Raman spectrum is fully identified when the molecule, the branch and  $J''$  are specified. A generic Raman spectrum of diatomic molecules is shown in figure 3.3.

## 3.2. Raman line intensities

After the previous discussion whether a Raman transition is allowed or forbidden, this section will present the parameters that determine Raman line intensities. This is essential for the compositional analysis of tritium gas mixtures using Raman spectroscopy and hence for the scope of this work.

In case of diatomic molecules, the intensity of Raman scattered light of a certain Raman

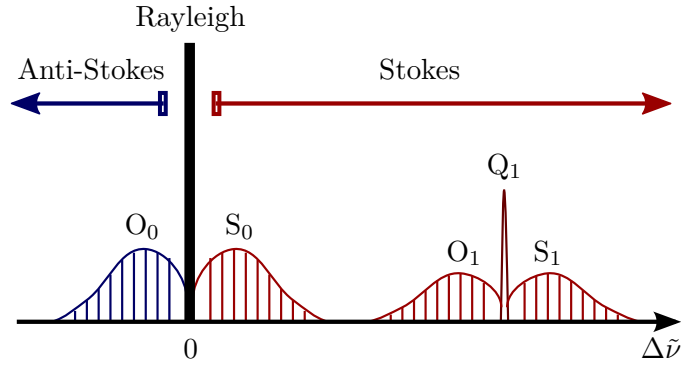


**Figure 3.3.: Generic Raman spectrum of a diatomic molecule.** The branches are labelled according to table 3.3. The splitting of the lines in the  $Q_1$  branch is less prominent than in the other branches. The line intensity distribution will be explained in the next section. Figure based on [Hak06].

transition is typically expressed by

$$I(\varphi, \theta)_{p^s, p^i} = k_{\tilde{\nu}} \cdot \tilde{\nu}_s^4 \cdot N_i \cdot \Phi(a, \gamma, \varphi, \theta)_{p^s, p^i} \cdot \mathcal{I} \quad (3.26)$$

where  $\tilde{\nu}_s$  is the wavenumber of the Raman scattered light [Lon02]. Before discussing the other parameters, it shall be noted that eq. (3.26) is only valid if the power of the scattered light is measured [McM06]. If the employed detector system counts the number of scattered photons, which is the case for the charged-coupled device (CCD) detector employed in this work, eq. (3.26) needs to be modified to

$$I(\varphi, \theta)_{p^s, p^i} = k_{\tilde{\nu}} \cdot \tilde{\nu}_0 \cdot \tilde{\nu}_s^3 \cdot N_i \cdot \Phi(a, \gamma, \varphi, \theta)_{p^s, p^i} \cdot \mathcal{I} \quad (3.27)$$

by replacing one of the  $\tilde{\nu}_s$  terms with the wavenumber  $\tilde{\nu}_0$  of the incident laser light. This modification takes into account that every scattered photons carries the energy  $E = h\nu = hc\tilde{\nu}$  which obviously varies over the spectral range of the Raman spectrum.

$k_{\tilde{\nu}} = \pi^2/\varepsilon_0^2$  is a constant where  $\varepsilon_0$  is the vacuum permittivity.  $p^s$  and  $p^i$  are parameters and indicate the line polarisation plane of the scattered ( $p^s$ ) and incident ( $p^i$ ) light. The Raman intensity is proportional to the power density  $\mathcal{I}$  of the incident laser light and to the number of molecules  $N_i$  in the initial molecular state and volume being probed by the laser beam.  $N_i$  can be decomposed into

$$N_i = \frac{N g_i e^{-\frac{E_i}{k_B T}}}{Q} \quad (3.28)$$

with the total number of molecules in the scattering region  $N$  and the statistical weight  $g_i$  of the the initial  $i$  state ( $i$  represents all relevant quantum numbers). The exponential Boltzmann factor  $\exp(-E_j/k_B T)$  takes into account the thermal population of the initial rotational-vibrational state of energy  $E_i$  for a given temperature  $T$ .  $Q = \sum_j g_j \exp(-E_j/k_B T)$  is the partition function which normalises  $N_i$ . The intensity distribution caused by the Boltzmann term is illustrated in figure 3.3 for the  $O$  and  $S$  branches.

The statistical weight accounts for the degeneracy of molecular states and is given by the product

$$g_i = g_v g_N \cdot (2J'' + 1) \quad (3.29)$$

of the vibrational and nuclear weighting factors  $g_v$  and  $g_N$  respectively and of a pure rotation weighting factor  $g = (2J'' + 1)$ .  $J''$  is the rotational quantum number of the lower energetic state involved in the Raman scattering. Vibrational states of diatomic molecules are non-degenerate and hence  $g_v = 1$ .

The treatment until now was valid for all types of diatomic molecules but  $g_N$  has to be treated differently for hetero-nuclear and homo-nuclear diatomic molecules. In a hetero-nuclear molecule, no parity is defined and  $g_N = 1$ . In a homo-nuclear molecule the nuclear weight  $g_N$  takes different values for odd and even  $J''$  states (table 3.4) due to the nuclear spin of the nuclei and hence modulates the intensity of rotational Raman lines within a branch. This will be briefly discussed in the next paragraph.

The total wave function of a molecule in the Born-Oppenheimer approximation is given by the product

$$\Psi = \psi_{\text{el}} \psi_{\text{vib}} \psi_{\text{rot}} \psi_{\text{nuc}} \quad (3.30)$$

of the electronic, vibrational, rotational and nuclear-spin wave functions. The parity of  $\Psi$  is given by the parity of  $\psi_{\text{rot}} \psi_{\text{nuc}}$  as both  $\psi_{\text{el}}$  and  $\psi_{\text{vib}}$  have always positive parity in the context of this work [Dem05]. For a homo-nuclear molecule made of fermionic nuclei (e.g.  $\text{H}_2$ ,  $\text{T}_2$ ),  $\Psi$  has to be anti-symmetric under exchange of the nuclei (i.e.  $\Psi$  has negative parity) due to the Pauli principle. Rotational states with odd  $J''$  have negative parity and hence can only be populated in molecules in which  $\psi_{\text{nu}}$  has a positive parity. Vice versa, rotational states with even  $J''$  (positive rotational parity) exist only in molecules in which  $\psi_{\text{nu}}$  has a negative parity. For  $\text{H}_2$  and  $\text{T}_2$ , one has  $g_N = 3$  nuclear wave functions ( $|\uparrow\uparrow\rangle$ ,  $|\downarrow\downarrow\rangle$ , and  $[|\uparrow\downarrow\rangle + |\downarrow\uparrow\rangle]/\sqrt{2}$ ) which are symmetric under the exchange of nuclei but only  $g_N = 1$  anti-symmetric state ( $[|\uparrow\downarrow\rangle - |\downarrow\uparrow\rangle]/\sqrt{2}$ ). For this reason the intensity of odd- $J''$  rotational lines of  $\text{H}_2$  and  $\text{T}_2$  is enhanced by a factor  $g_{N,\text{odd}}/g_{N,\text{even}} = 3$  with respect to even- $J''$  lines. In case of  $\text{D}_2$  which consists of bosonic nuclei (nuclear spin  $I = 1$ ), the total wave function has to be symmetric. Accordingly, the even- $J''$  states are only populated in molecules whose nuclear wave function has positive parity while the odd- $J''$  states exist only in molecules with negative parity nuclear wave functions. As there are six nuclear wave functions with positive parity and three with negative parity, even- $J''$  rotational lines in a  $\text{D}_2$  Raman spectrum are a factor of  $g_{N,\text{even}}/g_{N,\text{odd}} = 6/3 = 2$  more intense than odd- $J''$  lines (table 3.4).

The Raman intensity  $I(\varphi, \theta)_{p^s, p^i}$  (eq. (3.27)) depends on the polarisation state  $p_i$  of the incident light and on the experimenter's choice which polarisation component  $p_s$  of the scattered light is observed. Also the overall scattering geometry of the experiment, i.e. at which angles  $\varphi$  and  $\theta$  (defined in figure 3.4) the scattered light is collected, has to be considered. The line strength function  $\Phi(a, \gamma, \varphi, \theta)_{p^s, p^i}$  is a molecular-specific and Raman-transition-specific function which contains all these dependencies. The line strength function is connected to the matrix element of the transition polarisability operator that was introduced in the section before. As this work focuses on Raman scattering on gases,

**Table 3.4.: Influence of  $J''$  on nuclear weight  $g_N$ .** The rotational Raman line intensities of the homo-nuclear isotopologues  $\text{H}_2$ ,  $\text{D}_2$  and  $\text{T}_2$  are effected by the nuclear spin statistics, while those of the hetero-nuclear molecules  $\text{HD}$ ,  $\text{DT}$ , and  $\text{HT}$  are not. For details see main text. According to [Lon02, Dem05].

	$\text{H}_2, \text{T}_2$	$\text{D}_2$	$\text{HD}, \text{HT}, \text{DT}$
Parity of total wave function	Negative	Positive	not defined
Nuclear spin of each nucleus	$\frac{1}{2}$	1	$\frac{1}{2}, 1$
Number of nuclear wave functions $\psi_{\text{nuc}}$ with			
positive parity	3	6	–
negative parity	1	3	–
Nuclear weight $g_N$			
$J''$ odd	3	3	1
$J''$ even	1	6	1

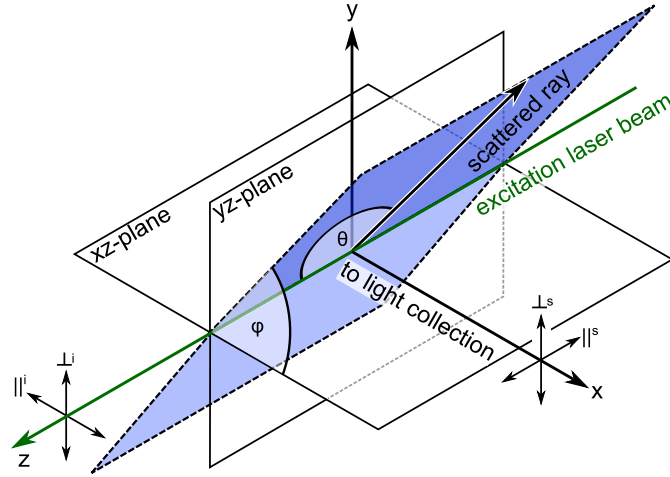


**Figure 3.4.: Definition of scattering angles  $\varphi$ ,  $\theta$ .** The breadboard surface of the laser setup (not shown) is parallel to the  $xz$ -plane. The polarisation components (parallel and perpendicular) of the incident and scattered light are defined with respect to the  $xz$ -plane. Figure from [Sch13b].

i.e. on samples that consist of a large number of isotropically oriented molecules, the elements of the transition polarisability matrix  $\alpha$  have to be averaged over all molecular orientations. This averaging results in tensor invariants, which are inherent quantities of the transition polarisability tensor but independent of the chosen coordinate system. Two of these are of relevance for diatomic molecules, namely the mean polarisability  $a$  and the anisotropy  $\gamma$  (for details see 'isotropic averages' in section A.14 of [Lon02]). In case of a diatomic molecule, i.e. a molecule with cylindrical symmetry, which is aligned along the z-axis of the coordinate system,  $\alpha$  can be simplified according to  $\alpha_{xx} = \alpha_{yy}$  and  $\alpha_{xy} = \alpha_{yz} = \alpha_{zx} = 0$ , and  $a$  and  $\gamma$  expressed in terms of the remaining, independent elements of  $\alpha$

$$a = \frac{1}{3}(2\alpha_{xx} + \alpha_{zz}), \quad \gamma = |\alpha_{zz} - \alpha_{xx}|. \quad (3.31)$$

In this work, a vertically polarised laser beam ( $p^i = \perp^i$ ) is used as excitation source. In this case the line strength functions of pure vibrational transitions ( $Q_1$  branch) of both polarisation components ( $p^s = \perp^s$  and  $p^s = \parallel^s$ ) of the scattered light are given by

$$\Phi(a, \gamma, \varphi, \theta)_{\perp^s, \perp^i} = a^2 \cos^2 \varphi + b_{J''}^{(2)} \frac{\gamma^2}{45} (4 - \sin^2 \varphi) \quad (3.32)$$

$$\Phi(a, \gamma, \varphi, \theta)_{\parallel^s, \perp^i} = a^2 \cos^2 \theta \sin^2 \varphi + b_{J''}^{(2)} \frac{\gamma^2}{45} (3 + \cos^2 \theta \sin^2 \varphi) \quad (3.33)$$

with the Placzek-Teller factor

$$b_{J''}^{(2)} = \frac{J''(J'' + 1)}{(2J'' - 1)(2J'' + 3)} \quad (3.34)$$

that depends on the rotational state  $J''$  of the molecule [Lon02]. In this work the Raman scattered light is collected parallel to the surface of the optical breadboard ( $\varphi = 0^\circ$ ) and in a  $\theta = 90^\circ$  angle with respect to the vertically polarised laser light. Since the collection optics have a large aperture to maximise the signal intensities, the line strength functions have not only to be evaluated for these distinct angles but integrated over a finite solid angle when calculating realistic Raman signal intensities. The development of the necessary mathematical and computational algorithms was started in [Fis10] and completed in [Sch13b], where detailed information can be found.

The theoretical framework for the calculation of Raman spectra of diatomic molecules is now complete as explicit formulas and guidelines were given

- to calculate the energy terms of molecular states (eq. (3.17)) and, based on these, the Raman shift of vibrational-rotational transitions,
- to determine if a certain transition is quantum mechanically allowed (eq. (3.25), table 3.3), and
- to calculate the intensity of the corresponding line in the Raman spectrum (eq. (3.27)).

A Raman spectrum of T<sub>2</sub> and DT which was measured within the scope of this work (run C148, details in 4.6.2) is shown in figure 3.5. The various Raman branches and the discussed intensity distribution within a branch are clearly visible. The spectrum is typical for the Raman spectra that will be acquired during the KATRIN experiment for quantitative compositional analysis of the WGTS source gas.

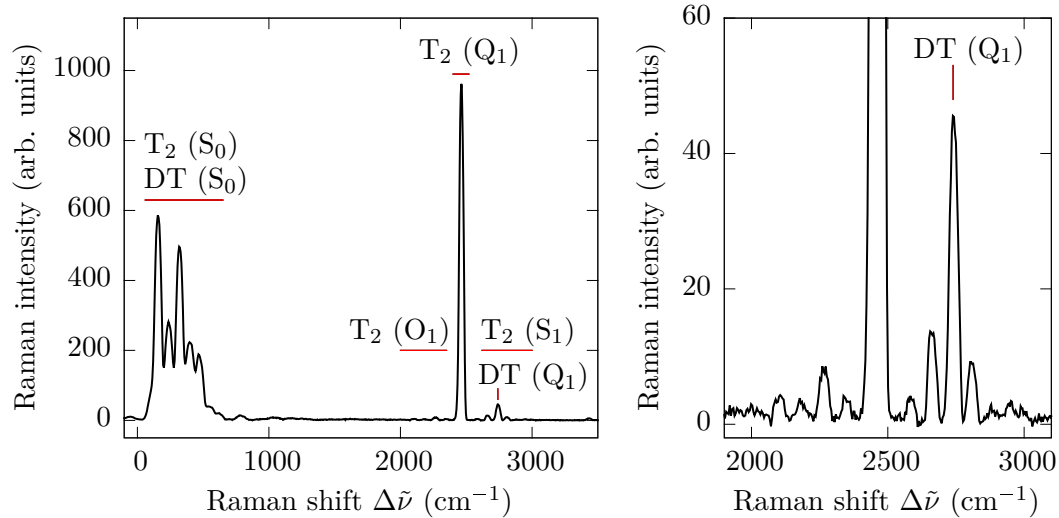


**Figure 3.5.: Raman spectrum of T<sub>2</sub>, DT mixture.** *Left:* Overview spectrum with S<sub>0</sub> branches around 0–600 cm<sup>-1</sup> (only partly resolved by the spectrometer) and O<sub>1</sub>, Q<sub>1</sub> and S<sub>1</sub> branches around 2000–3000 cm<sup>-1</sup>. *Right:* Details of O<sub>1</sub>, Q<sub>1</sub> and S<sub>1</sub> branches of T<sub>2</sub> and Q<sub>1</sub> branch of DT which overlaps with the S<sub>1</sub> ( $J'' = 2$ ) line of T<sub>2</sub>. Both Q<sub>1</sub> branches cannot be resolved with the spectrometer employed in this work (details in chapter 4) and therefore appear as a single line with slightly distorted line profile.

### 3.3. Quantitative analysis of Raman spectra of hydrogen isotopologues

The aim of the foregoing sections was to explain the structure of Raman spectra of diatomic molecules from the theoretical point of view. This section will turn towards the experimental side and focus on the question how Raman spectroscopy is applied in the KATRIN experiment to extract accurate quantitative information on the composition of tritium gas mixtures from measured Raman spectra. KATRIN is expected to be operated over a period of about five years in successive measurement runs, each about 60 days long [KAT05]. During such a 60 days period, the KATRIN Raman system, including the real-time data analysis of Raman spectra, has to run autonomously to provide data for neutrino mass analysis but also give direct feedback to the Inner Loop operators. Therefore special care has to be taken to ensure that the validity of the employed analysis procedures and algorithms is continuously guaranteed. In addition, the analysis has to be robust enough to cope with changing experimental conditions during the unattended operation. This section will summarise how Raman spectra are quantitatively evaluated in the KATRIN experiment and what preceding works were necessary to reach the current status.

Due to the large relative mass difference of the hydrogen isotopes H, D, and T (mass ratio 1:2:3), the Q<sub>1</sub> branches of the isotopologues do not overlap (figure 3.6) and hence are promising candidates for quantitative analysis. For 532 nm laser irradiation, they are found according to eq. (3.3) between 612 nm (T<sub>2</sub>) and 683 nm (H<sub>2</sub>), i.e. in a part of the visible spectrum for which optical spectrometers and detectors of sufficient optical

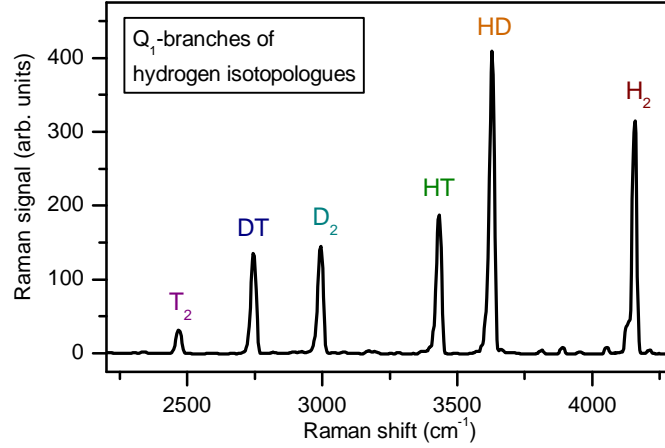


**Figure 3.6.: Raman spectrum of all hydrogen isotopologues.** The  $Q_1$  branches of the isotopologues are well separated due to the large relative mass difference of the hydrogen isotopes. Figure from [Sch13b].

resolution and sensitivity are available. Further advantages of the  $Q_1$  branches over other Raman branches can be found in [Sch13b] and [Sch09]. With the optical spectrometer employed in this work (details in chapter 4.2), it is possible to record all  $Q_1$  branches within one spectrum acquisition at the expense that the rotational substructure of the individual branches cannot, or just to some degree, be resolved. Therefore, the complete  $Q_1$  branches are chosen as the feature in the Raman spectrum on which the quantitative analysis is based. The following discussion will only focus on one individual Raman line for each isotopologue for the sake of simplicity. The results can be extended to a complete branch by appropriate superposition as described in detail in [Sch13b].

The line intensity  $I(\varphi, \theta)_{p^s, p^i}$  of a certain isotopologue and Raman transition was already defined in eq. (3.27). In order to acquire quantitative information on the gas composition, e.g. to measure  $N_i$  in eq. (3.27), the spectral sensitivity function

$$\eta(\tilde{\nu}) = \frac{I(\varphi, \theta)_{p^s, p^i, \text{exp}}}{I(\varphi, \theta)_{p^s, p^i}} \quad (3.35)$$

has to be taken into account which originates from the wavelength-dependent transmission and sensitivity of the optical spectrometer system and detector, respectively. Therefore eq. (3.27) is extended to

$$I(\varphi, \theta)_{p^s, p^i, \text{exp}} = \underbrace{\eta(\tilde{\nu}_s) \cdot k_{\tilde{\nu}} \cdot \tilde{\nu}_0 \cdot \tilde{\nu}_s^3 \cdot \Phi(a, \gamma, \varphi, \theta)_{p^s, p^i}}_R \cdot \mathcal{I} \cdot N_i \quad (3.36)$$

for a realistic description of experimentally measured Raman line intensities. All molecular- and transition-specific constants can be combined with the experimental parameters into a molecular-, transition- and experiment-specific response function  $R_x$ , which brings eq. (3.36) into the form

$$S_x = R_x \cdot N_x \quad (3.37)$$

where  $S_x$  is the Raman signal belonging to the isotopologue  $x$  and  $N_x$  the corresponding molecular number density. The measurement procedure can be simplified by introducing relative Raman line intensities

$$\begin{aligned} S_{x,\text{rel}} &= \frac{S_x}{\sum_j S_j} \\ &= \frac{R_x \cdot N_x}{\sum_j R_j \cdot N_j}, \end{aligned} \quad (3.38)$$

i.e. normalising each individual Raman branch to the sum of all Raman signals. Consequently, the relative Raman intensities become immune to unavoidable laser power and wavelength fluctuations as  $\mathcal{I}$  and  $\tilde{\nu}_0$  (and  $k_{\tilde{\nu}}$ ) cancel out in the ratio.

Several prerequisites have to be fulfilled for an accurate quantitative gas analysis:

- comprehensive understanding of the Raman spectra of all hydrogen isotopologues, namely unambiguous identification of Raman lines,
- determination of the response functions, i.e.
  - knowledge of the line strength functions of the relevant transitions and isotopologues with sufficient confidence, and
  - measurement of the spectral sensitivity of the Raman system, and
- development of algorithms for accurate analysis of measured spectra.

These prerequisites will be briefly discussed.

### Comprehensive understanding of Raman spectra of hydrogen isotopologues

Raman spectroscopy on hydrogen isotopologues (including the tritiated species HT, DT, T<sub>2</sub>) has been the subject of persistent theoretical and experimental interest for about 35 years, especially but not exclusively in the community related to nuclear fusion where tritium and deuterium is used as fuel for future fusion power plants.

Because of its simplicity, the hydrogen molecule has been of significant importance from the theoretical point of view as a test bed for quantum mechanical (ab-initio) calculations and hence prediction of energy levels, Raman shifts and line intensities. One of these calculation was carried out by Kolos and Wolniewicz [Kol64] in 1964 whose initial work was followed by many subsequent improvements. In the paper by Schwartz and LeRoy [Sch87], published in 1987, a comprehensive summary of the development is given. The findings presented in said paper are instrumental to the arguments put forward in the following paragraphs.

The first known experimental determination of molecular constants of T<sub>2</sub> by Raman spectroscopy was performed in 1978 by Edwards et al. [Edw78]. In 1987 Veirs and Rosenblatt measured the Raman shifts of various transitions of all isotopologues with an accuracy of better than 1 cm<sup>-1</sup> [Vei87]. In 1992, high-resolution Raman measurements of hydrogen isotopologues and tritiated methane species were performed by U. Engelmann at KIT (at that time named KfK (Kernforschungszentrum Karlsruhe)) [Eng92, Eng97]. A joint US-Japanese collaboration developed and operated Raman systems at the TSTA

facility at Los Alamos National Laboratory and at the Tritium Engineering Laboratory in Japan [Ohi92, Ohi96]. First research on Raman spectroscopy on hydrogen isotopologues at Tritium Laboratory Karlsruhe (TLK) was done by Taylor et al. in 2001 although not yet with tritiated species [Tay01].

Due to the decision to construct the KATRIN experiment at KIT research on Raman spectroscopy was resumed at TLK with the aim to achieve the capability of continuous compositional gas analysis. Richard Lewis performed first measurements with flowing non-tritiated gas mixtures and was able to show that the KATRIN requirements would very likely be reached, albeit only for relatively long acquisition times of 1000 s [Lew07]. The measurements were extended to static mixtures of all hydrogen isotopologues [Stu10a] within the work of Magnus Schlösser who also investigated numerous systematic effects [Sch09]. In 2010, the tritium circulation test loop LOOPINO was commissioned at TLK and Raman spectroscopic measurements on circulating gas mixtures with purified tritium gas (tritium purity > 90%) were performed for the first time at the Tritium Laboratory Karlsruhe [Stu10b, Fis10]. As a result of continuous improvements of the Raman system, the KATRIN requirements of 0.1% relative precision could be reached at that time already in 250 s acquisition time [Fis11] and as more recently reported even within less than 60 s [Sch13b].

Theoretical predictions of Raman shifts have reached spectroscopic accuracy, i.e. an agreement with experimental values of better than  $1 \text{ cm}^{-1}$  [Mül98], already in 1968 in case of  $\text{H}_2$  [Kol68]. For the other isotopologues this was achieved at least since the work by Veirs and Rosenblatt [Vei87]. Summarising, it can be stated that Raman spectra of hydrogen isotopologues are sufficiently well understood to allow an unambiguous identification of Raman lines. The prediction of line intensities was until recently not fully validated for all hydrogen isotopologues as it will be shown in the next paragraph.

**Calculation of line strength functions** In section 3.2, the line strength function has been introduced as a molecular-specific function that determines the intensity for each Raman transition and isotopologue. The molecular-specific information is contained in the two tensor invariants  $a$  and  $\gamma$  which have to be accurately known to enable an accurate compositional gas analysis from measured Raman signal intensities. The invariants can be calculated by quantum mechanical ab-initio calculations, as done in the paper by Schwartz and Le Roy [Sch87] which was the state of the art for hydrogen isotopologues until recently. But since no confidence levels and hence information on the trueness of the calculated tensor invariants were available, an inestimable and hence unacceptable uncertainty remained when using them for quantitative analysis of Raman spectra.

An experimental validation of so-called depolarisation ratios, for all hydrogen isotopologues has been performed by the KATRIN Raman group using the tensor invariants that were kindly recalculated by R. J. Le Roy for 532 nm laser excitation as used in this experiment. The validation showed that nearly all of the calculated depolarisation ratios of the  $Q_1(J'')$  lines of all six hydrogen isotopologues agree with the experimental results within 5% ( $1\sigma$ ) [Jam13a, Jam13b, Sch13b]. Hence the calculated tensor invariants can be used together with the propagated uncertainties of said experimental validation for the quantitative analysis of Raman spectra in the KATRIN experiment.

**Measurement of spectral sensitivity of the Raman system** The question of measuring the spectral sensitivity  $\eta(\lambda)$  of the light collection and analysis system (details on the individual components in section 4.2) were topic in several theses at KIT [Bru13, Rup12, Sch13b]. A NIST<sup>1</sup>-traceable luminescence standard (type SRM 2242 [Cho07, NIS08]) was identified as an ideal light source because of its certified intensity profile (certified region  $\Delta\tilde{\nu} = 150\text{--}4000\text{ cm}^{-1}$ ) which covers nearly all Q<sub>1</sub> branches of the hydrogen isotopologues. Although the luminescence standard has to be operated under conditions slightly different from those specified by NIST, its feasibility of measuring response functions of Raman systems was proven for the non-radioactive isotopologues by S. Rupp who reached a measurement uncertainty of  $< 3.1\%$  [Rup12]. The calibration procedure has been further investigated, optimised and cross-checked in a round robin test using three different Raman systems at TLK. The general concept and theoretical model of the spectral calibration as developed in [Rup12] could be verified but a deviation for one of the Raman setups was found [Bru13] which is currently under investigation. The concept of spectral calibration using the SRM2242 standard could be successfully incorporated in the overall calibration scheme for the KATRIN Raman system by M. Schlösser [Sch13b] who combined the SRM2242 spectral calibration with Raman measurements of accurately known non-tritiated gas mixtures. The deviation between both methods was determined to be  $(1.9\pm 3.1)\%$ . i.e. consistent with zero indicating the good agreement of both methods. In summary, it can be stated that the KATRIN Raman system can be calibrated with high accuracy: The molar fractions in a tritium dominated gas mixture (97.7% T<sub>2</sub>, 1.5% DT, 0.3% HT, 0.3%D<sub>2</sub>, 0.4% HD) can be measured with a relative uncertainty of 0.1% in case of T<sub>2</sub> and  $\sim 5\%$  for the other isotopologues which easily fulfils the requirements of the KATRIN experiment [Sch13b].

**Algorithms for accurate analysis of measured Raman spectra** The algorithms for pre-processing and analysing Raman spectra are of special importance when one aims at the extraction of quantitative information. Therefore, this aspect has been already tackled by R. Lewis [Lew07] who developed algorithms for the compensation of optical imperfections (astigmatism) of the spectrometer and for the removal of spurious pixels in the raw CCD images that are caused by cosmic muons passing through the sensor chip during acquisition. The extraction of signal intensities was further refined in [Sch09]. At that time, the analysis was based on several NI<sup>TM</sup> LabVIEW<sup>TM</sup> and OriginLab<sup>®</sup> OriginPro<sup>®</sup> programs and routines which required manual fine adjustments by the user and still had to be run offline, i.e. after data acquisition.

To simplify the data analysis but also to reduce the open parameters to be chosen by the user, the data analysis package SpecTools<sup>2</sup> was developed which also includes significant improvements of the algorithms for cosmic ray removal, background removal, and peak fitting [Jam13c, Sch13b, Jam13a]. The package is based on LabVIEW<sup>TM</sup> to ensure compatibility with the operation software of the KATRIN Raman system and allows a batch-wise offline analysis of Raman data. A simplified diagram of the analysis chain in SpecTools is shown in figure 3.7. SpecTools permits the accurate analysis of Raman spectra as successfully demonstrated in [Jam13c] where concentration ratios

---

<sup>1</sup>National Institute of Standards and Technology, Gaithersburg, Maryland, US

<sup>2</sup>Source code, documentation and tutorials available under <http://spectools.sourceforge.net>.

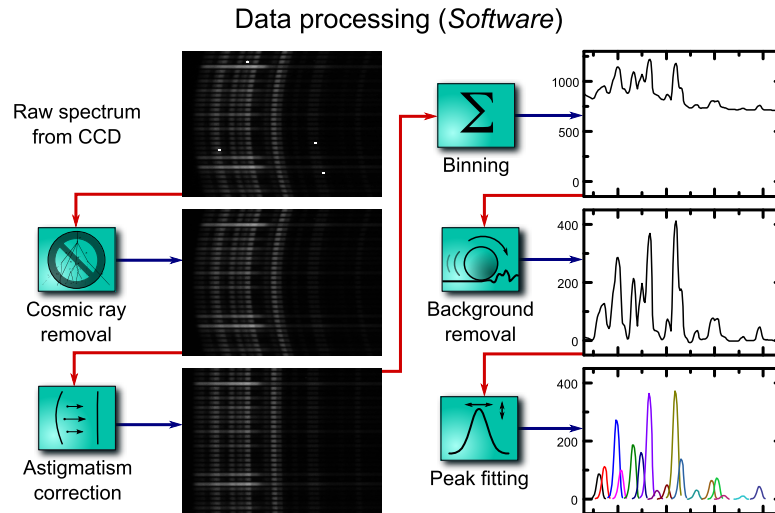


**Figure 3.7.:** Data flow diagram of SpecTools. For details see text. Figure from [Sch13b].

of  $^{16}\text{O}^{17}\text{O}$ ,  $^{16}\text{O}^{18}\text{O}$ , and  $^{14}\text{N}^{15}\text{N}$  with respect to the dominating isotopologues  $^{16}\text{O}^{16}\text{O}$  and  $^{14}\text{N}^{14}\text{N}$ , respectively, were extracted from Raman spectra and full agreement with isotopic abundance data was found.

In order to provide accurate compositional information in real time as requested by the KATRIN experiment, a further development of SpecTools towards a framework for automated acquisition and analysis of Raman data is necessary. This task which was accomplished within [Kas12] and this work will be described in chapter 6 where also more details on the individual data analysis procedures of SpecTools are given.

As presented in the paragraphs above, most of the prerequisites for quantitative compositional gas analysis were already solved at the beginning of this work or currently under investigation. However, several on first glance potentially inconspicuous but essential aspects concerning the software for operation and data analysis, the commissioning of the hardware, and test for detrimental processes affecting the system were still open. These tasks have been tackled in this work and will be presented in the next chapters.



## 4. The KATRIN Raman system

### LARA3: Setup and commissioning

This chapter discusses the experimental setup and the commissioning of the KATRIN Raman system which was constructed within the scope of this thesis using the experience gained by the KATRIN LARA group. A brief summary of the most relevant findings is given in the next section. The actual experimental setup including the tasks and properties of the individual subcomponents is described in detail in section 4.2. As the KATRIN Raman system was constructed and commissioned in two steps, the differences between the interim version *LARA3pre* and the final system *LARA3* are presented in this section. The objectives and experimental conditions of the various commissioning measurements are summarised in section 4.3 before they are discussed in detail: Commissioning of *LARA3pre* with static gas mixtures (section 4.4), test of the Finesse laser before installation (section 4.5), and finally the commissioning of the KATRIN Raman system with circulating gas mixtures (section 4.6) to operate the system under similar conditions as in future neutrino mass measurements. The chapter concludes with an evaluation of the system performance with respect to the requirements defined by the KATRIN experiment (section 4.7).

#### 4.1. Experience from preceding Raman system prototypes

Research and development for the KATRIN Raman system had started with the work by Richard Lewis [Lew07]. Until the beginning of the present thesis, two Raman systems at TLK (internally labelled 'LARA1' and 'LARA2') and one system at Swansea University were constructed, operated and continuously optimised [Sch09, Stu10b, Stu10a, Fis10, Her11, Kas12, Jam13a]. Extensive efforts have been made by the KATRIN Raman group and the author to characterise the experimental systems and their components and to determine both interfering and beneficial effects (details e.g. in [Bai11, Sch11c, Jam13c, Sch13b, Sch13d, Sch13a, Fis14]). Each of the already existing systems has certain positive but also negative particularities which impact on the performance, operation or reliability of the system. Since the KATRIN Raman system (labelled 'LARA3' according to the TLK internal nomenclature) shall push the limits with respect to sensitivity, precision and reliability and hence has to be fully optimised, the existing Raman systems can be considered as prototypes in this context. Therefore, a short summary of selected results and insights based on the experience with the prototype systems is given, before the experimental setup of the KATRIN Raman system is described in the next section.

### **Laser instabilities**

Fluctuations and drifts of laser wavelength [Lew07], power [Stu10b, Fis10, Fis11] and beam pointing [Stu10b, Fis10, Fis11] have been observed in the LARA1 and LARA2 system. Wavelength stability is only a minor issue in the KATRIN Raman setup due to the smallness of the drifts with respect to the large splitting of the relevant Raman lines and the resolution of the spectrometer gratings employed in the systems [Lew07]. Although variations of the laser power do not affect the accuracy of the Raman measurement (due to the calculation of relative Raman intensities) they should nevertheless be avoided since the precision of the measurement deteriorates for decreasing laser power. Beam pointing stabilities have a similar detrimental effect in so far as they result in a decreased overlap of the laser beam in the Raman sample cell with the narrow visual field of the light collection system [Sch09] which will reduce the amount of collected Raman scattered light. Strong correlations of the ambient temperature with laser parameters, especially beam pointing, were found. Thus, a stable operation of the lasers with respect to all of these aspects is only possible when active temperature stabilisation of the laser head is ensured [Fis10, Kud11]. But even then the laser parameters must still be monitored during long-term operation to identify gradually arising dysfunctions before they become severe issues.

### **Damage of anti-reflection coated optical windows after contact with tritium gas**

The windows of the Raman sample cell are anti-reflection coated to minimise the transmission losses of laser and scattered light and hence to maximise the signal-to-noise ratio in the Raman spectrum. A severe degradation of these windows (figure 4.1) was observed after three months of contact with highly purified tritium gas (200 mbar absolute pressure, tritium purity  $\geq 90\%$ ) [Stu10b, Fis11]. This caused a loss of laser power in the sample cell and changed the wavelength-dependent transmission coefficient  $T(\lambda)$  of the windows and hence the spectral sensitivity of the light collection system. Such a behaviour cannot be accepted for long-term operation in the KATRIN experiment. The reasons for the damage were investigated in this work and suitable countermeasures implemented in the KATRIN Raman system as it will be shown in this and the following chapters.

### **Temperature sensitivity of monitoring devices**

Monitoring of the laser power can be performed by dumping the laser beam on a thermopile sensor at the end of the beam path or by picking-up and monitoring a small fraction of the beam using a photo diode. The generated photo current is afterwards amplified and converted to a voltage by a transimpedance amplifier and digitised with an analogue-to-digital converter (ADC). Temperature dependent drifts of the spectral sensitivity of photo diodes on the  $10^{-3}/\text{K}$  level were measured by A. Bainbridge [Bai11]. In addition, severe drifts of the transimpedance amplifiers used in the first-generation electronics were observed [Fis10]. The components for laser power monitoring should therefore be carefully selected with respect to stability and their intended application.

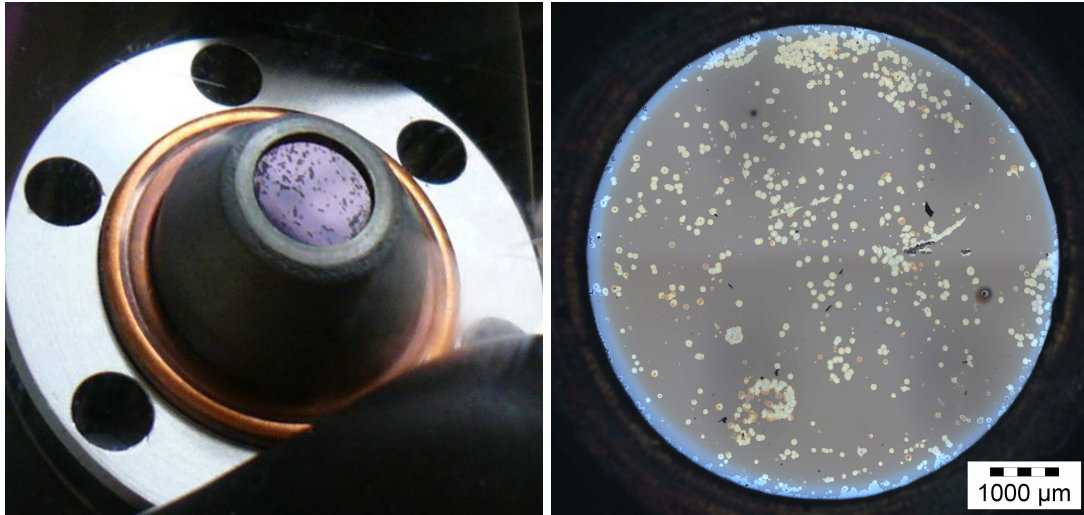


**Figure 4.1.: Degradation of anti-reflection coated optical windows after contact with highly purified tritium gas.** *Left:* Window in dismounted vacuum flange (CF16) with spot-like damaged areas on the tritium facing window side. *Right:* Microscopy image of the damaged AR coating of another window, acquired at Fusion Material Laboratory (IAM-WBM, KIT). Details in chapter 5.

### Layout of optical beam path

The available space for the optical beam path was limited in the prototype Raman systems due to the large dimensions of the installed components (e.g. the laser head in the LARA1 system) and the limited breadboard size (e.g. in the LARA2 system). This resulted in components which are difficult to access, lacking space for extensions of the beam path and caused restrictions for visual inspection of the beam position during alignment. Therefore, sufficient space for the beam path should be allocated in the KATRIN Raman system. In order to ensure the stability of the components and simplify their alignment, as many components as possible should be installed in 'cage systems', i.e. mounted in holders that are threaded on rods and hence automatically located in a straight line. Several reference points (e.g. pinholes and apertures) should be installed in the beam path to allow for reproducible beam alignment during the maintenance phases of KATRIN since this task will be performed by trained but non-expert personal during KATRIN operation.

## 4.2. Experimental setup of LARA3

The optical setup consists of three main sections: The excitation beam path, the sample cell, and the light collection and analysis system. In addition a set of monitoring sensors and parameters are necessary for unattended long-term operation of the system. The KATRIN Raman system will be described in the next sections.

#### 4.2.1. LARA3*pre*: A pre-stage of the KATRIN Raman system

The KATRIN Raman system LARA3 was constructed and commissioned in two phases because certain components (e.g. the laser) were not yet delivered, and because selected aspects were still under investigation at the time of the first construction and commissioning phase. The intermediate version will be called LARA3*pre* in the following while the final version of the experimental setup is called LARA3. A sketch of the layout of the optical beam paths of both systems is illustrated in figure 4.2. Both systems use a so-called *double pass* configuration, i.e. the laser beam is back-reflected after passing the Raman sample cell (LARA cell) the first time. The beam 'recycling' increases the effective laser power in the LARA cell and accordingly the signal-to-noise ratio in the Raman spectra by a factor of up to two. There are two major differences between the systems:

- LARA3*pre* was operated with a less powerful and stable laser than LARA3 (3 W instead of 5 W optical power, 0.08% instead of 0.06% power stability over 24 hours).
- The back-going laser beam was reflected sideways in LARA3*pre* by a sharp edged pick-up mirror (labelled PM in figure 4.2) after passing the Raman cell. This resulted in non-overlapping beams in the LARA cell, and to ambiguity during alignment and hence put great demands on the person doing the alignment. LARA3 uses an optical isolator to prevent the back-going beam from reaching the laser, which allows for a full match of both beams in the sample cell and hence makes a more simplified and reproducible alignment possible.

The individual components will be discussed in the following sections. If not stated explicitly, the information given are valid for both systems.

#### 4.2.2. Excitation beam path and laser

In this section, the beam path of both versions of the KATRIN Raman setup is described. The function and working principle of the optical components will be presented where necessary and beneficial for the understanding. Further general information on the optical components can be found in standard optics textbooks, e.g. [Hec02].

##### Layout of excitation beam path

The laser beam is guided by two mirrors (labelled M1, M2 in figure 4.2) towards the LARA cell which is filled with or flown through by the gas to be analysed. Based on the two mirrors, the beam can be adjusted independently in all spacial degrees of freedom (horizontal and vertical position, pitch) to reach 85 mm height and to pass the LARA cell centrally. In order to maximise the intensity of the Raman scattered light that is collected by the collection optics (L3, L4), the laser beam has to be vertically polarised with respect to the surface of the breadboard. This maximises the line strength functions (eq. (3.33)) of the Raman lines in the  $Q_1$  branches. The lasers in this work emit horizontally polarised light which makes a half-wave plate ( $\lambda/2$ ) necessary to rotate the plane of laser

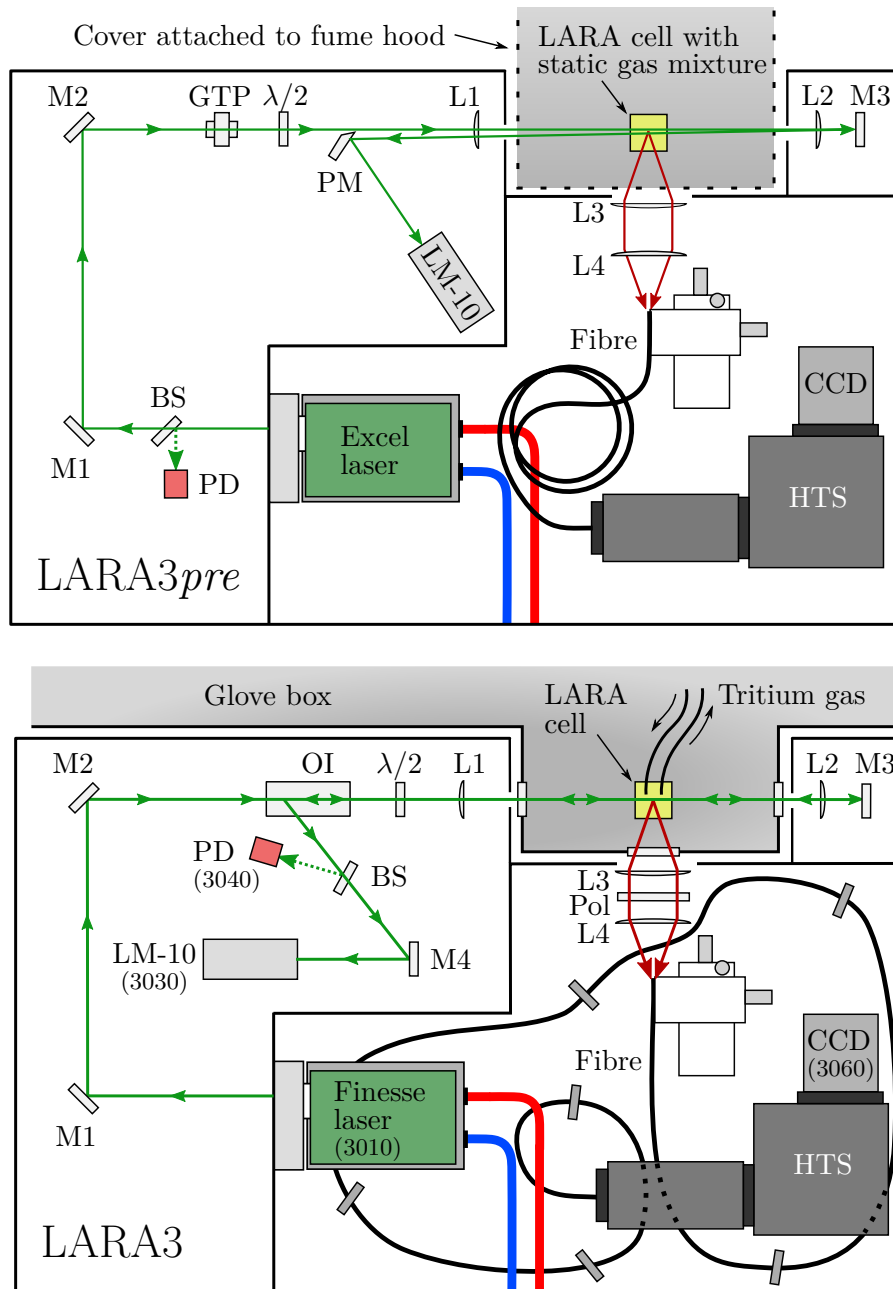


**Figure 4.2.: Layout of optical beam path of LARA3pre (top) and LARA3 (bottom).** Permanently installed pinholes for beam alignment not shown. Abbreviations (in alphabetical order): BS - beam sampler, OI - optical isolator, GTP - Glan Taylor polariser, HTS+CCD - HTS spectrometer and Pixis CCD,  $\lambda/2$  - Half waveplate,  $L_i$  - plano-convex lens  $i$ , LM-10 - thermopile power meter (Coherent LM-10),  $M_i$  - laser mirror  $i$ , PD - photo diode (including neutral density filter and diffuser plate), PM - 'Pick-up' laser mirror, Pol - linear sheet polariser. *Bottom:* The numbers in parentheses are the nnnn identifier which are used to identify the sensors and active devices KATRIN-wide (details in table 4.3).

polarisation. As the lasers do not emit perfectly linearly polarised light<sup>1</sup>, the polarisation of the beam is 'cleaned' passing through the half-wave plate. In case of LARA3*pre* this is accomplished by a Glan-Taylor polariser (GTP) which consists of birefringent prisms and hence deflects the light with the unwanted polarisation component out of the beam path [Arc48]. Based on the extinction ratio of 10<sup>5</sup>:1 of the employed Glan-Taylor polariser [Tho09], the beam can be considered afterwards as de-facto linearly polarised<sup>2</sup>. For LARA3, this is automatically done by the optical isolator (OI) which is primarily used to avoid back-reflection of the beam into the laser head and will be described in more detail further below.

The collimated laser beam is focused by a plano-convex lens (L1, 250 mm focal length) onto the centre of the LARA cell to maximise the laser power density and hence the Raman signal. After passing the cell, the divergent beam is collimated by an identical lens (L2), back-reflected (M3), refocused (L2) onto the LARA cell centre and finally again collimated (L1). Based on the reasonable assumption of a Gaussian laser beam profile and the calculation given in [Lew07], the f=250 mm lenses focus the laser beam (2.07 mm beam diameter measured at 1/e<sup>2</sup> intensity, 532 nm) down to a beam waist of  $\omega_0=42 \mu\text{m}$  in the centre of LARA cell. The beam size at the LARA cell centre should match the field of view of the collection optics (discussed in section 4.2.4) and is also of importance in the context of laser-induced damage (topic of section 5.4).

The back-going beam is deflected away from the forward-going one after passing L1 to prevent it from reaching the laser head which would cause laser instabilities, reduce the lasing efficiency (optical output power / laser pumping power) and, in the worst case, lead to permanent damage of the laser head. In LARA3*pre*, a D-shaped sharp-edged mirror (PM) picks up the back-going beam that was separated at this position by about 1 mm from the forward-going one. Although this worked surprisingly reliable in LARA3*pre*, it has two drawbacks: The beams do not or only partly overlap in the LARA cell. The alignment of the beams in the LARA cell is not very reproducible. The latter aspect is caused by contradicting requirements, namely that the beams should be as close as possible to maximise the Raman signal intensity but still separated sufficiently to guarantee that the beam is fully deflected even in the case of horizontal beam movement. This trade-off causes a severe ambiguity for the personnel during alignment and hence conflicts with the aim of a simple and reliable procedure for (occasional) beam alignment during the projected five years of KATRIN operation. Therefore a more reliable solution is implemented in LARA3 based on an optical isolator (OI) which acts as the optical counterpart of an electric diode: The beam in forwards direction experiences a nearly unhindered transmission (89.5% transmittance [Tho12]) of the laser light. The back-going is deflected out of the beam path which strongly suppresses the light intensity that goes back into the laser (suppression by -41.4 dB, i.e. by about  $1.5 \cdot 10^4$  [Tho12]). The working principle of the optical isolator is illustrated in figure 4.3.

A photo diode (PD) monitors a small fraction of the laser beam which is reflected from a beam sampler (BS). A neutral density filter mounted in front of the photo diode reduces the impinging laser power to less than 1 mW to avoid saturation. In addition, a diffuser

---

<sup>1</sup>Typically up to 1% admixture of the other, unwanted, polarisation state. Details in the section 4.2.2.

<sup>2</sup>Unwanted polarisation contributions can be again generated in optical components by stress-induced birefringence. This effect but also its treatment in data analysis were demonstrated in [Sch13b]

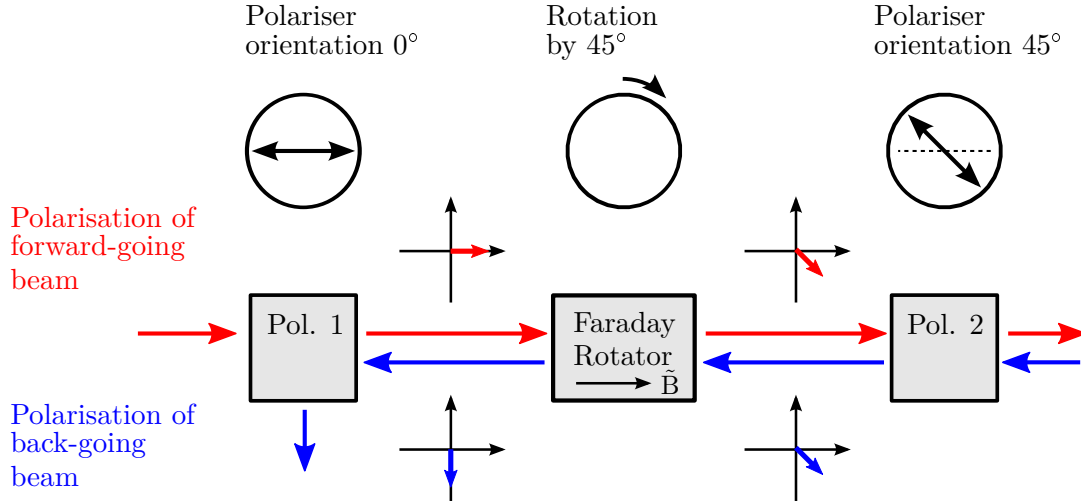


**Figure 4.3.: Working principle of an optical isolator.** An optical isolator utilises the Faraday effect, i.e. the rotation of the plane of polarisation in a medium that is placed in a magnetic field. The rotation direction is determined by the orientation of the magnetic field (and not by the propagation direction of the light). The rotation angle is given by the length of the material and the material specific Verdet constant (in units rad/Tm). An optical isolator consists of two polarisers and one Faraday rotator. The polarisation of the laser beam is rotated twice by  $45^\circ$  when passing the Faraday rotator in forward and backward direction, respectively. Consequently, the first polariser blocks the back-going beam. In high-power applications, as in this work, the blocked beam is not internally absorbed by the polariser but deflected sideways to be externally dumped.

plate destroys the coherence of the beam and hence potential interference patterns on the photo diode surface (e.g. Newton's rings [Hec02]) which can cause distortions of the photo diode reading. Although photo diode readings are known to be effected by temperature drifts and hence are not suitable for precise power readings [Bai11, Fis10], they fulfil an important task concerning laser safety: In case of a failure of one of the optical components, the beam is typically deflected, absorbed or scattered. Thus, the photo diode signal will drop by a significant amount. This can be detected and used to automatically trigger an interlock system to close the laser shutter and hence reach a safe condition. In case of LARA3*pre* which was not intended for extensive long-term operation a photo diode position at the very beginning was sufficient. In LARA3 a position at the very end of the beam path was chosen to monitor as many components as possible. Finally, the laser beam is dumped on a thermopile power meter (LM-10) which absorbs the beam and measures the beam intensity and position. The mirrors M1–M3, which have an influence on the beam position in the LARA cell, are mounted in extra stable mounts (Thorlabs, POLARIS-K1). This is motivated by past observations of significant temperature induced vertical beam movements of about  $100\mu\text{m}/\text{K}$  at the position of the LARA cell (extracted from [Fis10]) which could not solely be explained by laser beam walk.

## Laser

Both lasers employed in this work are diode pumped solid state lasers (DPSS) which operate in continuous wave (cw) mode at 532 nm output wavelength. In this work the lasers will be referred to according to their manufacturer given names, i.e. *Excel* and *Finesse*. They are based on the 1064 nm fundamental wavelength of a neodymium-doped yttrium orthovanadate (Nd:YVO4) crystal [Cla14] which is frequency doubled by a lithium triborate ( $\text{LiB}_3\text{O}_5 = \text{LBO}$ ) crystal [Cla14, Che89]. The output power of the Finesse laser is stabilised via the regulation of the laser power supply on the basis of an internal photo diode reading [Cla14]. DPSS Nd:YVO4 lasers were chosen because they allow stable and reliable operation with sufficiently large laser power ( $>1$  W) [Trä07] which is necessary in Raman scattering experiments with gases at about  $\leq 1$  bar absolute pressure. The  $Q_1$  branches of hydrogen isotopologues are located in the spectral range of 610–685 nm when using 532 nm as excitation wavelength. For this spectral region, detectors with high spectral sensitivity are available. Hardware parameters of both lasers are listed in table 4.1.

The Excel laser was used in Raman measurements at TLK before but only mounted on a fan-cooled heat sink at that time. Severe laser instabilities with respect to laser power and beam pointing were observed and related to changes of the ambient temperature [Fis10]. In particular the vertical beam position which is crucial for the alignment of the collection optics (section 4.2.4) was affected. In order to improve the stability of laser parameters, an active temperature stabilisation of the laser head was implemented and tested within [Kud11] and this work. Temperature drifts of the laser head induced by changes of the ambient temperature were reduced to 3% of the initial value and a power stability of  $\leq 1$  mW at 2 W absolute power (water chiller set point  $20.5^\circ\text{C}$ , measured for 14 h) was reached [Kud11]. The Excel laser was used in LARA3*pre* (section 4.4) until the Finesse laser was delivered to KIT.

The Finesse laser is superior to the Excel laser due to its increased 5 W output power and operation stability. The laser head is mounted on a tailor-made heat sink which is connected to a water chiller unit. With this setup temperature fluctuations of the laser head could be reduced to a standard deviation of 20 mK during the test and characterisation of the Finesse laser (section 4.5). In case of a failure of the water chiller unit the laser automatically shuts down when reaching  $40^\circ\text{C}$  in the laser head. The Finesse laser features a serial interface (RS-232) for read-out of operational parameters (see section 4.2.5) and for remote services by Laser Quantum personnel. To establish such a connection, the computer connected to the laser has to have access to the internet<sup>3</sup> and a special software has to be started by the operator at TLK to establish the connection to Laser Quantum. Afterwards the service technician can remote control the laser, read-out and adjust operation parameters and perform test routines.

---

<sup>3</sup>All systems at TLK must not be accessible from outside of TLK during normal operation for safety and security reasons. Therefore a remote service of the laser is only permitted after explicit approval by the local security authorities.

**Table 4.1.: Parameters of lasers and water chillers.**  $\sigma_T$  is the achieved standard deviation of the laser head temperature. The temperature set points of the chiller were determined within the commissioning measurements. Laser data taken from characterisation protocols of manufacturer [Las08, Las10, Las11].

Parameter	Unit	Excel	Finesse
Manufacturer		Laser Quantum, UK	
Specified Power	W	2	5
Transverse mode		TEM <sub>00</sub>	
Ellipticity of beam		1:1.12	1:1.13
Polarisation orientation		horizontal	
Polarisation ratio		> 100:1	
Beam diameter (1/e <sup>2</sup> )	mm	1.8	2.53 / 2.07 †
Stability (over 24 h)	%	0.12	0.06
RMS power noise	%	0.10	0.11
Remote control and parameter read-out		No	Yes
Water chiller		Termotek P103-17865-4	Melcor Laird MRC 150
Chiller set point	°C	20.5	24
Temperature stability $\sigma_T$	K	<0.07	0.02
Operation in		LARA3 <i>pre</i>	LARA3

† The laser has been serviced by the manufacturer during this work (see section 4.5). The laser diameter was 2.53 mm before the service and afterwards 2.07 mm.

### 4.2.3. Raman sample cell (LARA cell)

The Raman sample cell (hereafter referred to as 'LARA cell') is made of a hollow cubic stainless steel body (figure 4.4) based on the design by Taylor et al. [Tay01]. Tritium gas can be filled into the cell or flown through via two valves. Optical access is possible by custom made view ports, located on the side surfaces of the cell body. As being part of the primary system of the KATRIN Inner Loop, the LARA cell has to fulfil stringent requirements [TLA13]:

- Full metal construction of cell body and gaskets. Certification according to EN 10204/3.1. Approval of non-metal materials (windows) by concession request
- Ultra vacuum leak-tightness (maximum leak rate below  $10^{-9} \frac{\text{mbar}\cdot\text{l}}{\text{s}}$ )
- Radiographic examination of welding seams

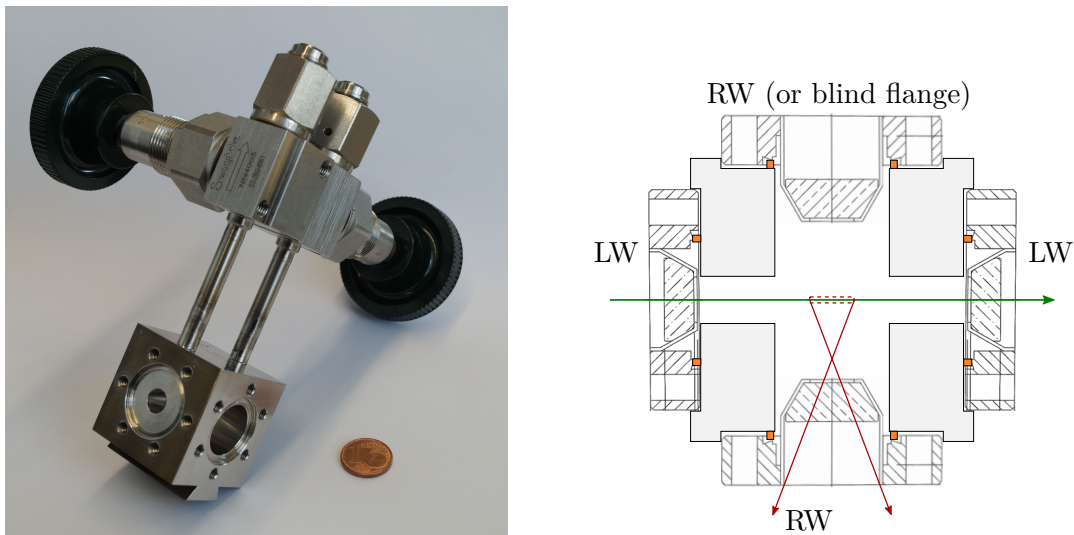


**Figure 4.4.: Raman sample cell (LARA cell) with tapped holes.** *Left:* Cell body with valves before mounting of windows. *Right:* Schematic cross section of LARA cell with windows (screws not shown). The laser beam accesses the cell through the laser windows (LW). The scattered light is observed through one of the Raman windows (RW) which are recessed to reduce the cell volume. A 6–7 mm long section of the beam (dashed box) is in the field of view of the collection optics located on the outside of the cell. The windows are welded in CF16 flanges and mounted with copper gaskets (orange) on the cell body. All windows are anti-reflection coated to minimise reflections. More details in main text and section 5.2.

In this work, two slightly differing versions of cell bodies are used: A cell body following closely the original design [Tay01] with protruding studs for mounting of the windows and a cell body for which the studs were replaced by tapped holes in the cell body (figure 4.4). The modified version simplifies the manufacturing process and eliminates the risk of breaking studs during window mounting. Apart from this difference, the cell bodies are nearly identical and hence will not be further distinguished.

The optical windows are made of fused silica (amorphous  $\text{SiO}_2$ ) and are diffusion bonded into flanges based on procedures developed and described in [Eng92, Eng97, Tay01]. Anti-reflection coatings applied on all window surfaces minimise the reflection of laser light (532 nm AR-coating applied on laser windows), and Raman scattered light (450–700 nm broad band coating applied on Raman windows). This allows for a maximisation of Raman signal but is also necessary because of laser safety reasons: An uncoated fused silica surface would produce a 175 mW reflection when being illuminated perpendicularly with a 5 W laser beam<sup>4</sup>. Such a beam would have to be safely absorbed to prevent an injury to operating personnel or damage to components.

In the case that the LARA cell is operated with samples with an activity above  $10^{10}$  Bq, it has to be located inside a second containment. As this will be the case during KATRIN operation, a dedicated glove box extension (the so-called *Appendix*, shown in the bottom

<sup>4</sup>Using Fresnel equations [Hec02] for an air-glass interface and normal incidence. Refractive indices  $n_{\text{air}} \approx 1$ ,  $n_{\text{SiO}_2} = 1.4607$  [Bas09]. Reflectance  $R = ((n_{\text{air}} - n_{\text{SiO}_2}) / (n_{\text{air}} + n_{\text{SiO}_2}))^2 = 3.5\%$ .

**Table 4.2.: LARA cell parameters.**

Component	Parameter	Value
Cell body	Manufacturer	KIT main workshop
	Material	Stainless steel (1.4571/316Ti)
Valves	Manufacturer	Swagelok, 76694 Forst, Germany
	Type	SS-2BG-8861 NN4005 <sup>†</sup>
	Connector type	VCR 1/4" female
Windows	Manufacturer	CCFE Special Techniques, Culham Science Centre, Abingdon, Oxfordshire, UK
	Material	Fused silica <sup>‡</sup> , bonded into CF16 flange
Complete cell	Volume <sup>◊</sup>	$V_{2+2} = (7.1 \pm 0.7) \text{ cm}^3$ $V_{2+1} = (9.95 \pm 0.02) \text{ cm}^3$
	Leak rate	$<1.5 \cdot 10^{-10} \text{ mbar l/s}$ [Sir13]

<sup>†</sup> Custom made, based on SS-4BG series.

<sup>‡</sup> Anti-reflection coated by LASEROPTIK GmbH, Garbsen, Germany (Details in section 5.2).

<sup>◊</sup>  $V_{2+2}$ : Cell with two laser windows and two Raman windows.  $V_{2+1}$ : Cell with one Raman window replaced by blind flange.

part of figure 4.2) has been installed to have optical access to the cell while being installed in the glove box [Stu10b, Fis11]. A compilation of technical information on the LARA cell is found in table 4.2. Detailed information on the anti-reflection coatings is found in chapter 5 where the influence of ambient, chemical, and radiological conditions on the windows is discussed.

#### 4.2.4. Light collection and analysis system

The task of the light collection and analysis system is to collect the scattered light from the LARA cell and to perform the spectral analysis of the acquired Raman spectrum.

##### Collection optics and fibre bundle

The scattering region in the LARA cell is imaged 1:1 by two collection lenses (L3, L4 figure in 4.2) onto a fibre bundle (figure 4.5) that feeds the light into a spectrometer. The focus point of the first lens (L3) is located in the centre of the LARA cell to collimate the scattered light. The second lens (L4) focuses the light onto the tip of the fibre bundle (C Technologies Inc., FA-FOR02-BU01, 48 fibres). The fibres in the fibre bundle are aligned at both ends of the bundle along a line to match the horizontal laser beam in the LARA cell and vertical entrance slit of the spectrometer. The width of the entrance slit defines the spectral resolution and light strength of the spectrometer. Typically, a trade-off between two spectrometer properties has to be found when setting the entrance slit width: The narrower the slit the better the spectral resolution but also the smaller

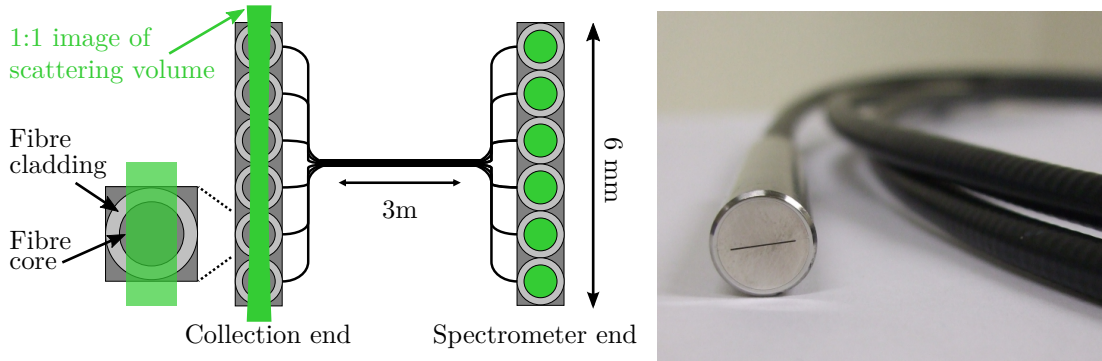


**Figure 4.5.: Fibre bundle.** The bundle consists of 48 optical fibres which are aligned at both ends along a line to match the laser beam profile. The core of each optical fibre is  $100\ \mu\text{m}$  in diameter and surrounded by a cladding with  $125\ \mu\text{m}$  diameter. *Left:* Schematic drawing of fibres and scattered light from laser beam which is imaged 1:1 on the fibres by the collection optics. *Right:* Photograph of fibre bundle end. Figures from [Fis10].

the light throughput of the spectrometer. This can be partly circumvented thanks to the usage of a fibre bundle. Due to the small diameter ( $100\ \mu\text{m}$ ) of the fibres in the bundle, the slit of the spectrometer can be fully opened and the fibre bundle becomes the effective entrance slit which determines the spectral resolution. The benefit of this setting is the increased light intensity reaching the CCD which yielded a signal-to-noise ratio in the Raman spectrum, which was up to a factor of five higher than in standard slit-image configuration, without a significant loss of spectral resolution [Jam13a].

Two aspects of the light collection system were modified during the upgrade of LARA3*pre* to LARA3:

- Replacement of the standard plano-convex collection lenses L3 and L4 (Thorlabs LA1145-A, 75 mm focal length) with achromatic ones (Thorlabs AC508-075-A-ML, 75 mm focal length) to minimise the influence of chromatic aberrations on the spectral sensitivity of the Raman system.
- Fixation of the fibre bundle on the breadboard and installation of a linear sheet polariser (Pol) between the lenses of the collection optics to determine the polarisation of the light before entering the fibre bundle.

This issue of chromatic aberrations was identified during the commissioning of LARA3*pre* (see discussion in section 4.4). The latter modification was performed to reduce systematic shifts of the spectral sensitivity of the light collection and analysis system: T. James found that the scattered light is only partly depolarised when passing the fibre bundle, i.e. a fraction of the initial light polarisation is maintained, and that movements of the fibre bundle change the degree of depolarisation in the fibre [Jam13a]. Due to the polarisation dependence of the grating efficiency [Pri10b], a movement of the fibre would change the measured Raman signal intensity which would be misinterpreted as a change of the gas composition. The fibre bundle was therefore fixed on breadboard in LARA3. A linear sheet polariser (Thorlabs LPVISE200-A, aligned for transmission of vertically polarised light) is used to unambiguously determine the line strength function which are necessary for the calibration of the KATRIN Raman system [Sch13b].

### Spectrometer and charge-coupled device sensor (CCD)

The spectral analysis is performed by a high-throughput lens spectrometer with a medium resolution diffraction grating (Princeton Instruments, HTS, 600 grooves/mm, 750 nm blaze wavelength). The HTS is optimised for high light collection power through its low f-number of  $f/1.8$ . The charged-coupled device sensor (CCD) (Princeton Instruments, Pixis2KB,  $512 \times 2048$  pixels) is used to acquire the spectrum that consists of spectral lines. Cooling of the CCD sensor by a thermoelectric element to  $T_{\min} = -75^\circ\text{C}$  helps to reduce the thermal noise in the CCD acquisitions and correspondingly to increase the signal-to-noise ratio in the Raman spectrum.

The resolution of the HTS+Pixis2KB system is not sufficient to resolve the rotational substructure of the vibrational  $Q_1$  branches (demonstrated in figure 3.5). However the covered spectral range is wide enough to simultaneously detect the  $S_1$  and  $Q_1$  branches of all hydrogen isotopologues [Stu10a] which are located in the interval  $\Delta\tilde{\nu} = 0 - 4200 \text{ cm}^{-1}$ . Therefore and because of its high light strength, the HTS spectrometer is ideally suited for gas composition monitoring within the context of the KATRIN experiment. If for other applications high-resolution spectroscopy is intended (e.g. [Sch13b]), other spectrometers are available at TLK.

Apart from Raman scattering, also Rayleigh scattering occurs in the LARA cell. Hence the Raman scattered light is superimposed with light that is not shifted in wavelength but is about a factor of 1000 [Hen70] more intense. As this could cause interfering reflections inside the spectrometer, a long-pass edge filter (Semrock LP03-532RU-25) is installed in front of the spectrometer entrance slit to block light with  $\lambda \leq 536 \text{ nm}$  (corresponding to  $\Delta\tilde{\nu} \leq 154 \text{ cm}^{-1}$ ) from entering the spectrometer [Sem12].

#### 4.2.5. Monitoring systems and auxiliary equipment

A set of sensors is installed in the KATRIN Raman system to monitor the status of the individual components and experimental parameters which are relevant for a safe and stable operation of the system. The reliable operation of the Raman system is essential for the KATRIN experiment as the neutrino mass can only be properly extracted from the data when all required sub-systems, including the Raman system, are simultaneously in operation. Additionally, the duty cycle of the KATRIN sub-systems has to be as high as possible to reach the required 3 years of accumulated data taking within the projected five years of KATRIN operation. This section gives an overview of the sensors and monitored hardware parameters in the KATRIN Raman system. The procedures for automated evaluation of the acquired sensor data are described in chapter 6.

#### Finesse laser

The operation parameters of the Finesse laser can be read-out via a serial connection and used to monitor the status of the laser. Of special importance are the output laser power and the current of the laser diodes that optically pump the lasing material. As the Finesse laser internally monitors and actively stabilises its output laser power to the  $10^{-3}$  level at 5 W output power (see section 4.5), a drop of the laser power by more than 50 mW can be considered as a clear indication for a malfunction of the laser. Such

a drop in laser power could happen in the case that the efficiency of the pump diodes or even the lasing medium itself degrades, e.g. due to stress or ageing. Therefore it is meaningful to regularly monitor the pump diode current during long-term operation as this parameters inversely proportional to the lasing efficiency. In case a steady increase of the pump diode current at constant output laser power is observed the laser should be checked by an expert and if necessary serviced remotely or by personnel on site.

#### **Thermopile sensor (LM-10)**

A quadrant thermopile sensor (Coherent, PowerMax-USB LM-10) is used as a beam dump at the end of the beam path to safely absorb the laser beam. By measuring the heating-up of the surface exposed to the laser beam with respect to an internal reference temperature, the device measures the laser power within a range of 10 mW to 10 W with 10 mW resolution and <2% accuracy [Cohb, CoHa]. Due to the segmentation of the sensor surface, a beam position measurement is additionally possible (spacial resolution 0.015 mm [Fis10]). This is of interest since especially vertical beam movements in the LARA cell will decrease the intensity of the collected light and hence worsen the signal-to-noise ratio of the Raman spectra [Sch09, Fis10].

#### **Photo diode (PD)**

Photo diodes operated at reversed bias voltage are sensitive tools for measurement of light intensity [Trä07], although the photo diode reading is not used for high precision laser power monitoring because of the known temperature dependence of the photo diode output [Trä07]. This effect was shown to be significant in dedicated test measurements performed by A. Bainbridge who found consistent values of the temperature dependence of about  $10^{-3}/\text{K}$  for two different types of Si photo diodes [Bai11]. The photo diode employed in the system (Thorlabs, SM1PD1A) is used to monitor the integrity of the beam path and to trigger a safety shutdown of the beam shutter in case of a malfunction (discussed in the paragraph 'Laser interlock system' below). The temperature dependence of the photo diode is for this purpose not of relevance.

#### **Pixis2KB (CCD)**

The CCD sensor chip can be cooled to  $-75^\circ\text{C}$  to minimise thermal noise in the acquired CCD images. The temperature set point of the CCD sensor chip is set once per run within the software for data acquisition and the CCD automatically takes care of cooling and temperature stabilisation. The current chip temperature can be read out only between two successive acquisitions. The temperature of the CCD sensor chip was found to be stable within typically less than 0.1 K which is sufficient for the measurements. Nevertheless, a continuous monitoring of the CCD temperature is necessary during long-term operation to detect malfunctions of the thermo-electric cooling element or of the isolation vacuum surrounding the CCD sensor chip. If not directly detected, such malfunctions would decrease the signal-to-noise ratio in the subsequently acquired Raman spectra and finally could lead to Raman measurements that do not fulfil the 0.1% precision as required by the KATRIN experiment. Such scenarios are not unlikely as a failure of the cooling system of a similar CCD detector (Princeton Instruments, Pixis400) was

already experienced at TLK within the work of S. Mirz and R. Gröbke [Mir14, Grö14] and of R. Lewis [Lew07].

### Laser water chiller

The temperature stabilisation of the laser head is crucial for the stable operation of the laser with respect to laser power and beam pointing. Besides the negative effects on the laser during a chiller malfunction, the potential harm of a loss of cooling water into the Raman system is a serious threat that has to be immediately detected when occurring. The water chiller operated in combination with the Finesse laser in LARA3 (Melcor Laird MRC 150) has a serial interface (RS-232) and allows to monitor the temperature of the cooling water and several status flags for hardware errors.

### Wavemeter

It is intended to install a custom-made wavemeter in the KATRIN Raman system to monitor the laser wavelength. Since the wavelength of the Finesse laser is currently not absolutely known, Raman shifts  $\Delta\tilde{\nu} = (1/\lambda_{\text{Laser}} - 1/\lambda_{\text{Raman}})^{-1}$  cannot be accurately determined. Additionally, the laser has a bandwidth of  $\delta\nu = 50$  GHz [Las] which translates into a wavelength stability of  $\delta\lambda = 0.05$  nm using  $c = \nu\lambda$  and error propagation. A wavelength drift of 0.05 nm will again cause the measured Raman shifts in the spectrum to vary by  $1.7$   $\text{cm}^{-1}$  which is not sufficient to unambiguously identify potentially upcoming unknown features in the Raman spectra. However, this is not an issue for the identification of the  $Q_1$  branches of the hydrogen isotopologue which are separated by  $186$ – $529$   $\text{cm}^{-1}$  in the Raman spectrum. The wavemeter is based on a design of White and Scholten [Whi12] and was commissioned and tested at Swansea university [Jon13]. The wavemeter is fibre coupled and can easily be implemented into the Raman system by installing a beam sampler into the beam path, e.g. between the laser shutter and mirror M1 (see figure 4.2), which guides a small fraction of the laser beam into the fibre of the wavemeter. The read-out of the wavemeter is already fully implemented in the operation software *LARASoft* (chapter 6) of the KATRIN Raman system and the installation and commissioning is ongoing at the time of writing this work [Her14].

### Position sensitive detector

Another planned upgrade of the KATRIN Raman system is the installation of a beam position sensing detector (Thorlabs, PDP90A). This device shall replace the position measurement of the thermopile LM-10 sensor whose resolution degrades for large off-centre beam positions ( $r > 3$  mm) and when only one detector segment is illuminated. The position sensitive detector will be installed in a similar fashion as the wavemeter, i.e. it will monitor a reflection of the beam from a beam sampler.

The readings of the sensors already integrated into the KATRIN Raman system are summarised in table 4.3. The table also includes the unambiguous identifier of each sensor reading which is necessary to integrate the Raman system into the global data acquisition and management framework of KATRIN (described in section 6.3.8).

**Table 4.3.: LARA3 sensors and hardware parameters.** Range and resolution stated if available. Interface specifies the connection to the LARA computer. nnnn and zzzz are parts of the identifier 611-XXX-M-nnnn-zzzz which uniquely labels KATRIN-wide every LARA component and sensor reading.

Device				Sensor value					
Type	Name	Manufacturer	Interface	nnnn	Parameter	Unit	Range	Resolution	zzzz
Laser	Finesse	Laser Quantum	RS232	3010	Laser operation mode	bool	on / off		0002
					Laser power	mW	0 – 5500	1	0003
					Pump diode current	%	0 – 100	0.1	0004
					Laser head temperature	°C		0.01	0005
					Power supply temperature <sup>†</sup>	°C		0.01	0006
Chiller	MCR 150	Melcor Laird	RS232	3012	Water temperature	°C	2 – 40	< 0.1	0002
					No faults	bool	true / fault		0003
					Fan failure	bool	true / fault		0004
					Tank level low	bool	true / fault		0005
					Pump failure	bool	true / fault		0006
					Pump slow	bool	true / fault		0007
					Pump off	bool	true / fault		0008
Thermopile	LM-10	Coherent	USB	3030	Laser power	mW	10 – 10000	10	0002
					Horiz. beam position	mm	-8 – 8	0.015	0003
					Vert. beam position	mm	-8 – 8	0.015	0004
Photo diode	SM1PD1A	Thorlabs	‡	3040	Laser power	V <sup>◇</sup>	0 – 10	0.0006	0002
CCD	Pixis:2KB	Princeton Instruments	USB	3060	CCD temperature	°C	-75 – 30	0.1	0002
Pt100	S1320	Systemtechnik AB	‡	4060	Breadboard temperature	°C		0.06	0002

<sup>†</sup> Read-out not yet implemented in software for operation of the Raman system.

<sup>‡</sup> Voltage measurement by analogue-to-digital converter (NI<sup>™</sup>, USB-6009, 14 bit).

<sup>◇</sup> Photo current to voltage conversion with transimpedance amplifier.

Apart from sensors and the read-out of hardware parameters three auxiliary systems and components are necessary for the operation of the Raman system.

### **Laser interlock system**

The lasers employed in this work are class 4 lasers and hence special safety provisions have to be made for the Raman system. One major requirement of the German accident prevention regulations (laser light) [Unf04] is the separation of the laser area from the normal laboratory environment and the protection of people in case of unintentional access of the laser area. In case of the KATRIN Raman system, the enclosure of the system acts as a barrier between laser area and normal laboratory space. The lid of the system is monitored and the removal of the lid triggers the interlock system to immediately close the laser shutter. In case of a damage of an optical component the laser emission has to be interrupted to prevent further damage of the system and injury of personnel. A damage of one of the beam path components will cause the beam to be scattered/absorbed by the damaged optic or even reflected out of the normal beam path. Thus the photo diode voltage will very likely drop which triggers the laser interlock system to close the shutter. By placing the photo diode at the very end of the beam path the integrity of nearly all optical components can be monitored. The laser interlock system is realised by custom-made analogue circuits which are robust and fail-safe in case of a power-failure of the interlock system.

### **Light sources and optics for wavelength calibration**

The HTS spectrometer is wavelength calibrated by acquisition of reference spectra with known line positions. Atomic neon, argon or mercury spectra are typically used as they offer a sufficient quantity of narrow spectral lines distributed over the spectral range of interest. A second order polynomial is used to fit the wavelength of the spectral lines as a function of pixel number along the (dispersive) horizontal axis of the CCD sensor chip. The wavelength calibration of the KATRIN Raman system will be performed regularly, e.g. between every neutrino mass measurement run, to check the status of the spectrometer settings (details in section 7.4). In order to simplify this calibration procedure for the operators and to reduce the risk of misalignment or damage of optical components in the Raman system, the necessary components for wavelength calibration should be permanently installed in the system without disturbing the normal Raman measurements. A proposal for such a system is shown in appendix A.

### **Luminescence standard for spectral calibration**

The measurement of the spectral sensitivity of the light collection and analysis system is essential for the calibration of the Raman system. For this reason a NIST-traceable luminescence standard was identified as reference light source with certified spectral shape as already discussed in section 3.3. Current work in the Raman group at TLK focuses on the investigation of systematic effects in the emission spectrum of the standard due to its non-standard usage. Secondly, a special mount for the luminescence standard is being constructed which resembles the geometry of the LARA cell (including cell windows). The aim of these efforts is to generate the luminescence light under conditions as similar as possible to those present during normal Raman scattering in the LARA cell. Ideally,

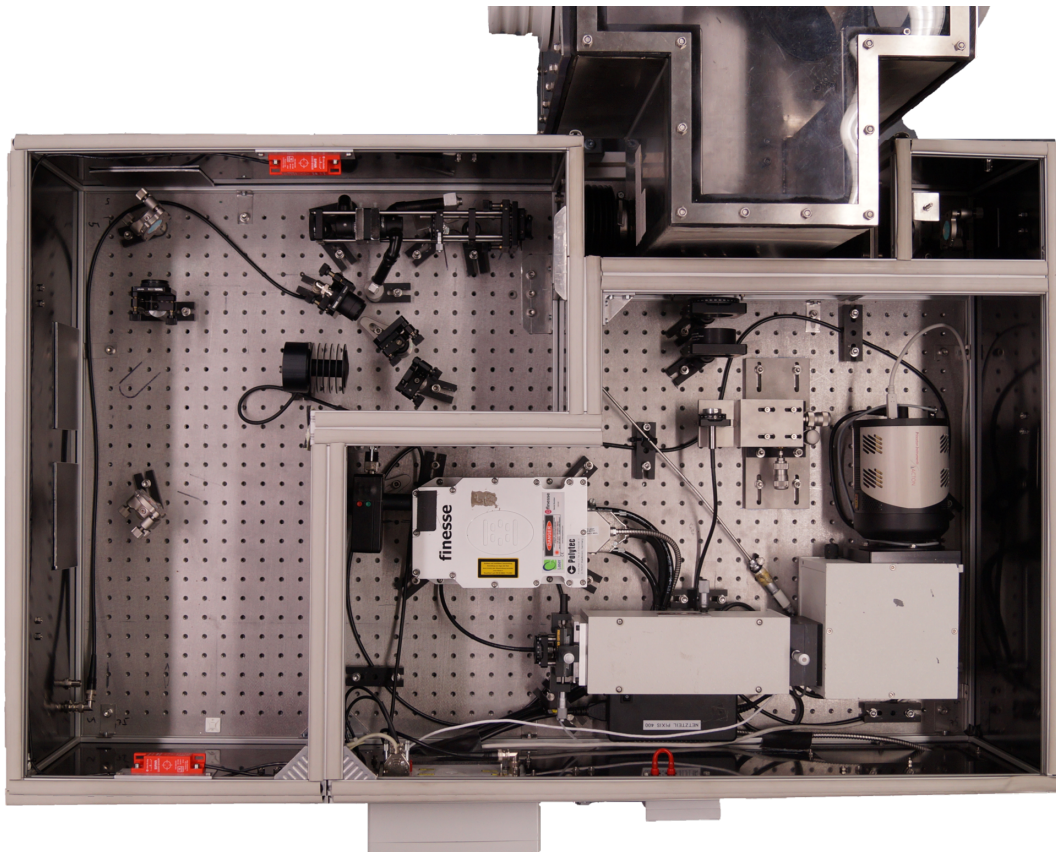


**Figure 4.6.: Top view of the KATRIN Raman system.** The laser area comprises the left and the small top right compartments and the section in the glove box (component visible at the top of the image). The left compartment houses most of the laser beam path and is monitored against opening of the lid by the red sensors of the laser interlock system. The small top right compartment and the section in the glove box are permanently closed by physical provision during laser operation. The bottom right compartment is free of accessible laser light and therefore not part of the laser area. On the picture, the Raman system is connected to the mobile glove box 'MuLI' (details in [Kas12]) which has a similar LARA-glove box interface as the 'Appendix' of the Inner Loop system.

the luminescence standard will be installed in the glove box at the position of the cell for regular measurements of the spectral sensitivity.

After the detailed discussion of the layout of the optical beam paths in the KATRIN Raman system and the tasks and properties of the individual subcomponents, this section is concluded with figure 4.6 which shows a top view of the KATRIN Raman system.

### 4.3. Overview and objectives of LARA3 commissioning

The KATRIN Raman system was commissioned in three steps:

- The LARA3*pre* system was commissioned with static gas mixtures and used to study systematic effects in the light collection system (section 4.4).
- The Finesse laser was characterised after its delivery (section 4.5) and installed into the KATRIN Raman system. Simultaneously, the LARA3*pre* system was upgraded to the LARA3 system, i.e. the beam path and light collection system was improved (details described in section 4.2).
- In the third step the LARA3 system was operated at the LOOPINO facility [Stu10b, Fis11] with circulating tritium gas mixtures (section 4.6), i.e. under conditions similar to those present in future KATRIN neutrino mass measurements.

The commissioning of the KATRIN Raman system was meant to answer a variety of questions that emerged from past experiments (see section 4.1) or are of general relevance for the KATRIN experiment. The most important ones are:

- How effective and reliable is the double pass configuration of the beam path to increase the effective laser power in the beam path?
- How stable is the output power and beam pointing of the Finesse laser? Is the Finesse laser sufficiently stable to perform Raman measurements without laser-related effects as experienced in former Raman measurements [Stu10b, Fis11]?
- Are there (not yet identified) effects which influence the accuracy, relative precision, or reliability of the Raman measurements?
- What was the origin of the coating damages of the tritium-facing LARA cell windows that were experienced in previous Raman measurements at the LOOPINO facility [Stu10b, Fis11]? How can these damages be avoided in the future?
- What is the level of detection and the achieved relative precision of the KATRIN Raman system for a KATRIN relevant gas mixture? What is the minimum acquisition time to achieve 0.1% relative precision?

These questions will be addressed in the next sections, and the overall findings are summarized in section 4.7.

### 4.4. Commissioning of LARA3*pre* with static gas mixtures

The construction and commissioning of the LARA3*pre* system was done in cooperation with Sebastian Mirz who also performed a first analysis of the acquired data [Mir11]. Two commissioning runs were performed with the LARA3*pre* system:

### LARA3*pre* run 1

Raman measurements of a H<sub>2</sub>:HD:D<sub>2</sub> gas mixture to study the influence of chromatic aberration in the light collection system on the accuracy of the Raman measurement.

### LARA3*pre* run 2

Raman measurements of gas mixture consisting of helium and hydrogen isotopologues including tritium to determine the relative precision which can be achieved with LARA3*pre*.

Both measurements could be performed outside of a glove box because the gas mixture did not contain tritium at all (run 1) or its activity was below 10<sup>10</sup> Bq, respectively (run 2). Details on the gas mixtures and experimental parameters are listed in table 4.4

#### 4.4.1. LARA3*pre* run 1: Characterisation of light collection system and double pass configuration

The light collection system of LARA3*pre* consists of two plano-convex lenses which image the scattering region in the LARA cell 1:1 onto the entrance of the fibre bundle (figure 4.7). The wavelength of the Raman Q<sub>1</sub> branches of the hydrogen isotopologues cover the spectral region of about 610–685 nm for 532 nm excitation wavelength. The lenses in

**Table 4.4.: Overview of LARA3*pre* runs.**

	LARA <i>pre</i> run 1	LARA <i>pre</i> run 2
Objective	Characterisation of the light collection system and double pass configuration	Long-term test of system; monitoring of system performance
Method	Variation of distance between fibre bundle and collection lens	Long-term monitoring of gas composition
Gas sample	26.3% H <sub>2</sub> , 47.4% HD 26.3 % D <sub>2</sub> [Sch13b]	98.89% <sup>4</sup> He, 0.83% T <sub>2</sub> , 0.18% HT, 0.07% DT, 0.04% <sup>3</sup> He <sup>†</sup>
Total pressure	1500 mbar	889 mbar
Laser power	about 1.9 W	about 2 W
Configuration	Single and double pass	Double pass
Acquisition time	20 s	300 s
Binning groups <sup>◊</sup>	5	5

<sup>†</sup> Based on gas chromatography at the time of cell filling, i.e. 34 days before the start of the measurement run [Fan11]. D<sub>2</sub>, HD and H<sub>2</sub> below level of detection.

<sup>◊</sup> Effective number of pixels in the vertical, i.e. non-dispersive, direction of the CCD detector array due to on-chip binning [Jam13a].

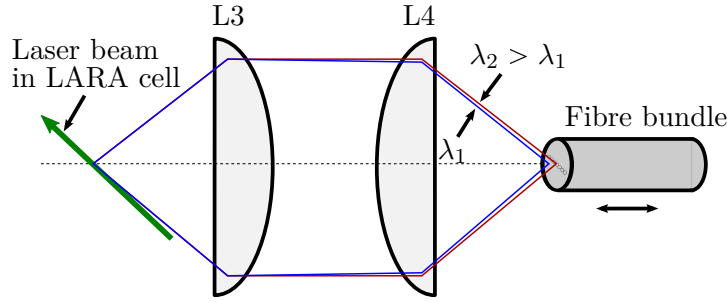


**Figure 4.7.: Chromatic aberration in light collection system.** The plano-convex lenses cannot image the scattered light of all wavelengths simultaneously onto the fibre bundle entrance due to chromatic aberration. Here: light with wavelength  $\lambda_1$  is not perfectly focused while light with wavelength  $\lambda_2$  is.

the light collection system are made of borosilicate glass (N-BK7, Schott) whose refractive index changes by about 0.15% within the spectral region of interest ( $n_{616 \text{ nm}} = 1.51569$ ,  $n_{688 \text{ nm}} = 1.51339$  [Tho14a]). The focal length  $f$  of a plano-convex lens with refractive index  $n$  is given by [Hec02]

$$f = \frac{R}{n - 1} \quad (4.1)$$

where  $R$  is the curvature radius of the convex side of the lens (assuming that the lens is operated in air). Hence the focal length of the collection lens differs due to chromatic aberration by 0.34 mm for 616 nm and 688 nm which again means that the collection system cannot be aligned simultaneously for the full spectral range. In consequence, the amount of scattered light which is injected into the fibre bundle will depend on the wavelength of the light and on the alignment of the light collection system. While the former aspect has been studied in the past [Rup12], the latter aspect has not yet been investigated.

The aim of this measurement was to quantify the influence of the alignment of the collection optics onto the spectral sensitivity of the light collection system, i.e. to study how much the relative intensities change due to a misalignment of the system.

### Measurement procedure

Raman measurements of a LARA cell filled with a static  $\text{H}_2$ , HD and  $\text{D}_2$  gas mixture (1500 mbar total pressure, details in table 4.4) have been performed. The distance of the fibre bundle to the focus lens L4 has been successively varied in 0.2 mm increments over the full movement range (4 mm) of the 3-axis translation stage which holds the fibre bundle: The parameter range was once scanned from 0 mm to 4 mm and afterwards back to 0 mm. The 3-axis translation stage was mounted on the optical breadboard such that the optimal fibre bundle position can be reached within the available translation range. The accuracy of the fibre bundle position reading is  $\pm 0.1$  mm. For each fibre bundle position, two spectra were acquired to enable the usage of the TCCR routine

of SpecTools [Jam13c] for removal of cosmic ray artefacts in the spectrum. Further parameters, e.g. laser power, beam position, etc. were not measured. The laser was operated at constant output power (about 2 W) but a sudden drop in laser power (e.g. caused by a mode jump) has presumably occurred once within the measurement as it will be seen below.

The described procedure was performed for both single- and double-path arrangements of the laser beam through the LARA cell:

- 'Single pass' configuration, i.e. dumping the laser beam after passing the LARA cell the first time.
- 'Double pass' configuration, i.e. back-reflecting the beam after passing the LARA cell the first time to increase the effective laser irradiance in the LARA cell. This configuration is shown in figure 4.2 top.

In contrast to the first analysis performed by S. Mirz [Mir11], in this work the data analysis was done with the SpecTools toolkit which was published in 2012. This allowed one to employ the ShapeFit routine in SpecTools for line intensity determination while S. Mirz determined the line intensities by summation of bins within a user-specified Raman shift interval around the peak centres. The absolute and relative Raman intensities of the  $Q_1$  branches of all three hydrogen isotopologues have been determined for each fibre bundle setting using the SpecTools settings summarised in appendix B.

## Results and discussion

An example Raman spectrum (0.4 mm fibre bundle position, single pass configuration) is shown in figure 4.8. The absolute and relative Raman intensities for the single pass configuration are shown in figure 4.9. The following observations can be made:

- The absolute Raman intensities of all hydrogen isotopologues reach a maximum value for a fibre bundle position in the range 0.2–0.6 mm. This position also

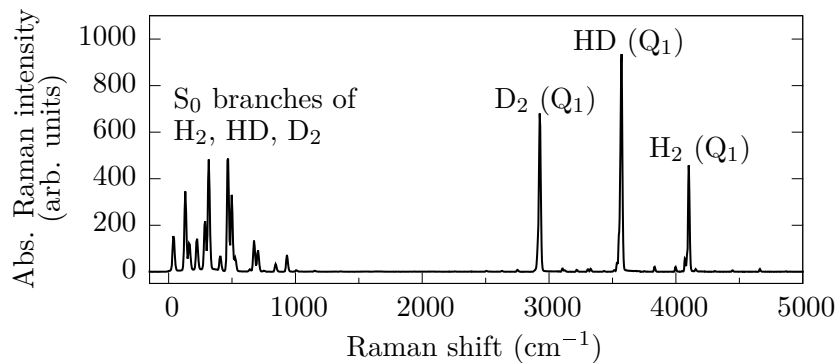


**Figure 4.8.:** Processed Raman spectrum of  $H_2$ ,  $HD$ ,  $D_2$  gas sample for fibre bundle at 0.4 mm and single pass configuration.

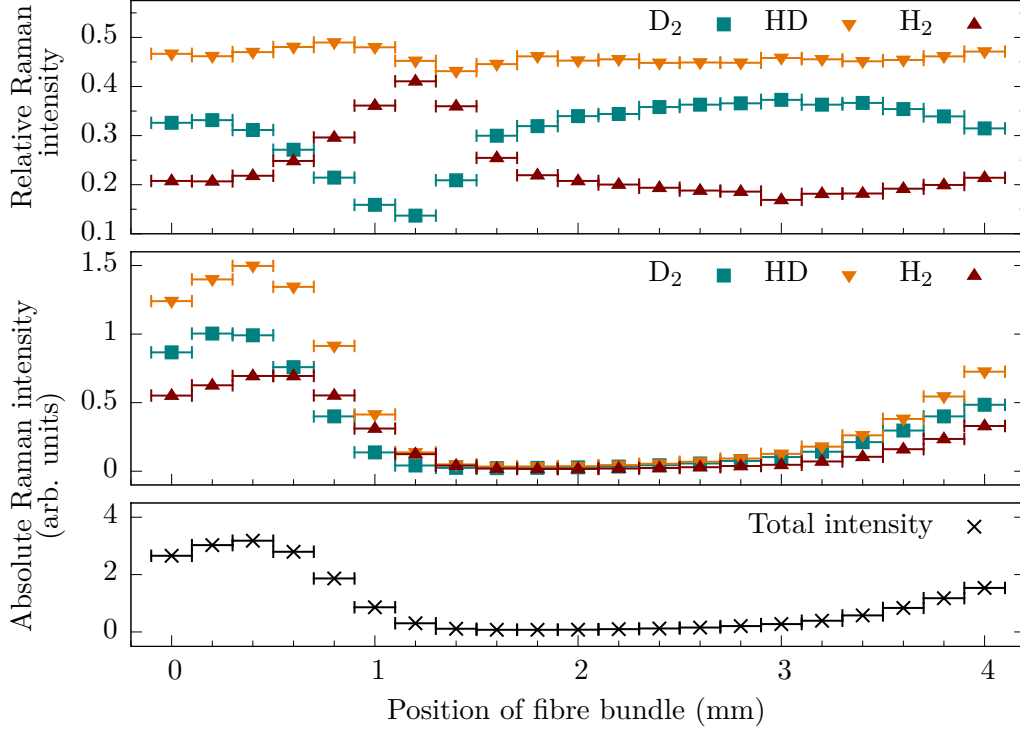


**Figure 4.9.: Influence of chromatic aberration of collection optics in single pass configuration on Raman intensities.** The fibre was stepwise moved from 0 to 4 mm and back again. The total intensity is the sum of all absolute Raman intensities. For details see main text.

coincidences with the optimum distance calculated from the back-focal length<sup>5</sup> of the lens.

- The absolute Raman intensities drop for larger position values of the fibre bundle and reach zero level at a position of about 1.4 mm where the fibre bundle is completely out of focus.
- The absolute intensities slowly increase for larger fibre bundle distances ( $> 3$  mm) that are far away from the expected optimum positions. The origin of this feature is currently unknown. Potentially the scattered light is reflected by one of the inner stainless steel surfaces of the cell and then imaged by the collection lenses. This feature is not an issue during alignment of the optics due to the large distance to the optimum fibre bundle position.
- The relative intensities vary significantly over the full position range of 0–4 mm and even within the 0.2–0.6 mm region a distinct variation is still present. These variations are statistically significant as the statistical uncertainty of the relative intensities is smaller than the size of the symbols as it will be seen from the results of the double pass configuration.

<sup>5</sup>The back-focal length is the distance of the focal point to the plane surface of the lens L4.

The results of the double pass configuration are shown in figure 4.10 and in general agree with the results of the single pass configuration. The following additional observations are worthwhile to note:

- The absolute Raman intensities peak at similar positions (0.2–0.6 mm) as in the single pass configuration but this time a second peak around 2.1 mm is observed. On first glance, this could be interpreted as an image of the second beam passing the cell but this seems to be unlikely as will be seen from the discussion of the absolute intensities.
- The absolute intensities do not fully agree for both sweeps over the fibre position range but a common drop (about 20–30%) of all absolute Raman intensities is found at 1.6 mm fibre bundle position. The most likely explanation is a drop in laser power caused by a laser mode jump during the measurement run. Such distinct changes of laser power were also regularly experienced in other measurement runs performed with the Excel laser (e.g. in figure 4.12).
- Apart from the data points affected by the potential drop in laser power, the absolute intensities for 0.2–0.6 mm fibre bundle position increased by  $(97 \pm 5)\%$  in comparison to the single pass configuration. It is therefore unlikely that the peak around 2.2 mm is a direct image of the back-going laser beam because in this case a doubling of the absolute Raman intensities around 0.2–0.6 mm would not be expected.
- The relative Raman intensities are, as expected, unaffected by the drop in laser power and the data of both sweeps of the fibre bundle position deviates from each other by less than the symbol size in figure 4.10. This strengthens the significance of the observed variation of relative intensities due to the alignment of the fibre bundle.

## Conclusions

The absolute Raman intensities have been increased by a factor of  $1.97 \pm 0.05$  in the region of reasonable alignment (0.2–0.6 mm fibre bundle position) by changing from single to double pass configuration. Hence the theoretical maximum amplification factor of two was actually reached and the concept of increasing the effective laser power in the LARA cell was successfully demonstrated. The double pass configuration can therefore be used to improve the precision and level of detection of the KATRIN Raman system while keeping the acquisition time fixed or to reduce the acquisition time and hence become more sensitive to short term fluctuations in the gas composition while keeping the precision fixed.

The chromatic aberration of the collection optics was found to significantly affect the measured relative Raman intensities and hence impact the accuracy of the gas composition measurement by Raman spectroscopy. Even in the fibre bundle position range of 0.2–0.6 mm where the absolute Raman intensities reach their maximum value, a variation of the relative intensities by up to 20% is found (figure 4.11). Under these conditions the double pass and single pass configurations show an identical behaviour and hence also

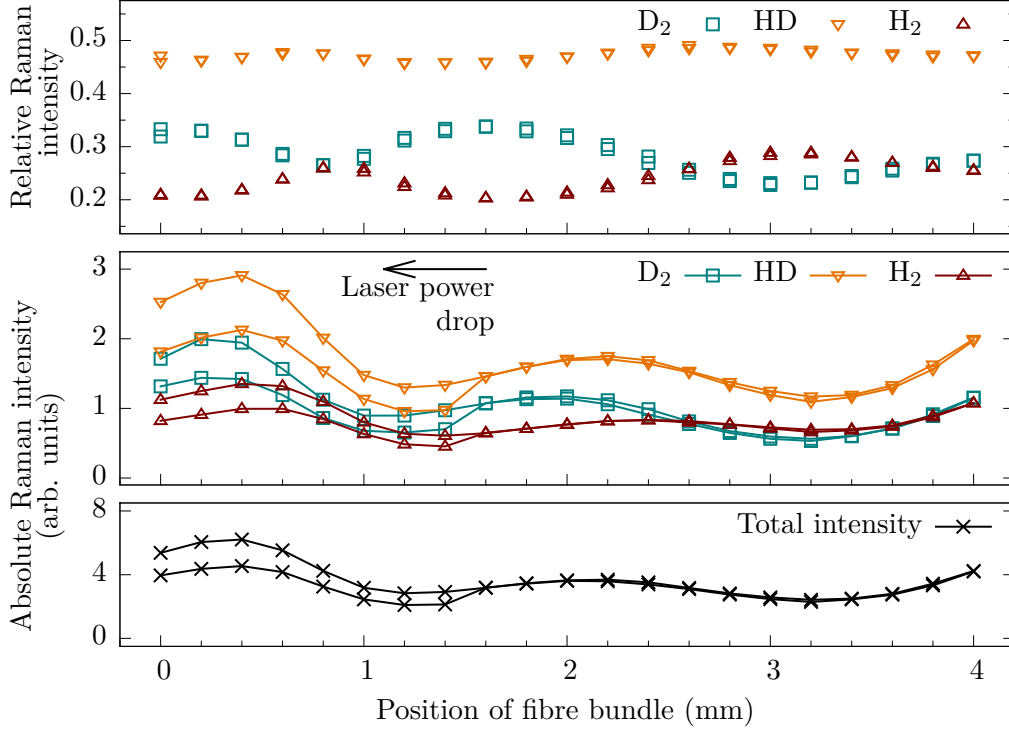


**Figure 4.10.: Influence of chromatic aberration of collection optics in double pass configuration on Raman intensities.** The fibre was stepwise moved from 0 to 4 mm and back again (data points connected by lines to guide the eye where necessary). The total intensity is the sum of all absolute Raman intensities. For details see main text. The accuracy of the position reading ( $\pm 0.1$  mm) is not indicated by error bars for clarity. A drop in laser power occurred at 1.6 mm during the back movement which affected all Raman line intensities equally. Hence the relative Raman intensities are not affected. For further discussion see main text.

prove the significance of the found variations of the spectral sensitivity of the light collection system. The measurement of the spectral sensitivity of the complete light collection and analysis system was not yet possible at the time of these tests, hence the relative Raman intensities could not be corrected for this effect. This becomes clear when comparing the measured relative Raman intensities (28–33%  $\text{H}_2$ , 46–48% HD, 21–25%  $\text{D}_2$ ) with the actual gas composition (26.3%  $\text{H}_2$ , 47.4% HD, 26.3%  $\text{D}_2$ ) which is accurately known to the sub percent level due to the special mixing procedure that was applied for the sample production [Sch13b].

During the alignment of the collection optics the distance of the fibre bundle to the lens L4 is varied in order to maximise the absolute Raman intensity of a selected Raman branch. Which Raman branch is selected depends on the present gas mixture, since a reasonably high absolute Raman intensity is needed and the Raman branch has to be well separated from other features in the spectrum. As it was seen from figure 4.9 and 4.10, the absolute Raman intensities of the different isotopologues peak at slightly different fibre bundle positions, i.e. the available gas mixture and the choice of the employed Raman branch for alignment will determine which spectral sensitivity is realised in the light collection system.

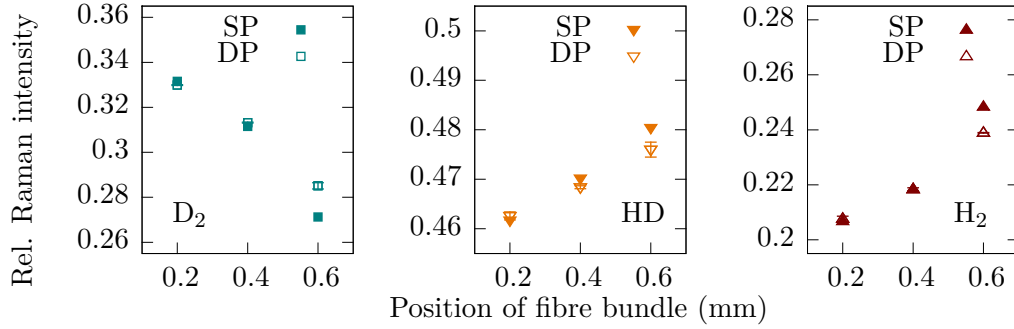


**Figure 4.11.: Comparison of rel. Raman intensities measured in single pass (SP) and double pass (DP) configuration (detail of figure 4.9 and 4.10).** The results of both measurements in DP configuration have been averaged. Half of the deviation between both DP measurements has been used as an estimate of the precision (indicated by vertical error bars). The uncertainty of the fibre bundle position ( $\pm 0.1$  mm) is not shown for clarity. An overall agreement between the SP and DP data sets is found, i.e. both show a clear dependence of the relative Raman intensities on the fibre bundle position.

This is not really significant for the operation of the KATRIN Raman system as the spectral sensitivity of the light collection and analysis system will be measured after each change or realignment, using the procedure developed in the past [Rup12]. Nevertheless it is of interest to reduce the number of components that have an influence on the spectral sensitivity or at least to reduce the strength of their influence. For this reason the standard plano-convex collection lenses L3 and L4 were replaced by achromatic lenses within the upgrade of LARA3*pre* to the LARA3 system.

The double pass configuration of LARA3*pre* in which the back-going beam is not overlapping with the primary one and is deflected out of the primary beam path by a sharp edged mirror (PM in figure 4.2, page 67) was found to work but remained delicate to align. The necessary balance between reducing the beam-to-beam distance in the cell and safely picking the back-going beam with the mirror PM could be achieved but required extensive experience in laser alignment. Therefore a more reliable and simpler to align solution should be used for the long-term operation of the KATRIN Raman system which will be typically operated and maintained by trained but non-expert personnel. Therefore an optical isolator is used in the LARA3 system instead of the mirror PM to reduce the complexity of the alignment but ensure that the back-going beam is deflected out of the primary beam path and finally dumped.

#### 4.4.2. LARA3*pre* run 2: Long-term test and monitoring of system performance

The task of the second run of LARA3*pre* was to test the system under realistic conditions, i.e. during long-term operation, to determine if the system can be operated stably and which relative precision can be achieved.

Before the measurement and results are discussed in detail, a brief summary is given:

- The gas composition of a static gas mixture of  $^4\text{He}$  and tritium (99.16%  $^4\text{He}$ , 0.83%  $\text{T}_2$ , 0.18% HT, 0.07% DT, 0.04%  $^3\text{He}$ ,  $p_{\text{tot}} = 889$  mbar) was monitored over a total period of about 150 hours.
- A relative precision of  $(4.01 \pm 0.11) \cdot 10^{-3}$  was achieved for the relative Raman intensity of  $\text{T}_2$  for 2 W laser power and 300 s acquisition time. The partial pressure of  $\text{T}_2$  was about 7.3 mbar and hence a factor of 20-30 lower than in the Inner Loop of KATRIN. Therefore, the 0.1% relative precision requirement of KATRIN should be easily be reached even when reducing the acquisition time.
- Atomic emission lines of helium and hydrogen were observed in the Raman spectra due to the electronic excitation of these atoms by tritium  $\beta$ -decay. This is of special interest since the mono-atomic helium normally cannot be detected by Raman spectroscopy. First steps towards a quantitative analysis of such gas mixtures were made within in subsequent works [Sch14a].

### Measurement procedure and data analysis

The LARA cell was filled with a static gas mixture that contained about 99.16%  $^4\text{He}$  and traces of hydrogen isotopologues and  $^3\text{He}$  (details in table 4.4) at a total pressure of 889 mbar.<sup>6</sup> Helium is mono-atomic and not subject to molecular excitations and hence should not be visible in a Raman spectrum. Therefore the effective Raman-related gas composition, i.e. considering only Raman active species, is 76.8%  $\text{T}_2$ , 16.5% HT, and 6.8% DT at a total pressure of 9.6 mbar. However, these values have to be treated with care since they are based on a gas chromatographic measurement that was performed 34 days before the start of the LARA3pre run. As it will be seen from the Raman measurements in this run, compositional changes were actually occurring in the gas mixture.

Continuous Raman measurements (300 s acquisition time per spectrum) were performed during two periods of about 47 h and 113 h duration. The measurements were paused between both periods for about 65 h because the LARA3pre system was not yet officially approved to be operated fully autonomously and unattended over the weekend. The laser power and beam position was measured by the thermopile power meter installed at the end of the beam path. The temperature in the laser enclosure was monitored, also during most of the 65 h long measurement pause. All hardware sensors were read-out every second. For the analysis of the Raman spectra SpecTools was employed using the settings summarise in appendix B. 14 branches/lines were fitted in each spectrum: all (six)  $\text{Q}_1$  branches of hydrogen isotopologues, six lines independent of laser excitation, and two lines overlapping with the  $\text{Q}_1$  branch of HD. Further details about the origin of these lines will be given in the next paragraph.

### Results and discussion

The sensor parameters (laser power, beam position, temperature) are shown in figure 4.12.

<sup>6</sup>The motivation for such a gas mixture was to demonstrate that Raman spectroscopy can also be used to monitor gases mixtures that will arise in the breeding blanket of nuclear fusion reactors [Dem12].

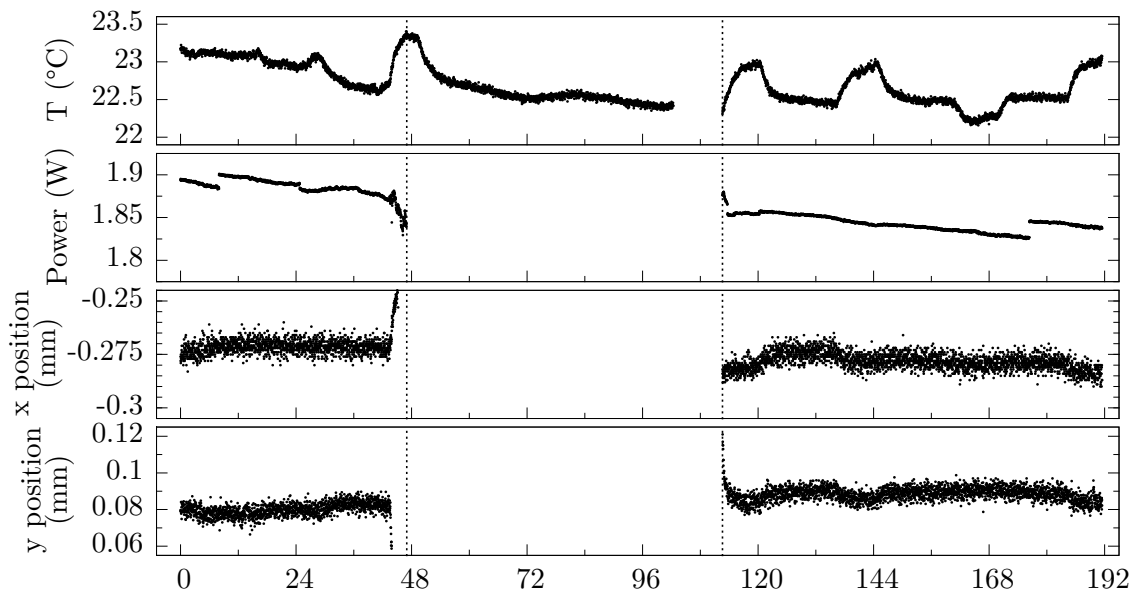


**Figure 4.12.:** Temperature in the laser enclosure, beam power, and beam position during LARA3pre run 2. The laser operation was interrupted between 47–113 h (period indicated by dashed lines). The temperature read-out failed in the period 102–113 h. A drop in laser power is found. The strong beam movement around 45 h is most likely due to a malfunction and successive shutdown of the water chiller of the laser.

The temperature in the system varied within about 1 K due to the known cycles of the ventilation system of laboratory [Fis10]. In contrast to measurements in the past [Fis10], the beam position of the Excel laser was most of the time only marginally affected ( $\Delta x < 0.004$  mm,  $\Delta y < 0.01$  mm) by the laboratory temperature cycles due to the temperature stabilisation of the laser head by the water chiller. Only around  $t = 45$  h a severe beam movement is found which is explained by an unnoticed shutdown of the water chiller triggered by a low water level in the water reservoir. The fact that this has happened about 2 hours before the intended shutdown of the laser has to be considered as a coincidence. The laser power measured by the thermopile sensor shows a mostly linearly decreasing trend (approximately 0.3 mW/h) which is interrupted by sudden changes of the laser power and a continuous decrease of the laser power during the failure of the water chiller. The sudden changes of the laser power are most likely attributed to mode jumps of the Excel laser. In total the laser power has decreased by about 3% over the course of about 192 h which is within specification. The operation of the laser can be considered as stable and reliable and hence not negatively impacting on the Raman measurements as long as the temperature stabilisation by the water chiller is ensured. Therefore the status of the water chiller should be continuously monitored in the KATRIN Raman system.

An example Raman spectrum is shown in figure 4.13. Due to the low partial pressures of the gaseous Raman-active species the spectrum is dominated by the broad Raman features around 0–1300  $\text{cm}^{-1}$  which originate from the fused silica windows ( $\text{SiO}_2$ ) of the LARA cell [Sch09]. The  $\text{Q}_1$  branches of all hydrogen isotopologues are present in

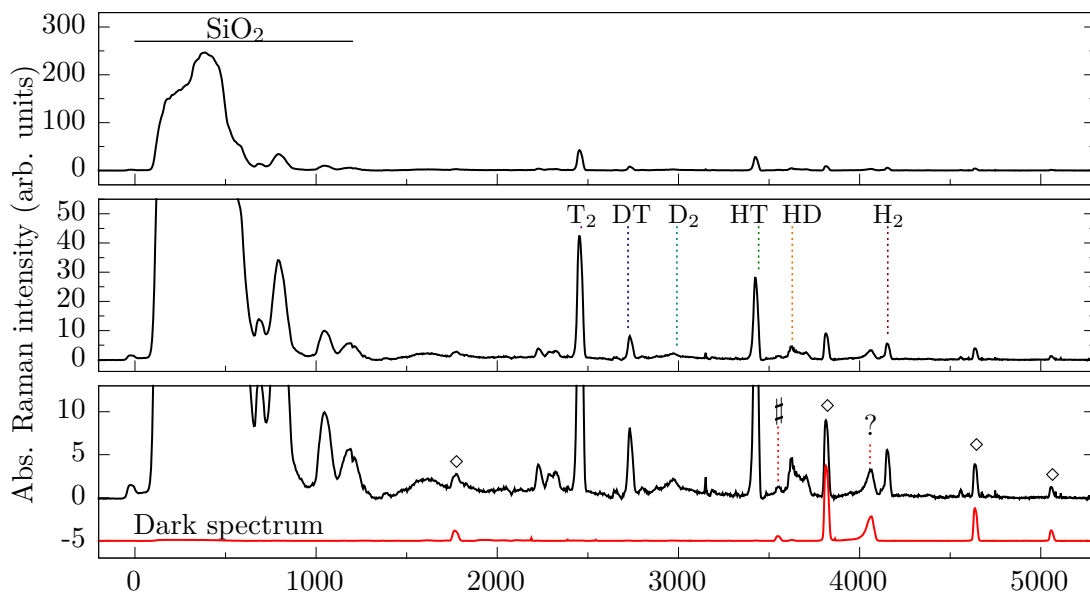


**Figure 4.13.: Raman spectrum and dark spectrum from LARA3pre run 2.** *Top:* Full spectrum with known Raman features from SiO<sub>2</sub> windows of LARA cell [Sch09] and Raman lines of gaseous species. *Middle:* Attribution of Q<sub>1</sub> branches of the hydrogen isotopologues. *Bottom:* Attribution of low intensity lines which are independent of laser excitation and hence also present in the dark spectrum (vertically shifted for better visibility):  $\diamond$  Helium atomic emission lines.  $\#$  Hydrogen H $_{\alpha}$  emission line.  $?$  unidentified. For details see main text.

the spectrum albeit the deuterium Q<sub>1</sub> branch is close to the noise and background limit and the Q<sub>1</sub> branch of HD is overlaid by a broad feature that consists of approximately two or three other lines or branches. An identification of the overlaying features is only partly possible because of two reasons: (i) the limited resolution of the HTS spectrometer which does not allow to fully resolve the overlaying lines and hence precisely determine the wavelength of scattered light, and (ii) the lack of the accurate knowledge of the laser wavelength which is needed to convert the line positions into Raman shifts which are needed for identification. Nevertheless candidates for the features can be given, namely H<sub>2</sub>O ( $\nu_1$ :  $\Delta\tilde{\nu} = 3657.1 \text{ cm}^{-1}$ ), HDO ( $\nu_3$ :  $\Delta\tilde{\nu} = 3707.5 \text{ cm}^{-1}$ ), and HTO ( $\nu_3$ ,  $\Delta\tilde{\nu} = 3716.6 \text{ cm}^{-1}$ ) whose symmetric ( $\nu_1$ ) and asymmetric ( $\nu_2$ ) stretch modes are exactly in that region of the spectrum [Zob96].

Apart from the Q<sub>1</sub> branches of the hydrogen isotopologues several low intensity lines are found in the spectrum that are independent of laser excitation. Potential light leaking into the enclosure was checked and excluded implying that these lines have to be emitted by an internal process of the gas sample. All but one of these lines are identified as atomic emission lines of helium and hydrogen (table 4.5).

The energy released by the  $\beta$ -decay of tritium is sufficient to electronically excite helium and tritium atoms in the gas mixture which again can de-excite via the emission of light in the visible range [Wex69, Sch82]. The effect has been further studied by M. Schlösser, O. Pakari et al. to investigate the feasibility of a quantitative analysis of helium in

**Table 4.5.: Attribution of atomic emission lines observed in LARA3pre run 2.**

The line positions were determined by fitting with typically 0.03 nm uncertainty corresponding to about  $1 \text{ cm}^{-1}$  when neglecting the uncertainty of the laser wavelength. The emission lines of the different helium and hydrogen isotopes cannot be resolved with the present spectral resolution of the spectrometer. Literature values  $\lambda_{\text{lit}}$  for the wavelength of the emission lines from [Kra13].

$\lambda$ nm	$\Delta\tilde{\nu}$ $\text{cm}^{-1}$	Nucleus	Transition	$\lambda_{\text{lit}}$ nm
587.25	1768	He	$3^3\text{D} \rightarrow 2^3\text{P}$	587.56
655.87	3550	H	$3^2\text{d} \rightarrow 2^2\text{p}$ ( $\text{H}_\alpha$ )	656.28
667.55	3817	He	$3^1\text{D} \rightarrow 2^1\text{P}$	667.82
678.43	4057	not identified		
706.28	4638	He	$3^3\text{S} \rightarrow 2^3\text{P}$	706.52
727.91	5059	He	$3^1\text{S} \rightarrow 2^1\text{P}$	728.13

tritium containing gas mixtures by combining Raman spectroscopy with the detection of said atomic emission lines [Sch14a]. The key towards a quantitative analysis is the accurate understanding of the competing de-excitation processes since also de-excitation by intermolecular collision, i.e. without light emission, is possible. This yields to non-linear dependencies of the emission light yield on the partial pressures of tritium and helium which have to be known to determine the helium concentration from a measured emission spectrum. If a quantitative analysis of such gas mixtures can be achieved, the technique could improve the accountancy and process monitoring in the breeding blanket of fusion power plants [Bor13].

The 14 lines/branches fitted in each spectrum are shown for one spectrum in figure 4.14. The lines L1 and L2 next to the HD  $\text{Q}_1$  branch are most likely stretch modes of  $\text{H}_2\text{O}$ , HDO, and/or HTO. Three minor deviations between fit and spectrum can be found: The L1 and L2 lines and the HD  $\text{Q}_1$  branch are not sufficient to fully fit the broad feature, the baseline of the spectrum is not completely flat, especially around the  $\text{Q}_1$  branch of  $\text{D}_2$ , and finally, the line shape of the unidentified (emission) line around  $4100 \text{ cm}^{-1}$  is significantly different from the other line shapes. The first two deviations will have an impact on the numerical results but at moderate scale because of the large absolute Raman intensities of  $\text{T}_2$  and HD in comparison to  $\text{D}_2$  and HD.

The relative Raman intensities were calculated on the basis of the hydrogen isotopologues, i.e. only the sum of these six absolute Raman intensities was used for normalisation. This was necessary since the ratio of light yield and partial pressure for the hydrogen and helium emission lines is unknown and the origin of the broad feature fitted by the L1 and L2 lines is not fully clear. As a consequence, the relative Raman intensities of all 14 fitted lines and branches will add up to more than 1 (to 1.31–1.36) but the results for the hydrogen isotopologues themselves will be consistent. The time series of selected relative Raman intensities is shown in figure 4.15 where all hydrogen isotopologues, the

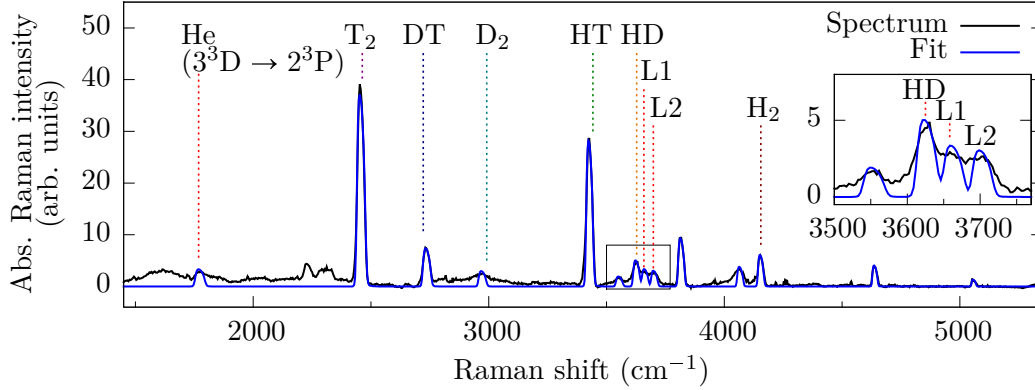


**Figure 4.14.: Example spectrum of LARA3pre run 2 with fitted branches and lines.** Only the spectral region around the fitted lines is shown. All  $Q_1$  branches of hydrogen isotopologues are fitted and all emission lines listed in table 4.5. The lines L1 and L2 are used to coarsely fit the broad feature that overlaps with the  $Q_1$  branch of HD around  $3650 \text{ cm}^{-1}$ .

lines L1 and L2, and one selected He emission line are shown. The following observations can be made:

- The relative Raman intensities are no meaningful quantities for the period of no laser excitation where the spectrum consists mainly of a flat but noisy baseline (apart from the atomic emission lines). For this well-known reason the respective period will not be further considered.
- The relative intensity of the helium emission line is on first order constant in time.
- All other relative Raman intensities show a clear trend which can be reasonably approximated by linear functions.
- The relative Raman intensity of tritium is the only one that decreases in time while all others increase.

At first glance, the variation of the gas composition might be in contradiction to the fact that a 'static' gas mixture was monitored. But it demonstrates that the available energy released by tritium  $\beta$ -decay triggers chemical exchange processes which do not occur in non-tritiated mixtures as e.g. the  $\text{H}_2:\text{HD}:\text{D}_2$  mixture used in the LARA3pre run 1. The relevant processes in the gas mixture can be grouped into two classes:

- Gas-gas interactions, e.g. the isotope exchange between the individual gas species depending on the concentration gradient in the mixture. This can explain the increasing relative intensities of HT and DT and the simultaneous decrease of the  $\text{T}_2$  relative Raman intensity.
- Gas-wall interactions between the gas and the stainless steel body of the LARA cell. Stainless steel contains hydrogen and to some extent deuterium atoms on interstitial lattice sites. When exposed to tritium gas, the hydrogen atoms start to diffuse towards the surface and desorb into the gas phase due to the concentration gradient. On the other hand, tritium gas becomes adsorbed on the surface, dissolves

and diffuses into the bulk material [Gor62] and replaces the hydrogen atoms on the interstitial sites. This process will in total increase the number of hydrogen atoms in the gas phase and accordingly decrease the number of tritium atoms. The rise of the relative Raman intensity of H<sub>2</sub> and HT can be related to this process as well as the decrease of the relative Raman intensity of T<sub>2</sub>. Also the increase of the relative intensities of D<sub>2</sub> and DT are likely attributed to this process.

The linear fit of the relative Raman intensities gives reasonable agreement. For longer monitoring times, exponential functions might be more suitable as shown in former measurements [Fis11]. The deviation of the measured data from the fit can therefore be used to quantify the precision of the Raman spectroscopic gas composition measurement. The histograms of the fit residuals for the hydrogen isotopologues are plotted in figure 4.16 showing a close to Gaussian distribution around zero. The standard deviation  $\sigma$  of the Gaussian distribution is a quantitative measure for the precision. When dividing by the mean relative Raman intensity, the relative precision  $\sigma/\bar{I}_{\text{rel}}$  is determined for each isotopologue. As can be seen from table 4.6, the best relative precision is achieved for T<sub>2</sub> ( $\sigma/\bar{I}_{\text{rel}} = (4.01 \pm 0.11) \cdot 10^{-3}$ ) which is the most abundant Raman-active species in the gas mixture. These values strongly depend on the gas sample and the experimental conditions, i.e. laser power, acquisition time and alignment of the system. Taking into account that the T<sub>2</sub> partial pressure will be a factor 20–30 higher in the Inner Loop of KATRIN and the laser power of the Finesse laser will be a factor 2.5 higher than the in the measurement here, 0.1% relative precision should be easily reached for the T<sub>2</sub> branch even when reducing the acquisition time.

**Table 4.6.: Achieved relative precision  $\sigma/\bar{I}_{\text{rel}}$  in LARA3pre run 2.** Partial pressures based on gas chromatographic analysis [Fan11]. D<sub>2</sub>, HD, and H<sub>2</sub> were below level of detection.  $\bar{I}_{\text{rel}}$  mean relative Raman intensity,  $\sigma$  standard deviation of fit residual (from figure 4.16),  $\delta_\sigma$  fitting uncertainty of  $\sigma$ . The uncertainty of  $\sigma/\bar{I}_{\text{rel}}$  is calculated by error propagation of  $\delta_\sigma$ .

	Partial pressure (mbar)	$\bar{I}_{\text{rel}}$	$\sigma$ ( $10^{-3}$ )	$\delta_\sigma$ ( $10^{-5}$ )	$\frac{\sigma}{\bar{I}_{\text{rel}}}$ ( $10^{-3}$ )
T <sub>2</sub>	7.4	0.44	1.78	5	$4.01 \pm 0.11$
DT	0.6	0.084	1.240	1.5	$14.8 \pm 0.2$
D <sub>2</sub>	-	0.03	1.46	6	$46 \pm 2$
HT	1.6	0.32	1.69	4	$5.28 \pm 0.12$
HD	-	0.05	1.40	3	$26.4 \pm 0.6$
H <sub>2</sub>	-	0.067	0.822	0.8	$12.24 \pm 0.13$

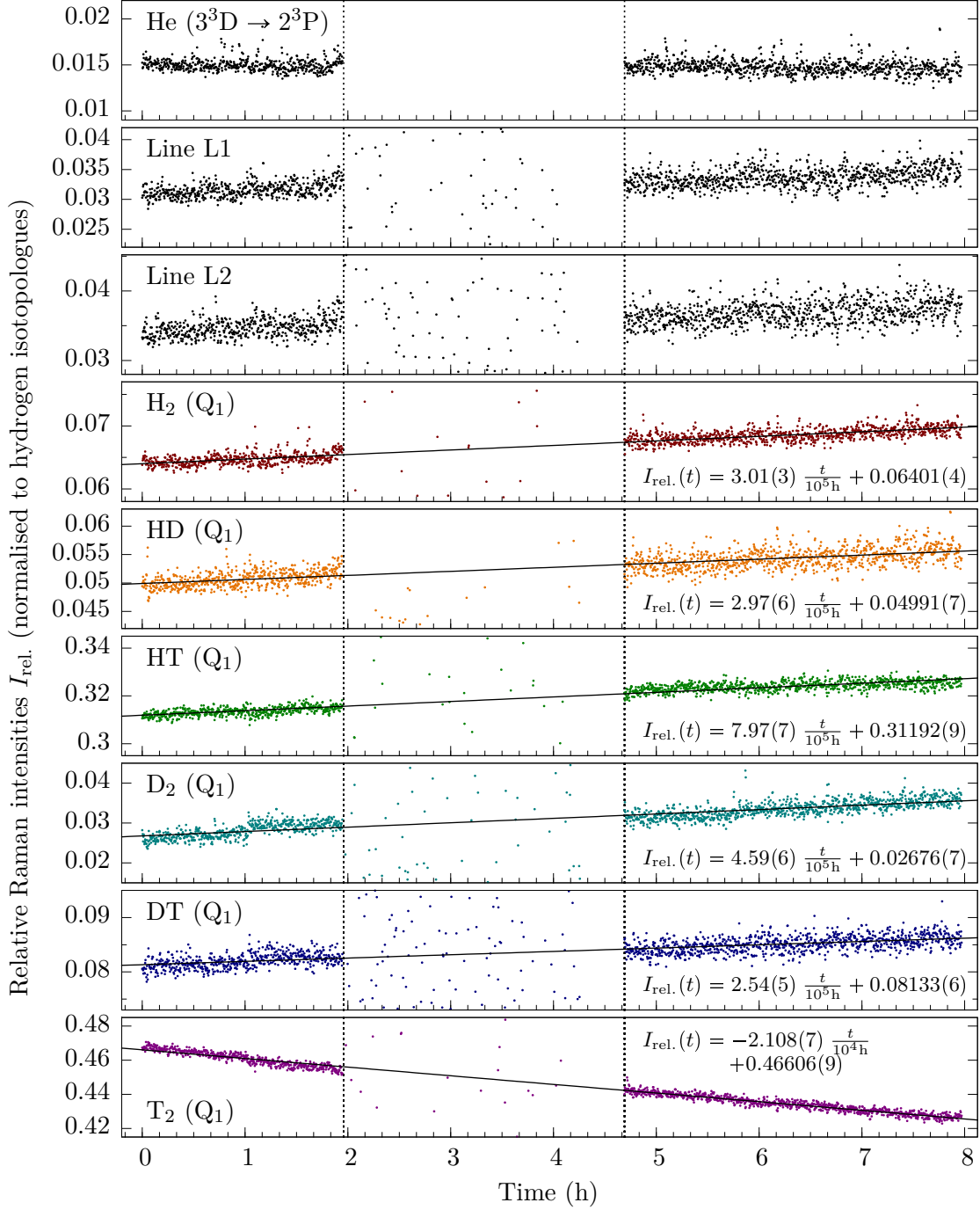


**Figure 4.15.: Relative Raman intensities of LARA3pre run 2.** The Raman intensities are normalised to the hydrogen isotopologues only, i.e. excluding the He( $3^3\text{D} \rightarrow 2^3\text{P}$ ), L1, and L2 lines. L1 and L2 were used to fit the broad feature in the spectrum overlapping with the  $Q_1$  branch of HD. During the off-period of the laser (47 h–112h) only the baseline and the atomic emission lines are present in the spectrum which causes the relative intensities to fluctuate. The relative Raman intensities are fitted by linear functions (solid lines). The uncertainty in the last digits of the fit parameters is given in parentheses. Further discussion in main text.

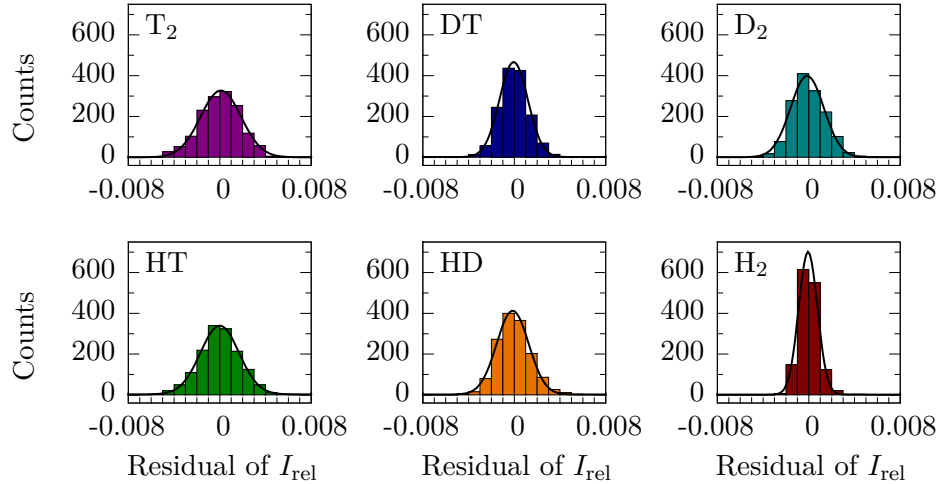


**Figure 4.16.:** Histograms of residuals of linear fit of  $I_{\text{rel}}$  for LARA3pre run 2. All histograms are fitted by Gaussian distributions  $y = y_0 + A \cdot \exp[-(x - x_c)^2/(2\sigma^2)]$  to determine the standard deviation  $\sigma$  of the histograms.

## 4.5. Characterisation of the Finesse laser

The Finesse laser was selected for the KATRIN Raman setup to be able to operate at higher laser power (5 W instead of 2 W) and with improved stability with respect to laser power and beam pointing fluctuations. After the delivery of the laser, these parameters have been investigated as a function of the temperature set point of the water chiller unit (MCR 150). The laser was installed in the enclosure of the LARA2 system [Fis10] from which the LARA cell was removed (figure 4.17). The remaining beam path consisting of two mirrors, a focus lens ( $f=250$  mm) and a beam sampler, resembling the normal configuration for Raman measurements. The laser was operated at nominal output power (5 W) while the temperature set point of the water chiller was subsequently raised in 2 K increments from 20 to 34°C over a period of about 120 hours. The laser parameters (LM-10 sensor data and internal Finesse data) were acquired every second and are shown in figure 4.18. The following observations were made:

- The laser did not reach stable operation conditions for the 22°C and 28 – 34°C set points for which fluctuations of all parameters are observed. The origin of these issues was a faulty pump diode which was replaced by the manufacturer after the test. The data of these temperature set points is therefore not further considered.
- The water chiller stabilises the laser head temperature within less than  $\pm 0.1$  K around the equilibrium temperature which is 3.4 – 4 K above the chosen temperature set point. Hence the laser head temperature is mostly decoupled from the temperature fluctuations in the laboratory ( $\Delta T_{\text{max}} = 4$  K) which were found in the past to be a significant influence on the laser parameters [Fis10]. For temperature set points above 32°C the maximum temperature of the laser head is reached and the laser automatically switches off.

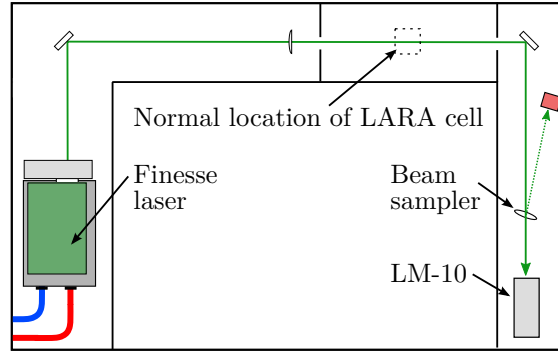


**Figure 4.17.: Layout of beam path for test of Finesse laser.** The laser was tested in the enclosure of the LARA2 system [Fis10]. A beam sampler was installed in the beam path and hence reduced the laser intensity at the LM-10 sensor. The length of the beam path was about 1.5 m from the laser head to the LM-10 sensor.

- The trends of both power readings are consistent with each other but the absolute power reading of the LM-10 sensor is about 0.4 W lower than the internal reading of the Finesse. This is caused by optical losses along the beam path (especially by the beam sampler). The consistency between the absolute LM-10 power reading with the internal one of the Finesse laser was checked in later measurements. An agreement within 0.01 W was found. The laser power is only marginally affected by the choice of the water chiller temperature set point which demonstrates the robustness of the internal power stabilisation of the laser.
- The beam pointing is strongly affected by the laser head temperature which again depends on the chosen temperature set point. The vertical beam position at the LM-10 sensor changes by up to 0.15 mm when changing the temperature set point by 2 K. As the light collection system is very sensitive to vertical beam movements<sup>7</sup>, this demonstrates the importance of the temperature stabilisation of the laser head. The horizontal beam position is also affected but to a much lesser extent.

The most stable operation of the laser was achieved for 24°C as set point of the water chiller. This data set was therefore analysed in more detail. The time series and histograms of the sensor readings are shown in figure 4.19 and the mean values and standard deviations are listed in table 4.7. The laser power and beam pointing fluctuations within this period were close to or even below the numerical resolution of the thermopile sensor which is 10 mW and 10 μm, respectively. The deduced values for mean and standard deviation must therefore be considered as estimates of the actual quantities. Nevertheless it can be stated that the laser power was stabilised over a period of 13 hours to <5 mW at 5 W absolute value, i.e. to the 10<sup>-3</sup> level. Vertical and horizontal beam pointing instabilities were reduced to about 5 μm at the position of the LM-10. At the position of the LARA cell the beam movements are likely to be reduced by a factor of about 1/3 because of the reduced arm length of the optical beam path.

<sup>7</sup>A vertical beam movement of 38 μm at the cell position already causes a reduction of about 22% of the collected light intensity.

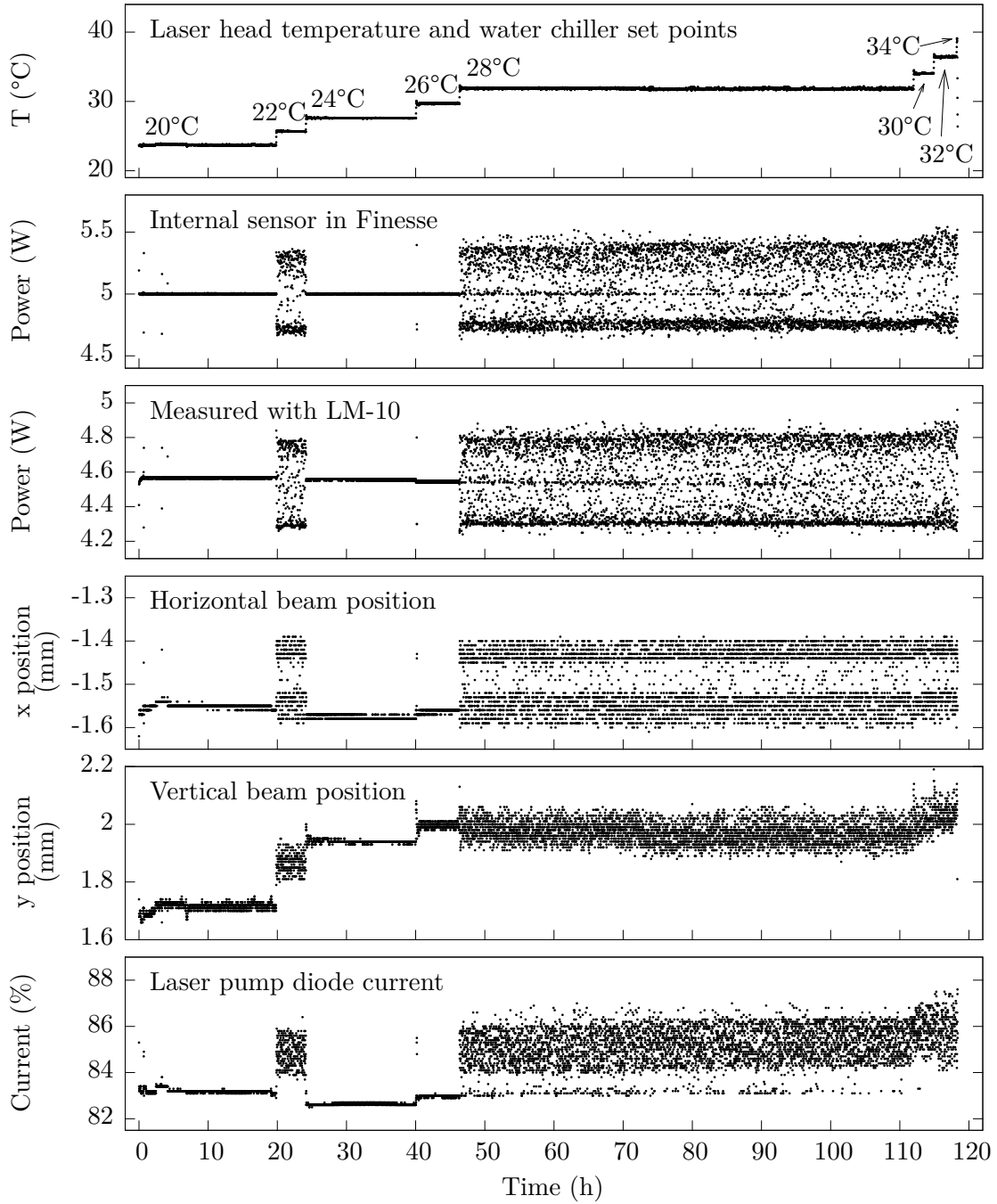


**Figure 4.18.: Parameters of Finesse laser for different water chiller temperature set points.** The temperature set point of the water chiller was changed in 2 K increments from 20 to 34°C. The temperature set points are indicated in temperature profile of the laser head. The laser overheated and automatically shut off at the 34°C setting. The laser pump diode current is given relative to a maximum value defined by the manufacturer. Severe fluctuations of the laser parameters are visible for various settings. For details see main text.

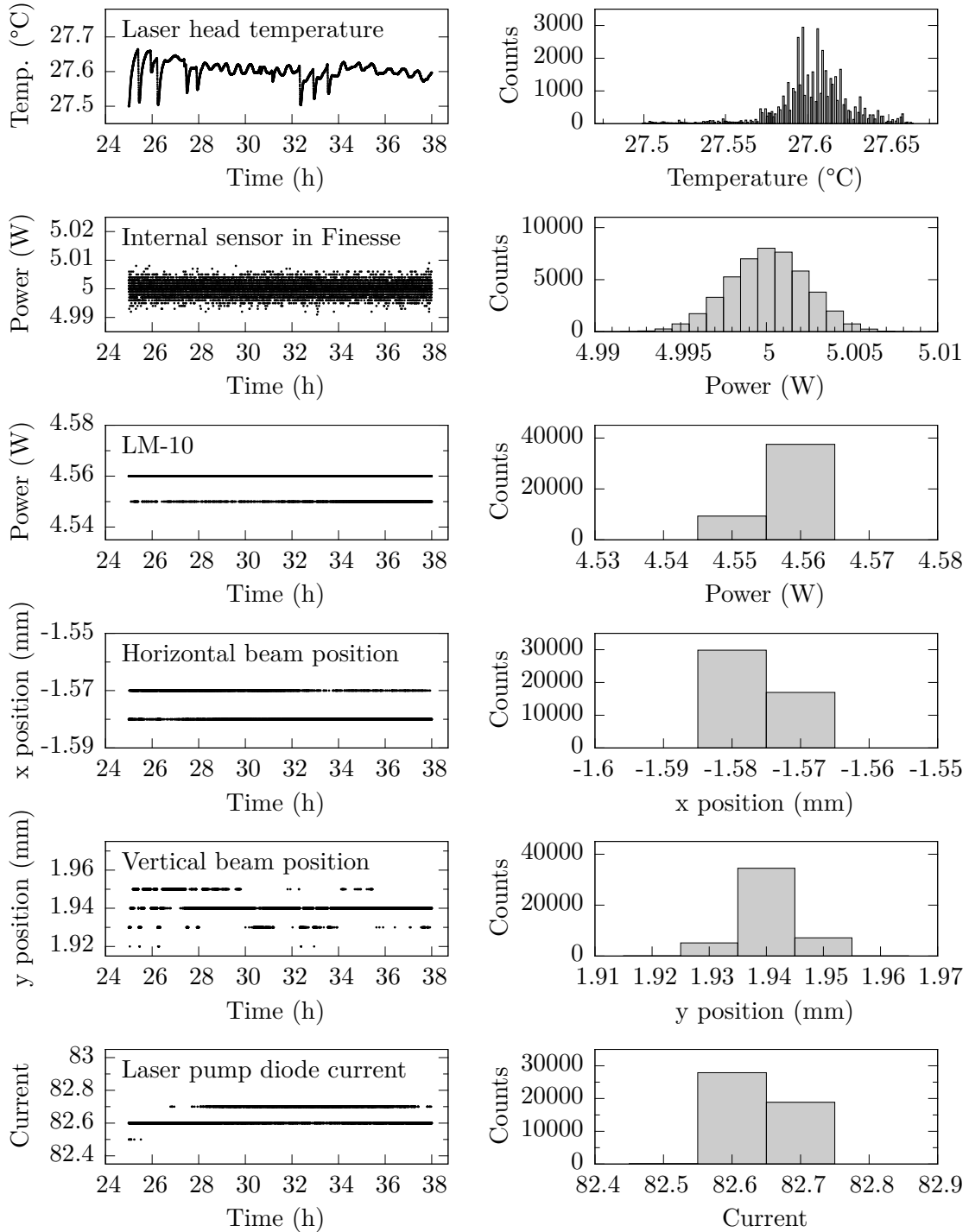


**Figure 4.19.:** Finesse laser parameters for 24°C water chiller temperature set point (detail of figure 4.18). The first hour of operation at 24°C is not shown and analysed as the laser needs time to reach a new steady state. *Left:* Time series of sensor readings. *Right:* Histograms of sensor readings. The power and beam pointing fluctuations are of the order of the resolution of the LM-10 sensor read-out. The bin sizes of the histograms were set according to the (read-out) resolution of the sensors. For details see main text.

**Table 4.7.: Statistical analysis of laser parameters for 24°C temperature set point of water chiller.** The mean values and standard deviations were calculated from the data set shown in figure 4.19.

	Unit	Mean value $\bar{y}$	Stand. dev. $\sigma$	$\sigma/\bar{y}$ ( $10^{-3}$ )
Laser head temperature	°C	27.60	0.02	0.9
Laser power (Finesse)	W	5.000	0.002	0.5
Laser power (LM-10)	W	4.558	0.004 <sup>◊</sup>	0.9 <sup>◊</sup>
Horizontal position (LM-10)	mm	-1.576	0.005 <sup>◊</sup>	- †
Vertical position (LM-10)	mm	1.940	0.005 <sup>◊</sup>	- †
Pump diode current	%	82.64	0.05	0.6

<sup>◊</sup> Estimate only because sensor readings was limited by sensor resolution.

<sup>†</sup> Not meaningful to calculate because absolute beam position can be arbitrarily set.

In conclusion the test of the Finesse laser is considered as successful as the superior stability of the laser parameters was demonstrated for the 24°C temperature set point of the water chiller. The commissioning of the Finesse laser therefore is a significant improvement of the KATRIN Raman system since laser power and pointing instabilities which have been a severe issue in past works at TLK [Stu10b, Fis10] are significantly reduced. On the other hand the appearance of severe operation instabilities of the laser show that even diode pumped solid state (DPSS) lasers which are generally considered as robust and easy to operate, are still complex systems that need special care and close monitoring.

## 4.6. Commissioning of LARA3 at the LOOPINO facility

After the upgrade of LARA3<sub>pre</sub> to LARA3 by installation of the Finesse laser and the optical isolator into the beam path (details in section 4.2), the LARA3 system was commissioned with circulating highly purified tritium gas mixtures. The aim of this measurement was to test the system under conditions (with respect to pressure, tritium concentration, flow rate) similar to those present during future neutrino mass measurement runs of KATRIN. The Inner Loop of KATRIN is not operated with tritium before the WGTS cryostat is connected to the components of the Inner Loop inside the glove box. Therefore, the LOOPINO facility [Stu10b] was utilised as a mock-up system. The LOOPINO facility can be considered as a simplified version of the Inner Loop and was installed to enable Raman measurements with highly purified tritium gas mixtures. The first Raman measurements with circulating tritium gas at TLK were successfully performed with this facility in 2010 [Stu10b, Fis11]. Within the scope of these measurements also the coating damages were experienced which were mentioned in section 4.1.

Before the measurements and results are discussed in detail, a brief overview of the results is given:

- A component made of polytetrafluoroethylene (PTFE) was identified in LOOPINO. This component has presumably triggered the formation of corrosive tritiated hydrofluoric acid and hence enhanced or even solely caused the coating damage that was experienced in the past LOOPINO operation. The component was replaced by a full metal version before the start of the Raman measurements and coating damages of the type observed previously did not occur any longer.
- LOOPINO was filled with pure tritium gas and the gas circulation was started. A 200 mbar pressure set point was chosen for the LARA cell to mimic the conditions in the Inner Loop of KATRIN.
- The KATRIN Raman system was successfully operated with the new operation software LARASoft which automatically analysed the Raman spectra and calculated the relative Raman intensities within 1 s after each spectrum acquisition (details on LARASoft in chapter 6).
- Isotope exchange reactions and the formation of tritiated methane species were observed in the gas composition. This is in agreement with the results from the past operation of LOOPINO [Stu10b, Fis11].
- A relative precision of  $3 \cdot 10^{-4}$  was achieved for the relative Raman intensity of  $T_2$  for 29.5 s acquisition time, i.e. the KATRIN requirement of 0.1% was surpassed by some margin.
- The Raman measurements were stopped after about 5 days because of the identification of a laser-induced coating damage on the laser window of the LARA cell. The cause for the damage was presumably the increase of the effective laser power to 10 W due to the double pass configuration combined with a decrease of the laser-induced damage threshold of the anti-reflection coatings due the nitrogen atmosphere in the glove box.
- All results are evaluated with respect to KATRIN in section 4.7. The occurrence of the laser-induced coating damage and the performance of optical coatings in glove box and tritium gas environments are further investigated in chapter 5.

#### 4.6.1. The tritium circulation test loop LOOPINO

##### Description of LOOPINO

The LOOPINO facility is a closed tritium circulation loop (figure 4.20) that features certain key components to experimentally simulate the gas circulation in the Inner Loop:

- A buffer vessel which can be pressure stabilised using the pressure sensor RPM83401 and the PID controlled regulation valve VAI83406,
- a pump (PCO83320) to drive the gas circulation, and
- a LARA cell (LRC80210) which is located inside the glove box but can be optically accessed by the Raman system via a custom-made hardware interface (the so-called 'Appendix', figure 4.21).

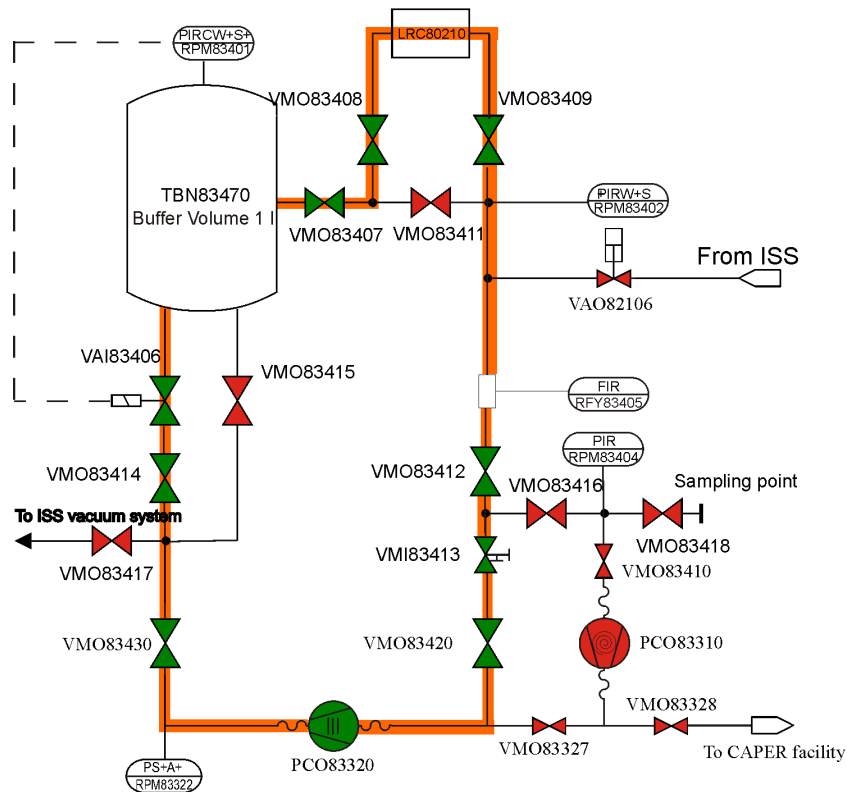


**Figure 4.20.: Flow diagram of LOOPINO.** The flow path and valve positions (green=open; red=closed) are highlighted for normal operation mode. The pressure in TBN83470 is measured by the pressure sensor RPM83401 and controlled by the automatic valve VAI83406. The LARA cell (LRC80210) is located between the TBN83470 and the needle valve VMI83413 which limits the gas flow rate. Tritium gas (purity >95%) can be received from the isotope separation system (ISS) [Dör02]. The gas can be transferred to the CAPER facility [Bor05] for tritium recovery. Image source [Stu10b].

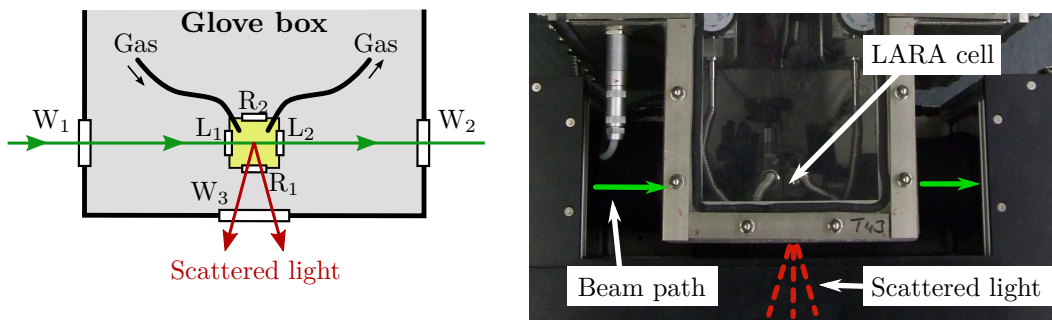


**Figure 4.21.: The 'Appendix'. A hardware interface for Raman measurements with LARA cells inside the glove box.** *Left:* Schematic drawing of the Appendix with all windows labelled: Appendix windows ( $W_i$ ), laser ( $L_i$ ) and Raman ( $R_i$ ) windows of LARA cell. *Right:* Top view of LARA system (black box) attached to Appendix with indicated beam paths. All beam paths are enclosed for laser safety reasons and to reduce the background in the Raman spectra.

The successful stabilisation of the buffer vessel pressure to better than 0.3 mbar was already demonstrated in previous works [Stu10b]. The conductance of the WGTS capillary and beam tube is simulated by a needle valve (VMI83413) which can be used to adjust the gas flow rate in the loop. The pressure in the LARA cell can be considered as identical to the pressure in the buffer volume because of the needle valve and the flow meter RFY83405 which are limiting the conductance of the complete circulation loop [Stu10b]. In contrast to the Inner Loop, no permeator is installed in LOOPINO and hence impurities (e.g.  $^3\text{He}$ , hydrocarbons) cannot be separated from the gas stream. Therefore, the rise of impurities is expected during the circulation of gas in LOOPINO over the course of days. A detailed description of LOOPINO can be found in [Stu10b].

### Preparation of LOOPINO for Raman measurements

During the last operation phase of LOOPINO, the optical coatings of the inner window surfaces of the LARA cell were damaged (section 4.1). To investigate the cause of the damage and to avoid repeated damage, several actions were performed before LOOPINO was operated again:

- Evacuation of LOOPINO and flushing of the section around the LARA cell with hydrogen to enforce isotope exchange reactions and hence to decontaminate LOOPINO.
- Disconnection of the LARA cell to investigate the window damage (see next chapter).
- Replacement of the automatic valve VAI83406 by a full-metal version.
- Leak test of LOOPINO to ensure an integral leak rate  $< 10^{-8} \frac{\text{mbar}\cdot\ell}{\text{s}}$ .
- Installation of a new LARA cell (cell #6, details in table 4.8)
- Leak test of LOOPINO to ensure an integral leak rate  $< 10^{-8} \frac{\text{mbar}\cdot\ell}{\text{s}}$ .
- Purging of LOOPINO with 98%  $\text{H}_2$ , 0.8%  $\text{N}_2$ , 0.4% HD, 0.2% HT, 0.2  $\text{D}_2$  (total pressure 200 mbar) and evacuation.

The replacement of the automatic valve became necessary because it was found that the installed valve unintentionally contained a polytetrafluoroethylene (PTFE, also known as Teflon<sup>®</sup>) valve seat<sup>8</sup> (figure 4.22). PTFE is one of the materials that should not be installed into tritium bearing systems since it is prone to radio-chemical degradation effects which can also trigger the formation of hydrogen fluoride species and the corrosive (tritiated) hydrofluoric acids [Cla06, Dep93]. The valve was therefore suspected to have boosted the window damage experienced before or to even be even to be its sole cause. It was consequently replaced by a valve that is fully based on metal components including the valve seat. Harmful effects on optical coatings in tritium environment will be discussed in detail in chapter 5.

<sup>8</sup>A valve seat is the seal that separates the inlet from the outlet side of the valve in closed state.

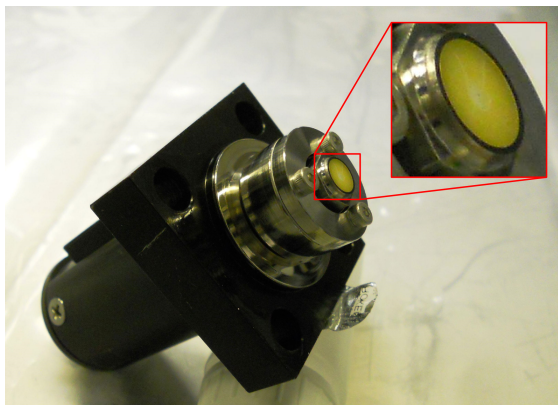


**Figure 4.22.:** Dismantled regulation valve VAI83406 of LOOPINO. The valve seat made of polytetrafluoroethylene (PTFE) is enlarged in the inset. The yellowish discoloration of the initially white PTFE is most likely caused by tritium-induced degradation. The picture was taken inside a glove box.

#### 4.6.2. Monitoring of a circulating tritium gas mixture (run C148)

##### Measurement procedure and analysis

The Raman system was operated in this measurement run with the new LARASoft software which combines the Raman and sensor data acquisition with the SpecTools toolkit for data analysis. The relative Raman intensities were automatically calculated by LARASoft from each acquired spectrum within less than 1 s after its acquisition. This is an essential feature for future neutrino mass measurement runs because the Inner Loop operators must have real-time feedback in order to react immediately on variations of the gas composition. LARASoft will be discussed in detail in chapter 6.

The wavelength calibration of the spectrometer and the preparation of line shape templates for the ShapeFit routine in LARASoft were done before the start of the measurement run using the spectrum of a Ne calibration light source. Note that the system to measure the spectral sensitivity of the light collection and analysis system was not yet available at the time of this test run.

All parameters necessary for the analysis of the Raman spectra with LARASoft were set before the start of the measurement run and are listed in appendix B.3. Seven lines were fitted, namely the  $Q_1$  branches of the hydrogen isotopologues and a potential  $Q_1$  branch of  $N_2$  which would arise in case of a leak in LOOPINO.

LOOPINO was filled with about 90 mg tritium gas from the isotope separation system (corresponding to  $pV = 0.348$  mbar·l according to the ideal gas law or to  $3.14 \cdot 10^{13}$  Bq when assuming 95% isotopic purity). Tritium circulation along the flow path shown in figure 4.20 was started. A pressure set point of 200 mbar for the buffer vessel was chosen and the flow rate was reduced by adjustment of the needle valve (VMI83413) to 103 sccm to mimic similar conditions in the KATRIN Inner Loop. The continuous Raman measurements were started after completion of the filling process and performed

**Table 4.8.: Overview of LARA3 operation at LOOPINO (run C148) and details on windows of LARA cell.** The integrity of the windows has been verified by optical inspection before mounting on the LARA cell body #6. More details on the coatings will be given in section 5.2.

	Run C148
Gas sample	'Pure' T <sub>2</sub> gas from ISS <sup>†</sup> , i.e. isotopic purity $\varepsilon_T > 0.9$
Total pressure	200 mbar
Laser power	5 W
Acquisition time	29.5 s
Measurement period	30 s
Binning groups <sup>◊</sup>	11
Laser windows (L <sub>1</sub> , L <sub>2</sub> )	AR532nm/0° coating on both sides Electron beam deposition (F-02558, batch 27010H1) Windows were not in contact with tritium before.
Raman windows (R <sub>1</sub> , R <sub>2</sub> )	AR450-700nm/0° coating on both sides Electron beam deposition (B-05267, batch unknown) Windows were not in use before.
Data analysis	Real-time analysis with LARASoft: Calculation of relative Raman intensities within less than 1 s after each spectrum acquisition.

<sup>†</sup> Isotope separation system [Dör02].

<sup>◊</sup> Effective number of pixels in the vertical, i.e. non-dispersive, direction of the CCD detector array due to on-chip binning [Jam13a].

over about 5 days with 29.5 s acquisition time and a measurement repetition period of 30 s (details in table 4.8).

The only data manipulation steps that were performed offline, i.e. manually after the measurement run are,

- the exclusion of data when the Raman system was opened during operation to check the laser beam path,
- the fitting of the relative Raman intensities as a function of time,
- the determination of the relative precision of the Raman measurement using the histogram of the fit residuals and the mean relative Raman intensity, and
- the investigation of systematic effects due to disturbing spectral features.

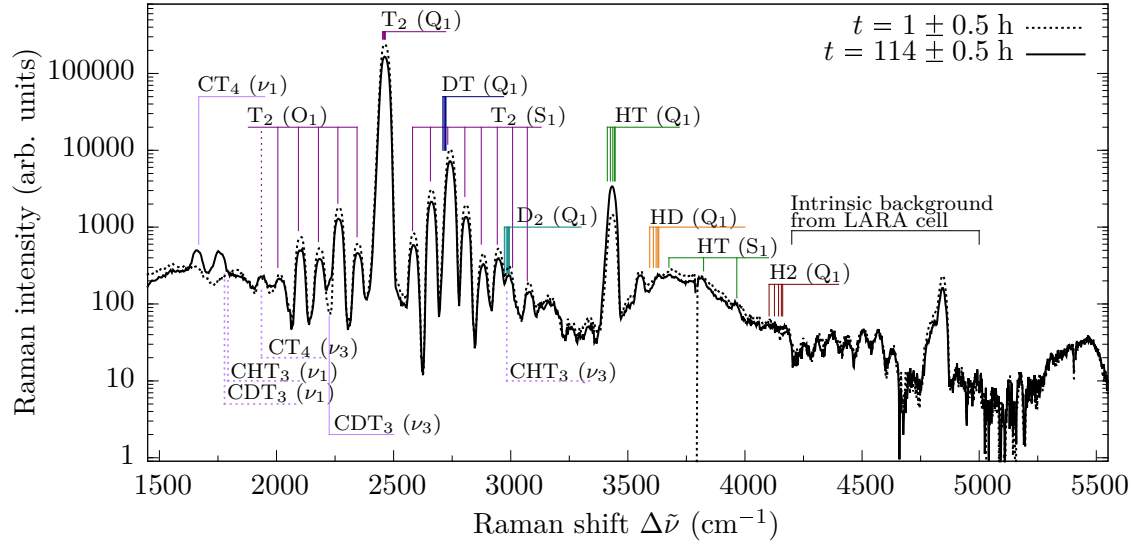


**Figure 4.23.:** Averaged Raman spectra at time  $t = 0.5 - 1.5$  h and  $t = 113.5 - 114.5$  h of run C148. For each date 120 subsequent spectra were averaged for noise reduction. The Raman lines and branches are labelled according to [Stu10b, Eng92, Eng97]. The  $Q_1$  branches of DT and  $D_2$  overlap with  $S_1$  lines of  $T_2$ . Ambiguous labels are indicated by dotted lines. Tritiated methane species  $CT_4$ ,  $CHT_3$ , and  $CDT_3$  were formed during the  $>100$  h of gas circulation. The position of the potential  $\nu_1$  lines of  $CHT_3$  and  $CDT_3$  deviate by about  $20$   $\text{cm}^{-1}$  from the values in ref. [Eng92, Eng97]. The features at  $\Delta\tilde{\nu} > 4300$   $\text{cm}^{-1}$  are not related to gas species as they were also observed in Raman spectra of the evacuated cell.

## Results and discussion

Two Raman spectra, taken at the beginning and at the end of the measurement run, are shown in figure 4.23. The  $Q_1$  branches of  $T_2$  and HT can unambiguously be identified in the spectra. The  $Q_1$  branch of  $D_2$  is overlapping with the  $S_1(J''=6)$  and  $S_1(J''=7)$  lines of  $T_2$  and the  $Q_1$  branch of DT is overlapping with the  $S_1(J''=3)$  lines of  $T_2$ . As it will be shown, both overlaps will have an influence on the quantification of the Raman intensities. The  $Q_1$  branches of HD and  $H_2$  are low in intensity and their Raman intensities will be affected by background noise and the residual curvature of the background which is clearly visible in the logarithmic representation of the spectrum.

The formation of tritiated methane species, namely  $CT_4$ ,  $CDT_3$  and presumably  $CHT_3$  can be concluded from the spectral features which emerge around  $\Delta\tilde{\nu} \approx 1650 - 1900$   $\text{cm}^{-1}$  and  $\Delta\tilde{\nu} \approx 2230$   $\text{cm}^{-1}$  in the  $t = 114 \pm 0.5$  h spectrum. The observed peak positions for  $CHT_3(\nu_1)$  and  $CDT_3(\nu_1)$  deviate from the values in [Eng92, Eng97] but this discrepancy cannot be resolved until a laser wavelength measurement is installed in the system and the spectrum is re-measured with a high resolution spectrometer. The formation of methane species is expected since no permeator is installed in LOOPINO. For Raman shifts  $\Delta\tilde{\nu} > 4300$   $\text{cm}^{-1}$  a periodic pattern is visible in the spectrum which has a broad branch-like peak around  $4600$   $\text{cm}^{-1}$ . As this feature was also found in spectra of the evacuated cell before filling with the tritium gas, it is considered as a LARA cell intrinsic

background. The origin of this feature is currently not known but could also be related to a damage of the laser window  $L_1$  which will be discussed later.

The relative Raman intensities of the  $Q_1$  branches of the hydrogen isotopologues are shown in figure 4.24. The following observations can be made:

- Tritium dominates the gas mixture with a relative Raman intensity  $I_{\text{rel}}(\text{T}_2) \geq 0.935$ . The next most intense species are DT and HT with  $\approx 0.04$  and  $\leq 0.02$  relative intensity.  $I_{\text{rel}}(\text{T}_2)$  decreases in time and  $I_{\text{rel}}(\text{HT})$  increases due to isotope exchange reactions as also seen in LARA3*pre* run 2 and [Fis11].
- $I_{\text{rel}}(\text{DT})$  is constant in time indicating that the overlapping  $\text{T}_2 \text{S}_1(J''=3)$  line is only slightly contributing to the relative Raman intensity of DT as otherwise a decrease of  $I_{\text{rel}}(\text{DT})$  would have to be apparent. Nevertheless, this contribution should be considered in the future and a possible procedure is described in chapter 7.

A constant value of  $I_{\text{rel}}(\text{DT})$  also proves that there is currently no source of deuterium atoms in LOOPINO which would cause  $I_{\text{rel}}(\text{DT})$  to rise. This conclusion is reasonable since the system was only in contact with hydrogen and traces of tritium during the months before this measurement. Before the previous tritium operation of LOOPINO in 2010, the system had been operated with deuterium and a clear rise of DT was observed during the tritium run [Fis11]. The different behaviour of  $I_{\text{rel}}(\text{DT})$  in the current tritium run nicely demonstrates that the stainless steel in LOOPINO has an isotopic hysteresis due to the atomic diffusion of hydrogen isotopologues into and delayed release from the metal lattice of the stainless steel in the system. Such effects make a continuous gas composition measurement with LARA necessary in order to achieve successful neutrino mass measurement with KATRIN.

- The relative Raman intensities of  $\text{D}_2$ , HD and  $\text{H}_2$  are  $< 0.002$  and hence at least one order of magnitude smaller than those of HT. At this level, distortions due to the background and other features in the spectrum become significant:  $I_{\text{rel}}(\text{D}_2)$  fluctuates regularly between two values because of the vanishing  $\text{D}_2$  concentration and the nearby  $\text{S}_1$  lines of  $\text{T}_2$ .  $\text{H}_2$  is even more affected since the relative Raman intensity is constantly negative which can be related to the fact that the baseline in the ShapeFit fitting procedure was fixed at 100 but the baseline of the acquired spectra are below that value at the position of the  $Q_1$  branch of  $\text{H}_2$ .

The impact of the systematic shift of  $I_{\text{rel}}(\text{H}_2)$  on the other relative Raman intensities is investigated by setting  $I_{\text{rel}}(\text{H}_2)$  to zero:  $I_{\text{rel}}$  of  $\text{T}_2/\text{DT}/\text{HT}/\text{HD}$  decrease by less than  $(60/4/2/0.1) \cdot 10^{-5}$ , which corresponds to a relative shift of  $(6 \pm 2) \cdot 10^{-4}$  for each isotopologue. Systematic shifts of  $I_{\text{rel}}$  due to the calibration uncertainty of the KATRIN Raman system were determined for a similar gas mixture by M. Schlösser: There, relative shifts of  $10^{-3}$  for  $\text{T}_2$  and about 0.05 for the other isotopologues were found [Sch13b]. Therefore the present systematic effect is considered relevant for  $\text{T}_2$  but negligible for the other isotopologues. Nevertheless, this effect will not be an issue in future measurements because the fit parameters 'Absolute Raman intensity' can easily be constrained to positive values in the ShapeFit routine.

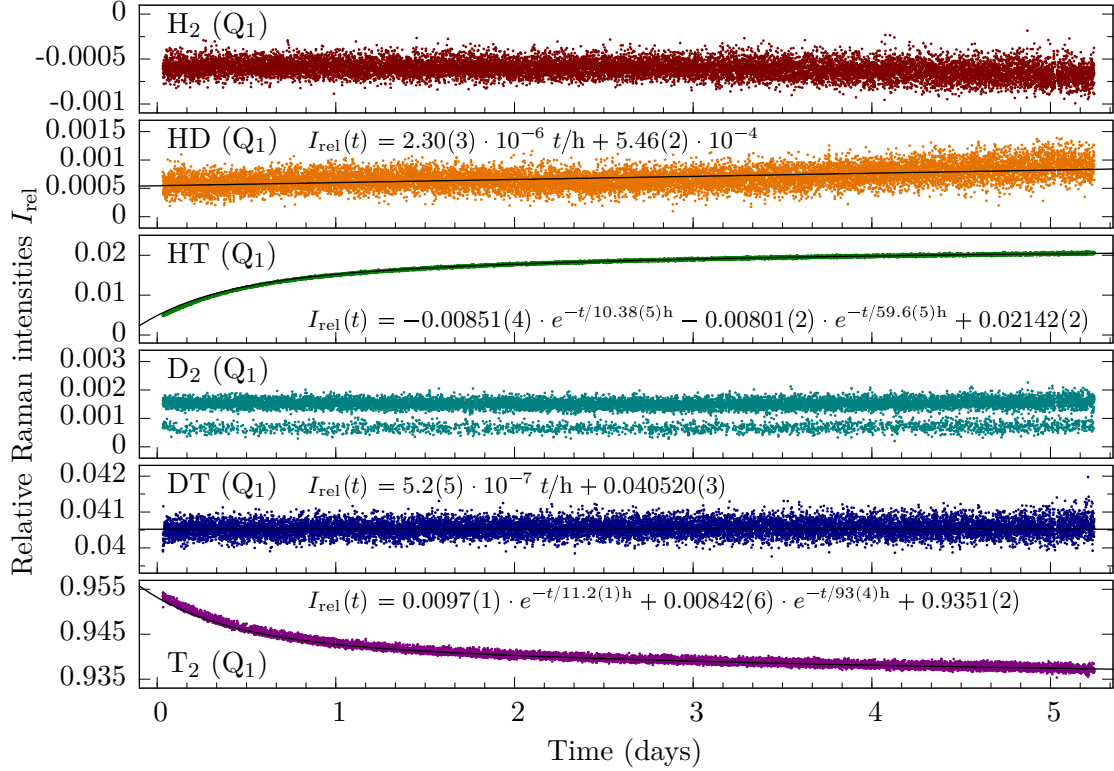


**Figure 4.24.: Relative Raman intensities measured in run C148.** The simultaneous formation of HT and decrease of  $\text{T}_2$  are caused by isotope exchange reactions between the gas and the hydrogen atoms stored in the stainless steel surfaces in LOOPINO. The trends of  $\text{T}_2$  and HT (DT and HD) are approximated by exponential (linear) functions. The uncertainty in the last digit of the fit parameters is given in parentheses. The  $\text{Q}_1$  branches of  $\text{H}_2$  and  $\text{D}_2$  are affected by disturbing influences (see main text) due to their low intensity and hence not fitted:  $I_{\text{rel}}(\text{H}_2)$  is continuously negative due to the baseline in the surrounding part of the spectrum and  $I_{\text{rel}}(\text{D}_2)$  alternates between two values due to the significant overlap of the  $\text{D}_2$   $\text{Q}_1$  branch with the  $J'' = 6, 7$  lines of the  $\text{T}_2$   $\text{S}_1$  branch.

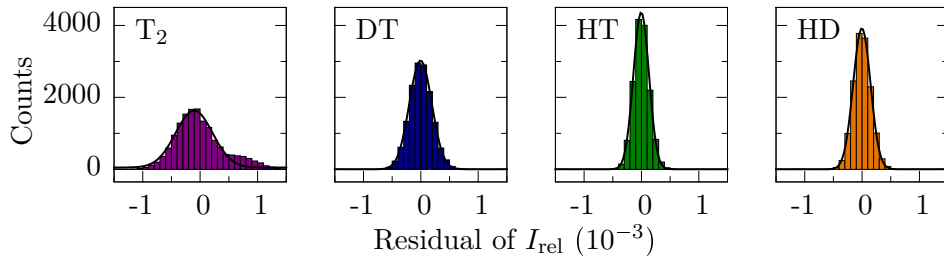


**Figure 4.25.: Histogram of residuals of  $I_{\text{rel}}$  of LARA3 run C148.** All histograms are fitted by Gaussian distributions  $y = y_0 + A \cdot \exp[-(x - x_c)^2/(2\sigma^2)]$  to determine the standard deviation  $\sigma$ . The residuals for  $\text{T}_2$  deviate slightly from a Gaussian distribution due to the data points of the period  $t < 1$  day.

**Table 4.9.: Achieved relative precision  $\sigma/\bar{I}_{\text{rel}}$  in LARA3 run C148.** The partial pressures are estimated from the relative Raman intensities, i.e. without taking the spectral sensitivity into account which can deviate by up to 15% from each other [Sch13b].  $\bar{I}_{\text{rel}}$  mean relative Raman intensity,  $\sigma$  standard deviation of fit residual (from figure 4.25),  $\delta_\sigma$  fitting uncertainty of  $\sigma$ . The uncertainty of  $\sigma/\bar{I}_{\text{rel}}$  is calculated by error propagation of  $\delta_\sigma$ .

	Partial pressure (mbar)	$\bar{I}_{\text{rel}}$	$\sigma$ ( $10^{-3}$ )	$\delta_\sigma$ ( $10^{-5}$ )	$\frac{\sigma}{\bar{I}_{\text{rel}}}$ ( $10^{-3}$ )
T <sub>2</sub>	188	0.9406	3.224	128	$0.343 \pm 0.014$
DT	8.1	0.0406	1.952	9	$4.81 \pm 0.02$
HT	3.5	0.0173	1.350	7	$7.79 \pm 0.04$
HD	0.14	0.00069	1.508	6	$219.1 \pm 0.9$

In order to determine the relative precision of the Raman measurements, the same procedure as for LARA3pre run 2 in section 4.4.2 is applied: Creation of histograms for the fit residuals (figure 4.25), fitting of the histograms with Gaussians to determine the standard deviation  $\sigma$ , and finally calculation of the relative precision  $\sigma/\bar{I}_{\text{rel}}$ . This was done for T<sub>2</sub>, DT, HT and HD and the results are listed in table 4.9. D<sub>2</sub> and H<sub>2</sub> have been omitted due to the presence of the discussed artefacts. The relative Raman intensity of T<sub>2</sub> can be monitored with a relative precision of  $3 \cdot 10^{-4}$ , and a relative precision of  $5 \cdot 10^{-3}$  and  $8 \cdot 10^{-3}$  is reached for DT and HT, respectively. It can be already stated at this stage that the system safely meets the  $10^{-3}$  requirement of KATRIN for the relative precision of the relative Raman intensity of T<sub>2</sub>. However, difficulties for the quantification of trace gas constituents as H<sub>2</sub> and D<sub>2</sub> became visible due to overlapping Raman lines of the more abundant species or due to the baseline. The issue has not yet been completely resolved but a procedure to treat it has been identified and will be presented in section 7.2.

The measurement run was stopped after about five days since the laser and sensor data acquired during the run (figure 4.26) indicated a continuously increasing loss of laser power in the beam path. In the following days, the Appendix and LARA cell windows were visually checked which made it necessary to temporarily interrupt the gas circulation in LOOPINO and reduce the pressure in the cell to 20 mbar for safety reasons. Finally, the pressure in the LARA cell was intentionally increased to 211 mbar before disconnection of the cell from LOOPINO. The LARA cell was stored to study the durability of its windows during long-term contact with highly purified tritium gas (discussed in chapter 5). A chronological overview of the cell pressures, LOOPINO operation conditions, and the performed actions is given in table 4.10.

A damage of the L<sub>1</sub> laser window of the LARA cell (recall figure 4.21 for window identification) and the formation of absorbing spots on nearly all optical components in the laser beam path system were found to be the cause for the experienced laser power losses during run C148. The spots were not present at the beginning of the run when the integrity of all components of the Raman system has been checked. However, the decreasing trend of the laser power measured by LM-10 and photo diode was already found in several test

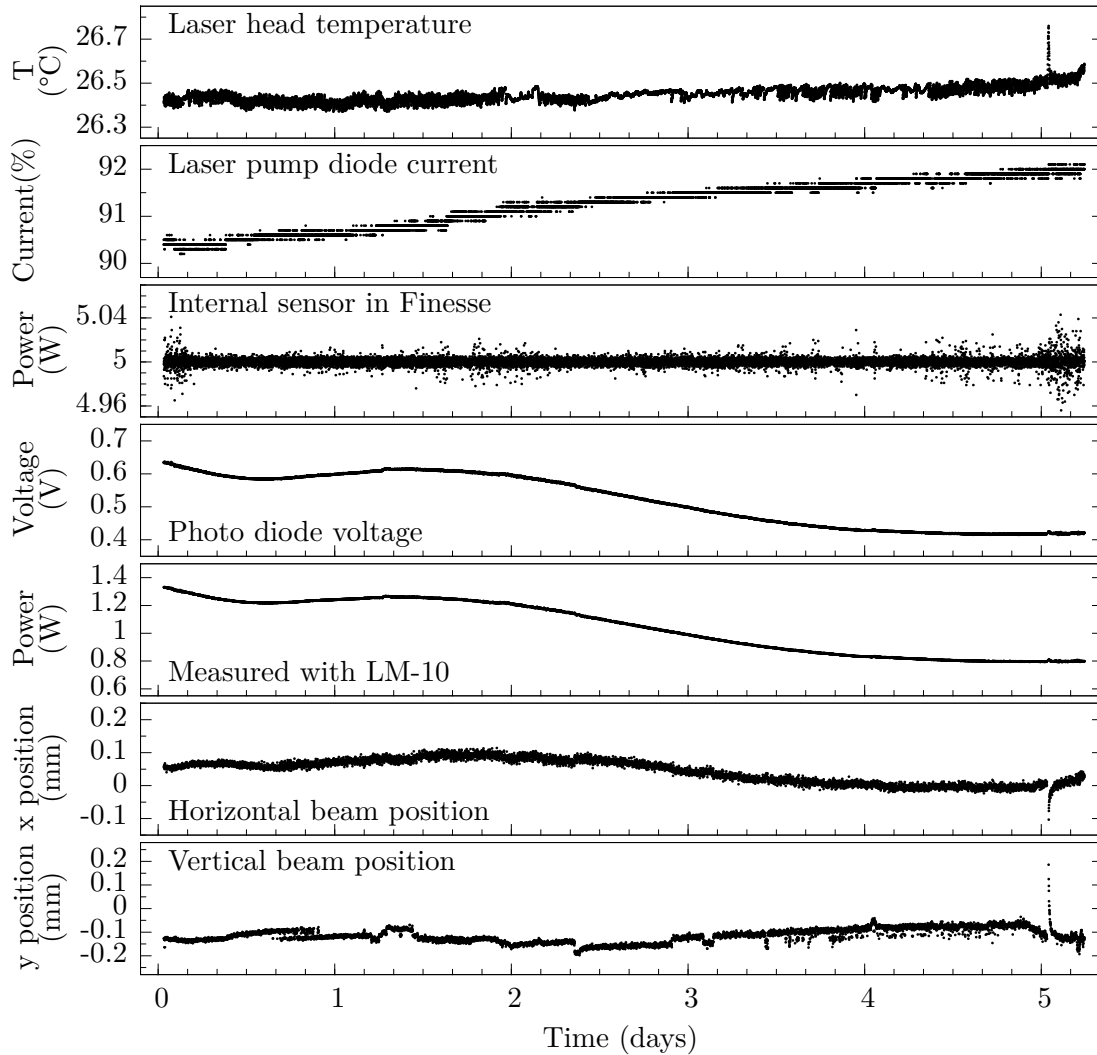


**Figure 4.26.: Laser and sensor data of run C148.** The laser internal power reading is constant apart from minor fluctuations. The continuously increasing pump diode current is most likely a sign of decreasing lasing efficiency (optical output power / pump current). Both beam power measurements located at the end of the beam path (LM-10 and photo diode) show consistent decreasing trends indicating the growth of power dissipating processes in the beam path. After about five days, the shutter was closed for about 15 min for inspection of the system. After re-opening, the beam positions and laser head temperature needed about 15 min to reach their initial values while increased laser power fluctuations were present until the end of the run. The occasional fluctuations in the vertical ( $y$ ) beam position are most likely related to mode jumps of the Finesse multi-mode laser.

**Table 4.10.: Chronological overview of LARA cell pressure (p), LOOPINO operation conditions, and performed actions.** The LARA cell #6 was used in the Raman measurement run C148 at the LOOPINO facility.

Date	Action	p (mbar)	Gas circulation
29.05.2013	09:26 Filling of LOOPINO with pure tritium gas, start of circulation and run C148	200	yes
03.06.2013	16:06 Stop of run C148	200	yes
05.06.2013	07:24 Circulation stopped, pressure reduction in LARA cell, study of Appendix and cell windows	20	no
07.06.2013	16:03 Circulation restarted	200	yes
14.06.2013	09:01 Intentional pressure increase, LARA cell disconnected from LOOPINO	211	no
01.07.2013	Visual inspection of LARA cell windows with optical microscopy, cleaning of windows with methanol	211	
02.09.2013	Visual inspection of LARA cell windows with optical microscopy	211	

measurements with the system which were performed in the weeks before run C148. This also clarifies why the laser power measured by the LM-10 sensor was only about 1.3 W at the beginning of run C148. The status of the optical components after run C148 will be discussed in more detail in the next section. Additionally, but independent of the laser power losses in the beam path, the laser pump diode current rose approximately linearly over the about five days of run C148 (figure 4.26). Extrapolating this trend with constant slope shows that the maximum allowed current (100%) would have been reached after additional 20-25 days of operation. Afterwards, the laser would not have been able to maintain the 5 W laser power output any more. Although a decrease of the laser power would not have affected the trueness of the relative Raman intensities, the precision would have been diminished due to the decreasing signal-to-noise ratio in the Raman spectrum. The laser was maintained after the run by the manufacturer in order to ensure that 5 W output power can again be achieved. As the laser shall be operated for at least two months during the KATRIN neutrino mass measurement runs, a reduction of the output laser power is suggested to ensure that the chosen output power can be continuously achieved, even in the case of decreasing lasing efficiency. This will be considered in chapter 7 where a proposal for the operation parameters of the KATRIN Raman system is given.

### 4.6.3. Status of optical components after run C148

After the stop of run C148, spots were found on all optics of the Raman system (figure 4.27). A measurement of the laser beam power at various positions in the beam path revealed that each spot reduced the laser power by about 5–10%. For the Appendix windows and the LARA cell, a cumulative laser power reduction by about 50% was measured.

The spots on the optics of the Raman system could be easily and residue-free removed with ethanol when sufficient access to the optical surfaces was possible. The optical isolator was shipped to the manufacturer for cleaning but could only be partly restored. The Appendix windows could not be fully cleaned and therefore were replaced. The fact that the spots could generally be removed with ethanol indicates that the coating itself was not damaged but some kind of organic surface contamination was generated on the optical surfaces. The contamination source was identified as evaporated polyvinyl chloride (PVC) from one of the enclosure walls of the Raman system which was burned by an intense laser reflection coming out of the Appendix window  $W_1$ . The origin of the back-reflection was found to be the first laser window ( $L_1$ ) of the LARA cell which exhibited a two-fold surface alteration: Two to three spot-shaped coating damages and a stripe-shaped feature passing through the spot-shaped features (figure 4.28). After disconnection, the LARA cell (filled with 211 mbar tritium gas) was transferred to another glove box where an optical microscope and methanol were available for visual inspection and cleaning, respectively. The stripe shaped feature could be removed by cleaning with a duster spray and methanol while the spot-shaped features mostly remained and became apparent as an actual coating damage (figure 4.28). Surface alterations with a diameter of  $< 50 \mu\text{m}$  were found on the inner surface of the laser and Raman windows  $L_1$ . These spots were just visible by eye. The resolution of the microscope at TLK was not sufficient to further resolve the spots. A negative effect on the Raman measurements was not experienced before. A repeated inspection of the LARA cell windows with the microscope at TLK after another 77 days, i.e. after 96.2 accumulated days of tritium filling, did not reveal significant changes to the findings.

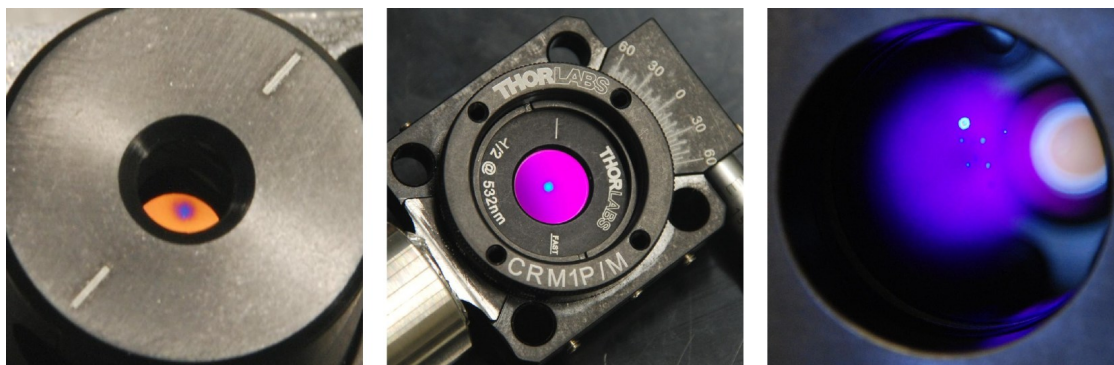


**Figure 4.27.:** Spots on selected optics after run C148. *Left:* Optical isolator *Middle:* Half waveplate *Right:* Appendix window  $W_1$ , outer surface. Several spots are visible and presumably due to earlier Raman measurement runs. The window  $L_1$  of the LARA cell is visible in the background.

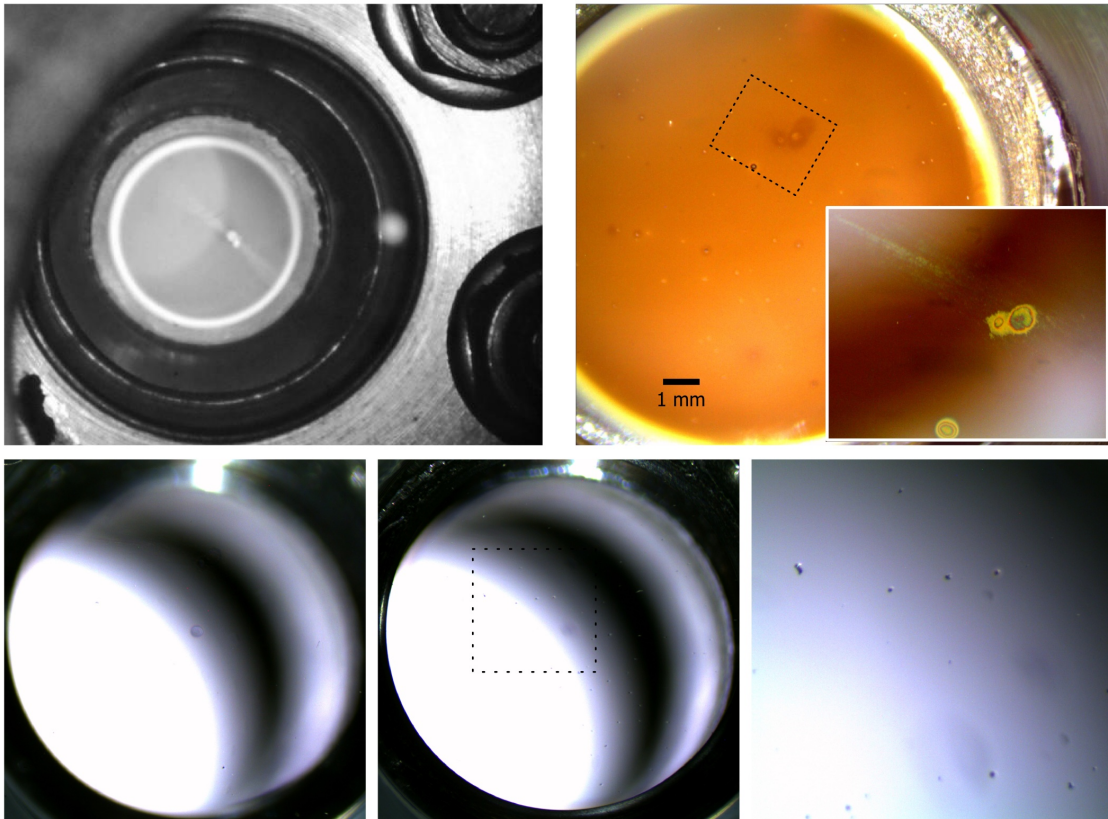


**Figure 4.28.: Damaged LARA cell window  $L_1$  after run C148.** The images were taken at varying cell orientation and hence varying lighting conditions. The ostensible variation of the positions of the spots on the outer window surface is caused by parallax. The coating is only visible in the top right image where reflection conditions were fulfilled. All images were acquired before cleaning of the outer window surface with methanol. *Top left:* LARA cell inside Appendix. Picture taken through Appendix window  $W_1$ . Two nearby spots and a stripe are visible on the outer window surface. The large but blurred white spot on the dark cone of the vacuum flange is the prominent spot on the Appendix window  $W_1$  (figure 4.27, right). The picture was converted to black and white to increase the contrast. *Top right:* Microscope image taken after disconnection from LOOPINO and after window cleaning with methanol. The approximate position of the inset picture is indicated. Especially the spot at the border of the inset image could not be removed by cleaning. *Inset:* Stripe and spot-shaped coating damages before cleaning with methanol. *Bottom row:* Microscopy images with focus on outer (*left*) and inner (*middle*) window surface. *Inset:* Magnified image of spots on inner surface (indicated by dashed box in middle image). A mean spot size of about  $40 \mu\text{m}$  was estimated.

The cause for the stripe-shaped feature is currently not identified but it has to be noted that a similar 'spot + stripe' pattern was also found on both laser windows of a LARA cell that was regularly operated for about 6 months within the context of the work by R. Größle [Grö14]. In that case the cell was located outside a glove box and also a different Raman system (with 3 W laser power) was employed. A correlation between the orientation of the stripe-shaped features with experimental parameters as e.g. laser polarisation could not be found in any of the cases.

In conclusion, the damage of the LARA cell window  $L_1$  and the consequential laser back-reflection are considered as the primary cause for the spot formation on the other optics. Since the windows of the LARA cell were checked before installation, two scenarios for the coating damage of the  $L_1$  LARA cell window seem possible:

- Deposition of dust or dirt onto the window surface during LARA cell installation in the Appendix. Subsequent coating damage due to increased laser absorption of the dust and dirt particles.
- Exceeding of the laser-induced damage threshold (LIDT) of the coating due to the perfectly overlapping beams in the double pass configuration of LARA3.

Although the first scenario cannot be excluded, the second appears more likely since the coating damage started to emerge within the first operation runs of the newly installed LARA3 double pass configuration in which both beams in the LARA cell were fully overlapped. The linear laser power density (laser power per beam diameter, unit: W/mm) at the LARA cell window  $L_1$  reached about 10% of the stated LIDT of the anti-reflection coating under standard conditions (table 4.11). As it will be discussed in detail in chapter 5, the performance of the employed coating type (electron beam deposition, EBD) is affected by environmental conditions, e.g. oxygen pressure, water

**Table 4.11.: Calculated laser power density at various positions in the LARA3 setup and comparison to laser-induced damage threshold (LIDT).** An effective laser power of 10 W, i.e. perfectly overlapping beams, was assumed. Laser beam diameter (measured at  $1/e^2$  intensity) taken from [Las11]. The calculation of beam sizes and power densities is shown in appendix C. The LIDT values depend on the experimental conditions, e.g. wavelength, beam diameter, pulsed or continuous wave operation, pulse length. Where available, these data are given in the footnotes.

Position	Beam diameter (mm)	Linear power density (W/cm)	Power density (W/cm <sup>2</sup> )	LIDT
Optical isolator (OI)	2.07	48.3	30.8	500 W/cm <sup>2</sup> †
Appendix window ( $W_1$ )	~ 0.83	~ 120	~ 1840	1 MW/cm <sup>2</sup> ◇
Cell window ( $L_1$ )	~ 0.11	~ 904	~ 10 <sup>5</sup>	~ 10 <sup>4</sup> W/cm ‡

† Optical isolator must not be operated above 40 W absolute laser power. Source: [Tho11].

◇ 1064 nm, cw. No LIDT available for  $\lambda = 532$  nm. Source: [CVI13].

‡ Source: [Hän27].

vapour concentration, and organic impurities from outgassing [Jen06, Rie08]. Therefore, a reduction of the LIDT can reasonably be expected in the nitrogen rich (concentration >96%) and nearly water vapour free (concentration in the ppm level) environment inside the glove box. However, a quantification of the expected LIDT reduction is not easily possible.

## 4.7. Evaluation of the results with respect to KATRIN

In section 4.3 a set of open issues and questions was listed which should be answered by the commissioning of the KATRIN Raman system. These questions will be used as guidelines to evaluate the performance of the Raman system in the commissioning measurements in the context of the KATRIN experiment.

### **How effective and reliable is the double pass configuration of the beam path to increase the effective laser power in the beam path?**

The double pass configuration of LARA3*pre* was found to increase the absolute Raman intensities by  $(97 \pm 5)\%$  (section 4.4.1) which corresponds to the maximum achievable amplification factor. The alignment of the LARA3*pre* double pass remained complex and thus should not be used in the Raman system for the neutrino mass measurement runs. The installation of the optical isolator beam path reduced the ambiguity during alignment as the back-going beam can be fully overlapping with the forward going one. This qualifies the double pass configuration to become a standard ingredient of the KATRIN Raman system beam path.

### **How stable is the output power and beam pointing of the Finesse laser? Is the Finesse laser sufficiently stable to perform Raman measurements without laser-related effects as experienced in former Raman measurements [Stu10b, Fis11]?**

The test of the Finesse laser showed that even though the laser is a 'turn-key to operate' component its internal parameters have to be well tweaked to achieve stable operation conditions. In case of the 24°C temperature set point of the water chiller unit, a superior laser power stability of  $5 \cdot 10^{-4}$  and negligible beam position fluctuations were found. This is a significant improvement in comparison to previous Raman systems at TLK that were affected by laser instabilities. On the other hand, the continuously increasing laser pump diode required several maintenance actions by the manufacturer and could limit the performance of the laser in the future. Therefore it is suggested to operate the laser at reduced output power (e.g. 3–4 W) to increase the safety margin of the laser internal parameters parameters, like the pump diode current, and to closely monitor the laser parameters. If the issue of decreasing lasing efficiency can be resolved, the Finesse laser can be considered as ideally suited for the KATRIN Raman system.

**Are there (not yet identified) effects which influence the accuracy, relative precision, or reliability of the Raman measurements?**

The spectral sensitivity  $\eta(\lambda)$  of the light collection system was not yet considered in these measurements and is one of the most dominant factors affecting the accuracy of the gas composition measurement. Effective procedures for the measurement of  $\eta(\lambda)$  and correction of the Raman data based on it were developed simultaneously to this work [Sch13b, Rup12] and can be implemented in the next measurements. It was shown in section 4.4.1 that the chromatic aberration of the light collection optics may affect the absolute Raman intensities by up to 20%. Even though this should in principle be corrected for by measuring  $\eta(\lambda)$  after each realignment of the system, the installation of achromatic lenses constituted a significant improvement of the system.

For the exact quantification of low-concentration species in the gas mixture (e.g.  $\text{H}_2$  and  $\text{D}_2$  in the LARA3 commissioning measurement C148 in section 4.6.2), the overlap of the 'signal' Raman lines with baseline or other spectral features has to be properly considered. M. Schlösser already demonstrated in [Sch13b] that instead of a single line a full Raman branch or even several of them can be used as a template for the ShapeFit fitting procedure of SpecTools. If applied to tritiated gas mixtures, this will very likely solve such issues in future measurements.

The operation of the Finesse laser at 5 W output power in the double pass configuration resulted in a gradual damage of the  $L_1$  laser window of the LARA cell. As this was most likely caused by reaching the LIDT of the window coating for the environmental glove box conditions the limit for the maximum effective laser power was found. In order to avoid such a damage in the future, more resistant coatings have to be found or the effective laser power should not be increased to 10 W any more. The latter would nicely coincide with the above discussed aspect that the Finesse laser should be operated below its maximum output power. Additionally, the shielding of the PVC walls of the laser enclosure walls with black anodised aluminium sheets is already planned.

**What was the origin of the coating damages of the tritium-facing LARA cell windows that were experienced in previous Raman measurements at the LOOPINO facility [Stu10b, Fis11]? How can these damages be avoided in the future?**

The occurrence of the initial, severe coating damage could not yet be linked unambiguously to a single cause; however, the identification of the PTFE containing regulation valve in LOOPINO which might have increased or even caused the formation of corrosive hydrofluoric acids in the system yielded a reasonable explanation. After the replacement of the valve no indications for similar coating damages were found yet although admittedly the exposure time of the windows was much shorter than during the measurements in 2010. This topic is subject of the next chapter where more detailed answers will be given.

**What is the level of detection and the achieved relative precision of the KATRIN Raman system for a KATRIN relevant gas mixture? What is the**

**minimum acquisition time to achieve 0.1% relative precision?**

The level of detection (LOD) specifies the minimum amount of a species that can be detected by an analytical measurement device.<sup>9</sup> Following [Lon83], the level of detection refers to the amount of a species whose signal is three times larger than the standard deviations of the baseline noise. Based on this definition, the partial pressure corresponding to the level of detection can be calculated in case of a Raman system by [Sch09]

$$p_{\text{LOD}} = \frac{3 \cdot \sigma_{\text{noise}}}{\sum_i I_{i,\text{abs}}} \cdot p_{\text{tot}} \quad (4.2)$$

where  $\sigma_{\text{noise}}$  is the standard deviation of the baseline noise in a flat part of the spectrum,  $I_{i,\text{abs}}$  is the absolute Raman intensity of the gas constituent  $i$ , and  $p_{\text{tot}}$  the total pressure of the gas mixture. The level of detection is evaluated for an arbitrary spectrum at the end of LARA3 run C148 ( $t = 4.76$  days).  $\sigma_{\text{noise}} = 13.52$  was calculated from a flat part of the spectrum (158 pixel wide) and  $\sum_i I_{i,\text{abs}} = 1.69 \cdot 10^6$  was extracted from the absolute intensity data which was calculated by LARASoft. Inserting these values and  $p_{\text{tot}} = 200$  mbar into eq. (4.2) results in  $4.8 \cdot 10^{-3}$  mbar for 29.5 s acquisition time. This means that traces of hydrogen isotopologues which have a relative concentration of

$$\frac{4.8 \cdot 10^{-3} \text{ mbar}}{200 \text{ mbar}} = 2.4 \cdot 10^{-5} \quad (4.3)$$

can be detected in the gas sample. This may be put into context to the level of detection determined for another Raman system at TLK, namely  $p_{\text{LOD}} = 6.8 \cdot 10^{-2}$  mbar (achieved for 10 s acquisition time) [Sch13b]. For 30 s acquisition time this would result in  $p_{\text{LOD}} = 2.3 \cdot 10^{-2}$  mbar which is a factor 4.7 worse than the level of detection achieved in this work. This difference is mainly due to the optimisation of the experimental setup which was done within this work.

A relative precision of  $0.34 \cdot 10^{-3}$  for  $T_2$ ,  $4.81 \cdot 10^{-3}$  for DT, and  $7.79 \cdot 10^{-3}$  for HT was achieved for 29.5 s acquisition time which clearly fulfils the KATRIN requirements although the system was operated with a damaged cell window. When scaling the relative precision, coarsely linking level of detection and length of acquisition time as being inverse to each other, the minimum acquisition time necessary to fulfil the  $10^{-3}$  precision for  $T_2$  is estimated to be of the order of 10 s. In case of reduced laser power but undamaged window a further reduction of the minimum acquisition time is expected.

**Additional lessons learnt and conclusion**

During the LARA3 commissioning measurement run C148, the LARASoft software (chapter 6) was used for the first time under realistic conditions to control the Raman system and to simultaneously perform the real-time data analysis. No adverse issues were encountered during the run and valuable experience on the necessary constraints for the fitting parameters was gained. All parameters for the analysis of the Raman spectra and the determination of the relative Raman intensities were defined before the start of the Raman measurements. Therefore, only minimal data manipulation and offline analysis

<sup>9</sup>This definition must not be mixed up with the level of quantification which is the minimum amount necessary for a quantitative analysis. For this level, the signal has to be ten times above the baseline noise [Lon83].

steps were necessary after the run to prepare the data for this thesis. The analysis of each Raman spectrum was done within 1 s after the acquisition of the spectrum, i.e. feedback on the gas composition in LOOPINO was available in real-time for the operators. This is an important step towards the full operation readiness of the KATRIN Raman system.

The commissioning of the KATRIN Raman system can be considered as successful because the effectiveness of the hardware and software improvements was demonstrated and the KATRIN precision requirements fulfilled. With respect to the decreasing lasing efficiency of the Finesse laser and to the presumably laser-induced damage of the LARA cell window, the limits of the Raman system were nearly reached or even exceeded. These experiences will be taken into account in chapter 7 where a proposal for the operational parameters of the system during the neutrino mass measurement runs is given.

## 5. Durability of optical coatings in tritium and glove box environments

Optical anti-reflection (AR) coatings are essential for the KATRIN Raman system to minimise laser power losses along the beam path and hence to maximise the signal-to-noise ratio in the Raman spectrum. As will be shown in this chapter, about 3.5% of the laser intensity is reflected at every uncoated interface between fused silica and air/vacuum. The significance of this effect can be easily demonstrated for the optics inside the Appendix (figure 5.1). If no optical coatings were applied on the Appendix windows ( $W_1$ ,  $W_2$ ) and the LARA cell laser windows ( $L_1$ ,  $L_2$ ), the laser beam would have to pass two uncoated optics, i.e. four uncoated interfaces, before reaching the tritium gas inside the LARA cell. This would reduce the effective laser power in the LARA cell by about 13% (neglecting multiple reflections). Therefore AR coatings are employed on all optics in the KATRIN Raman system, including those that are in contact with the atmosphere in the glove box ( $> 96\%$   $N_2$ ,  $< 4\%$   $O_2$ , and typically  $< 2$  MBq/m<sup>3</sup> tritium, water moisture in ppm range) or even pure tritium gas. The durability of optical coatings under such non-standard environmental conditions is essential for the reliable operation of the KATRIN Raman system. The coating damages that were encountered in the past during Raman measurements at the LOOPINO facility [Stu10b, Fis11] and the findings during the commissioning of the KATRIN Raman system have demonstrated that the durability of the coatings under these conditions cannot be taken for granted. Therefore the subject of coating durability is investigated within this chapter.

The basic working principles of optical multilayer coatings and selected coating deposition techniques are introduced in the first section of this chapter. In section 5.2 the coating issues that were experienced up to now at the Tritium Laboratory Karlsruhe are summarised. The special environmental conditions in a glove box and the presence of tritium can yield to a variety of harmful effects for optical coatings. Section 5.3 gives a review of these effects, evaluates their relevance for the KATRIN Raman system and

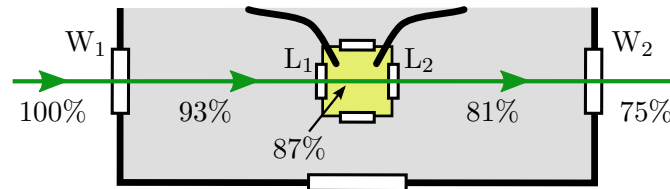


**Figure 5.1.:** Estimation of reflection losses for the case of uncoated windows. The relative laser power is shown along the beam path for the simplified case of no multiple reflections.

discusses if the cause for the experienced coating damages can be identified. As experimental data for the durability of optical coatings in tritium atmosphere is sparse but essential for the KATRIN Raman system, a dedicated durability test was performed (section 5.4). Within this test coating samples were exposed for up to 39 days to purified tritium gas and afterwards inspected by microscopy. Finally an improved coating scheme is presented in section 5.5 which will help to improve the durability of optical components when being in contact with tritium or glove box atmospheres.

## 5.1. Introduction to optical coatings

An optical coating consists of one or more thin layers of metallic or dielectric media that are deposited on a substrate material. The layer thickness can vary from the nm to the  $\mu\text{m}$  range. The thickness and material of each layer is specifically chosen to optimise the optical properties for the specific task. Metallic coatings are often used for mirrors. In this work fused silica or BK-7 glass are typically used as substrates of the optical components (windows, lenses, etc.). For anti-reflection coatings on such transmitting optics the coating materials obviously have to be transparent and dielectric coatings based on  $\text{TiO}_2$ ,  $\text{SiO}_2$ ,  $\text{MgF}_2$  or other metal oxides are often used.

### 5.1.1. Working principles of optical multilayer coatings

A light ray of wavelength  $\lambda$  propagating through the stack of coating layers will be partly reflected and transmitted at every layer interface (figure 5.2, left). The angles of incidence and refraction, respectively, are given by Snell's law  $n_i \sin \theta_i = n_t \sin \theta_t$  and the refractive indices  $n_i$  and  $n_t$  of the layers. The incident light is described by an electric plane wave  $\vec{E}_i(\vec{r}, t) = E_0 e^{-i(\vec{k}\vec{r} - \omega t)} \hat{n}$  where  $E_0$  is the electric field amplitude,  $\vec{k}$  the wave vector,  $\vec{r}$  the spacial position,  $\omega = 2\pi c/\lambda$  the angular frequency of the wave,  $t$  the time, and  $\hat{n}$  a unit vector perpendicular to  $\vec{k}$ . The electric field amplitudes  $E_r$  and  $E_t$  of the reflected and transmitted light rays are connected to  $E_0$  by the coefficients  $r$  and  $t$  which can be calculated from the Fresnel equations. For the exemplary case of a light polarised perpendicular to the plane of incidence,  $r$  and  $t$  are [Hec74]

$$r_{\perp} = \left( \frac{E_r}{E_0} \right) = \frac{n_i \cos \theta_i - n_t \cos \theta_t}{n_i \cos \theta_i + n_t \cos \theta_t} \quad \text{and} \quad t_{\perp} = \left( \frac{E_t}{E_0} \right) = \frac{2n_i \cos \theta_i}{n_i \cos \theta_i + n_t \cos \theta_t}. \quad (5.1)$$

The intensity of the reflected light is determined by  $r_{\perp}^2$ . For normal incident and an single interface between air ( $n_i \approx 1$ ) and fused silica ( $n_t = 1.46$  [Mal65]) about  $r_{\perp}^2 = 3.5\%$  of the light is being reflected. This demonstrates that AR coatings are necessary in the KATRIN Raman system as otherwise 3.5% are lost at every surface of an optical component.

In order to calculate the intensity of the reflected and transmitted fractions of a light ray by a double layer, not only the primary reflection at the layer surface but also multiple reflections inside the layer have to be considered (figure 5.2, right). In this case, also the phase difference  $\delta = 2\pi n_2 d \cos(\theta_t)/\lambda$  [Lip97] between adjacent beams due to the internal

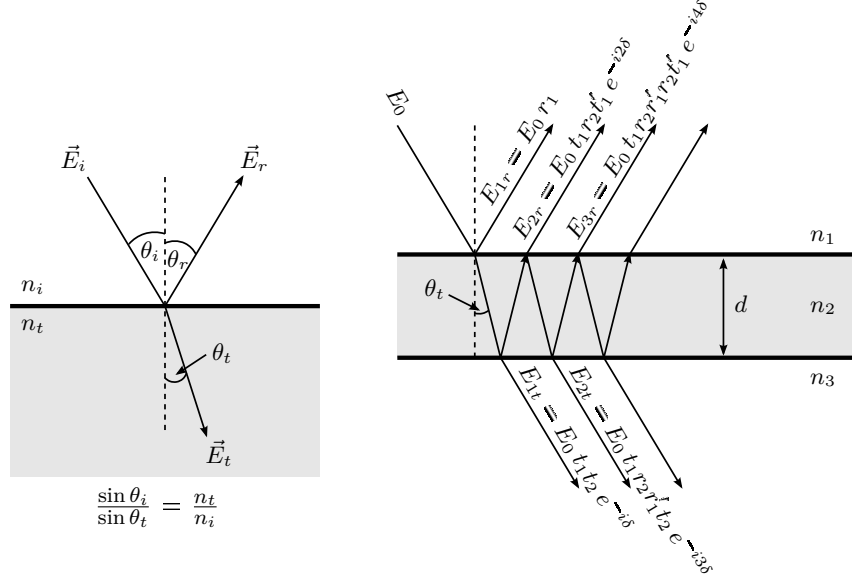


**Figure 5.2.: Snell's law and multiple reflections in a thin layer.** *Left:* Light ray at an interface between two transparent materials with refractive indices  $n_i$  and  $n_t$ . *Right:* Schematic path of light ray through a single layer ( $n_2$ ) deposited on a substrate ( $n_3$ ).  $r_i$  and  $t_i$  denote the amplitude reflection and transmission coefficients at surface  $i$ . The prime indicates that the interface is approached in opposite direction to the incident beam.  $\delta$  is the phase shift due to the passage through the layer  $n_2$ .

back-reflection has to be taken into account. The reflected light is a superposition of the different orders of multiple reflections which can be simplified to

$$E_r = E_{1r} + E_{2r} + E_{3r} + \dots = \left( \frac{r_1 + r_2 e^{-i2\delta}}{1 + r_1 r_2 e^{-i2\delta}} \right) E_0 \quad (5.2)$$

using the geometric expansion and the relations  $r = -r'$  and  $t_1 t_1' = 1 - r_1^2$  [Trä07]. As only intensities and not amplitudes are of relevance for measurements, the reflectance is calculated [Trä07]

$$R = \left( \frac{E_r}{E_0} \right)^2 = \frac{r_1^2 + 2r_1 r_2 \cos(2\delta_1) + r_2^2}{1 + 2r_1 r_2 \cos(2\delta_1) + r_1^2 r_2^2}. \quad (5.3)$$

This equation is sufficient to predict the intensity of the reflected light based on experimental parameters:  $\delta$  is determined from  $n_2$ ,  $\lambda$ ,  $d$ , and  $\theta_1$  ( $\theta_2$  is calculated from  $\theta_1$  via Snell's law).  $r_1$  and  $r_2$  can be calculated from the Fresnel equations (eq. (5.1)). In case of negligible light absorption the transmittance  $T$  can afterwards be calculated via  $R + T = 1$ .

For the special case of normal incidence ( $\theta_i = 0$ ) and a layer thickness such that  $n_2 d = \lambda/4$  is fulfilled a so-called quarter-wave coating is produced for which the reflectance  $R$  simplifies to

$$R = \left( \frac{n_2 n_0 - n_1^2}{n_2 n_0 + n_1^2} \right)^2. \quad (5.4)$$

If the refractive indices are also chosen such that  $n_2 n_0 - n_1^2 = 0$ , a vanishing reflectance is achieved for the chosen wavelength  $\lambda$ . This is an example for a simple anti-reflection (AR) coating which is optimised for a single wavelength. It will be demonstrated that the reflectance of a single layer can be tuned by a suitable choice of layer thickness and refractive indices. However, the availability of materials with the correct refractive index is limited and therefore a perfect match cannot be found in every case.

If the reflectance needs to be minimised over a broad spectral range, e.g. for broadband AR coatings as in the case of the Raman windows  $R_1$  and  $R_2$  of the LARA cell, or if a sharp rise of the reflectivity at a certain wavelength is desired, more than one layer is necessary. In such situations the calculation based on the procedure described before becomes extensive and other more sophisticated analytical or numerical methods are typically used. A detailed review of such methods and typical coating designs can be found in [Mac10].

### 5.1.2. Manufacturing methods of optical coatings

Optical coatings can be produced by additive and subtractive methods which again can be of physical or chemical nature [Pul99]. Subtractive methods are based on the removal or alteration of chemical constituents in the surface layer of the substrate material. Such techniques are not widely used for optical components and are therefore not further considered here. Additive methods are based on the deposition of the thin film material on the substrate. In chemical additive methods the coating is formed by chemical reactions of a precursor material near or on the surface to be coated. As the reaction product is solid it deposits on the surface and thus the coating is formed. Chemical Vapour deposition (CVD) is one specific chemical additive method widely used in the semi-conductor industry [Cho03].

Physical Vapour Deposition (PVD) is another branch of additive methods and of main interest in the following as all coatings employed in this work were manufactured by such methods. The general principle of PVD is based on three steps [Pul99]:

1. Evaporation of the coating material.
2. Transportation of the vaporised material towards the substrate to be coated.
3. Condensation of the vapour on the substrate followed by nucleation and film growth.

PVD methods are typically operated under vacuum conditions but depending on the specific method in varying vacuum regimes. The various methods are mainly distinguished by the way of vapour formation and the treatment of the growing thin film during the coating process. Selected PVD methods are compared in table 5.1 and more details can be found in [Pul99, Trä07, Ran96] and references therein. A typical kinetic energy of the vapour species can be attributed for each PVD method and a spread by about three orders of magnitude is found within the deposition methods compared in table 5.1. This has an impact on the density and porosity of the produced coating.

Electron-beam deposited (EBD) coatings which are produced by the thermal evaporation of the coating material have a very porous structure due to the low kinetic energy of the vapour species. If the deposited coating particles have a low mobility on the substrate surface, e.g. due to a high melting point of the coating material, a columnar structure is often found for EBD coatings [Dir77]. This is the case for most of the typically used dielectric materials for optical coatings apart from  $\text{SiO}_2$  which according to [Gue84] always forms a structureless film. The potential volumes between the columns are called voids and can be in contact to the atmosphere above the coating surface. This is an important aspect for the susceptibility of coatings to environmental conditions such as humidity, oxygen and potentially also tritium concentration. For metal oxide coatings like  $\text{SiO}_2$  also the stoichiometry is of interest, i.e. the oxidation state  $x$  of  $\text{SiO}_x$  calculated for a large statistical ensemble. Substoichiometric oxides ( $x < 2$ ) are often produced during the coating process due to the low chemical binding energies of the coating material (of the order of eV) in comparison to the kinetic energy of the particles that are impinging on the coating material during evaporation (e.g. electrons and ions with keV kinetic energy during electron beam evaporation and sputtering, respectively) [Pul99]. Substoichiometric oxides can be counteracted by reactive evaporation, i.e. the intentional release of oxygen into the coating chamber ( $p = 10^{-4}$  mbar) to enforce the oxidation close to or on the substrate surface [Pul99].

## 5.2. Coatings employed in the KATRIN Raman system and coating issues encountered

The coatings on transparent optical components in the Raman system are mostly anti-reflection (AR) coatings which were deposited by electron beam deposition (EBD). The only exceptions are the beam splitter (BS) and potentially the optics in the optical spectrometer which both will not be further considered here. Details on the coatings of interest are listed in table 5.2. The coatings of the LARA cell windows have in common that amorphous  $\text{SiO}_2$  is used as low-refractive material which also makes up the last layer of the coating stack.

EBD coatings have been chosen in the past because they have adequate optical properties (Reflectance  $R \leq 0.5\%$ ), are widely available on the market at low cost and because no severe issues were experienced in the past. The coating damage of the LARA cell windows during the first Raman measurements with highly purified circulating tritium gas [Stu10b, Fis11] was the first time that a severe damage was observed. These findings triggered the investigation of the coating durability in tritium atmosphere within this work. The aim of this task is to identify the cause of the experienced coating damage and to find optical coatings that can resist long-term operation in LOOPINO and the KATRIN inner loop. In parallel the setup and commissioning of the KATRIN Raman system was ongoing and coating issues during commissioning run C148 were experienced (described in chapter 4.6). All relevant coating issues are summarised and labelled in table 5.3 to serve as a starting point for the following discussion of harmful effects on dielectric coatings in glove box and tritium atmosphere.

**Table 5.1.: Comparison of selected physical vapour deposition coating manufacturing techniques.** Based on [Pul99, Trä07, Ran96] if not stated explicitly. The abbreviations in the parentheses will be used in the following.

	Thermal evaporation (EBD) <sup>□</sup>	Sputtering (MS) <sup>†</sup>	Ion beam sputtering (IBS)	Ion assisted deposition (IAD)
Method	Thermal evaporation by electrical (resistive) heating or by electron beam heating. Condensation of coating material on substrate.	Ejection of coating material by bombardment by ions. Ions produced by gas discharge or electrons on magnetron motion interacting with a working gas.	Ejection of coating material by bombardment by ions. Ions produced by plasma source directed onto target with coating material.	Vaporisation of coating material. Acceleration of ionised coating material towards substrate and/or ion bombardment of substrate during material deposition.
Energy <sup>‡</sup>	0.1 – 0.3 eV	1 – 10 eV	≤ 100 eV	10 – 100 eV
Pressure <sup>◊</sup>	10 <sup>-8</sup> – 10 <sup>-6</sup> mbar	10 <sup>-3</sup> – 10 <sup>-2</sup> mbar	10 <sup>-5</sup> – 10 <sup>-4</sup> mbar	10 <sup>-5</sup> – 10 <sup>-4</sup> mbar [Tar88]
Advantages	Pure thin films because of low pressure. Technique widely used in industry.	Denser coatings than for evaporation. Good resistivity against environmental effects.	Ultra-low loss coatings (absorption in ppm range) possible.	Dense coatings (even denser than bulk material).
Drawbacks	Porous structure due to voids and columnar film growth. Affected by environmental effects.	Higher impurity density due to high pressure working gas.	Deposition rate only 10% compared to sputtering or thermal evaporation.	

<sup>□</sup> Evaporation by electron beam heating is nowadays usually used. Therefore the term 'electron beam deposition' (EBD) will be used in the following.

<sup>†</sup> Magnetron sputtering (MS) is commonly used due to the increased sputtering efficiency.

<sup>‡</sup> Kinetic energy of vapour species before deposition.

<sup>◊</sup> Pressure in coating chamber during deposition process.

**Table 5.2.: Optical coatings on selected transparent components in the Raman system.** Listed are the windows of the LARA cell ( $L_i$  and  $R_i$ ), the Appendix windows ( $W_i$ ), and the transparent optical components in the beam path (generic label 'Optics'). All optics are coated on both sides by electron beam deposition (EBD). Both LASEROPTIK coatings consist of not more than five layers with a total thickness of less than 500 nm [Hän13].  $\text{SiO}_2$  is used in both coatings as low-refractive material.

Coating		Manufacturer, Type	Performance
	Description		
$L_1, L_2$	AR "V" coating for 532 nm	LASEROPTIK, B-05267 AR532nm/0° on UHV	$R < 0.3\%$
$R_1, R_2$	Broadband AR coating	LASEROPTIK, B-05272 AR450-700nm/0° on UHV	
$W_1, W_2$	AR "V" coating for 532 nm	CVI Melles Griot, <sup>◇</sup> W2-PW1-1525-C-532-0 <sup>†</sup>	$R \leq 0.25\%$ <sup>‡</sup>
$W_3$	Broadband AR coating	CVI Melles Griot, <sup>◇</sup> W2-PW1-1525-C-425675-0 <sup>†</sup>	$R_{\text{avg}} \leq 0.50\%$ <sup>‡</sup>
Optics	Broadband AR coating	Thorlabs, Coating code 'A' 350–700 nm	$R < 0.5\%$ [Tho14b]

<sup>◇</sup> Now IDEX Optics & Photonics (Albuquerque, NM, USA).

<sup>†</sup> Combined type number for window with AR coatings.

<sup>‡</sup> Per surface at 0° angle of incidence [CVI13]

**Table 5.3.: List of experienced optical coating damages at TLK.**

Label	Description	Involvement of		Surrounding medium	Potential cause	Reference
		Laser	Tritium			
D1	Extensive coating delamination on tritium facing sides of all cell windows	Yes	Yes	Tritium gas (200 mbar, > 90% purity, > $1.7 \cdot 10^7$ MBq/m <sup>3</sup> )	Formation of hydrofluoric acid due to PTFE component in LOOPINO	[Stu10b, Fis11], section 4.1
D2	Burnt spots and stripe-like feature on LARA cell windows L <sub>1</sub> and L <sub>2</sub>	Yes	(Yes)	Glove box atmosphere (1 bar, > 96% nitrogen, < 4% oxygen, < 2 MBq/m <sup>3</sup> tritium)	Spot: Laser-induced damage threshold exceeded Stripe: Unclear	Section 4.6.3
D3	Spots on all optics after burning of PVC by laser irradiation	Yes	No	Lab atmosphere	Laser-induced surface contamination with organic species	Section 4.6.3
D4	'Stars+stripe' features on LARA cell windows L <sub>1</sub> and L <sub>2</sub>	Yes	No	Lab atmosphere	Unclear	Section 4.6.3

### 5.3. Harmful effects on coatings in glove box and tritium environments

This section gives an overview of harmful effects on optical coatings that can occur in glove boxes and tritium bearing systems. After a description of each effect, their relevance for the experienced coating damages is discussed. Amorphous  $\text{SiO}_2$ , also called fused silica, is commonly used in the coatings relevant for this work. Especially since the most upper layer of the AR coatings is made of amorphous  $\text{SiO}_2$  to match the refractive indices of air/vacuum this material will be of special interest.

Amorphous  $\text{SiO}_2$  consists of  $\text{SiO}_4$  tetrahedrons which are organised such that rings with alternating O and Si atoms are formed (figure 5.3). A ring consists of a least three Si and O atoms each [Dev94]. Within a tetrahedron the O-Si-O angle is  $109.5^\circ$  while within a ring Si-O-Si angles between  $120^\circ$  and  $128^\circ$  can be encountered [Dev94].

An extensive review of harmful effects on amorphous  $\text{SiO}_2$  has been compiled by K. Schönung [Sch11d]. Therefore only the most relevant or not yet covered aspects will be discussed in the following.

#### 5.3.1. Radiation-induced densification

Irradiation of amorphous  $\text{SiO}_2$  can alter the microscopic structure but also the macroscopic properties of the material. The O/Si ratio  $x$  in amorphous  $\text{SiO}_x$  was measured by Pitts and Czanderna after the irradiation with 2–8 keV electrons. Values of  $x = 0.91$  to  $x = 0.63$ , i.e. deviations from the nominal value  $x = 2$ , were found depending on the electron energy and irradiation time [Pit86]. R.A.B. Devine reports the formation of point defects and a densification of amorphous  $\text{SiO}_2$  due to irradiation [Dev94]. The densification saturates at a value of about 3% when depositing  $6 \cdot 10^{26} \text{ eV/cm}^3$  by ionisation [Dev94]. Buscarino et al. report a saturation of the densification at about 4% for a dose of  $1.3 \cdot 10^{11} \text{ Gy}$  of 2.5 MeV electrons [Bus09]. The 3–4% densification is accompanied

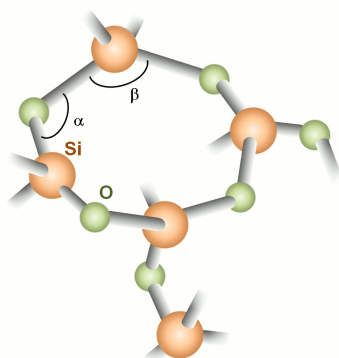


**Figure 5.3.: Schematic drawing of microscopic structure of amorphous  $\text{SiO}_2$ .** Inside a tetrahedron a Si-O-Si angle of  $\alpha = 109.5^\circ$  is realised. The O-Si-O angle  $\beta$  varies between  $120^\circ$  and  $128^\circ$ . Image from [Sch11d]

by an about 1% increase of the refractive index and changes in the microscopic ring structures of amorphous SiO<sub>2</sub> [Dev94]. Such structural changes were also observed by Raman spectroscopy [Boi03]. The densification was also explicitly observed for irradiation with 18 keV electrons by Norris and EerNisse [Nor74], i.e. for the exact energy range that is also relevant for KATRIN. Although the radiation-induced densification effect is on first glance a negative effect, it is nowadays also intentionally exploited during thin film deposition: In the ion assisted deposition (IAD) process, the substrate is bombarded by ions to increase the density of the thin films.

Two questions have to be answered in order to evaluate the impact of the densification effect on the optical coatings of the LARA cell windows:

- What irradiation dose do the window coatings of the LARA cell experience during normal operation and how large is it in comparison to the doses reported by R.A.B Devine ( $6 \cdot 10^{26}$  eV/cm<sup>3</sup>) and Buscarino et al. ( $1.3 \cdot 10^{11}$  Gy)?
- How does a 1% change of the refractive index in the coating affect the Raman measurements?

The calculation of the radiation dose the LARA cell windows are exposed to during a 60 days long operation in the KATRIN inner loop was started in [Sch11d]. A final answer could not be given because the penetration depth of the electrons into the coating material was not known. The penetration depth  $R$  of electrons into a solid material can be calculated by the Kanaya-Okayama formula [Kan72]

$$R = \frac{0.0276 \cdot \left(\frac{A}{\text{g/mol}}\right) \cdot \left(\frac{E}{\text{keV}}\right)^{5/3}}{Z^{8/9} \left(\frac{\rho}{\text{g/cm}^3}\right)} \mu\text{m} \quad (5.5)$$

where  $A$  is the atomic weight,  $E$  the kinetic energy of the electron,  $Z$  the atomic number and  $\rho$  the density of the solid. For SiO<sub>2</sub> ( $\rho = 2.2$  g/cm<sup>3</sup>,  $A_{\text{Si}} = 28$ ,  $Z_{\text{Si}} = 14$ ,  $A_{\text{O}} = 16$ ,  $Z_{\text{O}} = 8$  [Ber12]) a penetration depth of  $R(\text{Si}) = 612$  nm and  $R(\text{O}) = 575$  nm is found. For high-refractive coating materials as HfO<sub>2</sub> and Nb<sub>2</sub>O<sub>5</sub> the penetration depth decreases down to about 130 nm. The AR coatings B-05267 and B-05272 which are applied on the windows of the LARA cell consist of SiO<sub>2</sub> as low-refractive material, have less than five coating layers, and are thinner than 500 nm [Hän13]. Therefore it can reasonably be assumed that at least the most upper SiO<sub>2</sub> layer is fully exposed to the electron irradiation. The second coating layer however might fully absorb the electrons and hence protect the underlying layers from irradiation since it is made of a high refractive and hence strongly electron-absorbing material. Nevertheless, a definitive answer cannot be given as the layer thicknesses are not known. Therefore, for the dose estimation it is conservatively assumed that the electrons are absorbed within  $d = 100 - 500$  nm. Using the formalism developed in [Sch11d], the radiation dose the windows experience within 60 days is estimated to be  $D_{100} = 2.7 \cdot 10^9$  Gy in case of  $d = 100$  nm and  $D_{500} = 5.4 \cdot 10^8$  Gy for  $d = 500$  nm. Devine reported an energy of  $6 \cdot 10^{26}$  eV/cm<sup>3</sup> to be deposited by ionisation. This energy can be converted into a dose by division by the density  $\rho$  of SiO<sub>2</sub> yielding

$$D = \frac{6 \cdot 10^{26} \text{ eV/cm}^3}{2.2 \text{ g/cm}^3} = 4.4 \cdot 10^{10} \text{ Gy} \quad (5.6)$$

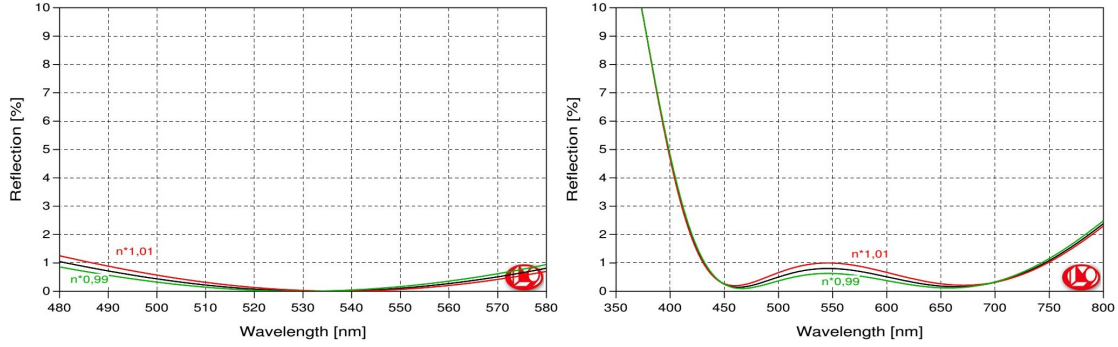


**Figure 5.4.: Effect of  $\pm 1\%$  refractive index variation of the first coating layer on the reflectance  $R$  of the AR coating.** The thicknesses of the coating layers were kept constant. *Left:* AR coating B-05267. The variation of the reflectance is negligible for the laser wavelength 532 nm. *Right:* AR coating B-05272. The reflectance varies by  $< 45\%$  in the spectral range of the  $Q_1$  branches of the hydrogen isotopologues (612–683 nm). Calculation and plots: Courtesy of LASEROPTIK.

which corresponds to about 30% of the value reported by Buscarino et al.. Thus, independent of the actual value of  $d$ , the saturation of the densification effect cannot be reached within a single 60 days operation period. However, the  $D_{100}$  and  $D_{500}$  doses are in the range that was investigated in [Nor74] where already a densification by up to 0.3% was measured. Within the expected KATRIN measurement time of three years and assuming  $d = 100$  nm, a dose of  $D = 4.9 \cdot 10^{10}$  [Sch11d] will be accumulated and hence the saturation of the densification effect might already be reached. Therefore, the densification effect is of relevance for the tritium facing AR coatings on the LARA cell windows and hence its effect on the Raman measurements must be estimated.

The effect of a refractive index variation  $\delta n$  was calculated by the coating manufacturer for the extreme case of  $\delta n/n = +1\%$  assuming that only the most upper layer is affected (figure 5.4). The coating layer thickness was kept constant in the calculation. Typically a reduction of the thickness occurs simultaneously and thereby partly counteracts the effect of the refractive index increase [Hän13]. The following results therefore must be considered as upper-limit. The variation of the reflectance is negligible for the B-05267 coating which is optimised for the laser wavelength. The variables (e.g. coating reflectance, Raman intensities, etc.) will be labelled in the following with the indices '0' and '+1%' to indicate if they are valid for the initial state or for the case of densified coating. For the broadband AR coating B-05272 which is applied on the Raman windows of the LARA cell a relative variation of the reflectance  $R$  of up to  $R_{+1\%}/R_0 - 1 = 43\%$  is found within the spectral region covered by the  $Q_1$  branches of the hydrogen isotopologues (612–683 nm). Using the absolute Raman intensities from an example spectrum (acquired within run C148 during the commissioning of the KATRIN Raman system; see section 4.6.2), the impact of the reflectance variation is propagated to the relative Raman intensities in two steps:

1. The absolute Raman intensities  $I_{\text{abs}}$  are calculated for the case of a densified coating ( $n_{+1\%}$ ) scenario from the absolute Raman intensities of the exemplary spectrum

using the ratio  $R_{+1\%}/R_0$  as scaling factor, i.e.

$$I_{\text{abs},n_{+1\%}} = \frac{R_{+1\%}}{R_0} \cdot I_{\text{abs},n_0}. \quad (5.7)$$

2. The relative Raman intensities  $I_{\text{rel},n_{+1\%}}$  of the hydrogen isotopologues are calculated for the  $n_{+1\%}$  scenario in the usual way, e.g. for  $T_2$  according to

$$I_{\text{rel},n_{+1\%},T_2} = \frac{I_{\text{abs},n_{+1\%},T_2}}{\sum_i I_{\text{abs},n_{+1\%},i}} \quad i = T_2, DT, D_2, HT, HD, H_2. \quad (5.8)$$

The results of the calculation are shown in table 5.4 where relative variations in the range of -0.26% to 7.02% are found for the relative Raman intensities.  $T_2$ , the most abundant gas constituent, is moderately affected (relative variation of -0.26%) while the other isotopologues experience already shifts in the low percentage range. This effect is exactly of the same order as the systematic uncertainty caused by the measurement uncertainty of the response functions [Sch13b]. However, it has to be kept in mind that the presented calculation is an upper estimate for the densification effect since the layer thickness was kept constant. The simultaneous reduction of the layer thickness that was not considered here will partly counteract the effect and hence reduce the variation of the relative intensities. Therefore, the influence of radiation-induced densification may or may not be relevant for the KATRIN Raman system. Certainly, the evolution of the window transmission should be monitored during long-term measurements with high-purity tritium.

**Table 5.4.: Influence of a +1% variation of the refractive index  $n$  in the first coating layer on the relative Raman intensities  $I_{\text{rel}}$ .** Abbreviations:  $R$  - Reflectance at the wavelength of the hydrogen isotopologue  $Q_1$  branch (from figure 5.4),  $Q(x) = x_{+1\%}/x_0$  - Ratio of the quantity  $x$  for the two cases of refractive index (initial and after densification),  $I_{\text{abs}}$  - absolute Raman intensity,  $I_{\text{rel}}$  - relative Raman intensity.

	R		$Q(R)$	$I_{\text{abs}}$		$I_{\text{rel}}$		$Q(I_{\text{rel}}) - 1$ (%)
	$n_0$ (%)	$n_{+1\%}$ (%)		$n_0$	$n_{+1\%}$	$n_0$	$n_{+1\%}$	
$T_2$	0.411	0.549	1.336	$1.6 \cdot 10^6$	2138295	0.9365	0.9340	-0.26
DT	0.333	0.456	1.369	69233	94806	0.0405	0.0414	2.25
$D_2$	0.265	0.373	1.408	2909	4095	0.00170	0.00179	5.10
HT	0.180	0.258	1.433	34939	50079	0.0204	0.0219	7.02
HD	0.163	0.228	1.399	1502	2101	$8.79 \cdot 10^{-4}$	$9.18 \cdot 10^{-4}$	4.44
$H_2$	0.197	0.228	1.157	0	0	0	0	0

### 5.3.2. Vacuum, hydrogen, and water moisture-related effects

The pressure regime in which an optical coating is operated at can have a significant influence on its optical properties and durability. Jensen et al. observed a 50% drop of the laser-induced damage threshold (LIDT) of EBD coated windows and a spectral shift of the transmittance maxima and minima by 5% when operating the coatings at vacuum conditions ( $5 \cdot 10^{-6}$  mbar) [Jen06]. Dense coatings deposited by IAD and IBS were not affected. Similar findings are reported in [Rie08, Ngu11]. Wagner et al. showed that evaporated thin films have an increased susceptibility for continuous hydrogen uptake in comparison to films produced by IAD [Wag89]. The porous structure of EBD coatings is attributed as the key property for the explanation of the experienced behaviour: Water and hydrogen that was stored in the porous EBD coatings will start to evaporate during evacuation and the O/Si ratio  $x$  of the  $\text{SiO}_x$  coating decreases. Both processes alter the physical and optical properties of the coating and increase the coating internal tensile stress which in total leads to a decrease of the LIDT [Jen06, Rie08, Ngu11, Bac97].

Tritium systems as the KATRIN inner loop are operated below atmospheric pressure (150–200 mbar, <1 mbar during evacuation) and at negligible oxygen concentrations. The glove boxes encapsulating the tritium systems are operated at atmospheric pressure but at a reduced oxygen concentration of <4% and a water concentration in the ppm range. Therefore the discussed effects can be of relevance for both the LARA cell windows and the Appendix windows. The permanent damage of the LARA cell laser windows (damage scenario D2) could reasonably be explained by the doubling of the laser power density due to the double pass configuration in LARA3 and by a decrease of the LIDT due to the glove box environment. A definite proof cannot be given here as LIDT measurements inside the glove box could not be performed due to the limited number of LARA cell windows. The stripe-like deposit on the windows on the laser windows which was also found in the damage scenario D2 is not related to this effect.

### 5.3.3. Laser-induced contamination

If organic species are outgassing in a sealed laser system, optical components in the system can become 'contaminated' due to the deposition of the outgassing species on their surface. At the positions where the optical components are irradiated by laser light (ranging from 157 nm to  $1\mu\text{m}$ ) the formation of a carbon-based deposit was regularly experienced [Hov94, Kun00, Tig08, Can05]. As a consequence, a severe decrease of the transmitted laser power occurred which led up to the complete failure of the laser system [Hov94, Can05]. Such processes are commonly referred to as laser-induced contamination.

Components in the laser system that contain silicones and aromatic hydrocarbons have been identified to strongly trigger the laser-induced contamination while the presence of certain epoxies and saturated hydrocarbons, incl. acetone and isopropyl alcohol, did not cause any effect [Hov94, Hov95, Hov96, Kun00]. Interestingly, the effect occurs predominantly under vacuum conditions and in nitrogen atmosphere while an oxygen concentration in the ppm range is sufficient to mostly prevent the effect [Tig08, Hov94,

Kun00, Hov96]. It was also shown that an already existing laser-induced contamination can be reversed by the inlet of oxygen [Tig08, Cho00].

The laser system can be operated for several hours before the first indication for a laser-induced contamination becomes apparent but afterwards a nearly instantaneous growth occurs [Hov94, Bec05, Bec06] which is accompanied by a rise of the local temperature on the optics [Bec06]. The formation process of laser-induced contamination is not yet fully understood but photochemical reactions of the outgassing species on the surface of the optical component are most likely starting the process [Hov94, Hov96]. After initiation also thermal processes are likely to occur as the emission of non-laser light was observed [Hov94].

Laser-induced contamination was found to be negligible on dense coating, e.g. produced by ion beam sputtering, while regularly occurring on the porous coatings produced by electron-beam deposition [Bec06]. This is most likely related to the increased susceptibility of the porous coatings surface to adsorb the gaseous contaminants which seems to be necessary to initiate the damage formation. Similar to the contamination formation process, also the role of oxygen is not yet solved. Several mechanisms are in general possible:

- The porous coating gets oxygen depleted when operated in the oxygen-poor environments as vacuum or nitrogen gas which again increases the concentration of defects in the coating.
- The deposited contaminant species are in an excited state which is necessary for the subsequent formation of the laser-induced contamination. Oxygen quenches the excited states and hence prevents further damage.
- The deposited contaminant species are oxidised and hence form volatile species such as CO<sub>2</sub>. In the case of UV lasers also the formation of ozone and atomic oxygen which are both chemically very aggressive has to be considered.

The cleaning of organically contaminated optics by a combined treatment with UV light and ozone is widely used and reviewed by J.R. Vig [Vig85].

Laser-induced contamination can unambiguously explain the formation of spots on all optical components of the Raman system in the commissioning run C148 after the burning of PVC by the laser beam (damage D3, table 5.3). In this case also the presence of oxygen in the system could not prevent the spot formation due to the presumable large concentration of evaporated and degenerated PVC. Similar effects were also found by Hovis et al. for contaminant concentrations in the 10<sup>-3</sup> range [Hov94]. Also the formation of the spot and stripe shaped features on the LARA cell inside the glove box (damage D2) but also outside the glove box (damage D4) seems to be related to laser-induced contamination since the features could be easily and residue-free removed by cleaning with isopropyl alcohol or ethanol.

The feasibility of a UV and ozone treatment of LARA cell windows is currently being investigated. In a first proof-of-principle experiment it could be shown that a spot on the LARA cell window can be removed by UV irradiation (figure 5.5). A currently ongoing bachelor thesis [Wec14] further investigates this method with the aim to optimise

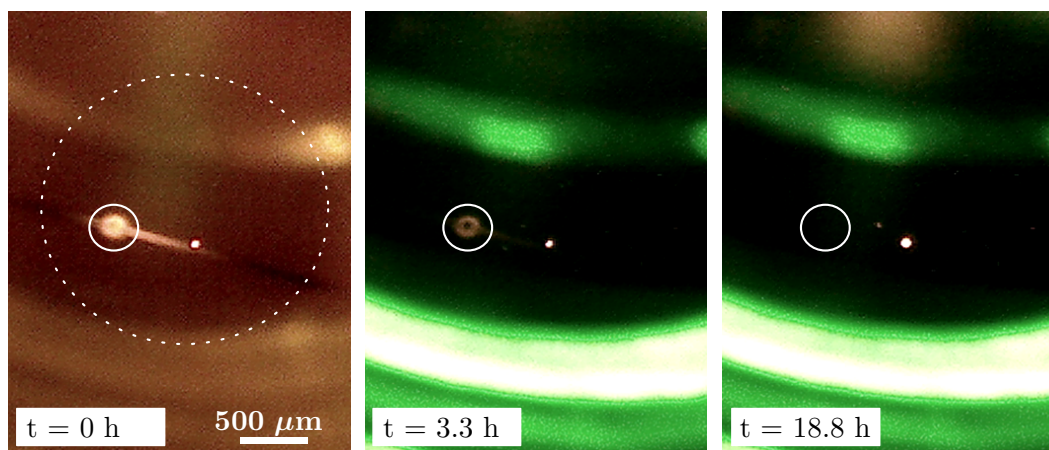


**Figure 5.5.: Removal of laser-induced contamination on a LARA cell window (Coating damage D4) by UV irradiation.** A mercury-vapour lamp was used as light source ( $\lambda = 184.9 \text{ nm}, 253.7 \text{ nm}, 365.0 \text{ nm}$ ). The pictures were taken with a microscope focused on the window surface. A spot-shaped (indicated by solid circle) and a stripe-like laser-induced contamination feature are visible as well as a permanent coating damage (white spot). The window was exposed to 532 nm laser light (approximate beam diameter indicated by dashed circle) during picture acquisition to increase the visibility of the features. The first picture was taken with laser protection glasses placed in front of the microscope to make the non-532 nm emission of the features visible. Despite of a laser power increase (visible by the increased brightness of the permanent coating damage) no indications for both laser-induced contamination features could be found after 18.8 hours of UV irradiation. Pictures: Courtesy of T. James.

the employed hardware and to determine if regular UV irradiation is necessary for a permanent suppression of spot formation on the LARA cell windows.

### 5.3.4. Formation of tritiated hydrogen fluoride species

Polymers and especially polytetrafluoroethylene (PTFE, also known as Teflon<sup>®</sup>) tend to degrade in the presence of tritium gas due to radio-chemical reactions that are triggered by the energy released in  $\beta$ -decay [Par71, Cla06, Cla07, Dep07]. The degradation deteriorates the mechanical properties of the polymer [Hed69] and hence can lead to the failure of the component. Therefore, polymers have to be avoided in tritium systems as much as possible. When chlorofluorocarbon polymers, e.g. PTFE or polyvinyl chloride (PVC), are exposed to tritium gas, corrosive gaseous species such as HF, HCl and their isotopologues can be produced [Dol78, Cla06, Cla07]. These can harm other components in the tritium system especially when water is present in the system and corresponding acid (e.g. hydrofluoric acid) is formed. Hydrogen fluoride in particular can dissolve fused silica under the formation of silicone tetrafluoride [Aig00]



and hence attack optical coatings. The same reaction can also occur for TF. Due the identification of the PTFE containing regulation valve in LOOPIONO (section 4.6.1),

the formation of hydrofluoric acids is thought to be a reasonable explanation of the severe coating damage D1 (table 5.3). After the replacement of the regulation valve by a full-metal version, no coating damage was observed since then.

In order to determine if hydrogen fluoride was present in LOOPINO when the coatings were damaged [Stu10b, Fis11], selected Raman spectra of the run are qualitatively re-analysed. The aim of this work is to check for Raman lines that can be attributed to the diatomic molecules HF, DF or TF. The analysis is done in three steps:

- determination of laser wavelength,
- calculation of Raman shifts for HF, DF, and TF using molecular constants, and
- search for HF, DF, and TF lines and branches in the Raman spectrum.

The wavelength of the laser (Coherent Verdi V5) used in 2010 in the Raman measurements at the LOOPINO facility [Stu10b, Fis11] was due to the absence of a wavemeter not accurately known; this leads to an uncertainty when identifying unassigned lines in the Raman spectrum. Therefore, the laser wavelength is now determined using the line position (measured in nm) and the known Raman shift of lines and branches in the Raman spectrum. 32 line positions are determined by fitting and could be assigned to Raman transitions of hydrogen isotopologues and tritiated methane species (table 5.5). Note that the refractive index of air is not taken into account.

The vacuum laser wavelength  $\lambda_{\text{laser}}$  is determined by fitting the measured Raman line positions  $\lambda$  with the function  $\lambda = (1/\lambda_{\text{laser}} - \Delta\tilde{\nu})^{-1}$  that can be easily deduced from eq. (3.3). The data and the fit are shown in figure 5.6 (left). Depending on the choice which Raman lines are considered in the fit (all 32 lines; only  $S_0$  lines; only  $O_1$ ,  $Q_1$ ,  $S_1$  lines), a shift of  $\lambda_{\text{laser}}$  is present (figure 5.6, right) which is of the same order or even larger than the uncertainty of  $\lambda_{\text{laser}}$  stemming directly from the fit. The vacuum laser wavelength when considering all 32 spectral lines is therefore

$$\lambda_{\text{laser}} = 532.00 \text{ nm} \pm 0.04 \text{ nm}(\text{fit}) \pm 0.09 \text{ nm}(\text{syst.}) \quad (5.10)$$

where the systematic uncertainty was set as half of the shift between the ' $S_0$  only' and ' $O_1$ ,  $Q_1$ ,  $S_1$  only' data sets.

The Raman shifts of HF, DF and TF were calculated for the various Raman branches according to

$$S_0 \text{ branch : } \Delta\tilde{\nu}(J'') = T(0, J'') - T(0, J'' - 2) \quad (5.11)$$

$$O_1 \text{ branch : } \Delta\tilde{\nu}(J'') = T(1, J'') - T(0, J'' + 2) \quad (5.12)$$

$$Q_1 \text{ branch : } \Delta\tilde{\nu}(J'') = T(1, J'') - T(0, J'') \quad (5.13)$$

$$S_1 \text{ branch : } \Delta\tilde{\nu}(J'') = T(1, J'') - T(0, J'' - 2) \quad (5.14)$$

using the molecular constants taken from [Mül98] and eq. (3.17) to calculate the term values  $T(v, J'')$ . The calculations were performed using the software developed by S. Mirz who also investigated the accuracy of the Raman shift calculation using the line positions of  $H_2$  and  $D_2$  [Mir14]. The relative difference of the line positions to the reference data was found to be  $<0.2\%$  for Raman lines with  $J'' \leq 5$  which is sufficient for the present

**Table 5.5.:** Wavelength (in air) of Raman lines  $\lambda$  determined by peak fitting in Raman spectra (fit uncertainty  $\delta$ ) and Raman shifts  $\Delta\tilde{\nu}_{\text{lit}}$  taken from [Stu10b, Eng92, Eng97]. For the Q<sub>1</sub> branches that cannot be resolved here, an effective Raman shift is stated which considers the convolution of the individual Raman lines.

$\lambda$ nm	$\delta$ nm	Molecule	Transition	$\Delta\tilde{\nu}$ cm <sup>-1</sup>
536.05	0.10	DT	S <sub>0</sub> ( $J'' = 0$ )	145.73
537.438	0.003	T <sub>2</sub>	S <sub>0</sub> ( $J'' = 1$ )	199.69
538.72	0.05	HT	S <sub>0</sub> ( $J'' = 0$ )	241.00
		DT	S <sub>0</sub> ( $J'' = 1$ )	
539.771	0.010	T <sub>2</sub>	S <sub>0</sub> ( $J'' = 2$ )	278.73
542.109	0.005	T <sub>2</sub>	S <sub>0</sub> ( $J'' = 3$ )	356.95
543.35	0.07	HT	S <sub>0</sub> ( $J'' = 1$ )	397.71
544.45	0.02	T <sub>2</sub>	S <sub>0</sub> ( $J'' = 4$ )	434.12
546.70	0.02	T <sub>2</sub>	S <sub>0</sub> ( $J'' = 5$ )	510.02
547.96	0.17	HT	S <sub>0</sub> ( $J'' = 2$ )	553.43
549.11	0.18	T <sub>2</sub>	S <sub>0</sub> ( $J'' = 6$ )	584.45
551.2	0.2	T <sub>2</sub>	S <sub>0</sub> ( $J'' = 7$ )	657.21
552.6	0.9	HT	S <sub>0</sub> ( $J'' = 3$ )	705.87
553	8	T <sub>2</sub>	S <sub>0</sub> ( $J'' = 8$ )	728.11
556	2	T <sub>2</sub>	S <sub>0</sub> ( $J'' = 9$ )	796.98
557	2	HT	S <sub>0</sub> ( $J'' = 4$ )	854.21
599.0	0.5	T <sub>2</sub>	O <sub>1</sub> ( $J'' = 5$ )	2093.19
602.1	0.2	T <sub>2</sub>	O <sub>1</sub> ( $J'' = 4$ )	2178.63
603.90	0.14	CDT <sub>3</sub>	$\nu_3$	2225.00
605.04	0.07	T <sub>2</sub>	O <sub>1</sub> ( $J'' = 3$ )	2262.14
607.97	0.19	T <sub>2</sub>	O <sub>1</sub> ( $J'' = 2$ )	2343.93
612.582	0.011	T <sub>2</sub>	Q <sub>1</sub> (eff)	2462.00
616.89	0.14	T <sub>2</sub>	S <sub>1</sub> ( $J'' = 0$ )	2580.87
619.75	0.03	T <sub>2</sub>	S <sub>1</sub> ( $J'' = 1$ )	2657.03
622.81	0.02	T <sub>2</sub>	S <sub>1</sub> ( $J'' = 2$ )	2737.00
		DT	Q <sub>1</sub> (eff)	
625.4	0.1	T <sub>2</sub>	S <sub>1</sub> ( $J'' = 3$ )	2803.94
628.2	0.3	T <sub>2</sub>	S <sub>1</sub> ( $J'' = 4$ )	2874.28
630.8	0.3	T <sub>2</sub>	S <sub>1</sub> ( $J'' = 5$ )	2942.29
632.5	0.5	CH <sub>3</sub> T	$\nu_3$	2983.00
635.9	1.0	T <sub>2</sub>	S <sub>1</sub> ( $J'' = 7$ )	3070.51
650.74	0.03	HT	Q <sub>1</sub> (eff)	3440.00
660.7	1.2	HT	S <sub>1</sub> ( $J'' = 0$ )	3675.26
667.5	0.7	HT	S <sub>1</sub> ( $J'' = 1$ )	3823.31

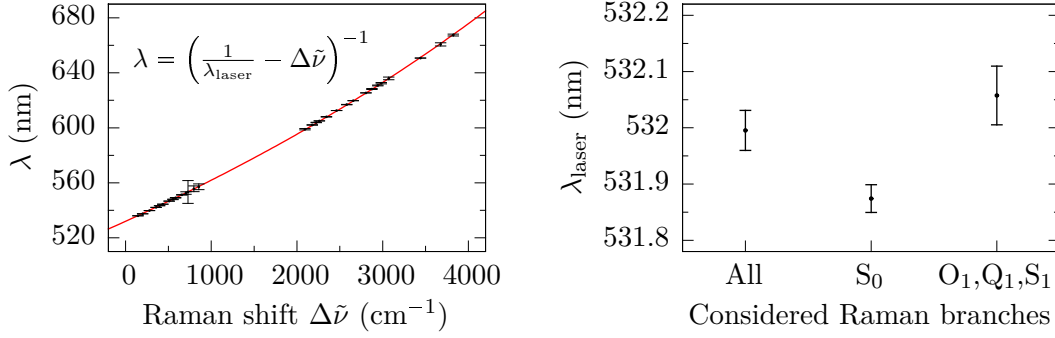


**Figure 5.6.: Determination of vacuum laser wavelength  $\lambda_{\text{laser}}$ .** *Left:* Fit of measured Raman line position  $\lambda$  as a function of Raman shift  $\Delta\tilde{\nu}$ . *Right:* Systematic shift of  $\lambda_{\text{laser}}$  depending on the choice which Raman lines are considered in the fit. The error bars indicate the uncertainty of  $\lambda_{\text{laser}}$  stemming from the fit.

application. The resulting Raman shifts are listed in table 5.6 and also indicated in the Raman spectrum (figure 5.7). No indication for TF is found in the spectrum because of an overlap of the TF  $Q_1$  branch with the  $T_2$   $Q_1$  branch that dominates the spectrum. Also for DF and HF which are assumed to be less abundant than TF in the gas mixture no indications can be found.

**Table 5.6.: Calculated Raman shifts of HF, DF, and TF.** For details see main text.

Raman branch	$\Delta v$	$\Delta J$	$J''$	Raman shift ( $\text{cm}^{-1}$ )		
				HF	DF	TF
$S_0$	0	2	0	123.4	65.1	41.5
	0	2	1	205.6	108.5	69.2
	0	2	2	287.8	151.8	96.8
$O_1$	1	-2	4	3666.1	2753.1	2345.7
	1	-2	3	3751.4	2797.6	2374.0
	1	-2	2	3835.2	2841.6	2402.0
$Q_1$	1	0	0	3958.5	2906.7	2443.5
	1	0	1	3957.0	2906.1	2443.2
	1	0	2	3953.9	2904.9	2442.5
	1	0	3	3949.3	2903.1	2441.4
$S_1$	1	0	4	3943.1	2900.8	2440.0
	1	2	0	4077.3	2970.0	2484.0
	1	2	1	4154.8	3011.6	2510.6
	1	2	2	4230.8	3052.6	2536.8

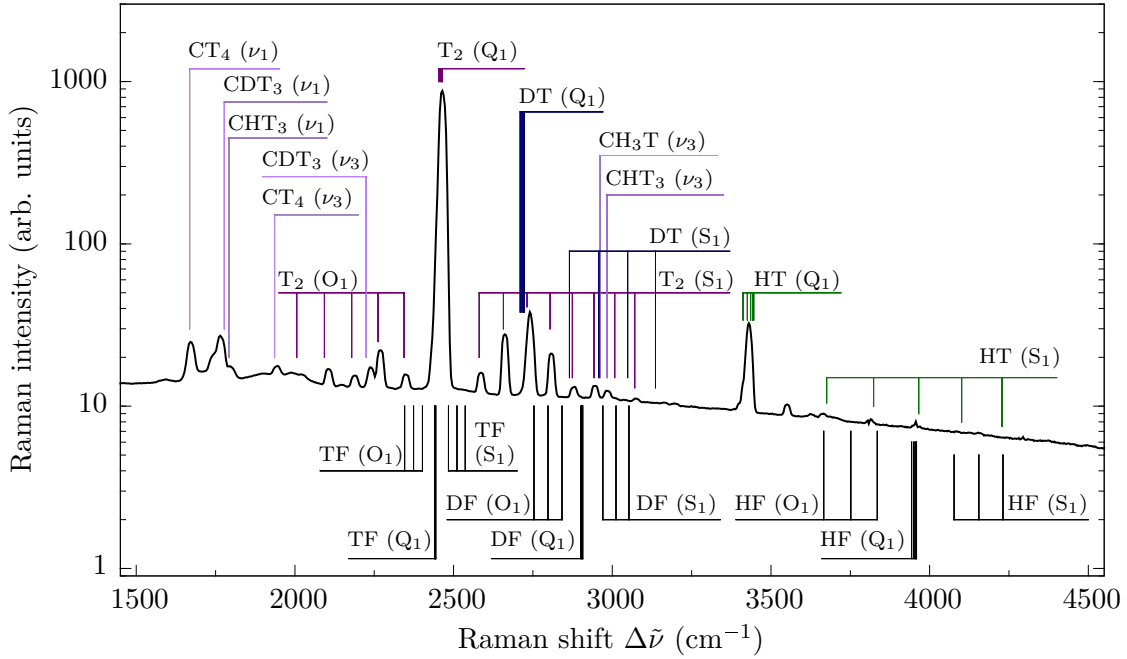


**Figure 5.7.: Raman spectrum with calculated HF, DT, TF line positions.** Measured spectrum of tritium gas mixture with identified Raman lines and branches of hydrogen isotopologues and tritiated methane species. 25 Raman spectra were averaged for noise reduction. The calculated line positions of the  $O_1$ ,  $Q_1$  and  $S_1$  branches of HF, DF and TF are shown for comparison. No indications for HF, DF, and TF are visible in the spectrum. For consistency, the first five lines are shown for each  $Q_1$  branch.

### 5.3.5. Conclusions

Several harmful effects have been discussed that can occur to optical coatings when being operated in glove boxes or tritium bearing systems. These effects have been evaluated with respect to their relevance for the long-term operation of the Raman system during KATRIN neutrino mass measurements. Furthermore, the suitability of each harmful effect to explain the experienced coating damages D1-D4 has been discussed. The following conclusions can be drawn:

- The radiation-induced densification of the  $\text{SiO}_2$  layer in the coating is expected to reach the saturation value of 3-4% if one batch of LARA cell windows is used over the complete course of the expected KATRIN operation. An upper estimate was determined for the impact of such a densification on the accuracy of the relative Raman intensities. The densification could cause a shift of the relative Raman intensities of the same magnitude as the systematic uncertainty due to the measurement uncertainty of the response function which are needed to convert the relative Raman intensities into molar fractions, i.e. concentration values. In reality, this effect is assumed to be less significant as also the thickness of the coating layers will reduce while being densified and hence counteract the effect. Therefore, this effect is currently not be considered to be of relevance.

- The permanent coating damage D2 could partly be caused by a drop of the LIDT due to the glove box environment. A unambiguous experimental verification is currently not possible. A reduction of the laser power was already suggested in section 4.7, although for other reasons. Therefore, a repeated coating damage should be prevented. However, this issue should be considered in the future.
- Laser-induced contamination was experienced within this work (damage D3) after the evaporation of PVC due to the LARA cell window damage D2. Also the appearance of spot and stripe shaped features on the LARA cell laser windows (damage scenario D4) seems to be related to this effect although the contamination source is not yet found. Two countermeasures are currently being explored. (i) The enclosure of the KATRIN Raman system will be covered with aluminium sheets to prevent PVC evaporation in case of a beam displacement or reflection. (ii) Cleaning of optical components after laser-induced contamination by UV light exposure and ozone formation or even the prevention of laser-induced contamination by these means is currently being investigated in a ongoing bachelor thesis [Wec14].
- Formation of tritium fluoride (TF) inside LOOPINO due to radiochemical reactions of tritium with a PTFE component in the regulation valve is most likely the reason for the experienced coating damage D1. The corrosive HF, DF, and TF species could not be identified in the Raman spectrum due to the overlapping Raman lines and branches of the hydrogen isotopologues. Nevertheless, clear evidence for radiochemical processes and hence the formation of TF was found by the observation of a yellowish discolouration of the valve seat of the regulation valve that was removed from LOOPINO and dismantled (section 4.6.1 and figure 4.22).
- Optical coatings produced by electron beam deposition (EBD) have a porous structure in comparison to coatings produced by the more energetic coating processes ion assisted deposition (IAD), magnetron sputtering (MS) and ion beam sputtering (IBS). During the literature review performed within the present discussion of harmful effects, the conclusion that dense coatings are less affected by harmful effects than EBD coatings was found throughout. Because the stability of the optical coatings is crucial for the reliable operation of the KATRIN Raman system, IAD, MS, and IBS coatings should therefore be considered as promising candidates for an upgraded coating scheme in the KATRIN Raman system.

#### **5.4. Durability test of optical coatings in highly purified tritium gas**

This section describes a durability test of optical coatings produced by different deposition methods which were intentionally exposed to highly purified tritium gas for 39 days. The aim of this test was to experimentally verify that dense optical coatings are more resistant against tritium in comparison to the currently employed coatings based on electron beam deposition. The tritium exposure of the coating samples was realised such that the conditions in the KATRIN inner loop were mostly reproduced, i.e. 150-200 mbar total

pressure and a tritium purity  $> 95\%$ . The integrity of the optical coatings was monitored by visual inspection using optical microscopy.

This work was performed in collaboration with K. Schönung and V. Schäfer. The design and construction of the experimental setup and the first measurements are described in detail in [Sch11d]. Detailed investigations of the experimental setup for the measurement of transmittance and reflectance were performed by V. Schäfer [Sch13f]. Both documents will be used for further reference where appropriate.

#### 5.4.1. Description of coating samples

The coating samples employed in this test cover all physical vapour deposition processes that were discussed in section 5.1.2, namely electron beam deposition (EBD), ion assisted deposition (IAD), magnetron sputtering (MS), and ion beam deposition (IBS). All coatings were applied on fused silica substrates (25.4 mm diameter, SQ2, SICO Technology, Austria). Since the samples were received from the running production processes of LASEROPTIK GmbH, they exhibit different spectral features ranging from semi-transparent mirrors in the visible range (coating sample 1) to coatings with simultaneous features in the visible and the near infra-red (coating sample 4). In addition, an uncoated fused silica substrate (Thorlabs, WG41050) was tested. Details on the samples can be found in table 5.7. Information on the structure and materials of each coating type and plots of the coating transmittance are shown in appendix D.1. For each coating type (labelled by an Arabic number in table 5.7) three specimens are available (labelled by a Latin number). The arabic and latin numbers are combined to a sample ID to uniquely label each coating sample, e.g. II3 is the second specimen of the IBS coating and I4 the first specimen of the EBD coating. Batches of coating samples are formed by arranging all coating with the same Latin number into one group. The batch is identified by the common Latin number, i.e. the batch I consists of the coating samples with the sample IDs I1, I2, I3, I4, and I6. Within the work of K. Schönung [Sch11d] also standard Raman and laser windows of the Raman system were tested. These formed the batch III but will not be discussed here. The Latin numbers of the coating samples discussed in this work are therefore I, II, and IV.

In order to simplify the handling of the coated glass substrates each substrate is mounted into a sample holder made of stainless steel (figure 5.8). The sample ID is marked on the mount for unambiguous identification of the sample and to distinguish both sides of the substrate.

In addition to the coating samples on plain substrates also the LARA cell windows (diffusion bonded into a CF16 vacuum flange) that were initially damaged during the first LOOPINO operation [Stu10b, Fis11] are investigated within the work.

#### 5.4.2. Experimental setup

The description of the experimental setup is split into two parts. In the first part the equipment for the controlled exposure of the samples to highly purified tritium gas is

**Table 5.7.: Details on coating types in durability test.** Explanation of the abbreviations: IAD - Ion assisted deposition, MS - Magnetron sputtering, IBS - Ion beam sputtering, EBD - Electron beam deposition. The column 'Spectral features' lists the transmittance T and reflectance R of the coatings for the specific spectral ranges and angles of incident. All coatings were produced by LASEROPTIK GmbH. The item number was defined by the manufacturer. The 1520-1640 nm anti-reflection (AR) coating of sample 4 is not further specified by the manufacturer. The coating type 5 belonged to a sol-gel coating which is not discussed here. More information can be found elsewhere [Sch11d]. Sample 6 is a uncoated fused silica substrate.

Coating type #	Technique	Spectral features	Item number	Substrate <sup>†</sup>
1	IAD	T = 5-6% at 580 nm	01021UR1	SQ2
2	MS	T < 0.4% at 1064 nm and 0°	11120M1	SQ2
3	IBS	T = 95% 930-980 nm T < 0.3% 1030-1100 nm at 0°	20120Q2	SQ2
4	EBD	R > 80% 580-680 nm R < 0.5% 900-1070nm T > 92% 1520-1640 nm at 45° AR 1520-1640 nm on backside	23120T1	SQ2
6	none	Uncoated substrate. R ≈ 4% at 0°		WG41050

<sup>†</sup> Manufacturer of substrates: SICO Technology, Austria (SQ2), Thorlabs, US (WG41050).

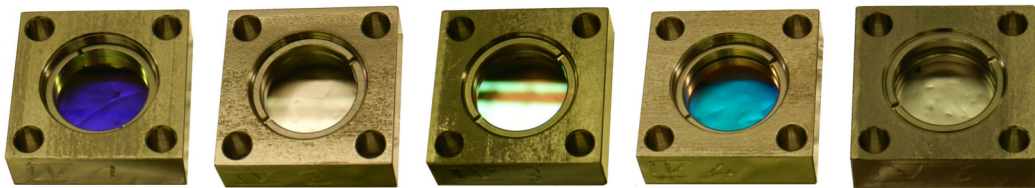


**Figure 5.8.: Coating samples IV1, IV2, IV3, IV4, and the uncoated substrate IV6 (from left to right) inside sample holder before exposure to tritium.** The fused silica substrates are mounted by two retaining rings inside the quadratic sample holders. Most coatings are visible by their colourful reflection. The ostensible irregularities on some coating samples are due to the work surface located underneath. The sample mounts can be stacked onto a holding structure to form the batch IV.

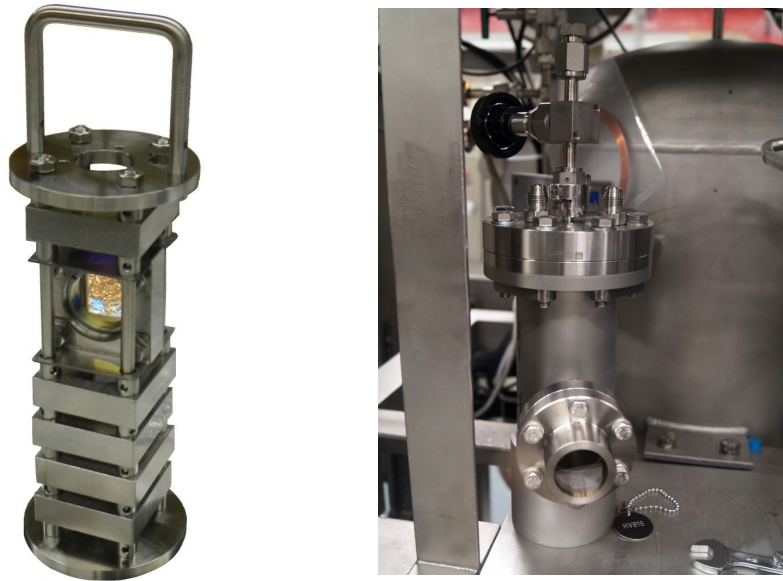


**Figure 5.9.: Holding structure and vessel for tritium exposure.** *Left:* Six coating samples are stacked in the holding structure. One coating sample is rotated to enable optical inspection. The structure visible on the coating sample surface is due to the working space surface located behind. *Right:* Vessel inside glove box. The holding structure can be inserted into the vessel through the top flange. Tritium gas can be injected through the inlet valve at the top flange. The vessel has two sapphire windows at the side (only one visible) for visible inspection of the rotated coating sample.

described. The second part deals with the monitoring of the integrity of the coating properties.

### Tritium exposure of coating samples

Each batch of coating samples is mounted onto a holding structure (figure 5.9, left) which separates the sample mounts from each other and allows to safely handle the complete batch, e.g. during the insertion into a vessel for tritium exposure. These vessels are cylindrical ultra-high vacuum components ( $\varnothing$  64 mm, length 270 mm) which fulfil the requirements for tritium operation [TLA13]. Four vessels are available for tritium exposure. Two of these are equipped with sapphire ( $\text{Al}_2\text{O}_3$ ) windows for visible access to the coating samples (figure 5.9, right). The volume of the vessel with (without) windows is 0.79 l (0.72 l). Sapphire was chosen as window material because of its hardness and general suitability for tritium containing systems<sup>1</sup>. After inserting the holding structure, the vessels are closed and filled with tritium gas via an inlet valve. During storage, the vessels can be disconnected from the tritium supply line. The vessels are evacuated and purged with hydrogen or helium gas for decontamination before removal of the samples.

<sup>1</sup>Sapphire windows could in principle also be used as substrate material for the LARA cell windows but without significant benefit: Sapphire has a refractive index of about 1.765 for 500-700 nm [Dob09]. For normal incident, the reflectance at one surface is 7.8% (eq. (5.1)). Therefore, optical coatings have to be applied on the substrate which will lead to the identical situation as for the currently employed fused silica windows. In addition, significant fluorescence compared to fused silica windows has been observed in the work of S. Rupp [Rup15].

Tritium filling of the vessels and vessel evacuation are performed by the CAPER facility [Bor05] which can supply tritium with up to 99% purity and hydrogen for decontamination. Also gas chromatographic analyses of the gas can be performed here [Läs02] of the gas mixtures. More details on the experimental setup and the handling procedures can be found in [Sch11d].

### **Determination of coating sample properties**

The integrity of the coating samples before and after tritium exposure was checked by visual inspection using optical microscopy and by measurements of the transmittance and reflectance. Other monitoring methods were not applied because of the necessary handling of the samples inside glove boxes after tritium exposure.

Two optical microscopes were available for visual inspection, one directly at the Tritium Laboratory Karlsruhe (Expert-DN, Müller GmbH, magnification up to  $\times 90$ ) and a more sophisticated one (GX51, Olympus) at the Fusion Material Laboratory (FML) of Institute for Applied Materials (KIT) with a maximum magnification of  $\times 1000$ . The GX51 microscope also has the option of differential interference contrast mode which can be used to visualise spatial variations of the optical path length (product of refractive index and distance along the beam path) in the sample [Mur01]. In order to examine the samples with the GX51 microscope, the samples had to be removed from the sample holders and directly placed onto the microscope. This procedure poses a risk that the samples become damaged (e.g. by scratches) or polluted (e.g. by dust, oils, etc.) which can have an impact on the further course of the study. Therefore only the samples of batch I were inspected with the GX51 microscope at the FML. The transports of the samples to the FML were performed according to the legal framework for transfer of radioactive material inside KIT [Kar09]. The contamination of the samples after tritium exposure was measured using wipe tests combined with liquid scintillation counting [Var09] (sensitive to surface contamination). Surface contamination in the range of  $10^6$  to  $10^8$  Bq/cm<sup>2</sup> was found on the sample holders. The coating samples themselves were not wipe tested as this could damage the samples. The samples (mounted in the holding structure) were inserted into a vacuum vessel which fulfils the same safety specifications as the vessels for tritium exposure. Based on calorimetry [Ale11] and wipe tests, a total tritium inventory  $(0.7 - 1) \cdot 10^{11}$  Bq was determined for the six samples, holding structure, and vacuum vessel. Additional packing of the vacuum vessel into a transport vessel, wipe tests, and dose rate measurements ensured the absence of radiation and contamination on the outside of the transport vessel.

For the measurements of transmittance and reflectance, a custom made setup was developed and installed in a glove box at the Tritium Laboratory Karlsruhe. Commercial devices were also considered but finally excluded due to the necessary adaptations for an operation inside a glove box. In the setup a laser beam is directed onto the coating sample and the reflected and transmitted fractions are measured by photo diodes. By normalising the photo diode signals to the laser power, the reflectance and transmittance can be calculated. Within the commissioning of the setup, issues with respect to reproducibility of the measurement were found [Sch11d]. These issues have been investigated in [Sch13f] and suitable countermeasures were proposed and also implemented. However, new measurements with the improved setup were not yet possible for this work due to

limited time resources. Therefore the evaluation of the coating integrity in this work is solely based on the acquired microscope images.

### 5.4.3. Inspection of already damaged LARA cell windows

The LARA cell windows that were damaged during the Raman measurements performed at LOOPINO in 2011 [Stu10b, Fis11] were inspected using the microscope at FML. Four microscope images of the damaged coating surfaces (including the one already shown in figure 4.1) are displayed in figure 5.10. Based on the analysis of the microscope images several statements can be made:

- All spots have a similar structure: A central point which is surrounded by coaxial rings. The circular shape is only disturbed if surface irregularities (e.g. scratches) are present.
- The laser windows do not exhibit special features at the position where the laser was passing through. In combination with the fact that the Raman windows were equally affected, a laser-induced damage can be excluded.
- The damages seem to cluster at positions where the coating is not uniform (e.g. at the rim) and hence potentially less robust.
- The largest damage found was about 250  $\mu\text{m}$  in size.
- The coating damage seems to occur in two steps: First a orange precursor is formed which then evolves to the dark coating damages.
- Using the differential interference contrast mode of the microscope, no indications for height differences were found. Therefore, a coating delamination seems unlikely but cannot be excluded.

Neither the cause for the damage nor the exact damage process could be revealed by this investigation. Nevertheless, valuable information about the coating damage were gained which will be used in the next section where the tritium exposure of the coating samples is discussed.

### 5.4.4. Tritium exposure of samples and status of samples

#### Status of coating samples before tritium exposure

Before exposure to tritium gas, the coating samples were checked with a GX51 microscope at the FML that is located outside the controlled area. The microscope is identical to the one that was used afterwards for the inspection after tritium exposure. No damages and surface irregularities could be found.

#### Exposure of coating samples to tritium gas

The batches of coating samples were exposed to tritium gas and inspected by microscopy according to table 5.8. During the periods in which the samples were not exposed to

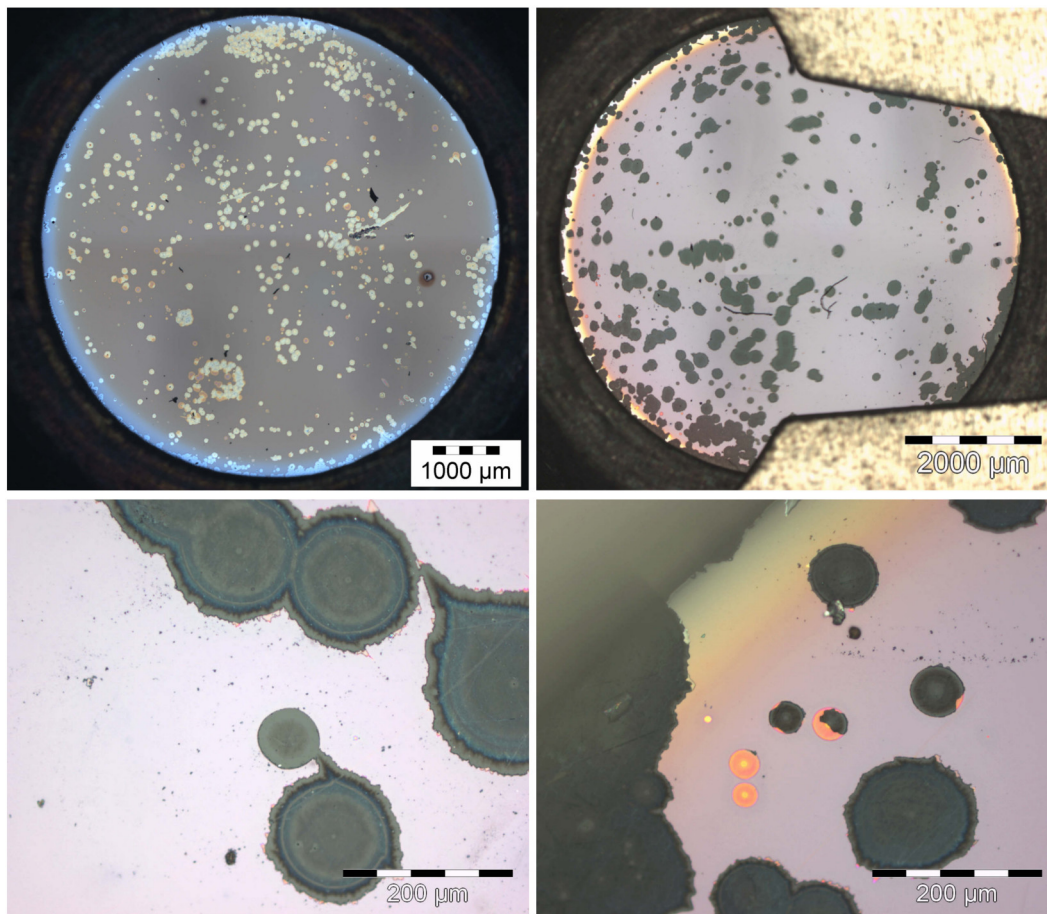


**Figure 5.10.: Microscope images of damaged AR coatings on LARA cell windows.** The coatings were exposed for about three months to tritium gas (200 mbar, purity >90%). All pictures show the inner, i.e. tritium facing surface of the windows. Both upper windows were produced by joining several overlapping images. *Top left:* Picture of laser window. Spot-shaped damages are distributed over the window surface. The coating fades out towards the rim (blue ring) due to shadowing effects of the surrounding vacuum in the coating process. This area seems to be more affected by the damages. Larger clusters of damage spots can also be found in the inner part of the coating. *Top right:* Picture of Raman window. Less damage spots are present in comparison to the laser window. The coating rim is also more affected than the inner coating sections. Parts of the coating is covered by the mounting clamps of the microscope. *Bottom left:* Close-up view of Raman window. Each coating damage is composed of coaxial rings around a spot which could be the position of the initial damage trigger. Surface irregularities like scratches seem to yield a non-circular growth of the damage. When individual damages get in contact, large areas of coating damage get formed. *Bottom right:* Close-up view of Raman window close to coating rim. The dark coating damages seem to emerge from orange circles.

**Table 5.8.: Overview of actions performed during durability test.** Storage in hydrogen gas was done to keep the sample batches under clean and reproducible conditions while bridging waiting times. Purging of the vessels with hydrogen or helium gas before opening is not listed.

Batch	Action	Time $t$ days	Duration days
I	T <sub>2</sub> exposure (200 mbar, purity > 90%)	0.0	17.0
	Inspection at TLK and FML	17.0	71.2
	T <sub>2</sub> exposure (200 mbar, purity >98%)	88.2	22.0
	Storage in H <sub>2</sub> (159-203 mbar <sup>†</sup> )	110.2	667.0
	Inspection at TLK and FML	776.1	
III	T <sub>2</sub> exposure (204 mbar, purity 97%)	0.0	9.9
	Storage in H <sub>2</sub> (148 mbar, purity )	9.9	70.9
	Inspection at TLK	80.8	
IV	T <sub>2</sub> exposure (204 mbar, purity 97%)	0.0	9.9
	Storage in H <sub>2</sub> (142 mbar)	9.9	23.8
	Inspection at TLK	33.7	

<sup>†</sup> The pressure was reduced to 159 mbar at  $t = 129.2$  days due to a gas composition analysis by gas chromatography.

tritium gas or currently being inspected they were stored in hydrogen gas to keep the samples in a clean and reproducible environment. Storage in vacuum was avoided due to the known susceptibility of EBD coatings to variations of the environmental conditions (section 5.3.2). The sample batch I was exposed to tritium gas for 17 days and afterwards inspected with the microscope at TLK. The sample holders were decontaminated using wetted tissues before their transport to the FML for the inspection with the GX51 microscope. The coating samples were installed in the sample holders during decontamination but not touched. Batches III and IV were exposed to tritium gas for 9.9 days and afterwards inspected with the microscope at the Tritium Laboratory Karlsruhe. Sample batch I was exposed to tritium for a second time and afterwards stored for 667 days in hydrogen. This long period was mainly due to the ongoing characterisation [Sch13f] of the transmittance and reflectance measurement experiment mentioned before (section 5.4.2). After the second tritium exposure of batch I, the inspection of the samples at the FML was repeated.

### General results (valid for all coating types)

Several findings were made for all coating samples independent of the coating type or sample batch:

- The coatings are mechanically damaged in the region where the retention ring of

the sample holder is in contact with the coating.

- Liquid droplets of about 50  $\mu\text{m}$  diameter were found on all coating samples of batch I (figure 5.11, top left) when inspecting the samples with the microscope at the FML at  $t = 17$  days. The origin of the liquid is uncertain but could be related to the decontamination of the sample holder before the transport of the batch to the FML. When inspecting the samples of batch I the second time at the FML, features were found on all sample surfaces that could be interpreted as a dried liquid (figure 5.11, top right).
- Surface pollution by dust grains or small textile fibres was found on most samples. This is not surprising when taking into account that the work surface in the glove box at the FML was covered with cleansing tissues. These were necessary on the one hand to prevent the coating samples from cross contamination with other radioactive isotopes that were handled in the glove box before and on the other hand to avoid extensive tritium contamination of the glove box. Most of the surface pollution could be removed with a duster spray.
- After the first tritium exposure (9.9 days and 17 days respectively) no indications for coating damages were found on all coating samples when inspecting the samples by eye or by microscopy at the TLK (magnification limited to  $\times 40$ ).

### **Results for dense coating types (IAD, MS, IBS) and uncoated substrate**

Even with the  $\times 500$  magnification of the GX51 microscope, no indication for a coating damage was found on the IAD, MS, and IBS samples and on the uncoated substrate. All surface irregularities found belonged to one of three classes: (i) Compatible with surface pollution that was not removed by the duster spray. (ii) Interpreted as the apparently dehydrated liquid droplets that were discussed above. (iii) Size smaller than about 5  $\mu\text{m}$  and therefore not fully resolved.

### **Results for EBD coating**

Surface alterations of the EBD coating were already visible after 17 days of tritium exposure when inspecting the sample I4 with the GX51 microscope (figure 5.11) while the microscope at TLK was not yet sufficiently sensitive. Based on an arbitrarily chosen but reasonably representative section (size 4.6 mm  $\times$  3.52 mm), a mean spot density of 1.25 spots/ $\text{mm}^2$  was found. All coating alterations have a common topology: A distinct spot of about 4  $\mu\text{m}$  in diameter, which is coaxially surrounded by a circular discolouration of about 100  $\mu\text{m}$  in diameter which gradually diminished towards the outer rim. After the second tritium exposure mostly consistent results were found. A mean spot density of 0.6 spots/ $\text{mm}^2$  was calculated from a surface of 9.2 mm  $\times$  7.04 mm. This values differs by about a factor of two from the previous value but can be considered as being in fair agreement when taking into account the arbitrary choice of the surface section and the different sizes of the sections. The coating damage was not only observed for sample I4 but also for the EBD samples in the other batches. In case of sample III4, the coating damage was visible by eye at  $t = 87$  days.

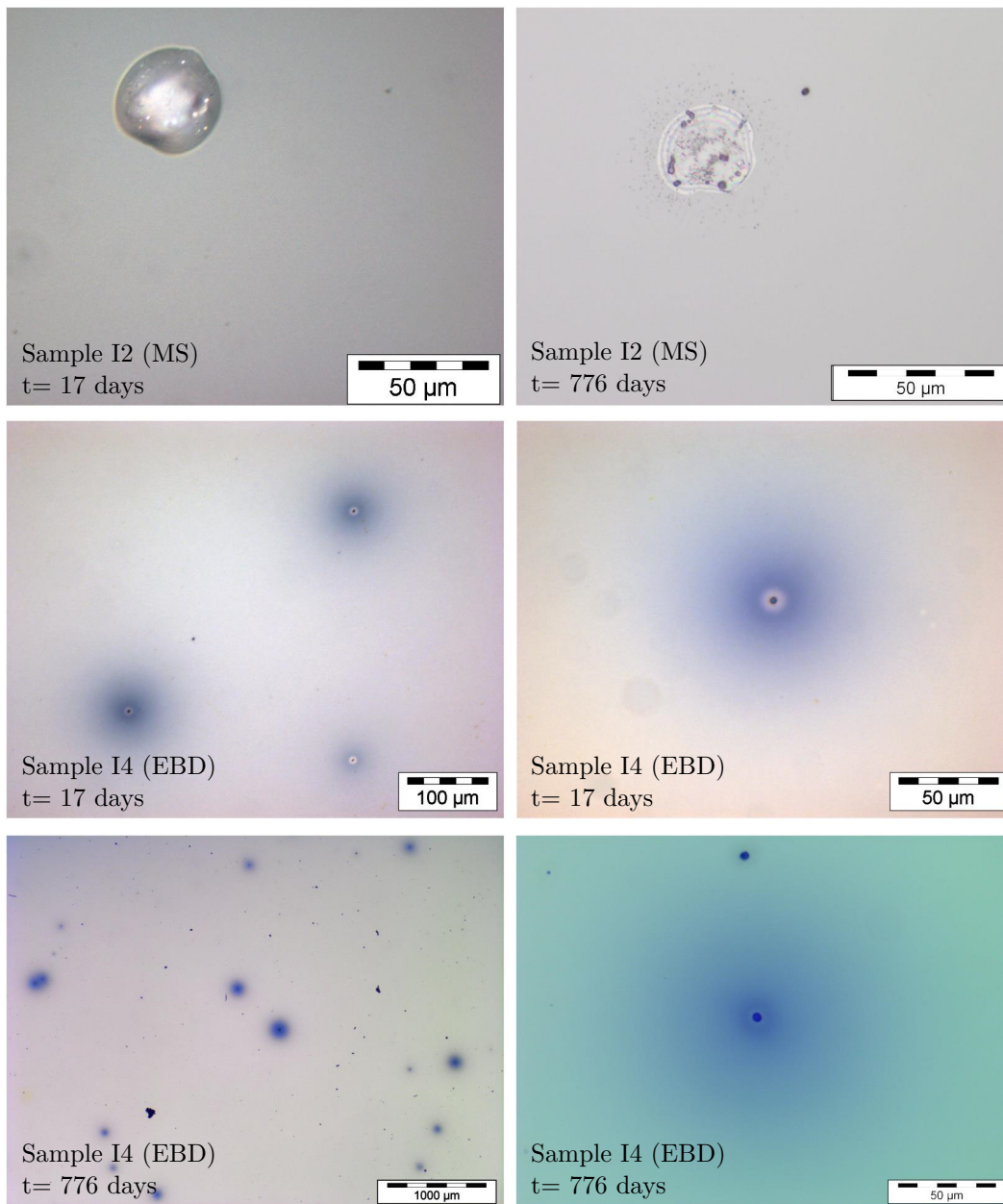


**Figure 5.11.: Microscopy images of coating samples after tritium exposure.** All images were acquired with the GX51 microscope at the FML and have been moderately adjusted in contrast to emphasise the findings. The relative time (days since start of first tritium exposure) of the image acquisition is shown on every picture. *Top left:* Example picture of liquid droplets that were found on all coating samples of batch I during the inspection at FML at  $t = 17$  days. *Top right:* Example picture of features that were found on all samples of batch I during inspection at  $t = 776$  days. These features could be explained by the potential drying of the liquid droplets that were found at  $t = 17$  days. *Middle row:* Coating damages of sample I4 (electron beam deposition) after first tritium exposure. The damages consist of a central spot with about  $4 \mu\text{m}$  diameter which is coaxially surrounded by a circular discolouration of about  $100 \mu\text{m}$  diameter. *Bottom row:* Coating damages of sample I4 (electron beam deposition) after second tritium exposure. The cause for the colour variation of the bottom right picture in comparison to the others is unexplained. A change of the illumination conditions seems most likely.

#### 5.4.5. Discussion of results

The EBD coating samples must be considered as damaged due to the observation of surface alterations after 17 days (batch I) or even only 9.9 days (batch III and IV). The observed damage topology of the EBD coatings has certain similarities to the damage D1 (figure 5.10) that was observed after the first LOOPINO operation with highly purified tritium gas: A pronounced central spot which is coaxially surrounded by ring-like structures. The different colouration of the ring-like structures (orange in case of D1 and blue for the EBD coatings in the present test) could be related to the different coating layouts and to different metal oxides as they were optimised for different spectral features. In the damage D1, the orange colouration was followed by a darkening or potentially even delamination of the coating which led to a significant loss in transparency at that position. This was not experienced in the present test. The lower exposure duration (39 days in comparison to three months) could in principle be responsible but more likely is the absence of (tritiated) hydrogen fluoride species in the test. This hypothesis is backed by the fact that such a severe coating damage was not experienced within the commissioning of the KATRIN Raman system after the replacement of the PTFE component in LOOPINO (section 4.6). A prolonging of the test after this work is under consideration. Then also PTFE could potentially be added to one of the sample batches to test the coating samples under more harmful conditions. However, such a test can only be performed if the handling and treatment of the potentially corrosive waste gas is ensured.

In contrast to the EBD coating samples, the dense coating types (IAD, MS, IBS) are regarded as undamaged after a total tritium exposure of 39 days. The absence of damage on the uncoated fused silica substrate also demonstrates that thin films have substantially different properties than the corresponding bulk material.

This test demonstrated the general susceptibility of porous EBD coatings to environmental effects which was already emphasised during the discussion of harmful effects on optical coatings in this section. In case of the present study the environmental conditions were rough vacuum, hydrogen environment (from chemical point of view), low water moisture concentration and especially ionising radiation due to tritium  $\beta$ -decay and the accompanying radio-chemical processes that can be triggered by the decay energy. With respect to KATRIN, EBD coatings should therefore be avoided inside the glove box to ensure the reliable operation of the KATRIN Raman system during neutrino mass measurement runs.

### 5.5. Improved coating scheme for LARA cell and glove box windows

Based on the findings of the sections 5.3 and 5.4, the selection of coatings for the LARA cell and Appendix windows was revised. The main goal was to avoid electron beam deposited coatings for optics that are in contact with tritium or laser irradiated inside the glove box. The recessed position of the Raman window in the vacuum flange (figure 4.4, page 72) and the maximum tolerable thermal treatment of the windows during coating

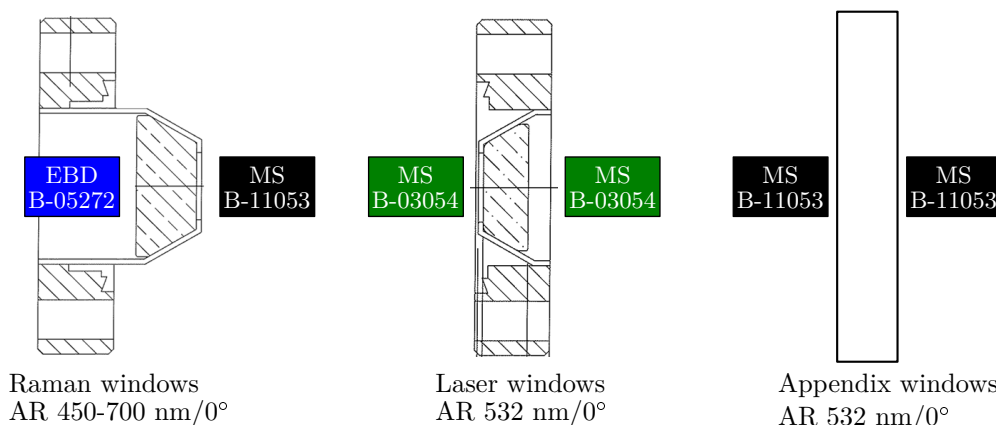


**Figure 5.12.: New coating scheme for LARA cell and Appendix windows.** All but one window surface are coated by magnetron sputtering (MS). The outer surface of the Raman window is coated by electron beam deposition (EBD) due to its recessed position in the vacuum flange. The coating identification numbers of the manufacturer (LASEROPTIK, Garbsen, Germany) are indicated.

(maximum temperature 250°C, maximum heating rate 4 K/min [Han13]) had to be considered in the decision process. The thermal limitations are due to the fact that the windows are diffusion-bonded into the vacuum flange before coating [Tay01] and the integrity of the diffusion-bonding welding seam cannot be guaranteed beyond these parameters.

Based on close consultation with the coating manufacturer a combination of magnetron sputtering and electron beam deposition was chosen for the new AR coating scheme (figure 5.12). The laser and Appendix windows were coated by magnetron sputtering. For the Raman windows magnetron sputtering was used for the inner window surface and electron beam deposition for the outer. Magnetron sputtering could not be used for the outer surface because of the recessed location of the window in the vacuum flange which would have caused a significant shadowing effect during coating. As the outer surface of a Raman window is neither in contact with pure tritium gas nor exposed to direct laser radiation, electron beam deposition can be tolerated here. The shadowing effect is also moderately present on the inner surfaces of the Raman and laser window (fig 5.13) but does not affect the performance of the windows. The wavelength dependence of the reflectance of the coatings is shown in appendix D.2.

In order to stay within the allowed temperature range, the magnetron sputtering was performed at 120°C and the windows were afterwards tempered at 230°C. Temperature ramping was done with gradients smaller than 4 K/min. In addition to the LARA cell windows, also plain glass substrates (Q2, S-00923, Ø38x6.35mm, SICO, Austria) were coated with a 532 nm AR coating to replace the Appendix windows W<sub>1</sub> and W<sub>2</sub>.

After coating, the LARA cell windows were mounted on a LARA cell body and leak tested to check the integrity of the diffusion-bonding welding seam. A leak rate of less than  $1.5 \cdot 10^{-10}$  mbar l/s was achieved which easily fulfils the requirement of  $1 \cdot 10^{-9}$  mbar l/s and hence demonstrates that the windows were not harmed during the coating process.

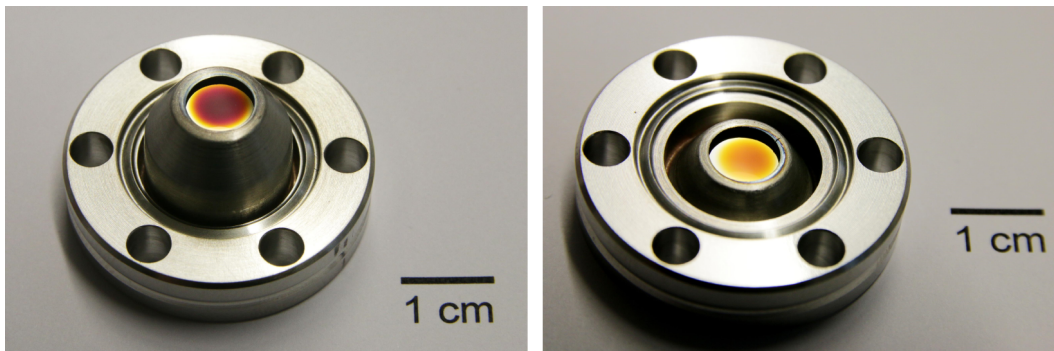


**Figure 5.13.: Raman (left) and laser (right) window after magnetron sputtering.** The coatings were illuminated under an obtuse angle to make the coating visible. The coatings do not fully reach to the edge of the windows due to the shadowing effect by the surrounding vacuum flange. This does not impose an issue for their functionality.

The magnetron sputtered windows will be employed in the next operation phase of LOOPINO to test the coatings under realistic conditions.

## 5.6. Conclusions

Optical coatings reduce laser power losses along the beam path and potentially harmful reflections, and hence increase the signal-to-noise ratio in the Raman spectrum. The stability of optical coatings also influences the accuracy of the Raman measurements since an unnoticed coating degradation in the windows  $R_1$  and  $W_3$  (figure 4.21, page 102) alters the spectral sensitivity of the light collection and analysis system. Durable optical coatings are therefore essential for the performance of the KATRIN Raman system. Until the observation of the severe coating damage during the Raman measurements at the LOOPINO facility [Stu10b, Fis11] no particular attention was paid to the employed coatings. Triggered by this event the subject of optical coatings in glove box and tritium environment has been addressed within this work and a variety of findings were made that (i) help to understand the coating damages that were experienced in the past, and that (ii) assist in the selection process for coatings of higher durability in future.

Radiation-induced densification of the coating layers was found to be not relevant for the KATRIN Raman system at the current stage. Clear indications were found in the literature review but also in experimental data acquired within this work that porous coatings like the currently employed EBD coatings are affected by the variation of environmental conditions as oxygen and water-moisture concentration, the presence of organic contamination and the operation pressure. In the durability test performed within this work, a damage of EBD coatings was observed after already 9.9 days of tritium exposure but no damages were found for the dense coating types. These results are also subject of a publication which is accepted for publication [Fis14].

In conclusion, the severe coating damage in the LOOPINO facility that was experienced in the past [Stu10b, Fis11] can be attributed to two likely causes:

- The presumable formation of corrosive hydrogen fluoride species inside LOOPINO due to the presence of a PTFE component and
- the general weakness of electron-beam deposited coatings under such non-standard environmental conditions.

While the first issue was solved by the replacement of the PTFE containing component with a full-metal version (section 4.6.1) the second is approached by the specification of an improved coating scheme for the LARA cell windows based on magnetron sputtering. These windows arrived at the end of this work and will be tested in the future, first outside glove boxes against laser-induced contamination and then within LOOPINO for long-term stability when being exposed to highly purified tritium gas.



## 6. Software for the operation of the KATRIN Raman system

The KATRIN Raman system has to run autonomously over the course of each about 60 days long neutrino mass measurement run. This can only be achieved if the system is operated by a software that controls all relevant components, reads-out and automatically analyses the acquired data and monitors the status of the system. The program 'LARASoft' was developed within this work in collaboration with F. Kassel [Kas12] and T. James in order to fulfil these requirements.

The aim of this chapter is to give a general overview of LARASoft. The requirements of the operation software for the KATRIN Raman system are discussed in section 6.1. Already existing software and its suitability for the operation of the KATRIN Raman system is evaluated in section 6.2. The concept of LARASoft is presented in section 6.3. The chapter concludes with the evaluation of LARASoft based on dedicated tests and the experience from the application of the software in this work.

### 6.1. Requirements for the LARA software package

The tasks of the LARA software package are generally speaking the acquisition, analysis, and display of Raman data and the monitoring of hardware parameters to ensure the reliable operation of the KATRIN Raman system. These individual tasks are discussed in more detail in the following three sections.

#### **Universal applicability**

Although the development of the software is focused on the the KATRIN Raman system, the program should be sufficiently generic so that it is also suitable to be used in the operation of all other Raman systems at the TLK. With this one would also prevent that operation software for individual Raman systems becomes fragmented, and hence further development and software maintenance would be greatly simplified. It is therefore important that features which are not needed for a specific Raman system (e.g. read-out of specific sensors) can be easily de-activated without influencing the general functionality of the software.

#### **Automated data acquisition and analysis**

The Raman raw data are the two dimensional CCD images which are continuously acquired with acquisition times typically in the range of 5-30 s. During the time exposure of the CCD sensor, other sensors in the system (e.g. laser power meter, beam position

and temperature sensors) and hardware parameters (e.g. laser diode pump current and CCD temperature) are typically read-out at a rate of 1 Hz and averaged over the complete acquisition period. Said parameters are recorded to be used to monitor the status of the KATRIN Raman system. Each Raman spectrum has to be analysed automatically almost in real-time, i.e. immediately after its acquisition and hence simultaneously to the acquisition of the next spectrum. The analysis has to be faster than the acquisition period to prevent the pile up of unanalysed data and to give fast feedback to the operators of the KATRIN inner loop.

The analysis of the two dimensional CCD images is based on the SpecTools toolkit (section 3.3) and comprises amongst other things the correction of artefacts due to cosmic rays and aberrations of the optical components, the correction for the spectral sensitivity of the light collection and analysis system, the binning of the spectrum<sup>1</sup>, background subtraction, peak fitting, and finally the calculation of molar fractions from the fit parameters. An essential requirement in this sequence is the correct treatment of systematic and statistical uncertainties in the various data processing steps and the propagation of uncertainties that stem from input data necessary for the data analysis.

### **System status monitoring**

Monitoring of all relevant system parameters is essential to guarantee the reliable operation of the system and to ensure the quality of the acquired Raman data. It is therefore important to not only measure the system parameters but also automatically evaluate them with respect to ranges for nominal operation mode. Each parameter evaluation has to result in a grading if the parameter is within specification (status 'ok'), if a deviation is present but not yet acute (status 'warning') or if the parameter is so far from its nominal range that a malfunction has to be assumed, or has really occurred (status 'failure'). As the Raman system is only one of many systems within KATRIN that have to be supervised simultaneously during neutrino mass measurements, a global status parameter ('ok'/'warning'/'failure') has to be compiled for the Raman system on the basis of the individual parameter gradings to enable the fast assessment of the system status. Effective procedures have to be defined that the operators are promptly informed in case the global status parameter of the Raman system changes to 'warning' or even to 'failure' to minimise the down time of the system and to prevent potential damage of the system. Notwithstanding this, an automatic shutdown has to be implemented for the event of safety-relevant incidents which pose a risk for personnel or major hardware components<sup>2</sup>.

### **Display and transmission of data**

The output data of the KATRIN Raman system is used within KATRIN in three ways:

---

<sup>1</sup>Binning is in this context the conversion of the two dimensional CCD image into a one dimensional array by summation of the pixel intensities along the non-dispersive vertical axis of the image.

<sup>2</sup>Emergency shutdown mechanisms are either already implemented in the relevant components (Finesse laser: Shutdown in case of overheating, section 4.2.2) or realised by explicit safety devices (Laser interlock system: Closing of shutter in case of enclosure opening or serious beam deflection due to the failure of an optical component, section 4.2.5). They will therefore be not further considered here.

1. As direct feedback for the operators of the inner loop, e.g. to decide when pure tritium has to be injected into the inner loop to keep the tritium purity above 95%.
2. For the operators of the KATRIN Raman system to ensure the reliable operation of the system and to investigate the system in detail in case of a malfunction.
3. In the neutrino mass analysis to correct for systematic effects related to the gas composition (section 2.3).

Therefore, the full output data of the Raman system has to be available locally at the Raman system and simultaneously transmitted into the global KATRIN data handling framework which is also responsible for data storage and backup [Kle14]. As the software will also be used for other Raman systems than the one of KATRIN, standalone operation must also be possible at any time.

### **User friendliness and automated parameter setting**

An intuitive graphical user interface is necessary to simplify the operation of the KATRIN Raman system and to avoid operation errors or misinterpretation of the system status. The personnel for the operation of the KATRIN source and transport section who are also responsible for the operation of the Raman system will be trained but generally will be no experts in Raman spectroscopy. About 100 parameters have to be correctly set to specify the data acquisition and analysis routines for the KATRIN Raman system. In order to reduce the responsibility of the operators, it must be possible to load a 'measurement template', i.e. a complete set of parameters which was pre-defined by an expert for the system which only has to be marginally adopted to the current situation.

## **6.2. Existing software for the operation of Raman systems and data analysis**

A range of software for the operation of Raman systems and the analysis of Raman data has been developed in the past years. This section discusses the available software in the context of the requirements for the LARA software package.

### **6.2.1. Data acquisition software**

Each of the Raman system prototypes was operated via custom-written LabView<sup>TM</sup> software which allowed the automated data acquisition, the read-out of sensors and to some extent the automated analysis of the data. Sensor read-out and other system-specific features were hard-coded in the software which limited the overall inter-system compatibility. As a consequence of this, substantial efforts for software maintenance were continuously necessary while the margin for significant improvements was very limited.

### 6.2.2. Data analysis software

The data analysis routines which are incorporated into in the data acquisition software of the Raman systems were mostly based on the stage of development of about 2011. Since then, substantial improvements of the analysis routines were achieved and finally compiled in the SpecTools toolkit within the scope of [Jam13c]. With this release, a significant step towards the completion of the data processing chain for the analysis of Raman data within KATRIN was made. However, the SpecTools toolkit can only be operated offline for batch analysis of data, i.e. after data acquisition.

### 6.2.3. Suitability of existing software for the operation of the KATRIN Raman system

The software for operation of the Raman systems does not offer the necessary prerequisites to fulfil all aforementioned requirements. Therefore, a complete re-design of the operation software became necessary. The routines of the SpecTools toolkit have proven their maturity and hence can be integrated into the new operation software.

## 6.3. LARASoft: Software for the automated operation of the KATRIN Raman system

The software LARASoft has been developed within this work in cooperation with F. Kassel [Kas12] and T. James with the aim to create an operation software for the KATRIN Raman system that fulfils all requirements defined in section 6.1. The program is fully based on LabView™ to take advantage of the existing drivers for control and read-out of hardware components and to be able to reuse the data analysis algorithms that were developed for the SpecTools toolkit. LARASoft is now routinely used at the Tritium Laboratory Karlsruhe for operation of up to four different Raman systems and for other smaller optical experiments. The commissioning of the KATRIN Raman system (section 4.6) was also performed with LARASoft. Further development of LARASoft is ongoing as a few requested features (e.g. handling of uncertainties and connection to the data handling framework of KATRIN) are not yet fully implemented.

The graphical user interface (GUI) of LARASoft is structured by several tabs. Each is associated with a specific aspect of LARASoft, e.g. general settings, sensor configuration, Raman data analysis, and display of data and results. This section gives a general overview of LARASoft based on the current stage of development (version 1.0.12). Technical aspects will only be discussed where relevant for the general understanding of LARASoft. More detailed information is available in the dedicated documentation [Tel13].

### 6.3.1. General software control

The general settings of a measurement run (a continuous acquisition of Raman spectra) are defined in the 'Main' tab of LARASoft (figure 6.1). These settings include the

acquisition time and the measurement period. As it will be shown in section 6.4, the measurement period has to be at least 0.5 s longer than the acquisition time for the CCD detector employed in this work. A description of the measurement run and the experimental parameters that cannot automatically be read-out by LARASoft, e.g. the spectrometer settings (spectrometer type, grating type, etc.) are entered manually in the 'Main' tab.

A measurement run is started and stopped by the buttons located in the global status and control line at the very bottom of the GUI. This line is visible on every tab and displays the most important information: Current operation mode of LARASoft ('Waiting', 'Acquisition running', 'Focus mode'), run number, and global status of the Raman system ('nominal', 'warning', 'failure'). The run number consists of a letter and a number, which is automatically generated by LARASoft, and unambiguously labels every measurement run. The letter identifies the Raman system ('C' for the KATRIN Raman system) whereas the number labels the measurement run. The run number of the commissioning of the KATRIN Raman system (presented in section 4.6) was C000148.

### 6.3.2. Selection and configuration of sensors and devices

The sensors and devices which are read-out by LARASoft are configured in the tab 'Sensors and devices' (figure 6.2). All supported sensors and devices are displayed and can be activated and configured on request. Dedicated dialogues are used for the configuration of the sensor settings as shown in figure 6.2 for the example of the analogue to digital converter.

### 6.3.3. System status monitoring

Each sensor value is evaluated with respect to intervals that were set by the user to determine the status of the sensor reading (figure 6.3). The resulting status of each sensor reading is either 'nominal', 'warning', 'failure', or 'out of range'. The 'LARA status monitoring' tab is shown in figure 6.4 where the user is provided with an overview of all sensor readings and the status and intervals of each reading. The global status of the Raman system (shown in the global status and control line at the bottom of the GUI) is determined by the most negative status of the individual sensor readings. For each sensor reading, the user can select if its status should be included when determining the global status of the Raman system. The status intervals of all sensor readings can be stored into and loaded from a text file to simplify the configuration.

### 6.3.4. Configuration of data analysis procedures

The data analysis of the Raman spectra is configured in the 'Data processing of individual spectra' tab (figure 6.5). The user can activate and configure individual processing steps and determine at which stages the (intermediate) data is stored. Most of the analysis procedures are based on the SpecTools package which is described in detail in [Jam13c]. The task and working principle of each processing step is described in the following:

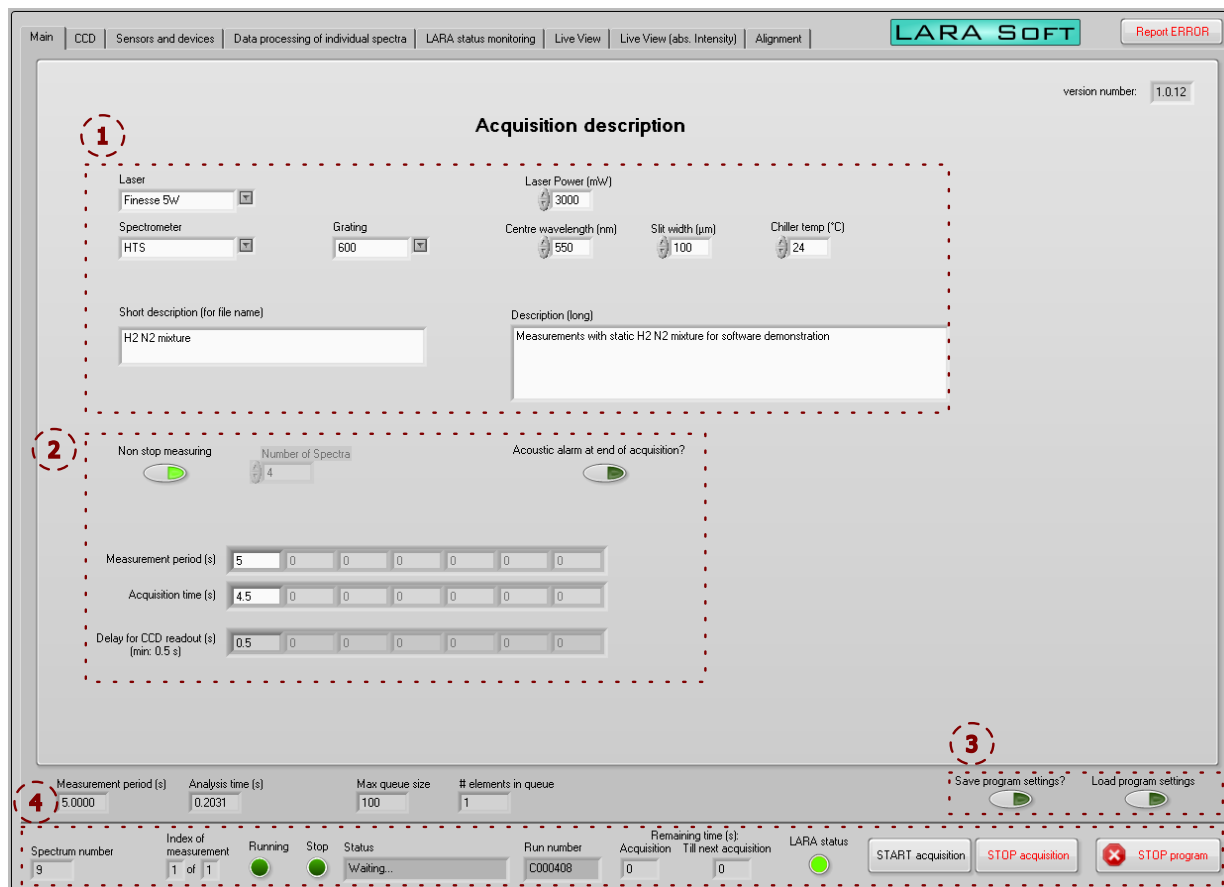


**Figure 6.1.: 'Main' tab of LARASoft.** The general settings of the measurement run are defined in this tab. (1) Description of experimental parameters. (2) Definition of measurement period and acquisition time. Selection if only a finite number of spectra is to be taken or if the measurement run continues until it is manually stopped by the user. (3) Buttons for loading and saving of measurement templates which comprise all parameters that can be set in LARASoft. These templates document all LARASoft settings in a form readable for machines and humans and allow for the easy repetition of a measurement by loading its measurement template. A measurement template is automatically stored on the computer at every start of a measurement run for documentation purposes. (4) Global status and control line of LARASoft (visible at every tab) showing: Status of LARASoft ('Waiting', 'Acquisition running', 'Focus mode'), run number, global status of the Raman system ('nominal', 'warning', 'failure'), buttons to start and stop the measurement run and to close LARASoft. The run number is automatically generated by LARASoft: If LARASoft is 'Waiting', the run number of the next run is shown. If LARASoft is acquiring data, the number of the current run is shown.

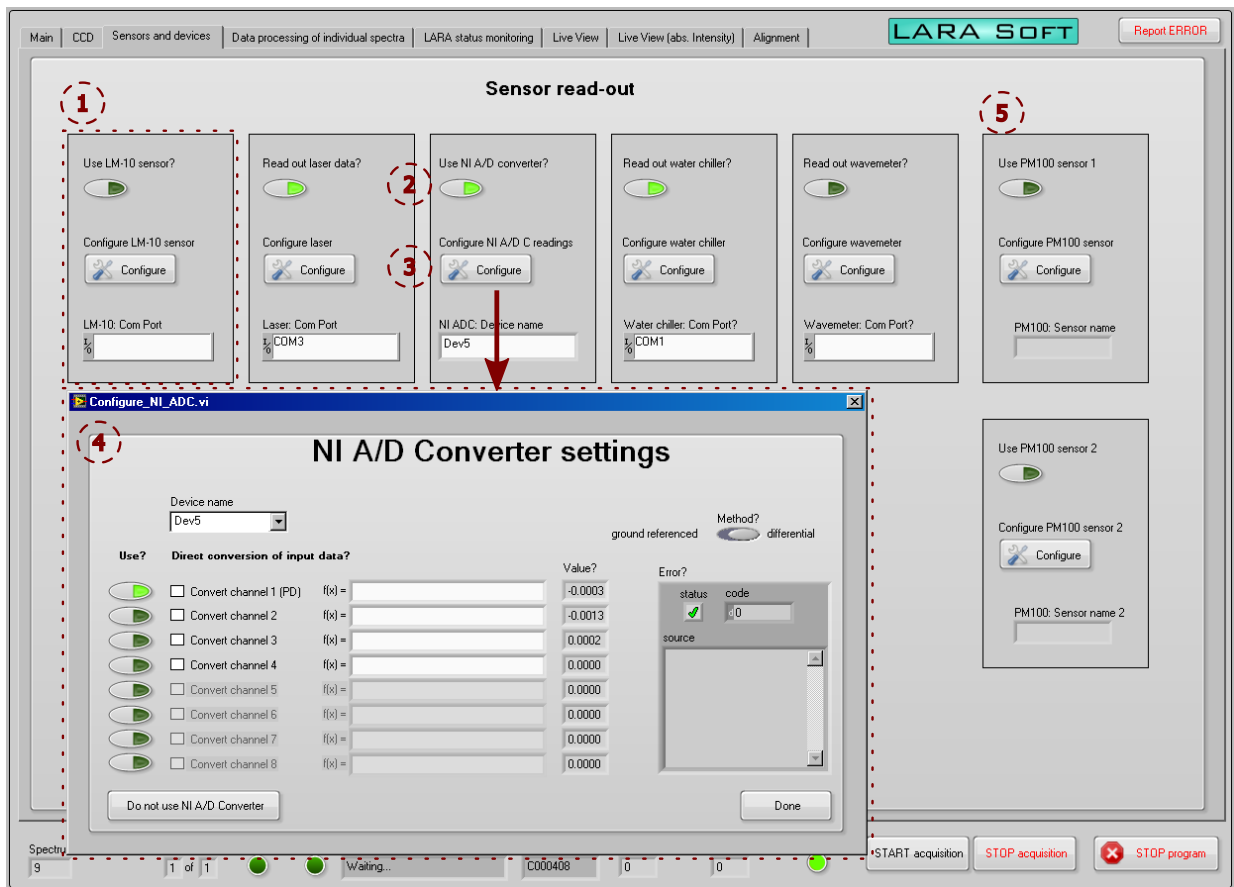


**Figure 6.2.:** 'Sensors and devices' tab of LARASoft. Sensors and devices are activated and configured in this tab. (1) Every sensor/device is symbolised by a box containing controls and indicators. (2) Control to activate a certain sensor. (3) Button to open the configuration dialogue of the sensor/device. (4) Configuration dialogue of the analogue to digital converter as example. (5) Boxes of PM100 laser power sensors which are used in other experiments at TLK.

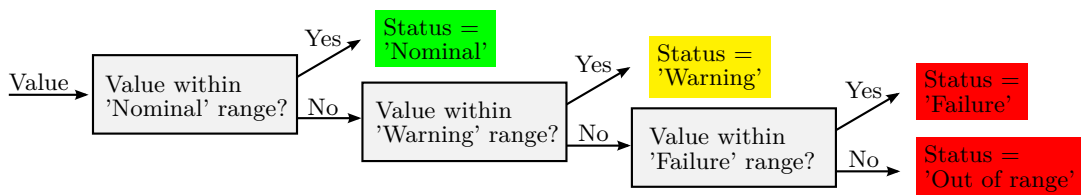


**Figure 6.3.:** Schematic drawing of algorithm for evaluation of a sensor values. Both status indicators 'Failure' and 'Out of range' will have identical consequences in LARASoft.

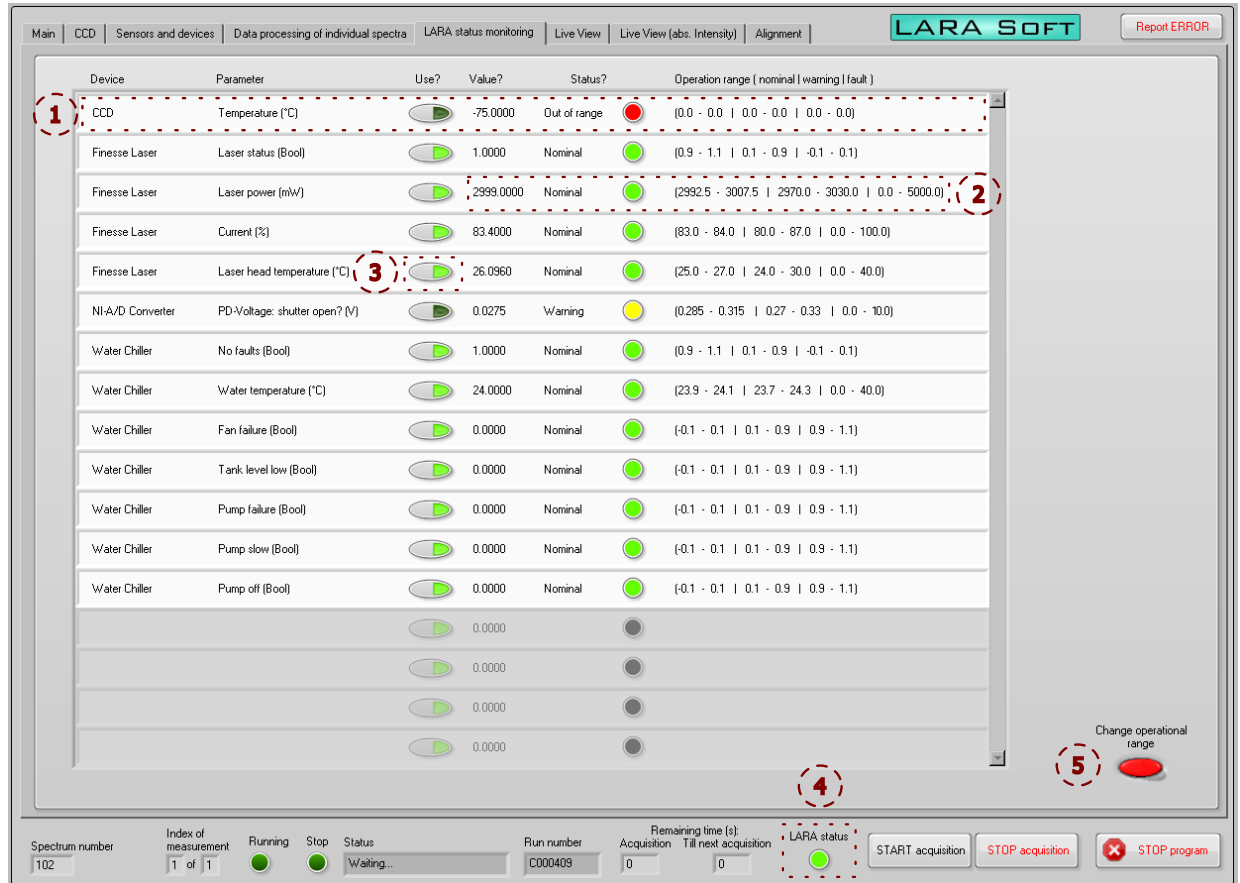


**Figure 6.4.: 'LARA status monitoring' tab of LARA Soft.** This tab lists all sensor readings of the Raman system and shows the status ('Nominal', 'Warning', 'Failure', 'Out of range') of each sensor reading. (1) Every sensor reading is indicated by one line. The list of sensor readings is automatically updated when (de)activating a sensor or device in the 'Sensor and devices' tab. (2) Value and status of sensor reading with respect to the operation ranges (indicated at the right): 'Nominal': green LED. 'Warning': yellow LED. 'Failure' or 'Out of range': red LED. (3) Button to determine whether the status of the sensor reading will be considered in the calculation of the global status the Raman system. (4) Global status of the Raman system indicated by a LED (same colour convention as described above). (5) Button to open the configuration menu where the operation ranges can be set, stored into files and read from files.

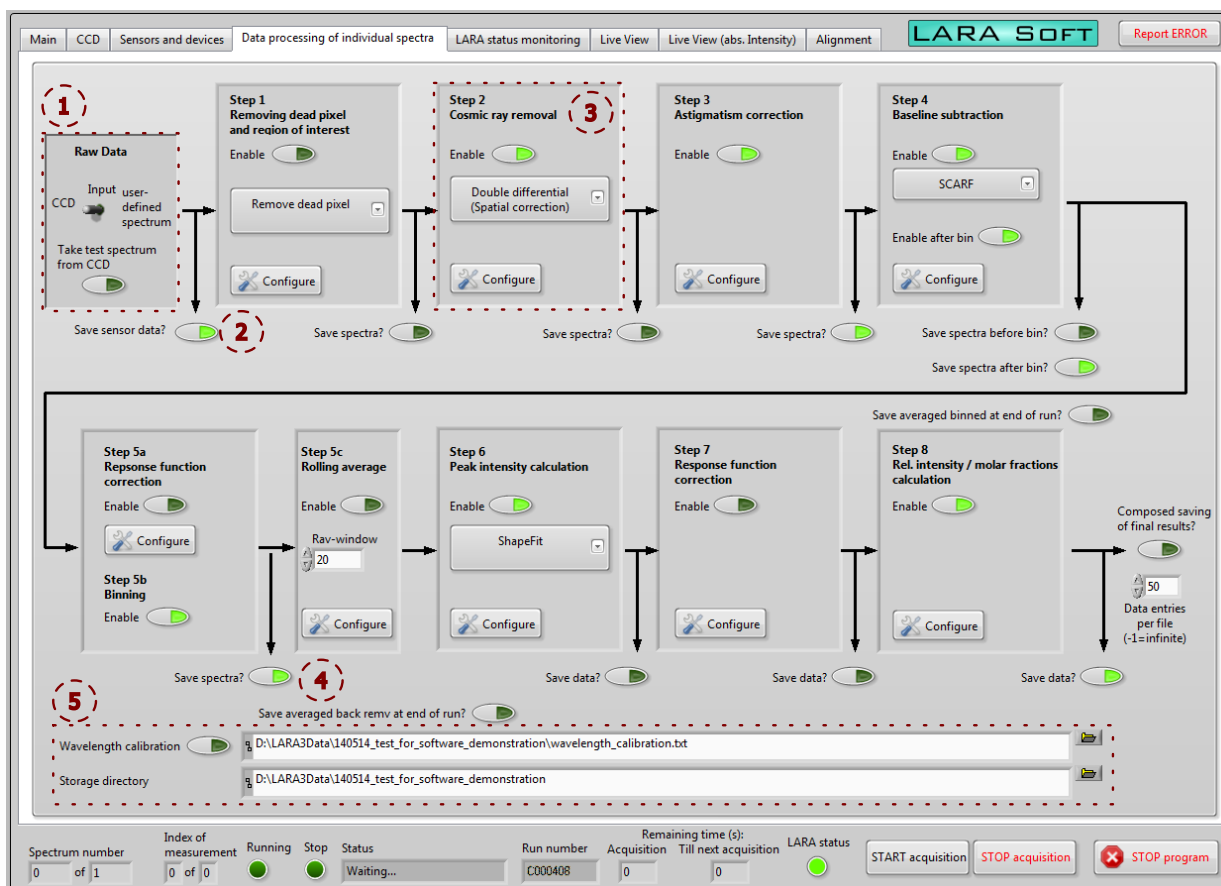


**Figure 6.5.: 'Data processing of individual spectra' tab of LARASoft.** The algorithms for the quantitative analysis of the acquired Raman spectrum are activated and configured in this tab. The data flow is indicated by arrows (data stream) and boxes (data source, processing algorithm, and data sinks). (1) Choice of data source. CCD images acquired in real-time by the CCD detector or already existing raw data (stored on the computer) can be processed by LARASoft. (2) Button to define if the readings of the sensors and devices are stored. The CCR raw images are always stored to ensure a potential reanalysis. (3) Example of a data processing step (here: Cosmic ray removal). The algorithm can be enabled, i.e. applied to the data, or bypassed. If different methods are available for the processing step, these can be selected in the drop-down menu. Detailed parameter setting is available by the opening of a configuration dialogue (similar to the configuration of sensors and devices). (4) Button to enable storage of intermediate data. (5) Location of input file for wavelength calibration (pixel to wavelength conversion) and definition of storage directory where all data generated by LARASoft are stored.

- Step 1 - Dead pixel and region of interest correction** 'Dead' pixels are pixels with an abnormal response which can be excluded from the analysis by replacing the intensity value of the dead pixel by the intensity of the neighbouring pixel. The area of the CCD sensor to be analysed in the following steps can be reduced by setting a region of interest.
- Step 2 - Cosmic ray removal** Muons produced by interactions of cosmic radiation in the atmosphere can produce high pixel intensity when passing through the CCD detector. These pixels are identified and corrected using one of two available methods. The first method determines such pixels by the comparison of pixel intensities along the vertical, i.e. non-dispersive, axis of the CCD sensor. The second method compares every pixel with its counterpart in the spectrum taken before and detects cosmic rays by the clear rise of the pixel intensity.
- Step 3 - Astigmatism correction** Aberrations in the spectrometer cause astigmatism, which is a distortion of the spectral lines that worsens the resolution and signal-to-noise ratio in the spectrum. The astigmatism is characterised before the Raman measurement and then corrected for as described in [Lew07].
- Step 4 - Baseline subtraction** The baseline of the spectrum is, in general, non-flat, e.g. due to fluorescence in the fused silica windows of the LARA cell, and has to be subtracted before peak fitting. The routine employed in LARASoft is based on the rolling circle filter and described in detail in [Jam13c, Sch13b, Jam13a]. It can be applied before and after binning of the spectrum (see step 5b).
- Step 5a - Response function correction** The influence of the spectral sensitivity of the light collection and analysis system and the line strength functions of the hydrogen isotopologues have to be corrected in the Raman spectrum in order to determine not only relative Raman intensities but molar fractions, i.e. the concentration of the gas constituents [Rup12, Sch13b]. This correction is applied to each individual row of the CCD detector. The exact procedure for this correction is subject of ongoing work at the time of writing this work.
- Step 5b - Binning** Summation of pixels along the vertical, non-dispersive, axis of the CCD chip. This is obligatory for the next processing steps.
- Step 5c - Rolling average** A rolling average can be applied to the spectrum to average over many spectra that are acquired sequentially. This can be used for noise reduction in spectra that are acquired with short acquisition times [Rup14].
- Step 6 - Peak intensity calculation** The absolute Raman intensities are determined by simple summation of pixel intensities within a specified interval or by fitting with the ShapeFit routine of SpecTools.
- Step 7 - Response function correction** The step has the same purpose as step 5 but operates on the spectrum after binning. Typically, this type of correction is only applied once, i.e. either before (step 5a) or after binning (step 7).
- Step 8 - Relative intensity calculation** The absolute Raman intensities are converted into relative Raman intensities or molar fractions (if the response function correction is also applied).

As already mentioned before, the treatment of uncertainties is not yet fully implemented in LARASoft and but was still ongoing at the time of writing. It is intended to output the concentration values of the hydrogen isotopologues in conjunction with one statistical and two systematic uncertainties:

**Statistical uncertainty** The statistical uncertainty of the molar fractions, i.e. concentrations, of the hydrogen isotopologues are determined from several parameters: the fit uncertainties from the ShapeFit routine and the statistical fluctuations of the baseline in the spectrum.

**Systematic uncertainty related to 'calibration'** The response functions of the Raman system are needed to convert relative Raman intensities into molar fractions of the hydrogen isotopologues. Generally speaking, each response function consists of the spectral sensitivity of the Raman system and the line strength of the Raman line/branch (see 3.3) and has to be measured independently to the Raman spectra (for details see [Rup12, Sch13b]). The 'calibration' related systematic uncertainty of the molar fractions are calculated by propagating the uncertainty of the response function through the analysis procedures.

**Systematic uncertainty related to 'pre-analysis'** The analysis routines described before can introduce a systematic uncertainty, e.g. by imperfect baseline removal. This is accounted for in a second systematic uncertainty. If this systematic uncertainty is large in comparison to the one related to 'calibration' and if the analysis routines are further improved in the future, the data can be re-analysed to decrease the total systematic uncertainty.

### 6.3.5. Real-time view of Raman spectrum and gas composition

The tab 'Live view' (figure 6.6) shows the acquired Raman spectrum before and after baseline subtraction and the extracted Raman intensities or molar fractions (if the response function correction is applied). The Raman intensities or molar fractions are displayed as a time series, in bar charts and as numbers. This tab is therefore ideal to give direct feedback to the operators working at the inner loop.

### 6.3.6. Raw CCD image and focus mode

The task of the 'Alignment' tab (figure 6.7) is to display all relevant data during alignment of the light collection and analysis system. These are the raw CCD images before and after astigmatism correction, the binned Raman spectrum, and the maximum pixel intensity. A so-called 'focus mode' can be started which corresponds to a continuous acquisition, analysis and display of Raman spectra but without storage of data. The graphical displays in this tab are also updated during normal acquisition of Raman data.

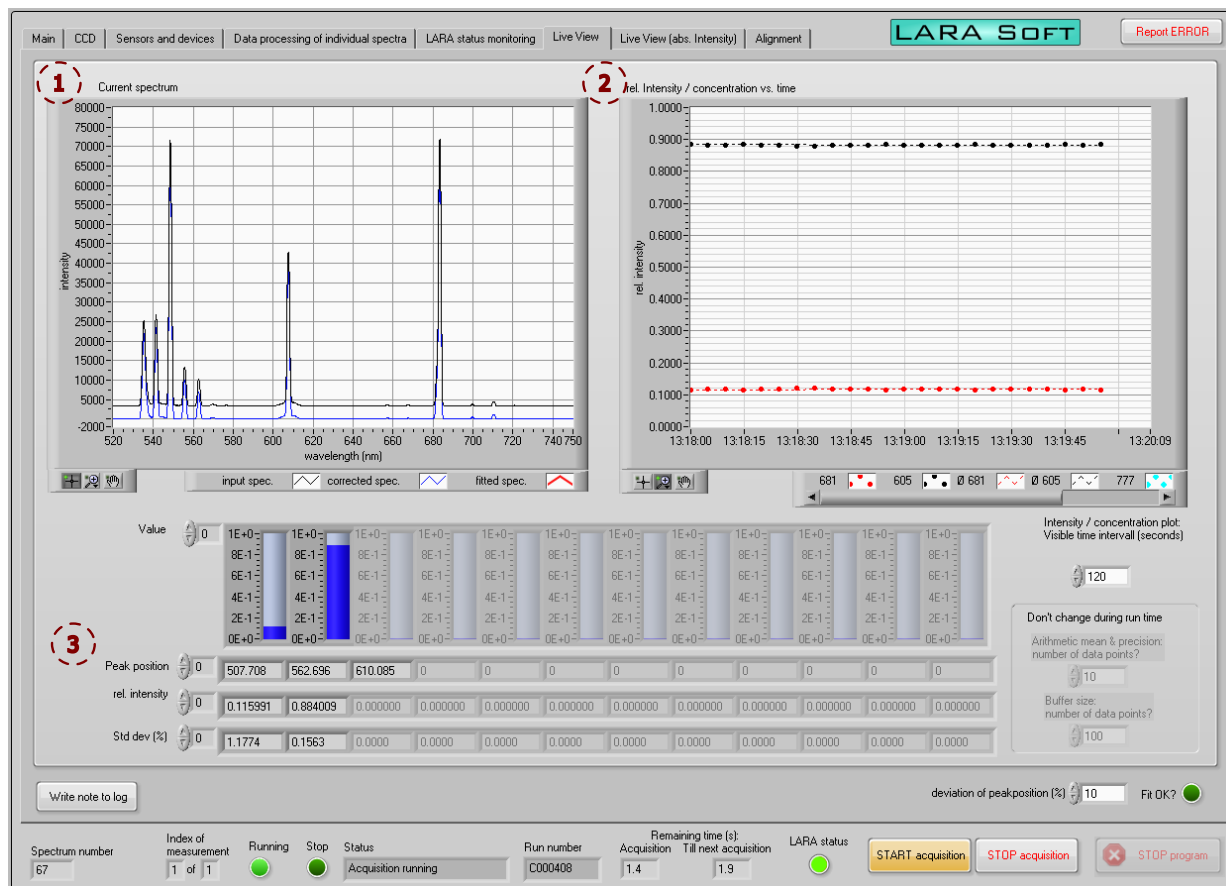


**Figure 6.6.:** 'Live view' tab of LARA Soft. This tab displays the acquired Raman data in real-time. (1) Example Raman spectrum ( $H_2$ ,  $N_2$  mixture) before (black) and after (blue) baseline subtraction. (2) Time series of relative Raman intensities or, if the spectral sensitivity correction is applied, of the molar fractions of the gas constituents. (3) Numerical display of results based on most recently analysed spectrum.

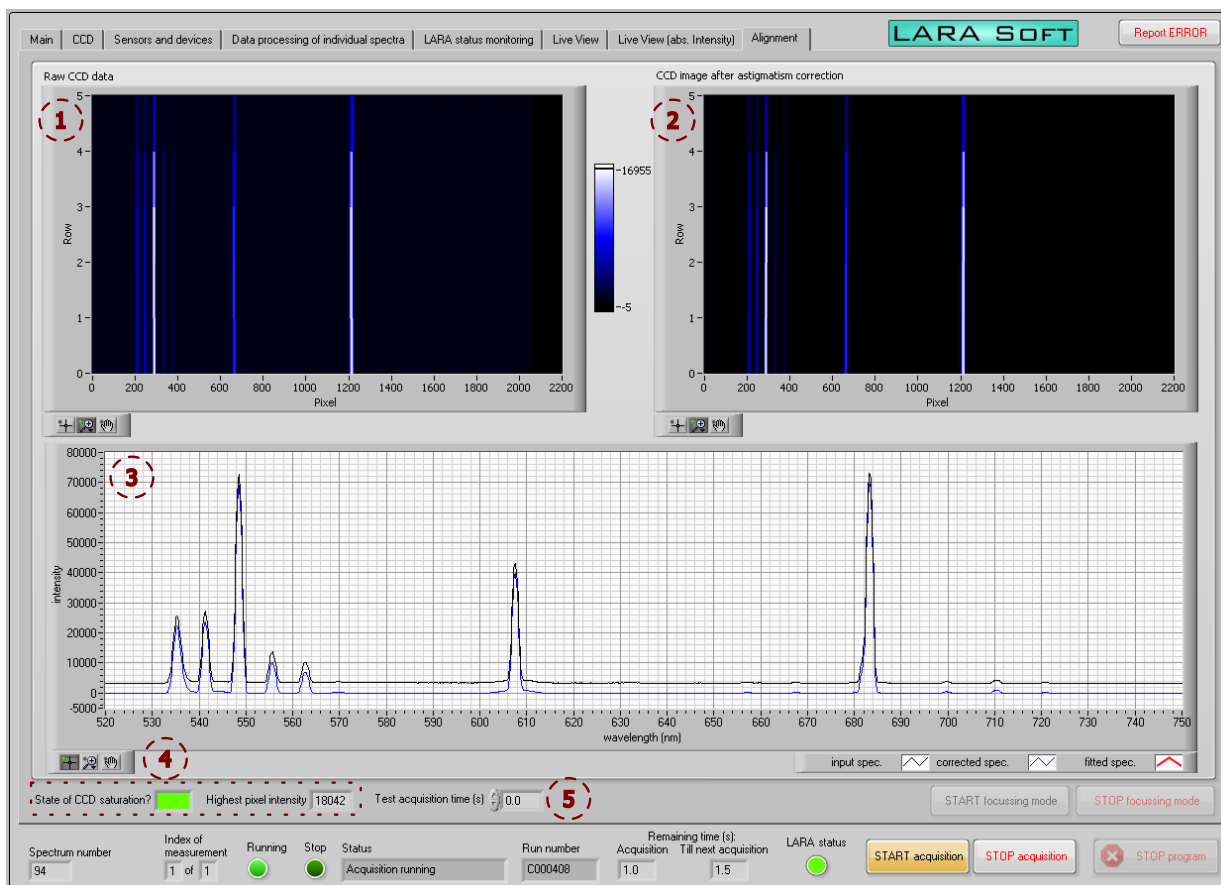


**Figure 6.7.:** 'Alignment' tab of LARASoft. The intended application of this tab is to support the operator during alignment of the Raman system. The raw (1) and astigmatism corrected (2) CCD images and the binned Raman spectrum (3) are displayed which allow the operator to judge the alignment of the light collection and analysis system. (4) Display of the maximum pixel intensity, e.g. for information during alignment and to ensure that the CCD detector is not saturated. (5) Acquisition time for alignment mode of LARASoft in which spectra are continuously taken and analysed but not stored.

### 6.3.7. Storage of settings in measurement templates

About 100 parameters have to be set in LARASoft to specify the acquisition of Raman data and the quantitative analysis of the spectra. In order to simplify the preparation of the system, a measurement template can be loaded into LARASoft (button on the 'Main' tab) which restores all parameters automatically. The measurement files are human-readable text files and hence also serve as a documentation of the settings in LARASoft. A measurement template is generated automatically at the start of every measurement run and stored in the same folder as the Raman data. An excerpt of a measurement file is shown below.

```
[Global_variables_Acquisition_Settings]
non stop measuring? = TRUE
Acquisition time (s) = 29.500000
Measurement period (s)_0 = 30.000000
Description (short) = "LARA3_tritium_filling_of_LOOPINO"
Description (long) = "LOOPINO was evacuated before filling with pure tritium from
ISS. Purity expected > 95%. Fitted peaks are: T2, DT, D2, HT, HD, H2, N2."
Run number = "C00000148"
```

### 6.3.8. Connection of LARASoft to the KATRIN data acquisition and management framework

The Raman data has to be automatically uploaded into the global data framework of KATRIN during neutrino mass measurement runs. Besides the integration of routines into LARASoft to access the KATRIN data handling framework, it is also necessary to uniquely label every output of the analysis routines and each sensor reading. This is done via the KATRIN identifiers which were already introduced in table 4.3 to label the sensor reading. Accordingly, all outputs of LARASoft (spectra, values, status labels, etc) are labelled (example shown in table 6.1). The integration of LARASoft into the KATRIN data framework is not yet fully established but ongoing work at the time of writing and is expected to be finished in the autumn 2014.

## 6.4. Evaluation of software performance with respect to KATRIN

In LARASoft, each CCD image is analysed during the acquisition of the following one (figure 6.8). In order to prevent pile up of data in the analysis chain of LARASoft, the duration of the spectrum analysis has to be shorter than the acquisition time (when neglecting the auto-adjustable pause between sensor read-out and the next time exposure). Therefore, the run time of LARASoft was tested by F. Kassel under selected experimental and data analysis parameters [Kas12]. It has to be noted that the auto-adjusting pause shown in figure 6.8 was not yet implemented at that time. The most relevant findings are summarised below:

**Table 6.1.: Example for labelling of analysis results.** All *zzzz* numbers are preceded by '611-RCR-8-0002-' to form a KATRIN-wide unambiguous identifier number. For each concentration value, one statistical and two systematic uncertainties are defined (description in section 6.3.4). All uncertainties are given in percentage points, i.e. in the same unit as the concentration value.

<i>zzzz</i>	Description	Name
0002	Concentration of T <sub>2</sub> (%)	CON_T2
0102	Stat. uncer. of T <sub>2</sub> concentration	CON_T2_stat_uncer
0202	Syst. calibration uncertainty of T <sub>2</sub> concentration	CON_T2_sys_cal_uncer
0302	Syst. pre-analysis uncertainty of T <sub>2</sub> concentration	CON_T2_sys_prean_uncer
0005	Concentration of HT (%)	CON_HT
0105	Stat. uncertainty of HT concentration	CON_HT_stat_uncer
0205	Syst. calibration uncertainty of HT concentration	CON_HT_sys_cal_uncer
0305	Syst. pre-analysis uncertainty of HT concentration	CON_HT_sys_prean_uncer

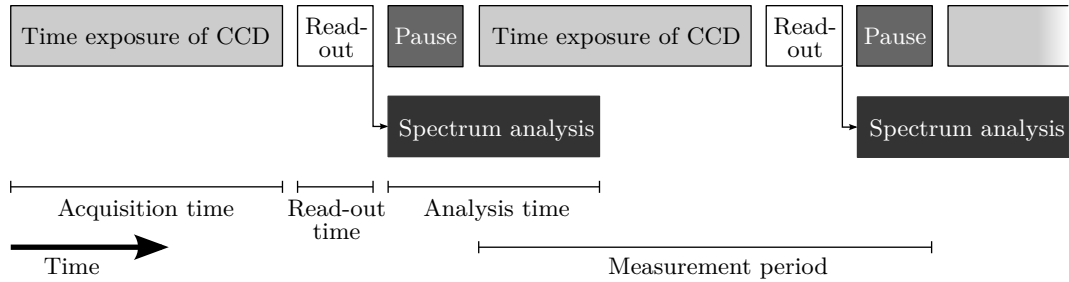


**Figure 6.8.: Schematic overview of the continuous data acquisition and analysis.** The CCD sensor is read-out after the time exposure. The length of the pause is automatically adjusted such that the set value of the measurement period is met. The spectrum analysis is performed simultaneously to the acquisition of the next spectrum. The length of the boxes are not to scale. The labels of the indicated periods are used in the main text.

- The read-out time consists of a constant contribution (about 0.1 s) and a contribution that rises with increasing number of pixels to be read-out. The constant contribution is attributed to general control sequences for the read-out of the CCD sensor. The variable contribution is caused by the sequential read-out of the pixels with a rate of 100 kHz. If no on-chip binning was used,  $512 \times 2048$  pixels would have to be read-out which takes about 10 s. For a typical setting of 5 binning groups, i.e.  $5 \times 2048$  effective pixels, the overall duration is only about 0.1 s.
- The analysis time is dominated by the ShapeFit procedure and depends in particular on the number of lines that are fitted simultaneously. The analysis time is on average less than 0.2 s if only one line is fitted but rises to about 0.8 s if 10 lines are fitted per spectrum. A linear dependence is found between analysis time and the number of lines fitted as long as the spectral lines are not affected by the noise level in the spectrum.
- Saving of the intermediate results after each processing step in LARASoft and the number of sensors to be read-out do not significantly influence the analysis time.

It can be concluded from the tests by F. Kassel that the CCD sensor read-out causes a minimum gap of about 0.2 s between two time exposures of the sensor if 5 binning groups are used. In order to be independent of the number of binning groups<sup>3</sup>, the measurement period is constrained to be at least 0.5 s longer than the acquisition time. A conservative estimate for the maximum duration of the spectrum analysis is 2 s, although in most cases less than 1 s is achieved. Combining both conservative estimates, a minimum measurement period of 2.5 s is suggested which is fully sufficient to operate the system with about 10–20 s acquisition time as projected for the neutrino mass measurement runs. Nevertheless, the system still can be operated at faster repetition rates, if it is ensured that the duration of the analysis routines is short enough or if a delay of the output of measurement results can be accepted.

In addition to the tests performed by F. Kassel LARASoft was also extensively used for the operation of all Raman systems at TLK. Three particular cases are noteworthy:

### **Operation with short measurement periods**

Raman measurements with an alternative sample cell design were performed using very short acquisition times of 0.1-0.5 s [Rup14, Jam14]. The analysis time was of the order of the acquisition time and hence measurement periods of less than 1 s could be achieved.

### **Operation within the scope of this work**

The commissioning measurements of the LARA3 system described in section 4.6 were performed with LARASoft. During the run, the system status monitoring system of LARASoft clearly indicated the laser power loss which was caused by window issues (section 4.6.3). This ensured that the operators were at every time aware of the increasing laser power loss in the system and could stop the measurement before more issues arose.

---

<sup>3</sup>More than eleven binning groups are typically not used. This is considered in the statement.

### **Long-term operation by non-expert personnel**

A Raman system was used at the Tritium Laboratory Karlsruhe to cross-calibrate an infra-red absorption experiment which aims at the compositional analysis of liquid hydrogen isotopologues mixtures [Mir14, Grö14]. Installation and commissioning of the Raman system at the experiment was done under the supervision of the author. Within this phase, also the measurement templates for LARASoft were generated. Afterwards, the Raman system was operated autonomously by the experiment operators on a daily basis over the course of about six months without significant need for support by Raman experts. Also for the analysis of the acquired Raman data, no support was necessary since the complete data analysis was done automatically and in real-time by LARASoft. This application demonstrates that a Raman system can be routinely operated by non-expert personnel using LARASoft.

The development of LARASoft is not yet finished: The handling of the spectral sensitivity correction and of measurement uncertainties will be amended in the next version. The connection of LARASoft with the global data handling system of KATRIN is ongoing work at the time of writing this work and but will hopefully be available for the next operation of the KATRIN Raman system. Nevertheless, the flexibility and maturity of the software has been demonstrated already at this stage. With LARASoft it is possible for the first time that a Raman system for high precision compositional analysis of tritium gas mixtures can be routinely operated by non-expert personnel. This is an essential step for the application of Raman spectroscopy within the KATRIN experiment but also for other applications beyond KATRIN.



## 7. Recommendations for the operation of the KATRIN Raman system

The KATRIN Raman system and similar Raman systems have been commissioned, operated and investigated in the last years within the scope of many theses [Lew07, Jam09, Sch09, Fis10, Stu10b, Bai11, Mir11, Sei11, Kas12, Rup12, Jam13a, Sch13b]. Valuable experience has been gained within these works, which led to the development of the KATRIN Raman system in its current state. The aim of this chapter is to briefly summarise recommendations for the operation of the KATRIN Raman system that can be concluded from this and other works.

The first section of this chapter focuses on aspects regarding the experimental setup while the second deals with the settings in LARASoft for data acquisition and analysis. Section 7.3 discusses which parameters should be monitored in particular during the operation of the system. Finally, a set of maintenance works and system checks that should be performed between two neutrino mass measurement runs are proposed in section 7.4.

### 7.1. Experimental aspects

#### **Double pass configuration**

The double pass configuration of the laser beam path using the optical isolator has been proven to be an effective and reliable option to increase the effective laser power and should therefore be permanently used.

#### **Laser operation**

The Finesse laser should be operated at reduced laser power, e.g. 3 W, to prevent damage of the LARA cell windows in double pass configuration and to increase the margin of the laser pump current, which was found in this work to steadily rise when being operated at full power.

#### **Optical coatings**

Different coatings with higher durability have been successfully tested "off-line", and it is proposed to use such coatings for all optical components which are exposed to the glove box atmosphere or tritium gas. If they perform as well as anticipated in the forthcoming LOOPINO tests, this coating type should become the standard for optical components in such environmental conditions.

### **Installation of additional instrumentation into the KATRIN Raman system**

A wavemeter for the continuous measurement of the laser wavelength is currently being commissioned and characterised [Her14]. In addition, a quadrant sensor for improved laser beam position measurements is under testing at the moment. Both sensors can easily be installed in the KATRIN Raman system and improve the monitoring capabilities.

### **Measures against laser-induced contamination**

In order to prevent laser-induced contamination several measures are suggested:

- Replacement of EBD coatings on LARA cell windows by magnetron sputtered coatings, which are less susceptible to laser-induced contamination.
- Depending on the results of the currently ongoing investigation [Wec14], occasional application of UV light and/or ozone could be employed. This could be used to prevent the formation of laser-induced contamination on optics inside the glove box where cleaning and replacement is not easily possible.
- Coverage of the inner surface of the laser enclosure with aluminium sheets to avoid evaporation of PVC in case of accidental laser back-reflection.

### **Installation of reference points in the beam path for alignment**

In order to simplify beam alignment and to improve the reproducibility of the beam path permanent reference points (e.g. pinholes) should be installed.

## **7.2. Data acquisition and analysis settings**

### **CCD parameters**

The CCD sensor should be operated with 5-7 binning groups, which is a reasonable compromise between noise reduction (the fewer binning groups the better), read-out time (the fewer binning groups the faster), and the ability to correct for aberrations of the optical components (the more binning groups the better). Other CCD parameters are chosen as before (sensor cooling to  $-75^{\circ}\text{C}$ , 100 kHz read-out rate and 'low noise' mode).

### **Acquisition time and measurement period**

Based on the results of this work an acquisition time of about 20 s is considered as sufficient to reliably fulfil the 0.1% relative precision requirement of KATRIN even when the laser power is reduced to 3 W. A further reduction of the acquisition time should in principle be possible, but cannot be accurately specified at this stage. However it is reasonable not to reduce the acquisition time significantly further in order to preserve a safety margin which ensures that the 0.1% relative precision requirement is met under all circumstances. The measurement period should be at least 0.5 s longer than the

acquisition time. Therefore an acquisition time of 19.5 s and a measurement period of 20 s is suggested.

### Operation ranges of system monitoring parameters

The ranges that define the status of the monitoring parameters ('ok'/'warning'/failure') in LARASoft have to be carefully chosen in order to be on the one hand, sensitive on detrimental effects but on the other hand to avoid regular false alarms due to statistical fluctuations. Of particular interest are the laser power measurements along the beam path and the laser pump diode current since these are sensitive to the most severe issues that were experienced up to now: loss of laser power due to coating degradation and laser-induced contamination, and the decrease of the lasing efficiency of the Finesse laser. For the Finesse output power (internally measured in the laser) very strict limits can be defined, e.g. 'warning' for relative deviations of more than 0.25%, which corresponds to five standard deviations of the laser beam power reading in section 4.5. For the two other laser power measurements (power meter and photo diode) and for the laser diode pump current it is suggested to set the limit for 'warning' at a relative deviation of 5% with respect to the laser power measured at the beginning of the run. The 'failure' state should be reached for a relative deviation by more than 10% from the nominal value. An example for the specification of the parameter ranges for the operation with 3 W laser power is shown in table 7.1.

### ShapeFit settings: Raman lines to be fitted

Besides the  $Q_1$  branches of the hydrogen isotopologues also the  $O_1$  and  $S_1$  branches of  $T_2$  should be fitted to be able to de-convolute the overlapping features in the spectrum (see next paragraph). In addition it is recommended to fit the  $\nu_1$  and  $\nu_3$  branches of the potentially arising tritiated methane species  $CT_4$ ,  $CDT_3$ , and  $CHT_3$ .

### ShapeFit settings: Line shape templates

There are two significant overlaps of spectral features in the Raman spectrum: The DT  $Q_1$  branch overlaps with the tritium  $S_1(J'' = 2)$  line and the deuterium  $Q_1$  branch overlaps with the tritium  $S_1(J'' = 5, 6)$  lines). In order to de-convolute these spectral features, not only a single line should be used as a line shape template, but the complete branches. In case of  $T_2$  the  $O_1$ ,  $Q_1$  and  $S_1$  branches should be used to generate the combined template since these branches will dominate the Raman spectra. However, only the area under the  $Q_1$  branch should be used for the quantitative analysis since the validity of the calibration procedure was only verified for this branch. This fitting method has been successfully applied within the scope of [Sch13b] where a clean HD Raman spectrum could be acquired from a spectrum of a  $H_2$ , HD,  $D_2$  gas mixture by the simultaneous subtraction of the  $H_2$  and  $D_2$  contributions. The challenge of this approach is to acquire the Raman spectra of the individual isotopologues.

**Table 7.1.: Example specification of parameter ranges for grading of system status.** The parameter ranges of the different grading states are defined for each sensor assuming the operation of the laser at 3 W. The nomenclature for the ranges of a parameter  $x$  is  $[a, b] = \{x \in \mathbb{R} \mid a \leq x \leq b\}$ . The grading algorithm is illustrated in figure 6.3. For boolean parameters, only the 'Failure' state is needed. The range of the 'Warning' state specified such that it cannot be reached. For the meaning of the nnnn and zzzz numbers see table 4.3 (page 78).

Device	Sensor value			Parameter range for grading					
Type	Name	nnnn	zzzz	Parameter	Unit	Nominal value	'OK'	'Warning'	'Failure'
Laser	Finesse	3010	0002	Laser operation mode	bool	1	[0.9, 1.1]	[0.1, 0.9]	[-0.1, 0.1]
			0003	Laser power	mW	3000	[2992.5, 3007.5]	[2950, 3050]	[0, 4000]
			0004	Pump diode current	%	83 <sup>†</sup>	[79, 87]	[75, 92]	[0, 100]
			0005	Laser head temperature	°C	26 <sup>†</sup>	[25, 27]	[23, 29]	[0, 40]
Chiller	MCR 150	3012	0002	Water temperature	°C	24	[23.95, 24.05]	[23.8, 24.2]	[0, 40]
			0003	No faults	bool	1	[0.9, 1.1]	[0.1, 0.9]	[-0.1, 0.1]
			0004	Fan failure	bool	0	[-0.1, 0.1]	[0.1, 0.9]	[0.9, 1.1]
			0005	Tank level low	bool	0	[-0.1, 0.1]	[0.1, 0.9]	[0.9, 1.1]
			0006	Pump failure	bool	0	[-0.1, 0.1]	[0.1, 0.9]	[0.9, 1.1]
			0007	Pump slow	bool	0	[-0.1, 0.1]	[0.1, 0.9]	[0.9, 1.1]
			0008	Pump off	bool	0	[-0.1, 0.1]	[0.1, 0.9]	[0.9, 1.1]
			Thermopile	LM-10	3030	0002	Laser power	mW	2700 <sup>†</sup>
0003	Horiz. beam position	mm				0 <sup>†</sup>	[-0.025, 0.025]	[-0.1, 0.1]	[-8, 8]
0004	Vert. beam position	mm				0 <sup>†</sup>	[-0.025, 0.025]	[-0.1, 0.1]	[-8, 8]
Photo diode	SM1PD1A	3040	0002	Laser power	V	0.3 <sup>†</sup>	[0.285, 0.315]	[0.27, 0.33]	[0, 10]
CCD	Pixis:2KB	3060	0002	CCD temperature	°C	-75	[-75.5, -74.5]	[-74, -76]	[25, -80]
Pt100	S1320	4060	0002	Breadboard temperature	°C	26 <sup>†</sup>	[25, 27]	[22, 30]	[0, 40]

<sup>†</sup> Estimated value only. Parameter ranges have to be adjusted to the actual nominal value during operation.

#### **ShapeFit settings: Constrains of the fit parameters**

The absolute Raman intensities which are determined by the ShapeFit procedure should be constrained to positive values to avoid negative (albeit small magnitude) Raman intensities as experienced in this work. Also the peak positions can be constrained around the expected value. The width of the allowed window depends on the wavelength stability of the Finesse laser which will be measured as soon as the wavemeter system is in operation.

### **7.3. Parameters to be monitored in particular during the operation of the KATRIN Raman system**

#### **Gas composition and tritium purity**

Naturally, the gas composition and the isotopic purity of the gas are of most interest during the operation of the Inner Loop.

#### **Laser pump diode current and laser power measurements**

The laser pump diode current and the laser power readings are crucial parameters of the system and should be closely monitored during the operation of the system. Stringent limits for the system status grading have been proposed in the section above. In addition to these it is meaningful to monitor the long-term trend of the laser pump diode current to detect slow degradation processes of the lasing efficiency even before a 'warning' state is reached.

### **7.4. Maintenance of the LARA system between two neutrino mass measurement runs**

#### **Measurement of the spectral sensitivity of the light collection and analysis system**

The spectral sensitivity of the light collection and analysis system should be measured directly after every run and compared to the spectral sensitivity that was measured before the previous one. If deviations are found, these must be taken into account in the analysis of the acquired Raman data, e.g. by a correction of the absolute values of the molar fractions or by an increase of the systematic uncertainty related to the spectral sensitivity.

#### **Check of integrity of optics**

The integrity of the optical components, i.e. the cleanness and surface quality, should be checked. Particular attention should be paid on the potential formation of laser induced contamination and back-reflections that were not present before the previous run.

### **Measurement of laser power along the beam path**

In conjunction with the check of the integrity of the optical components, the laser beam power should be measured along the beam path. The detection of a laser power drop after a specific optical element is a clear indication for an alteration of the component. This test should also be used to ensure that the laser internal power reading is consistent with the actual laser output power.

### **Check of beam alignment**

Even if no optics had to be touched in the aforementioned checks, a check of the beam alignment is strongly suggested. The beam position measurement during the previous run and the reference points installed in the beam path (e.g. apertures, targets; see section 7.1) allow one to evaluate whether a misalignment has occurred during the previous run and if realignment is necessary. It has to be kept in mind that the beam alignment is affected by the thermal conditions in and outside the enclosure and a stable beam position is achieved only after several hours of operation as it was shown in section 4.5 and 4.6.

### **Cleaning of optical components (if necessary)**

If necessary, optical components should be cleaned to prevent laser-induced damage in the forthcoming operation run. For minor organic contamination cleaning by duster spraying and a treatment by UV light and ozone (see section 5.3.3) could be sufficient. Mechanical cleaning which requires the touching or even removal of the optics from its mount should only be done when absolutely necessary as this will make a realignment of the relevant section of the beam path necessary.

### **Water level in the water chiller**

The water level in the water chiller circuit tends to slowly decrease due to evaporation of the water-ethanol mixture which is used as heat transfer medium. A regular check of the water level is therefore necessary to prevent the failure of the water chiller unit due to a low-level alarm during the next run.

### **Extrapolation of a (potential) trend of the laser pump diode current**

In case a trend of the laser pump diode current was observed in the previous run of the Raman system, the trend should be extrapolated to the end of the forthcoming run to estimate if negative effects have to be expected. In case an issue is anticipated for the laser operation a remote service can be performed by the manufacturer to assess if further actions are needed.

### **Wavelength calibration of the spectrometer**

The spectrometer should be wavelength calibrated after every measurement run to investigate if changes in the system have occurred.

### **Measurement of the spectral sensitivity of the light collection and analysis system**

If the alignment of the laser beam or of optics in the light collection system has been changed during maintenance, the spectral sensitivity should be re-measured at the end of the maintenance works.

### **Functional test of the laser interlock system**

The laser interlock system is essential for the safety during the operation of the Raman system. The functionality of the system should be tested by blocking of the photo diode during laser operation which triggers the automatic closing of the laser shutter. The threshold voltage at which the system triggers the shutter closing has to be adjusted in case the laser power or illumination of the photo diode was changed.

### **Activation of the laser interlock system**

Before the KATRIN Raman system is left for unattended operation, it has to be ensured that the laser interlock system is in operation. The jumper which bypasses the interlock system during maintenance work has to be removed and the interlock system activated.



## 8. Summary and outlook

The discovery of non-zero neutrino masses in oscillation experiments was the first definite proof for physics beyond the standard model of particle physics. Depending on their mass, neutrinos had a distinct influence on structure formation in the early universe. However, direct measurements of the fundamental neutrino mass scale have not yet been sensitive enough to provide a definitive value for the neutrino mass. The most stringent limits of about 2 eV (95% C.L.) were set by the Mainz and Troitsk experiments. The KATRIN experiment is designed to reach a sensitivity of 200 meV/c<sup>2</sup> (90% C.L.) and a 5 $\sigma$  discovery potential of 350 meV/c<sup>2</sup> and hence will be able to probe the neutrino mass scale to ranges relevant for cosmology and also help to scrutinise theoretical models of neutrino mass generation.

In order to achieve the design sensitivity of 200 meV/c<sup>2</sup>, it is essential to minimise and account for systematic effects in KATRIN. A set of systematic effects is connected to the purity of the tritium gas which will always contain, for technical reasons, traces of its isotopologues (DT, D<sub>2</sub>, HT, HD, H<sub>2</sub>). A variation of the gas composition on the one hand affects the overall count rate but also the shape of the  $\beta$ -spectrum near the endpoint. Therefore, it is necessary to continuously monitor the gas composition with a relative precision of 10<sup>-3</sup> and to include the actual gas composition into the neutrino mass data analysis.

Within the research and development works of the past years at the Karlsruhe Institute of Technology and Swansea University (Wales), three prototypes of Raman spectroscopy systems have been built for the inline and near to real-time analysis of the KATRIN source gas composition. Valuable experience was gained on the design, construction and operation of such systems. The aim of this work therefore was to setup and commission the Raman system that will actually be used for KATRIN on the premise to maximise the metrological performance of the system. Simultaneously, special care had to be taken to identify and keep under control all processes that might present a risk for the reliable operation of the system during the projected operation time of about five years.

The layout and the components of the KATRIN Raman system have been carefully chosen to optimise the metrological performance of the system, i.e. the relative precision and the level of detection, and to maximise the operation reliability. By installation of an improved laser system, laser power and beam pointing instabilities could be reduced to a negligible level. The collection optics were upgraded by achromatic lenses to reduce their influence on the spectral sensitivity of the light collection and analysis system. The effective laser power in the LARA cell was doubled by back-reflecting the laser beam after passing the cell the first time which increases the signal-to-noise ratio in the Raman spectrum.

The Raman system has been tested at the LOOPINO facility under realistic conditions, i.e. with circulating highly purified tritium gas (200 mbar total pressure, tritium purity  $\geq 90\%$ ). A level of detection of  $4.8 \cdot 10^{-3}$  mbar was achieved for 29.5 s acquisition time, i.e. traces of hydrogen isotopologues with a relative concentration of  $2.4 \cdot 10^{-5}$  can be detected. The level of detection has been improved by factor of five with respect to the most sensitive Raman system at TLK until now. In the Raman measurement, a relative precision of  $0.34 \cdot 10^{-3}$  was achieved for  $T_2$ , and  $4.8 \cdot 10^{-3}$  and  $7.8 \cdot 10^{-3}$  for DT and HT, respectively (partial pressures: 188 mbar  $T_2$ , 8.1 mbar DT, 3.5 mbar HT, 0.14 mbar HD). The 0.1% relative precision requirement of KATRIN was fulfilled for the dominating gas constituent  $T_2$  but at much shorter acquisition times than initially requested by the KATRIN experiment. The achieved improvements for the relative precision and level of detection demonstrate the success of the implemented optimisations for the KATRIN Raman system.

The anti-reflection coatings on the optics have to sustain intense laser irradiation over the course of months or even years. Also, they are located inside a nitrogen-filled glove box and they are in contact with tritium gas where also  $\beta$ -radiation and potential radio-chemical processes are present. A severe coating damage of the tritium-facing side of the LARA cell windows was experienced before the beginning of this work and clearly demonstrated that this issue must not be underestimated. The cause for the severe coating damage was found in a polytetrafluoroethylene (PTFE) polymer inside LOOPINO that has presumably formed corrosive hydrofluoride species when being exposed to tritium gas. After the removal of the PTFE component from LOOPINO, no coating damage was experienced any more.

In addition, harmful effects on optical coatings in glove box and tritium gas atmosphere have been studied. Electron-beam deposited coatings are in general more susceptible to environmental effects (variation of pressure, oxygen concentration, humidity) than dense coatings. This generic statement was also found to be valid in the context of durability of optical coatings in tritium gas. Electron beam deposited coating samples showed clear indications for coating alterations after already only about 10 days of exposure to tritium gas while still no indications were found on samples of ion assisted deposition, magnetron sputtered, and ion beam sputtering coatings even after 39 days. Therefore, electron-beam deposited coatings should not be used any longer in tritium environment. As the coatings of the LARA cell windows are currently based on this manufacturing technique, a batch of windows has been coated by magnetron sputtering and will be tested in the near future. It is expected that this will further reduce the risk of coating damages and hence increase the reliability of the KATRIN Raman system.

The study of harmful effects on coatings and the experience from the commissioning of the KATRIN Raman system have helped to foster the general understanding of coating-related effects which influence the KATRIN Raman system. This has led to a set of recommendations which will ensure that the Raman system can be reliably operated over extended periods while fulfilling the metrological requirements that are needed for the neutrino mass measurement runs of KATRIN. As a result, an acquisition time of 20 s and the operation of the laser at 3 W output power is suggested. This ensures that even short-term fluctuations can be monitored in the source while reliably fulfilling the  $10^{-3}$  relative precision requirement.

---

Thanks to the development and commissioning of LARASoft, the software for automated acquisition and analysis of Raman spectra, it is now possible for the first time that trained but non-expert personnel can operate a Raman system at the TLK. This is an essential step for the application of Raman spectroscopy in KATRIN.

In order to achieve the full operational readiness of the KATRIN Raman system, a few tasks still have to be completed:

- Implementation of the uncertainty handling in LARASoft and the establishment of the connection to the KATRIN data handling framework.
- Installation of reference points in the beam path for reproducible beam alignment after maintenance of the system.
- Test of the the ShapeFit routine with complete Raman branches as shape templates to disentangle the overlapping features in the Raman spectrum.
- Repeat-test of the Raman system at the LOOPINO facility using LARA cell windows with the magnetron sputtered window coatings.

These tasks are currently being approached by the KATRIN Raman group and are expected to be completed by the end of 2014. However, even at the present stage, Raman spectroscopy is not only a technique that can in principle be applied for gas compositional analysis but has become a reliable method that can be routinely employed in KATRIN, even by non-expert personnel. This is an important step on the track towards the neutrino mass measurement with the KATRIN experiment.

The development of Raman spectroscopy systems at the Tritium Laboratory Karlsruhe is motivated by the application within the KATRIN experiment. Apart from the primary task in KATRIN, also other areas of application exist and still arise for such Raman spectroscopy systems. It is anticipated that Raman spectroscopy will become a standard analytical tool within the Tritium Laboratory Karlsruhe (TLK) and it will help to monitor tritium experiments or to cross-calibrate other analytical systems. This was already successfully achieved for an infra-red absorption spectroscopy system which is currently being developed at TLK in the context of nuclear fusion [Woz14, Mir14, Grö14]. Raman systems like the one commissioned in this work can also be beneficially applied in the fuel cycle of future nuclear fusion power plants where accurate tritium accountancy and near to real-time process monitoring are essential for legal, operational but also scientific aspects. For these reasons, it is intended to install a Raman spectroscopy system in the experimental fusion reactor ITER which is currently being built in Cadarache, France [Sch13b]. The detection of atomic emission lines of helium with a Raman system might also have opened a door for tritium accountancy in helium gas streams which arise from the tritium breeding blankets of a fusion reactor. First steps towards a quantitative analysis of such mixtures have already been done [Sch14a].

Thus, the physics potential of Raman spectroscopic systems like the KATRIN system can still be expanded. Also, within astroparticle physics, new applications might arise in the future, e.g. when searching for heavy sterile neutrinos in the tritium  $\beta$ -spectrum.



## A. Proposed system for simple and reliable wavelength calibration

A system for the simple and reliable wavelength calibration of the KATRIN Raman system is proposed. The aim of this extension of the KATRIN Raman system is to simplify the process of wavelength calibration for the operators during the maintenance periods of the system between two neutrino mass measurement runs. This should increase the reliability of the system as the risk of misalignment of optical components is minimised. A CAD drawing of the system is shown in figure A.1.

The light of the mercury argon calibration light source (e.g. Ocean Optics, Hg-1) is fed via an optical fibre into the enclosure of the Raman system and collimated by an achromatic lens to a beam with about 7.2 mm diameter which is slightly larger than the width of the fibre bundle to be illuminated. A permanently installed mirror is tilted

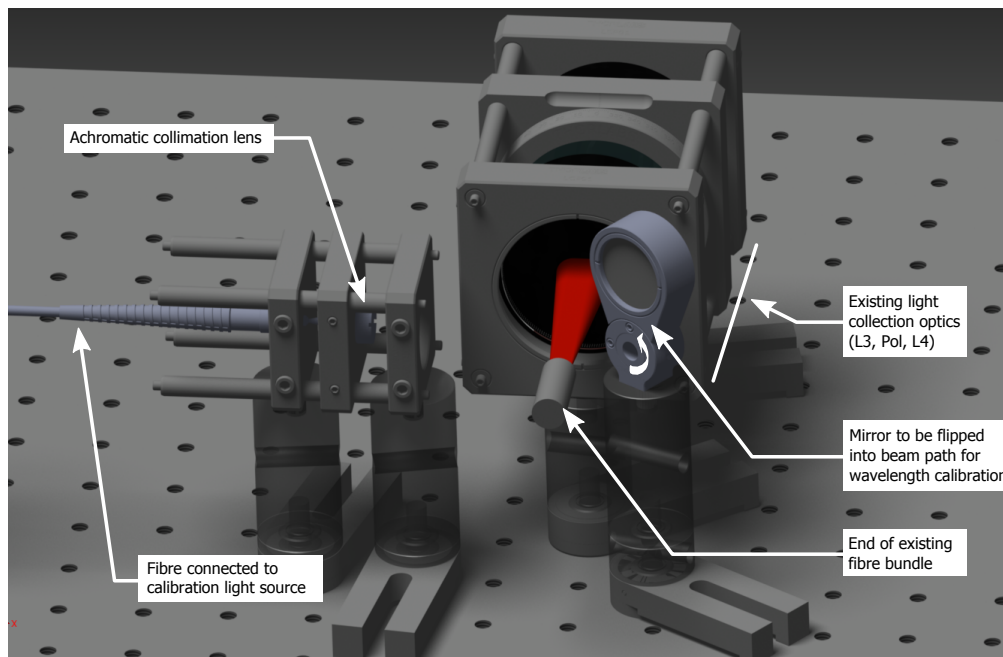


**Figure A.1.: CAD visualisation of proposed system for wavelength calibration of the HTS spectrometer.** Additional optics are installed next to the already existing collection optics (achromatic lenses L3 and L4 and polariser mounted in large cage system) and fibre bundle: The fibre holder and collimation lens (mounted in cage system) and the mirror to be flipped into the collection light path for wavelength calibration. The mirror does not interfere with the field of view of the fibre bundle (indicated by red rays) during normal Raman measurements. More details in main text.

**Table A.1.: Main components of the proposed wavelength calibration system.**  
 Manufacturer of all components: Thorlabs.

Type	Name	Comment
Fibre	M19L01	Multimode, solarisation resistant, 1 m 200 $\mu\text{m}$ core diameter, 0.22 NA, SMA
Fibre mount	SM1SMA	
Achromatic lens	AC080-016-A-ML	f=16 mm, effective aperture 7.2 mm
Mirror	BB1-E02	400–750 nm high reflectivity coating
Flip mount	TRF90/M	

into the light collection beam path between the second collection lens (L4) and the fibre bundle to temporarily guide the collimated light beam onto the fibre bundle end. After wavelength calibration, the mirror is tilted into its initial position and locked. In this configuration, the mirror does not reach into the aperture of the fibre bundle which was determined to have an opening angle of about  $5^\circ$  [Sch13b] and hence ensures that there is no negative impact on normal Raman measurements. The main optical components are listed in table A.1. The setup and alignment of the individual components is illustrated in figures A.2, A.3, and A.4. The components in the drawings are labelled according to their manufacturers names.

With the proposed system, only one mechanical operation has to be executed in the optical system for wavelength calibration which simplifies the effort and reduces the risk for operation errors. The proposed setup is being commissioned at the time of writing this work and will be permanently installed in the KATRIN Raman system if proven to be effective and reliable.

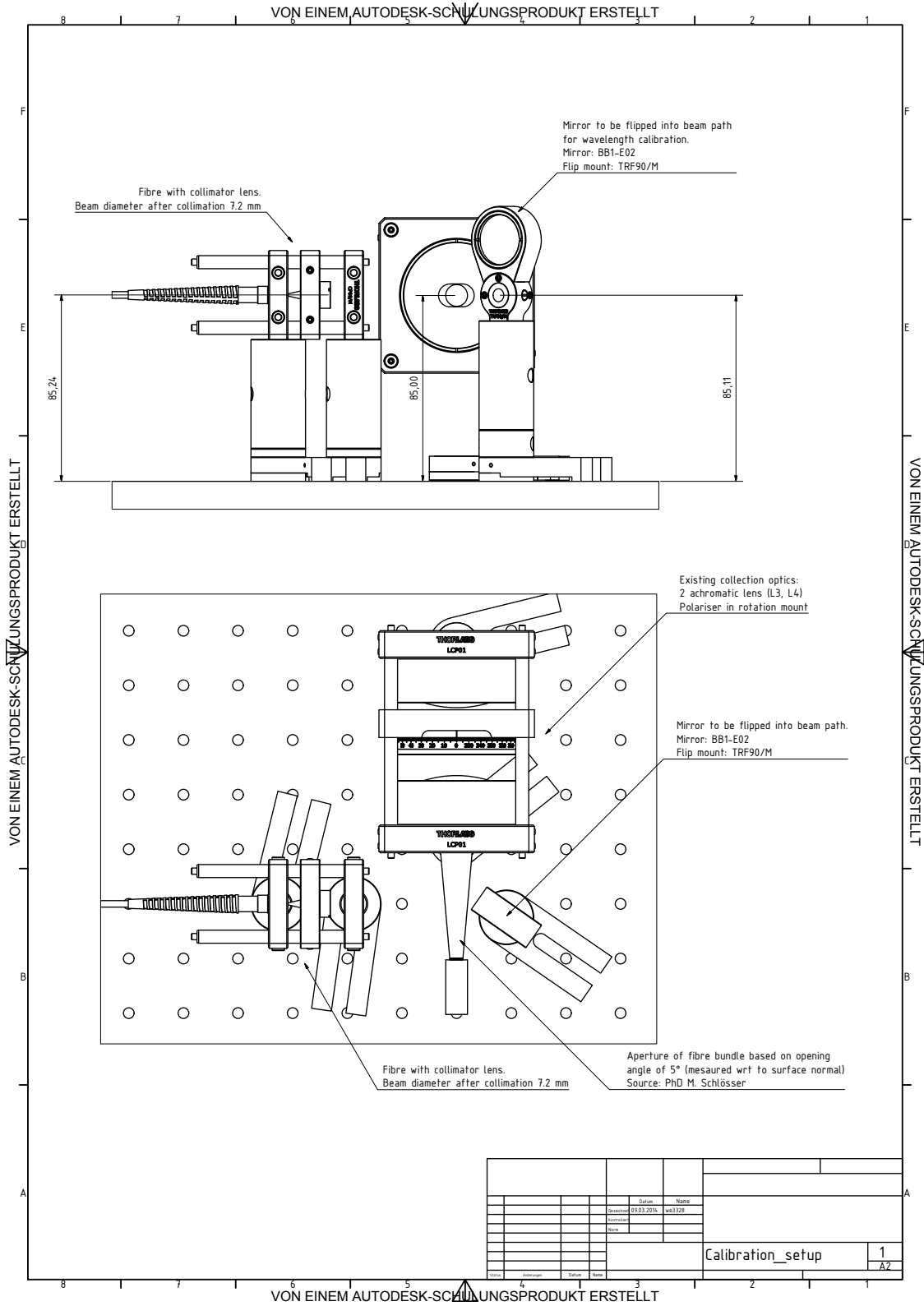


Figure A.2.: Overview drawing of system for wavelength calibration.

A. Proposed system for simple and reliable wavelength calibration

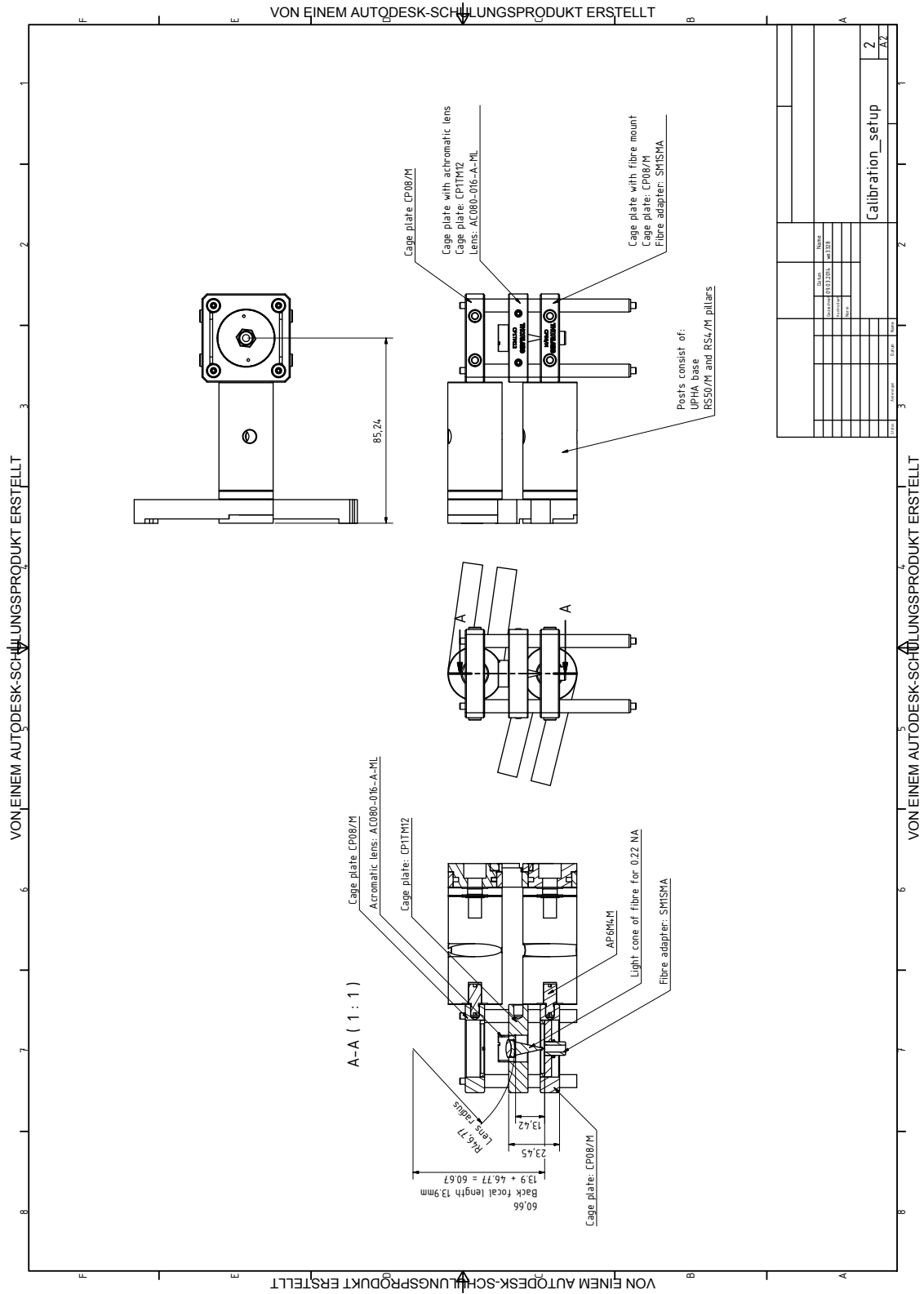


Figure A.3.: Drawing of the fibre mount with collimation lens.





## B. Procedures and SpecTools settings for analysis of Raman data

This appendix summarises the procedures and software settings that were applied to analyse the data from the LARA3*pre* and LARA3 measurements (chapter 4). The analysis of the Raman spectra has been done using the SpecTools framework [Jam13c] and the LARAsoft package (chapter 6).

### B.1. LARA3*pre* run 1

The following procedures and analysis were done offline, i.e. after the measurement run.

- Acquisition of 2 dark spectra, i.e. no laser excitation, to correct for potential light leakage into the enclosure the LARA3*pre* setup. The same experimental settings were chosen as in the actual Raman measurements (20 s acquisition time, CCD gain 3, read out rate 100 kHz, 5 binning groups).
- Cosmic ray removal of the dark spectra with SpecTools. Output: 2d array with  $5 \times 2048$  pixels.
- Pixel-wise subtraction of dark spectrum from acquired Raman spectra.
- Processing of a Raman spectrum to extract the D<sub>2</sub> peak shape that will be used by ShapeFit to fit the Q<sub>1</sub> branches in all spectra.
  - Applied routines: Region of interest, TCRR, RCS/SCARF, median baseline
  - Region of interest: x: 0–2047, y: 0–4
  - TCRR threshold: 200
  - RCF/SCRAF: 2 iterations, SG polynomial 3, baseline 0. Iteration 1: radius 100, SG sidepoints 100. Iteration 2: radius 120, sidepoints 140.
  - Median baseline interval
    - Data from single pass configuration: 1760–2049
    - Data from double pass configuration: 1900–2049

Resulting numerical peak shape intensity profile: 633.20704 960.23224, 1748.75938, 3787.78831, 5947.81889, 8459.85094, 12127.38428, 21543.41872, 33445.45405, 40765.49004, 37447.52646, 26238.56193, 14579.59534, 6817.6265, 2838.65522, 1060.18127

- Repetition of described SpecTools analysis for all Raman spectra, now also with ShapeFit routine:
  - Peaks to be fitted: 3
  - Consecutive parameters: yes
  - Baseline and positions: free
  - Fit range 750–1250
  - Max. iterations  $10^5$
  - Tolerance  $10^{-6}$ .
  - Peak 0: intensity 0.1, position 810
  - Peak 1: intensity 1, position 1002
  - Peak 2: intensity 0.5, position 1183

## **B.2. LARA3pre run 2**

The following procedures and analysis were done offline, i.e. after the measurement run.

### **B.2.1. Pre-processing and generation of necessary correction files**

- Acquisition of a neon line spectrum using a calibration light source.
- Generation of the astigmatism correction file using the 'Astigmatism-array-creator.vi' tool of SpecTools based on the neon line spectrum. Applied clipping bounds: (492,508), (510,528), (635,652), (684,698), (733,750), (935,953), (956,972), (1002,1021), (1060,1082), (1090,1110), (1250,1280), (1330,1365), (1455,1485), (1515,1545), (1695,1725), (1750,1765), (1790,1825)
- Wavelength calibration by line fitting in neon spectrum and allocation of literature values from [Kra13]. Fitting of third order polynomial to (pixel,wavelength) data set
- Extraction of peak shape of 659.89528 nm line from neon spectrum (necessary for ShapeFit routine) since line is close to the HT Q<sub>1</sub> branch, i.e. in the centre of the relevant part of the spectrum, well separated from other lines and has reasonable intensity. Subtraction of non-zero baseline below line.

### B.2.2. SpecTool analysis of Raman spectra in batch mode of SpecTools

- Applied routines: Dead pixel removal, region of interest, TCRR, Astigmatism correction, RCS/SCARF, median baseline, ShapeFit.
- Dead pixel removal: (1802,3) (1803,4)
- Region of interest: x: 10–2047, y: 0–4
- Astigmatism correction using astigmatism file generated before.
- TCRR threshold: 1800
- RCF/SCRAF: 2 iterations, SG polynomial 3, baseline 0. Iteration 1: radius 80, SG sidepoints 30. Iteration 2: radius 120, sidepoints 100.
- Median baseline interval: 1420-1500
- ShapeFit parameters:
  - Peaks to be fitted: 14
  - Consecutive parameters: no
  - Baseline: fixed, positions: free
  - Fit range 0–2047
  - Max. iterations  $10^5$
  - Tolerance  $10^{-6}$ .
  - Constraints: False
  - Peak 0: T<sub>2</sub>, intensity 1.7, position 655
  - Peak 1: DT, intensity 0.3, position 727
  - Peak 2: D<sub>2</sub>, intensity 0.1, position 790
  - Peak 3: HT, intensity 1, position 924
  - Peak 4: HD, intensity 0.17, position 984
  - Peak 5: H<sub>2</sub>, intensity 0.2, position 1167
  - Peak 6: He(587.56 nm), intensity 0.1, position 490
  - Peak 7: H(656.28 nm), intensity 0.05, position 961
  - Peak 8: He(667.82 nm), intensity 0.3, position 1047
  - Peak 9: Unknown(678.43 nm), intensity 0.15, position 1135
  - Peak 10: He(706.52 nm), intensity 0.2, position 1355
  - Peak 11: He(728.13 nm), intensity 0.1, position 1540
  - Peak 12: Overlapping line 1 with HD, intensity 0.1, position 997

- Peak 13: Overlapping line 2 with HD, intensity 0.1, position 1010

### **B.3. LARA3 run C148**

The analysis of the Raman data was done with LARAsoft in real-time, i.e. automatically and during data taking: The relative Raman intensities were calculated within less than 1 s after the acquisition of each Raman spectrum.

- Read-out sensors and devices: Finesse laser, Photo diode voltage, enclosure temperature, LM-10 power meter, water chiller
- Applied routines: Dead pixel removal, region of interest, TCRR, Astigmatism correction, RCS/SCARF, median baseline, ShapeFit, Calculation of relative Raman intensities.
- Acquisition time: 303; Measurement repetition period: 30 s.
- Dead pixel removal: (334,0), (334,1), (334,2)
- Region of interest: x: 0–2047, y: 0–11 (11 binning groups)
- Astigmatism correction using astigmatism file generated before.
- TCRR threshold: 200
- RCF/SCRAF: 2 iterations, SG polynomial 3, baseline 0. Iteration 1: radius 50, SG sidepoints 100. Iteration 2: radius 80, sidepoints 120.
- Median baseline interval: 1800–2000
- ShapeFit parameters:
  - Peaks to be fitted: 6
  - Consecutive parameters: no
  - Baseline: fixed (100), positions: free
  - Fit range 0–2047
  - Max. iterations  $10^5$
  - Tolerance  $10^{-6}$ .
  - Constraints: False
  - Peak 0: T<sub>2</sub>, intensity 5, position 684
  - Peak 1: DT, intensity 0.1, position 751
  - Peak 2: D<sub>2</sub>, intensity 0.1, position 827
  - Peak 3: HT, intensity 0.1, position 960
  - Peak 4: HD, intensity 0.1, position 1019
  - Peak 5: H<sub>2</sub>, intensity 0., position 1194

- Peak 6: N<sub>2</sub> branch / O<sub>1</sub> line of T<sub>2</sub>, intensity 0.1, position 651
- Calculation of relative intensities using peaks 0–5



## C. Calculation of beam sizes and power densities for Gaussian beams

The (linear) power density was used in section 4.6.3 (page 112 ) to evaluate if the experienced coating damages were caused by laser-induced processes. It is necessary for this evaluation to calculate the beam width of the Gaussian laser beam at various positions between the focus lens and the focus point inside the LARA cell. This appendix gives an overview how these calculations were performed.

### Prerequisites

The distances of the components of interest (focus lens, the Appendix window W1, and the cell window L1) to the focus point are indicated in figure C.1. The beam diameter at the focus lens is  $d = 2.07$  mm [Las11]. The calculation is based on the concept of Gaussian beams (figure C.1, right) and follows the treatment in [Trä07].

### Calculation of beam diameter as function of position $z$

The beam waist  $w_0$  can be calculated from experimental parameters [Trä07, eq. (3.339)]

$$w_0 = \frac{2\lambda f}{\pi d} = 33.5 \mu\text{m} \quad (\text{C.1})$$

where  $\lambda = 532$  nm is the wavelength of the light,  $f = 250$  mm the distance to the focus lens and  $d = 2.07$  mm the beam diameter at the focus lens . The beam width  $w(z)$

$$w(z) = \sqrt{w_0^2 + \frac{\lambda^2 z^2}{\pi^2 w_0^2}} \quad (\text{C.2})$$

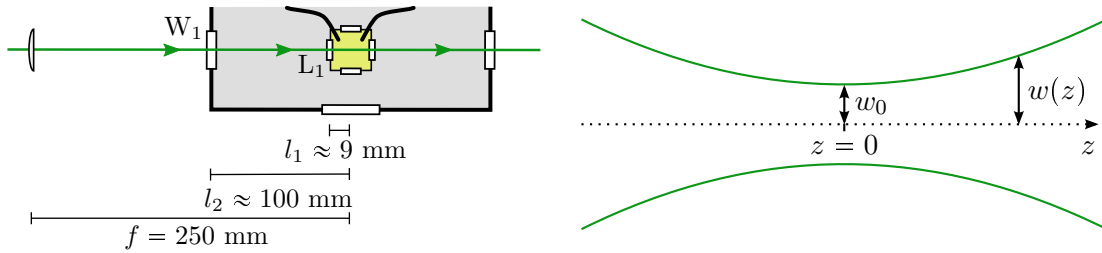


**Figure C.1.: Prerequisites for calculation of beam diameter.** *Left:* Distances of optical components with respect to focus point.  $l_1$ : LARA cell laser window  $L_1$ .  $l_2$ : Appendix window  $W_1$ .  $f$ : Focus lens. *Right:* Beam waist of a Gaussian beam at the focus point. The beam width  $w$  reaches its minimum  $w_0$  at the focus point  $z = 0$ .

can be calculated at an arbitrary position  $z$  along the beam path [Trä07, eq. (3.337)].

### Calculation of (linear) power density

The linear power density at a certain position  $z$  is the ratio

$$\text{Linear power density} = \frac{P}{2w(z)} \quad (\text{C.3})$$

of the laser power  $P$  and the diameter  $d(z) = 2w(z)$  of the beam. The power density is the ratio

$$\text{Power density} = \frac{P}{\pi w(z)^2} \quad (\text{C.4})$$

of the laser power  $P$  and the area which is illuminated at a certain position  $z$ . Both types of power density can be calculated for the laser beam at the position of the optical isolator (OI, located before the focus lens, illuminated by the collimated, unfocused beam), the Appendix window  $W_1$  and the LARA cell window  $L_1$  using an effective laser power of  $P = 10$  W. The results are shown in table C.1.

**Table C.1.: Calculated laser power density at various positions in the LARA3 setup.** The optical isolator is located in the collimated, i.e. unfocused, beam.

	$z$ (mm)	Beam diameter $d(z) = 2w(z)$ (mm)	Linear power density (W/cm)	Power density (W/cm <sup>2</sup> )
Optical isolator (OI)	-	2.07	48.3	297.1
Appendix window ( $W_1$ )	100	~ 0.83	~ 120	~ 1840
Cell window ( $L_1$ )	9	~ 0.11	~ 904	~ 10 <sup>5</sup>

# D. Details on optical coatings employed in this work

## D.1. Coating samples in durability test

The durability of optical coatings has been tested in section 5.4. This appendix gives information on the structure (table D.1) and transmittance (figure D.1 and D.2) of the coatings that were employed in the test.

**Table D.1.: Details on the materials and structure of the coating samples.** The total thickness is the sum of the thicknesses of the individual layers. Source: Courtesy of LASEROPTIK GmbH, Garbsen, Germany [Ebe14].

Coating type		Material (Total thickness)	Item number	Substrate
#	Technique			
1	IAD	HfO <sub>2</sub> (496 nm) SiO <sub>2</sub> (699 nm)	01021UR1	SQ2
2	MS	Al <sub>2</sub> O <sub>3</sub> (4677 nm) SiO <sub>2</sub> (5505 nm)	11120M1	SQ2
3	IBS	Ta <sub>2</sub> O <sub>5</sub> (2333 nm) SiO <sub>2</sub> (3709 nm)	20120Q2	SQ2
4	EBD	Nb <sub>2</sub> O <sub>5</sub> (2723 nm) SiO <sub>2</sub> (3591 nm)	23120T1	SQ2

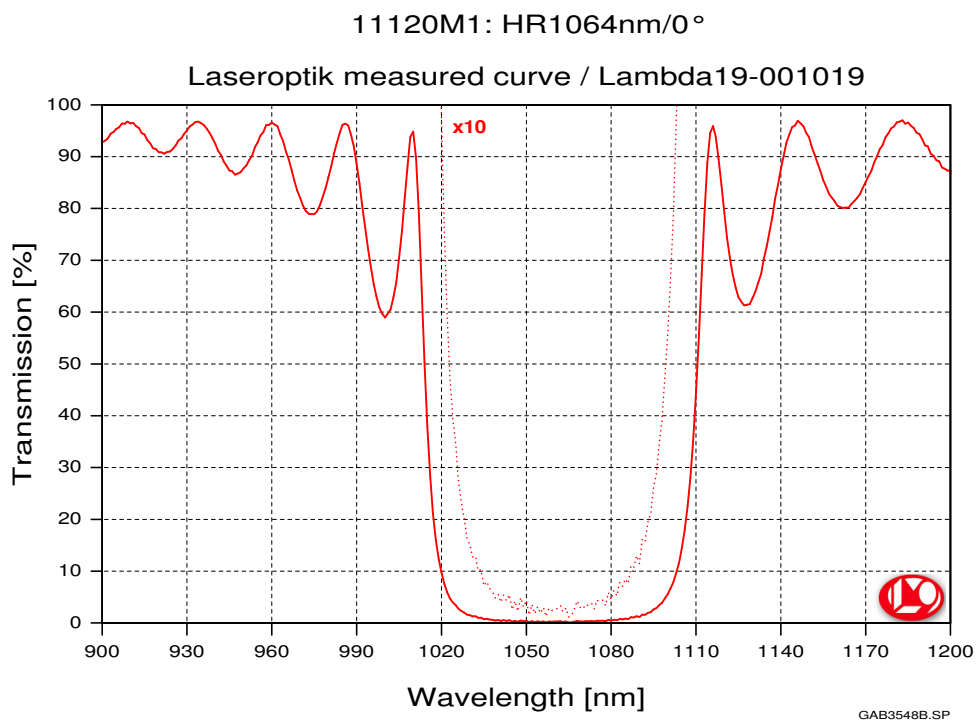
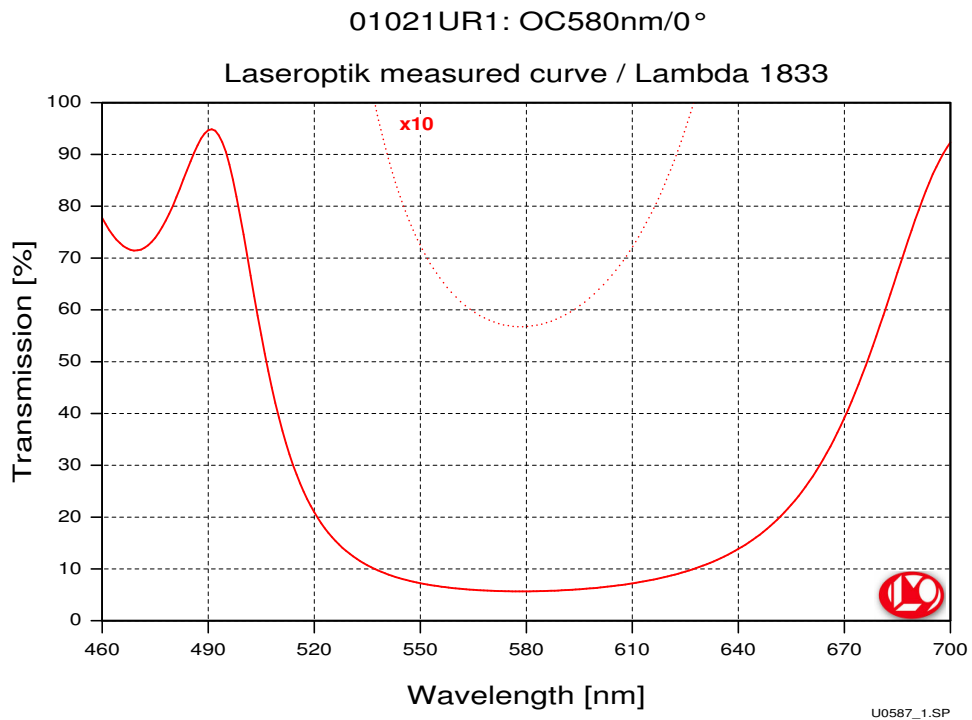


Figure D.1.: Transmittance plots of coating samples 1 (IAD, top) and 2 (MS, bottom). Courtesy of Heiko Hänsel, LASEROPTIK, Garbsen, Germany.

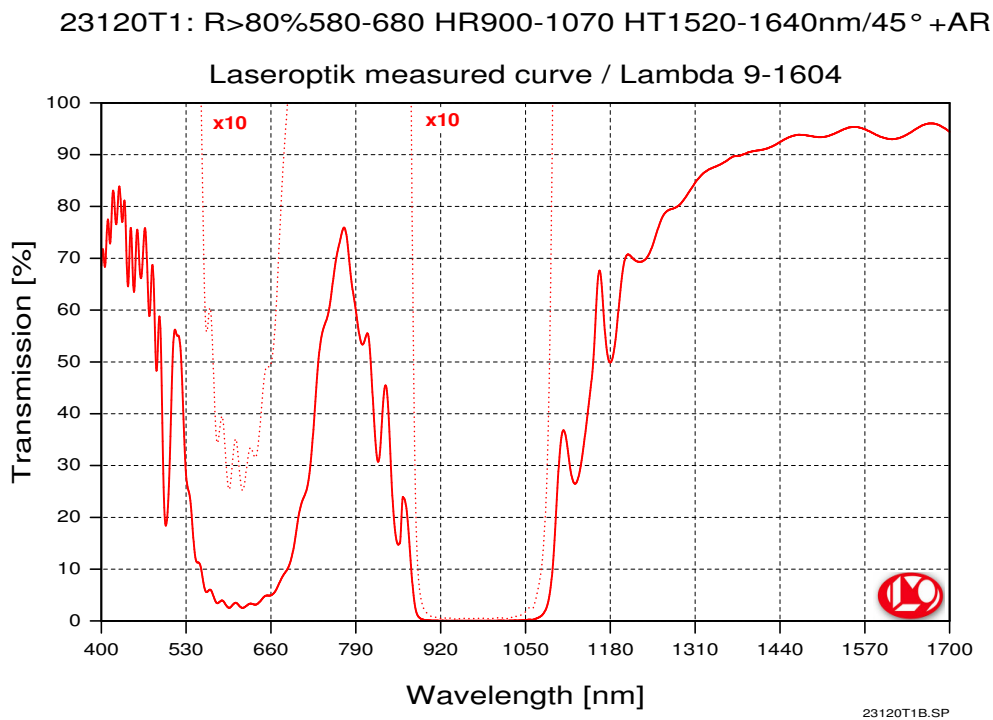
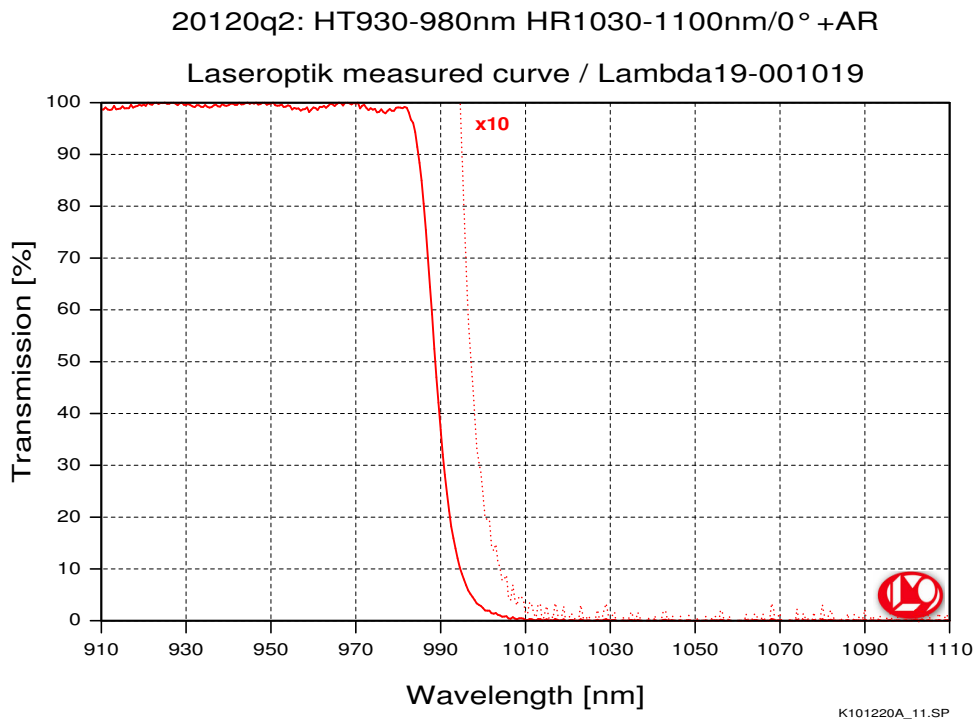
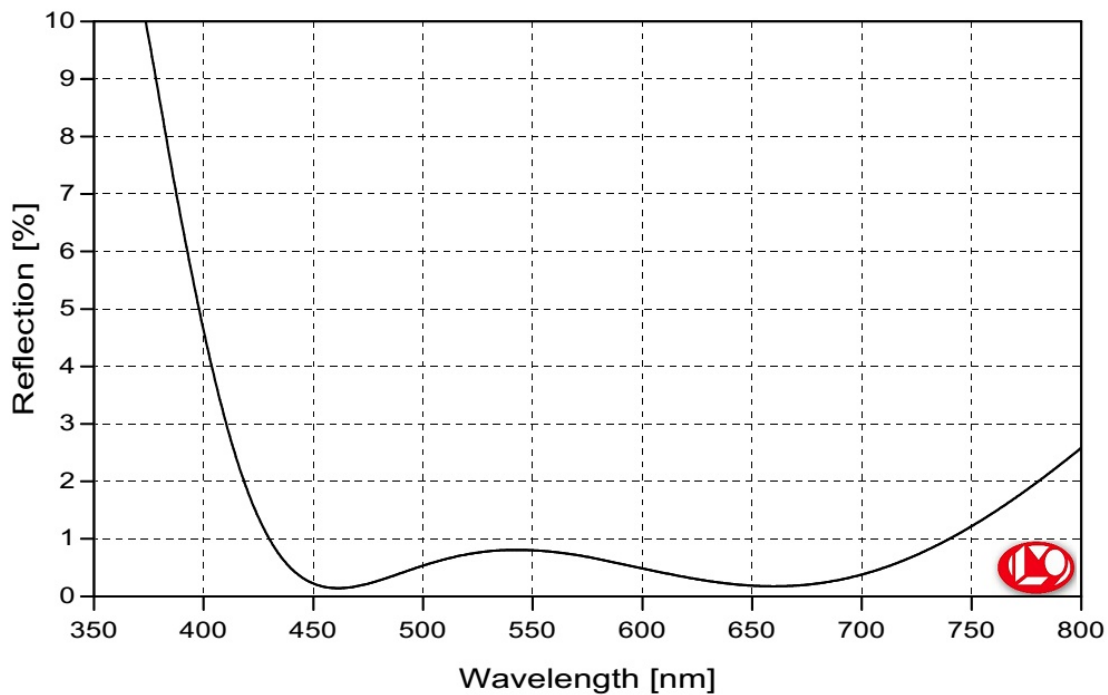
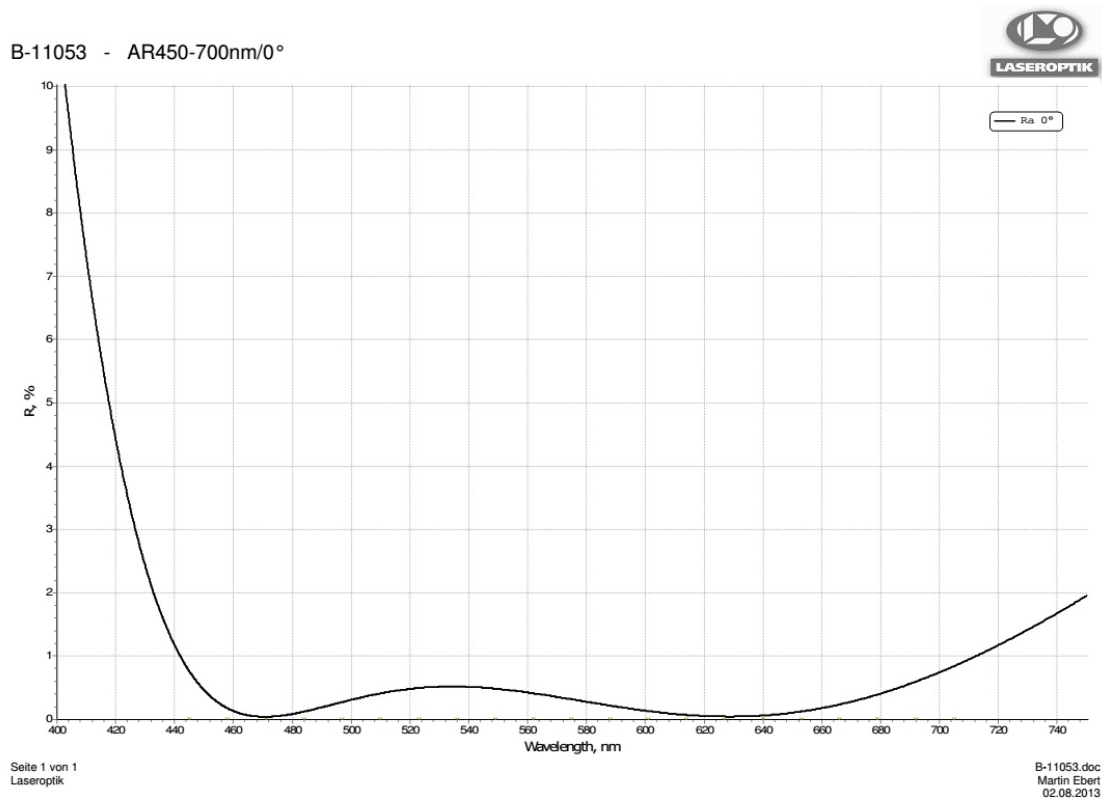


Figure D.2.: Transmittance plots of coating samples 3 (IBS, top) and 4 (EBD, bottom). Courtesy of Heiko Hänsel, LASEROPTIK, Garbsen, Germany.

## **D.2. Reflectance plots of improved coatings for LARA cell windows**

An improved scheme of optical coatings, mainly based on magnetron sputtering, was selected for the windows of the LARA cell (section 5.5). The reflectance curves (reflectance as a function of wavelength) of these coatings and the influence of the angle of incident are shown in figure D.3 and D.4.

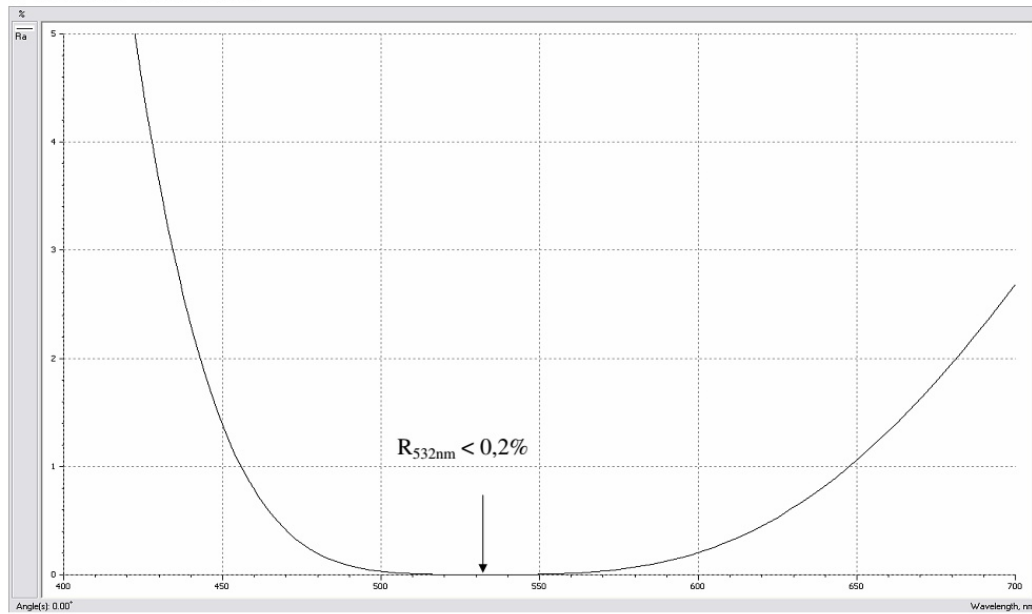


### B-05272: AR450-700nm/0° on UHV

**Figure D.3.:** Reflectance plots of broadband AR coating of LARA cell Raman windows based on magnetron sputtering and electron beam deposition. *Top:* Magnetron sputtering coating applied on the tritium facing surface of the Raman window. *Bottom:* Electron beam deposition coating applied on the surface of the Raman window towards glove box atmosphere. Source: LASEROPTIK, Garbsen, Germany.



B-03054: AR532nm/0°

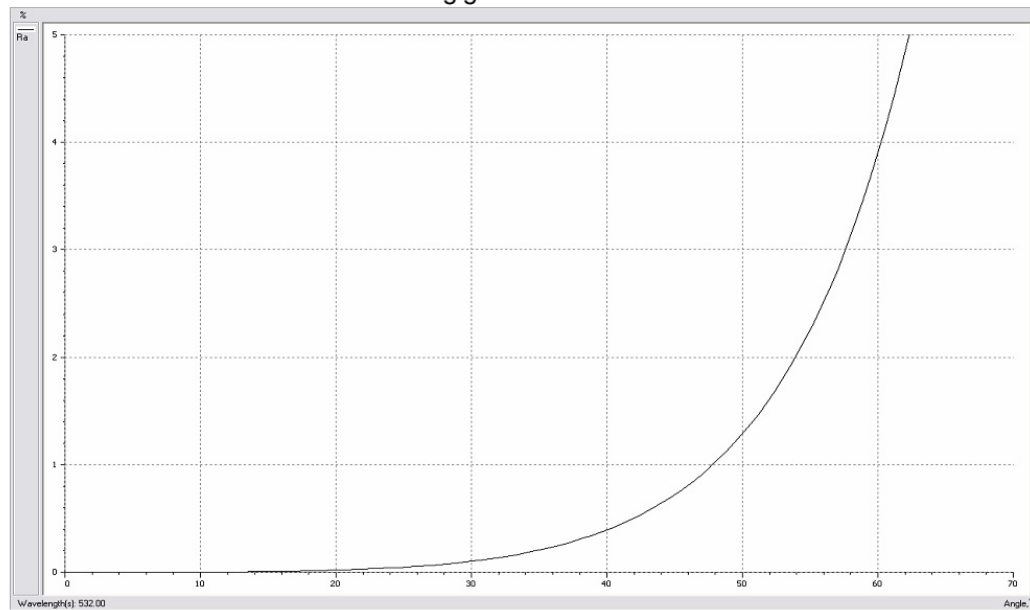


Seite 1 von 2  
Laseroptik

B-03054.doc  
Christian Petter  
02.07.2007



B-03054: AR532nm/0° Winkelabhängigkeit



Seite 2 von 2  
Laseroptik

B-03054.doc  
Christian Petter  
02.07.2007

**Figure D.4.: Reflectance plots of 532 nm AR coating of LARA cell laer windows based on magnetron sputtering. *Top:* Reflectance plot for normal incident. *Bottom:* Angular dependence of reflectance of AR coating. Source: LASEROPTIK, Garbsen, Germany.**

# Publications

Overview of papers and proceedings published in the context of this work.

## Peer-review publications

*Investigation of Durability of Optical Coatings in Highly Purified Tritium Gas*

S. Fischer, K. Schönung, B. Bornschein, R. Rolli, V. Schäfer, M. Sturm

Accepted for publication in *Fusion Sci. Technol.* (2014)

*Raman spectroscopy at the Tritium Laboratory Karlsruhe*

M. Schlösser, B. Bornschein, S. Fischer, T. James, F. Kassel, S. Rupp, M. Sturm, H. Telle

Accepted for publication in *Fusion Sci. Technol.* (2014)

*How-to make Raman-inactive helium visible in Raman spectra of tritium-helium gas mixtures?*

M. Schlösser, O. Pakari, S. Rupp, S. Mirz, S. Fischer

Accepted for publication in *Fusion Sci. Technol.* (2014)

*CAPER as central and crucial facility to support R&D with tritium at the TLK*

D. Demange, E. Fanghänel, S. Fischer, T-L. Le, F. Priester, M. Röllig, M. Schlösser, K. Simon

Accepted for publication in *Fusion Sci. Technol.* (2014)

*Accurate depolarization ratio measurements for all diatomic hydrogen isotopologues*

T. James, M. Schlösser, S. Fischer, M. Sturm, B. Bornschein, R. Lewis, and H. Telle

*Journal of Raman Spectroscopy*, **44** 6, 857-865 (2013), [doi:10.1002/jrs.4283](https://doi.org/10.1002/jrs.4283).

*Accurate calibration of the laser Raman system for the Karlsruhe Tritium Neutrino Experiment*

M. Schlösser, S. Rupp, H. Seitz, S. Fischer, B. Bornschein, T. James, H. Telle

*Journal of Molecular Structure* **1044** 61-66 (2013), [doi:10.1016/j.molstruc.2012.11.022](https://doi.org/10.1016/j.molstruc.2012.11.022).

*Automated Quantitative Spectroscopic Analysis Combining Background Subtraction, Cosmic Ray Removal, and Peak Fitting*

T. James, M. Schlösser, R. Lewis, S. Fischer, B. Bornschein, H. Telle

*Applied Spectroscopy* **67** 8 949-959 (2013). [doi:10.1366/12-06766](https://doi.org/10.1366/12-06766)

*Evaluation method for Raman depolarization measurements including geometrical effects and polarization aberrations*

M. Schlösser, T. James, S. Fischer, R. Lewis, B. Bornschein and H. Telle

*Journal of Raman Spectroscopy*, **44** 3 453-462 (2013), [doi:10.1002/jrs.4201](https://doi.org/10.1002/jrs.4201)

*Monitoring of the operating parameters of the KATRIN Windowless Gaseous Tritium Source*

M. Babutzka, M. Bahr, J. Bonn, B. Bornschein, A. Dieter, G. Drexlin, K. Eitel, S. Fischer, F. Glück, S. Grohmann, M. Hötzel, T. M. James, W. Käfer, M. Leber, B. Monreal, F. Priester, M. Röllig, M. Schlösser, U. Schmitt, F. Sharipov, M. Steidl, M. Sturm, H. H. Telle and N. Titov

New Journal of Physics October (2012) **14** 103046 2012

[doi:10.1088/1367-2630/14/10/103046](https://doi.org/10.1088/1367-2630/14/10/103046), [arXiv: 1205.5421v3](https://arxiv.org/abs/1205.5421v3) [physics.ins-det]

*Overview of R&D at TLK for process and analytical issues on tritium management in breeder blankets of ITER and DEMO*

D. Demange, C. Alecu, N. Bekris, O. Borisevich, B. Bornschein, S. Fischer, N. Gramlich, Z. Köllö, T-L. Le, R. Michling, F. Priester, M. Röllig, M. Schlösser, S. Stämmeler, M. Sturm, R. Wagner, S. Welte

Fusion Eng. Des., **87** 7-8, 1206–1213 (2012), [doi:10.1016/j.fusengdes.2012.02.105](https://doi.org/10.1016/j.fusengdes.2012.02.105)

*Monitoring of tritium purity during long-term circulation in the KATRIN test experiment LOOPINO using Laser Raman Spectroscopy*

S. Fischer, M. Sturm, M. Schlösser, B. Bornschein, G. Drexlin, F. Priester, R. Lewis, H. Telle

Fusion Sci. Technol. **60** 3, 925–930 (2011) [www.new.ans.org/pubs/journals/fst/a\\_12567](http://www.new.ans.org/pubs/journals/fst/a_12567)

[arXiv: 1208.1605v1](https://arxiv.org/abs/1208.1605v1) [physics.ins-det]

*Design implications for Laser Raman measurement systems for tritium sample analysis, accountancy and process-control applications*

M. Schlösser, S. Fischer, M. Sturm, B. Bornschein, R.J. Lewis, H. Telle

Fusion Sci. Technol. **60** 3, 976–981 (2011) [www.new.ans.org/pubs/journals/fst/a\\_12579](http://www.new.ans.org/pubs/journals/fst/a_12579)

### Non-peer reviewed

*Status of the windowless gaseous tritium source of KATRIN*

S. Fischer

Proceedings of "XV International workshop on Neutrino Telescopes", 2013, [POS\(Neutel 2013\) 071](https://arxiv.org/abs/1307.071)

*Accuracy of the Laser Raman system for KATRIN*

M. Schlösser, S. Fischer, M. Hötzel, W. Käfer

Proceedings of the International School of Physics "Enrico Fermi",

[arXiv: 1203.4099v1](https://arxiv.org/abs/1203.4099v1) [physics.ins-det].

*Status of the KATRIN experiment*

S. Fischer for the KATRIN collaboration

Proceedings of the XXIst International Europhysics Conference on High Energy Physics 2011, Proceedings of Science, [PoS\(EPS-HEP2011\)097](https://arxiv.org/abs/1109.097).

*Laser Raman Spectroscopy for KATRIN*

S. Fischer, M. Sturm, M. Schlösser, R. Lewis, B. Bornschein, G. Drexlin, H. Telle

Proceedings of XIV International Conference on Neutrino Physics and Astrophysics 2010, Nuclear Physics B (Proc. Suppl.) 229–232 (2012) 492, [10.1016/j.nuclphysbps.2012.09.129](https://doi.org/10.1016/j.nuclphysbps.2012.09.129)

# Index

- Ab-initio calculation, 58
- Amorphous SiO<sub>2</sub>, 127
- Anti-reflection coating, 120
- Appearance experiments, 7
- Appendix, 72, 101
- Atomic emission lines, 91
  
- Branch, 51
  
- Chromatic aberration, 83
- Coating, 120
  - Electron beam deposition, 127
  - Ion assisted deposition, 127
  - Ion beam sputtering, 127
  - Magnetron sputtering, 127
  - Manufacturing techniques, 122
  - Physical vapour deposition, 122
  - Sputtering, 127
- Column density, 28
- Cosmic microwave background, 16
  
- Depolarisation ratio, 59
- Diode pumped solid state laser, 70
- Dipole moment, 49
- Dirac mass term, 13
- Disappearance experiments, 7
- Double pass configuration, 66
  
- Electron neutrino mass, 26
- Endpoint energy, 26
  
- Final states distribution, 38
- Fresnel equation, 120
- Fused silica, 127
- Fusion material laboratory (FML), 142
  
- Gas-wall interaction, 93
  
- Hydrofluoric acid, 103, 133
- Hydrogen isotopologues, 29
  
- Hydrogen fluoride, 103, 133
  
- In-line measurement, 34
- Inner Loop, 33
- Isotope exchange reaction, 93
- Isotopic purity, 28
- Isotopologues, 29
  
- Karlsruhe Tritium Neutrino Experiment (KATRIN), 25
  
- LARA cell, 71
- LARA3, 66
  - LARA3*pre*, 66
- LARASoft, 153
- Large scale structure, 16
- Laser wavelength determination, 134
- Laser-induced contamination, 131
- Laser-induced damage threshold, 114
- Level of detection, 81, 116
- Line strength function, 53
- Long baseline neutrino oscillation experiments, 11
- LOOPINO, 100, 101
  
- MAC-E filter, 29
- Majorana mass term, 13
- Mixing angles, 6
- Molecular excitation, 45
  - Harmonic vibration, 47
  - Morse potential, 47
  - Rigid rotator, 46
  
- Neutrino
  - Detection, 4
  - Flavours, 4
  - Generations, 4
  - Inverted mass hierarchy, 12
  - Majorana mass, 18

- Mass, 12
- Normal mass hierarchy, 11
- Oscillation, 5
- Postulation, 4
- Quasi-degenerate neutrino masses, 12
- Sterile, 11
- Weak eigenstate, 6
- Nuclear spin, 53
- Optical coating, 120
- Optical isolator, 68
- Parity, 53
- Pauli principle, 53
- Placzek-Teller factor, 55
- PMNS matrix, 6
- Polarisibility
  - Anisotropy, 55
  - Mean polarisibility, 55
  - Tensor, 49
  - Tensor invariant, 55
  - Transition polarisibility operator, 50
- Polytetrafluoroethylene (PTFE), 103, 133
- Precision, 94
- Quantitative analysis, 56
- Quarter-wave coating, 121
- Radiation-induced degradation, 103, 133
- Radiation-induced densification, 127
- Raman
  - Branch, 51
  - Shift, 43
- Relative Precision, 94
- Relative Raman intensity, 58
- Response function, 57
- Schrödinger equation, 45
- Seesaw mechanism, 13
- Selection rules, 49
- Snell's law, 120
- Solar neutrino problem, 5
- SpecTools, 60
- Spectral sensitivity, 60
- Spectroscopic accuracy, 59
- Statistical weight, 52
- Sudbury Neutrino Observatory (SNO), 9
- Super-Kamiokande, 9
- Supersymmetry, 14
- Teflon, 103, 133
- Thermal evaporation, 127
- Thermopile power meter, 76
- Tritium, 25
  - $\beta$ -decay, 25
  - $\beta$ -spectrum, 25
  - Final states, 38
  - Isotopologues, 29
- Tritium Laboratory Karlsruhe, 33
- Wavenumber, 43
- WGTS, 28
- Windowless Gaseous Tritium Source, 28
- Yukawa coupling, 4

# Bibliography

- [Aar14] M. Aartsen et al., *Letter of Intent: The Precision IceCube Next Generation Upgrade (PINGU)* (2014).
- [Aba11] K. Abazajian et al., *Cosmological and astrophysical neutrino mass measurements*, *Astroparticle Physics* **35**, 4 (2011) 177 – 184.
- [Aba12] K. N. Abazajian et al., *Light Sterile Neutrinos: A White Paper*, ArXiv e-prints (2012) 1204.5379.
- [Abe08] S. Abe et al., *Precision Measurement of Neutrino Oscillation Parameters with KamLAND*, *Phys. Rev. Lett.* **100** (2008) 221803.
- [Abe11a] K. Abe et al., *Search for Differences in Oscillation Parameters for Atmospheric Neutrinos and Antineutrinos at Super-Kamiokande*, *Phys. Rev. Lett.* **107** (2011) 241801.
- [Abe11b] K. Abe et al., *Solar neutrino results in Super-Kamiokande-III*, *Phys. Rev. D* **83**, 5 (2011) 052010.
- [Abe11c] K. Abe et al., *The T2K experiment*, *Nuclear Instruments and Methods in Physics Research Section A: Accelerators, Spectrometers, Detectors and Associated Equipment* **659**, 1 (2011) 106 – 135.
- [Abe12] Y. Abe et al., *Indication of Reactor  $\nu^-e$  Disappearance in the Double Chooz Experiment*, *Phys. Rev. Lett.* **108** (2012) 131801.
- [Abe14a] K. Abe et al., *Observation of Electron Neutrino Appearance in a Muon Neutrino Beam*, *Phys. Rev. Lett.* **112** (2014) 061802.
- [Abe14b] K. Abe et al., *Precise Measurement of the Neutrino Mixing Parameter  $\theta_{23}$  from Muon Neutrino Disappearance in an Off-Axis Beam*, *Physical Review Letters* **112**, 18 (2014) 181801.
- [Acq06] R. Acquafredda et al., *First events from the CNGS neutrino beam detected in the OPERA experiment*, *New Journal of Physics* **8**, 12 (2006) 303.
- [Ada13] C. Adams et al., *The Long-Baseline Neutrino Experiment: Exploring Fundamental Symmetries of the Universe* (2013).
- [Aga10] S. Agarwal et al., *The effect of massive neutrinos on the matter power spectrum*, ArXiv e-prints , 3 (2010) arXiv:1006.0689 [astro-ph.CO].
- [Aga14] N. Agafonova et al., *Evidence for  $\nu_\mu \rightarrow \nu_\tau$  appearance in the CNGS neutrino beam with the OPERA experiment*, *Phys.Rev.* **D89** (2014) 051102.

- [Ago13] M. Agostini et al., *Results on Neutrinoless Double- $\beta$  Decay of Ge76 from Phase I of the GERDA Experiment*, Phys. Rev. Lett. **111** (2013) 122503.
- [Aha13] B. Aharmim et al., *Combined analysis of all three phases of solar neutrino data from the Sudbury Neutrino Observatory*, Phys. Rev. C **88**, 2 (2013) 025501.
- [Ahn01] S. Ahn et al., *Detection of accelerator-produced neutrinos at a distance of 250 km*, Physics Letters B **511**, 2-4 (2001) 178 – 184.
- [Ahn12] J. K. Ahn et al., *Observation of Reactor Electron Antineutrinos Disappearance in the RENO Experiment*, Phys. Rev. Lett. **108**, 19 (2012) 191802.
- [Ahn14] C. P. Ahn et al., *The Tenth Data Release of the Sloan Digital Sky Survey: First Spectroscopic Data from the SDSS-III Apache Point Observatory Galactic Evolution Experiment*, The Astrophysical Journal Supplement Series **211**, 2 (2014) 17.
- [Aig00] J. Aigueperse et al., *Ullmann's Encyclopedia of Industrial Chemistry*, chapter Fluorine Compounds, Inorganic, Wiley-VCH Verlag GmbH & Co. KGaA (2000), pp. 397–441.
- [Alb14a] J. Albert et al., *Search for Majorana neutrinos with the first two years of EXO-200 data*, Nature **510** (2014) 229–234.
- [Alb14b] J. B. Albert et al., *Improved measurement of the  $2\nu\beta\beta$  half-life of  $^{136}\text{Xe}$  with the EXO-200 detector*, Phys. Rev. C **89** (2014) 015502.
- [Ale11] C. Alecu et al., *Reachable Accuracy and Precision for Tritium Measurements by Calorimetry at TLK*, Fusion Sci. Technol. **60**, 3 (2011) 937–940.
- [An12] F. P. An et al., *Observation of Electron-Antineutrino Disappearance at Daya Bay*, Phys. Rev. Lett. **108**, 17 (2012) 171803.
- [An13] F. P. An et al., *Improved measurement of electron antineutrino disappearance at Daya Bay*, Chinese Physics C **37**, 1 (2013) 011001.
- [An14] F. P. An et al., *Spectral Measurement of Electron Antineutrino Oscillation Amplitude and Frequency at Daya Bay*, Phys. Rev. Lett. **112** (2014) 061801.
- [And98] K. Anderson et al., *The NuMI Facility Technical Design Report* (1998).
- [Arc48] J. F. Archard et al., *Improved Glan-Foucault Prism*, Journal of Scientific Instruments **25**, 12 (1948) 407.
- [Ase11] V. N. Aseev et al., *Upper limit on the electron antineutrino mass from the Troitsk experiment*, Phys. Rev. D **84**, 11 (2011) 112003.
- [Bab12] M. Babutzka et al., *Monitoring of the operating parameters of the KATRIN Windowless Gaseous Tritium Source*, New J. Phys. **14**, 10 (2012) 103046.
- [Bac97] H. Bach et al., editors, *Thin films on glass*, Schott series on glass and glass ceramics, Springer, Berlin (1997), pp. : DM 268.00.
- [Bah64] J. N. Bahcall, *Solar Neutrinos. I. Theoretical*, Phys. Rev. Lett. **12**, 11 (1964) 300–302.

- [Bah01] J. N. Bahcall et al., *Solar Models: Current Epoch and Time Dependences, Neutrinos, and Helioseismological Properties*, The Astrophysical Journal **555**, 2 (2001) 990.
- [Bah05] J. N. Bahcall et al., *New Solar Opacities, Abundances, Helioseismology, and Neutrino Fluxes*, Astrophys. J. Lett. **621**, 1 (2005) L85.
- [Bai11] A. R. Bainbridge, *A study into the effect of a lambda/2 plate on beam polarisation, design and testing of a photodiode temperature control system for monitoring laser power, and a test of the thermal properties of photodiodes.*, Master's thesis, Swansea University (2011).
- [Bar11] A. Barabash et al., *Investigation of double-beta decay with the NEMO-3 detector*, Physics of Atomic Nuclei **74**, 2 (2011) 312–317.
- [Bas09] M. Bass et al., *Handbook of Optics, Third Edition Volume IV: Optical Properties of Materials, Nonlinear Optics, Quantum Optics*, Handbook of Optics, McGraw-Hill Education (2009).
- [Bec05] S. Becker et al., *Accelerated low fluence laser ageing of AR coatings*, Proc. SPIE **5991** (2005) 59910M–59910M–11.
- [Bec06] S. Becker et al., *Laser-induced contamination of silica coatings in vacuum*, Proc. SPIE **6403** (2006) 64030J–64030J–12.
- [Bel95] A. I. Belesev et al., *Results of the troitsk experiment on the search for the electron antineutrino rest mass in tritium beta-decay*, Phys. Lett. B **350**, 2 (1995) 263 – 272.
- [Bel10] G. Bellini et al., *Measurement of the solar B8 neutrino rate with a liquid scintillator target and 3 MeV energy threshold in the Borexino detector*, Phys. Rev. D **82** (2010) 033006.
- [Bel12] G. Bellini et al., *First Evidence of pep Solar Neutrinos by Direct Detection in Borexino*, Phys. Rev. Lett. **108** (2012) 051302.
- [Ben13] C. L. Bennett et al., *Nine-year Wilkinson Microwave Anisotropy Probe (WMAP) Observations: Final Maps and Results*, The Astrophysical Journal Supplement Series **208** (2013) 20.
- [Ber12] Beringer J. et al., Particle Data Group, *2013 Review of Particle Physics and 2013 partial update for the 2014 edition*, Phys. Rev. D **86** (2012) 010001.
- [Ber13a] Beringer J. et al., Particle Data Group, *2013 Review of Particle Physics and 2013 partial update for the 2014 edition*, Phys. Rev. **86** (2013) 010001, neutrino mass, mixing, and oscillations.
- [Ber13b] Beringer J. et al., Particle Data Group, *2013 Review of Particle Physics and 2013 partial update for the 2014 edition*, Phys. Rev. **86** (2013) 010001, the Cosmological Parameters.
- [Bio87] R. M. Bionta et al., *Observation of a neutrino burst in coincidence with supernova 1987A in the Large Magellanic Cloud*, Phys. Rev. Lett. **58** (1987) 1494–1496.

- [Boi03] B. Boizot et al., *Raman spectroscopy study of beta-irradiated silica glass*, J Non-Cryst Solids **325** (2003) 22 – 28.
- [Boo96] N. E. Booth et al., *Low-temperature particle detectors*, Annual Review of Nuclear and Particle Science **46**, 1 (1996) 471–532.
- [Bor27] M. Born et al., *Zur Quantentheorie der Molekeln*, Annalen der Physik **389**, 20 (1927) 457–484.
- [Bor66] M. Born et al., *Dynamical theory of crystal lattices*, The international series of monographs on physics, Clarendon Pr., Oxford, repr. from corr. sheets edition (1966).
- [Bor05] M. Bornschein, B. and Glugla et al., *Successful Experimental Verification of the Tokamak Exhaust Processing Concept of ITER with the CAPER Facility*, Fusion Science and Technology **48**, 1 (2005) 11–16.
- [Bor11] B. Bornschein, *Between Fusion and Cosmology - The Future of the Tritium Laboratory Karlsruhe*, Fusion Sci. Technol. **60** (2011) 1088–1091.
- [Bor13] B. Bornschein et al., *Tritium management and safety issues in ITER and DEMO breeding blankets*, Fusion Engineering and Design **88** (2013) 466 – 471.
- [Bor14] B. Bornschein et al., *Commissioning and first results of KATRIN Inner Loop tritium processing system at Tritium Laboratory Karlsruhe*, Vacuum (2014), to be submitted.
- [Bra88] C. B. Bratton et al., *Angular distribution of events from SN1987A*, Phys. Rev. D **37** (1988) 3361–3363.
- [Bru98] A. S. Brun et al., *Standard Solar Models in the Light of New Helioseismic Constraints. I. The Solar Core*, The Astrophysical Journal **506**, 2 (1998) 913.
- [Bru99] A. S. Brun et al., *Standard Solar Models in the Light of New Helioseismic Constraints. II. Mixing below the Convective Zone*, The Astrophysical Journal **525**, 2 (1999) 1032.
- [Bru13] T. Brunst, *Durchführung von Messungen mit einem Lumineszenzstandard zur Kalibrierung des Laser-Raman-Systems für KATRIN*, Bachelor thesis, Karlsruhe Institute of Technology (2013).
- [Bus09] G. Buscarino et al., *Polyamorphic transformation induced by electron irradiation in a-SiO<sub>2</sub> glass*, Phys. Rev. B **80**, 9 (2009) 094202.
- [Can05] J. S. Canham, *Molecular contamination damage prevention: lessons learned from vacuum laser operation*, Proc. SPIE **5991** (2005) 59910E–59910E–10.
- [Cha14] J. Chadwick, *The intensity distribution in magnetic spectrum of  $\beta$ -rays of radium b + c*, Verhandl. Dtsch. phys. Ges. **16** (1914) 383.
- [Che89] C. Chen et al., *New nonlinear-optical crystal: LiB<sub>3</sub>O<sub>5</sub>*, J. Opt. Soc. Am. B **6**, 4 (1989) 616–621.

- [Che95] C. Chengrui et al., *A possible explanation of the negative values of  $m_{\nu_e}^2$  obtained from the  $\beta$  spectrum shape analyses*, International Journal of Modern Physics A **10**, 19 (1995) 2841–2849.
- [Cho00] R. Chow et al., *Reversible laser damage of dichroic coatings in a high-average-power laser vacuum resonator*, Proc. SPIE **3902** (2000) 283–291.
- [Cho03] K. Choy, *Chemical vapour deposition of coatings*, Progress in Materials Science **48**, 2 (2003) 57 – 170.
- [Cho07] S. J. Choquette et al., *Relative Intensity Correction of Raman Spectrometers: NIST SRMs 2241 Through 2243 for 785 nm, 532 nm, and 488 nm/514.5 nm Excitation*, Appl. Spectrosc. **61**, 2 (2007) 117–129.
- [Cla06] E. A. Clark et al., *Effects of Tritium Exposure on UHMW-PE, PTFE, and Vespel*, Technical report, Savannah River National Laboratory, Washington Savannah River Company, South Carolina (2006).
- [Cla07] E. Clark et al., *Effects of tritium on UHMW-PE, PTFE, and Vespel polyimide*, Fusion Science and Technology **52**, 4 (2007) 1007–1011.
- [Cla14] Clavereau, Julien, Product Manager Finesse, Laser Quantum, *Personal communication* (2014).
- [Coha] Coherent Inc., *Certificate of Calibration, PowerMax USB LM-10 (Partnumber 1168340), Certificate number 091216141946, 2009/12/16*.
- [Cohb] Coherent Inc., *Position Sensing Air-Cooled Thermopile Sensors to 100 W*, Coherent Inc., Santa Clara, CA 95054 USA, <http://www.coherent.com/products/index.cfm?fuseaction=popups.ShowAttributes&ID=700> (Accessed 2014/03/17).
- [ALE06] A. Collaboration et al., *Precision electroweak measurements on the Z resonance*, Phys. Rep. **427**, 5-6 (2006) 257 – 454.
- [CVI13] CVI Laser Optics, *Support Document, Windows, chapter 2.3* (2013).
- [Dan62] G. Danby et al., *Observation of High-Energy Neutrino Reactions and the Existence of Two Kinds of Neutrinos*, Phys. Rev. Lett. **9**, 1 (1962) 36–44.
- [Dav64] R. Davis, *Solar Neutrinos. II. Experimental*, Phys. Rev. Lett. **12**, 11 (1964) 303–305.
- [Dav68] R. Davis et al., *Search for Neutrinos from the Sun*, Phys. Rev. Lett. **20**, 21 (1968) 1205–1209.
- [Dem05] W. Demtröder, *Molecular physics : theoretical principles and experimental methods*, Wiley-VCH, Weinheim (2005).
- [Dem06] W. Demtröder, *Atoms, molecules and photons : an introduction to atomic-, molecular- and quantum-physics*, Springer, Berlin (2006).
- [Dem08] W. Demtröder, *Laser spectroscopy*, volume 2: Experimental techniques, Springer, Berlin, 4. ed. edition (2008).

- [Dem12] D. Demange et al., *Overview of R & D at TLK for process and analytical issues on tritium management in breeder blankets of ITER and DEMO*, Fusion Engineering and Design **87**, 7-8 (2012) 1206 – 1213, tenth International Symposium on Fusion Nuclear Technology (ISFNT-10).
- [Dep93] Department of Energy, United States, *DOE Fundamentals Handbook, Material Sciences, Vol 2 of 2 (DOE-HDBK-1017/1-93)*, volume 2, U.S. Department of Energy, Washington, D.C. 20585 (1993).
- [Dep07] Department of Energy, United States, *DOE Handbook, Tritium Handling and Safe Storage*, U.S. Department of Energy, Washington, D.C. 20585 (2007).
- [Dev94] R. Devine, *Macroscopic and microscopic effects of radiation in amorphous SiO<sub>2</sub>*, Nuclear Instruments and Methods in Physics Research Section B: Beam Interactions with Materials and Atoms **91**, 1-4 (1994) 378 – 390.
- [Dev13] P. S. B. Dev et al., *Constraining neutrino mass from neutrinoless double beta decay*, Phys. Rev. D **88** (2013) 091301.
- [Dir77] A. Dirks et al., *Columnar microstructure in vapor-deposited thin films*, Thin Solid Films **47**, 3 (1977) 219 – 233.
- [Dob09] E. R. Dobrovinskaya et al., *Sapphire : material, manufacturing, applications*, Micro- and opto-electronic materials, structures, and systems, Springer, New York, NY (2009).
- [Dol78] B. Doležel, *Die Beständigkeit von Kunststoffen und Gummi*, Hanser, München, 1. edition (1978).
- [Dos06] N. Doss et al., *Molecular effects in investigations of tritium molecule  $\beta$  decay endpoint experiments*, Phys. Rev. C **73**, 1 (2006) 025502.
- [Dou12] Double Chooz Collaboration, *Reactor  $\bar{\nu}_e$  disappearance in the Double Chooz experiment*, Phys. Rev. D **86**, 5 (2012) 052008.
- [Dör02] L. Dörr et al., *Upgrade of the isotope separation system at the Tritium Laboratory Karlsruhe*, Fusion Sci. Technol. **41**, 3P2 (2002) 1155–1159.
- [Dör05] L. Dörr et al., *The Closed Tritium Cycle of the Tritium Laboratory Karlsruhe*, Fusion Sci. Technol. **48**, 1 (2005) 262–267.
- [Doe08] L. Dörr et al., *A decade of tritium technology development and operation at the Tritium Laboratory Karlsruhe*, Fusion Sci. Technol. **54**, 1 (2008) 143–148.
- [Dre13] G. Drexlin et al., *Current Direct Neutrino Mass Experiments*, Adv. High En. Phys. **2013**, 293986 (2013) 39 pages.
- [Ebe14] M. Ebert, *Personal communication*, LASEROPTIK GmbH, Garbsen, Germany (2014).
- [Edw78] H. G. M. Edwards et al., *Pure rotational and vibration-rotational Raman spectra of tritium, 3H<sub>2</sub>*, Journal of the Chemical Society, Faraday Transactions 2 **74** (1978) 1203.

- [Ell27] C. Ellis et al., *The Average Energy of Disintegration of Radium E*, Proc. R. Soc. Lond. A. **117** (1927) 109–123.
- [Eng92] U. Engelmann, *Ramanspektroskopische und massenspektrometrische Untersuchungen der Wasserstoffisotope und isotop substituierter Methane*, Phd thesis, Kernforschungszentrum Karlsruhe (1992).
- [Eng97] U. Engelmann, *Raman Spectroscopic and Mass Spectrometric Investigations of the Hydrogen Isotopes and Isotopically Labeled Methane*, Translation of PhD thesis by James R. Jewett (Numatec Hanford Company) HNF-MR-0532, Institute for Radiochemistry, Karlsruhe Nuclear Research Center (1997).
- [Eng13] J. Engle et al., *Evaluation of  $^{163}\text{Ho}$  production options for neutrino mass measurements with microcalorimeter detectors*, Nuclear Instruments and Methods in Physics Research Section B: Beam Interactions with Materials and Atoms **311**, 0 (2013) 131 – 138.
- [Fan11] E. Fanghänel, *Measurement protocol for tritiated Gas Analysis by CAPER-GC, 160611,1.xls*, Karlsruhe Institute of Technology, Institute of Technical Physics, Tritium Laboratory Karlsruhe (2011).
- [Fer34] E. Fermi, *Versuch einer Theorie der beta-Strahlen. I*, Zeitschrift für Physik **88**, 3-4 (1934) 161–177.
- [Fis10] S. Fischer, *Investigations of laser stability in the KATRIN Raman setup and first depolarisation measurements with tritium at TLK*, Diploma thesis, Karlsruher Institut für Technologie (2010).
- [Fis11] S. Fischer et al., *Monitoring of tritium purity during long-term circulation in the KATRIN test experiment LOOPINO using laser Raman spectroscopy*, Fusion Sci. Technol. **60**, 3 (2011) 925–930.
- [Fis14] S. Fischer et al., *Investigation of Durability of Optical Coatings in Highly Purified Tritium Gas*, Fusion Science and Technology (2014), accepted for publication.
- [Fla11] R. L. Flack, *NEMO-3 and SuperNEMO: A search for zero neutrino double beta decay*, Nuclear Physics B - Proceedings Supplements **217**, 1 (2011) 53 – 55, proceedings of the Neutrino Oscillation Workshop (NOW 2010).
- [Fle09] A. Fleischmann et al., *Metallic magnetic calorimeters*, AIP Conference Proceedings **1185**, 1 (2009) 571–578.
- [Fog13] G. Fogli et al., *A global analysis of neutrino oscillations*, Nuclear Physics B - Proceedings Supplements **235-236**, 0 (2013) 125 – 132, f.
- [For11] J. Formaggio et al., *Resolving the reactor neutrino anomaly with the KATRIN neutrino experiment*, Physics Letters B **706**, 1 (2011) 68 – 71.
- [For12a] D. V. Forero et al., *Global status of neutrino oscillation parameters after Neutrino-2012*, Phys. Rev. D **86** (2012) 073012.

- [For12b] J. Formaggio, *Project 8: Using Radio-Frequency Techniques to Measure Neutrino Mass*, Nuclear Physics B - Proceedings Supplements **229-232** (2012) 371 – 375, neutrino 2010.
- [Pro12] J. A. Formaggio et al., *Measuring Neutrino Masses Using Radio-Frequency Techniques*, J. Phys. Conf. Ser. **375**, 4 (2012) 042005.
- [Fuk94] Y. Fukuda et al., *Atmospheric  $\nu_\mu/\nu_e$  ratio in the multi-GeV energy range*, Physics Letters B **335**, 2 (1994) 237 – 245.
- [GAL99] GALLEX Collaboration, *GALLEX solar neutrino observations: results for GALLEX IV*, Phys. Lett. B **447**, 1-2 (1999) 127 – 133.
- [Gas09] L. Gastaldo et al., *Low Temperature Magnetic Calorimeters For Neutrino Mass Direct Measurement*, AIP Conference Proceedings **1185**, 1 (2009) 607–611.
- [Gat01] F. Gatti, *Microcalorimeter measurements*, Nucl. Phys. B - Proc. Sup. **91**, 1-3 (2001) 293 – 296.
- [GER13] GERDA Collaboration et al., *Measurement of the half-life of the two-neutrino double beta decay of  $^{76}\text{Ge}$  with the GERDA experiment*, Journal of Physics G: Nuclear and Particle Physics **40**, 3 (2013) 035110.
- [GG12] M. Gonzalez-Garcia et al., *Global fit to three neutrino mixing: critical look at present precision*, Journal of High Energy Physics **2012**, 12 (2012) 123.
- [Gil10] W. Gil et al., *The Cryogenic Pumping Section of the KATRIN Experiment*, IEEE T. Appl. Supercon. **20**, 3 (2010) 316 –319.
- [Goe35] M. Goeppert-Mayer, *Double Beta-Disintegration*, Phys. Rev. **48**, 6 (1935) 512–516.
- [GM79] M. Gell-Mann et al., *Supergravity*, North-Holland, Amsterdam (1979), p. 315.
- [GNO05] GNO Collaboration, *Complete results for five years of GNO solar neutrino observations*, Phys. Lett. B **616**, 3-4 (2005) 174 – 190.
- [Gom13] M. Gomes et al., *Status of the MARE Experiment*, Applied Superconductivity, IEEE Transactions on **23**, 3 (2013) 2101204–2101204.
- [Gor62] J. Gorman et al., *Hydrogen permeation through metals*, Vacuum **12**, 1 (1962) 19 – 24.
- [Grö14] R. Gröble, *in preparation*, Ph.D. thesis, Karlsruhe Institute of Technology (2014).
- [Gri69] V. Gribov et al., *Neutrino astronomy and lepton charge*, Phys. Lett. B **28**, 7 (1969) 493 – 496.
- [Gro09] S. Grohmann, *Stability analyses of the beam tube cooling system in the KATRIN source cryostat*, Cryogenics **49**, 8 (2009) 413 – 420.
- [Gro11] S. Grohmann et al., *Precise temperature measurement at 30 K in the KATRIN source cryostat*, Cryogenics **51**, 8 (2011) 438 – 445.

- [Gro13] S. Grohmann et al., *The thermal behaviour of the tritium source in KATRIN*, *Cryogenics* **55-56** (2013) 5–11.
- [Gue84] K. H. Guenther, *Microstructure of vapor-deposited optical coatings*, *Appl. Opt.* **23**, 21 (1984) 3806–3816.
- [Hak06] H. Haken et al., *Molekülphysik und Quantenchemie: Einführung in die experimentellen und theoretischen Grundlagen*, Springer-Lehrbuch, Springer Berlin Heidelberg, 5. auflage edition (2006).
- [Han13] Hanks, Simon, CCFE Special Techniques, Culham Science Centre, Abingdon, Oxfordshire, *Personal communication* (2013).
- [Hec74] E. Hecht et al., *Optics*, Addison-Wesley (1974).
- [Hec02] E. Hecht, *Optics*, Addison-Wesley, San Francisco, 4. ed., international ed. edition (2002), previous ed.: 1998; pbk.
- [Hed69] P. Hedvig, *Electron spin resonance study of radiation degradation of polytetrafluoroethylene*, *Journal of Polymer Science Part A-1: Polymer Chemistry* **7**, 4 (1969) 1145–1152.
- [Hen70] P. J. Hendra et al., *Laser Raman spectroscopy. A review*, *Analyst* **95**, 1129 (1970) 321–342.
- [Her79] G. Herzberg et al., *IV. Constants of diatomic molecules*, number 4 in *Molecular Spectra and Molecular Structure*, Van Nostrand (1979).
- [Her11] P. Herwig, *Kalibrierung des KATRIN Laser Raman Systems mit nicht-tritiierten Wasserstoffisotopologen*, Diplomarbeit, Karlsruher Institut für Technologie (2011).
- [Her14] C. Herkommer, *Bachelor thesis in preparation*, Bachelor thesis, Karlsruhe Institute of Technology (2014).
- [Hig64] P. W. Higgs, *Broken Symmetries and the Masses of Gauge Bosons*, *Phys. Rev. Lett.* **13**, 16 (1964) 508–509.
- [Hir87] K. Hirata et al., *Observation of a neutrino burst from the supernova SN1987A*, *Phys. Rev. Lett.* **58** (1987) 1490–1493.
- [Hir88] K. Hirata et al., *Experimental study of the atmospheric neutrino flux*, *Physics Letters B* **205**, 2-3 (1988) 416 – 420.
- [Hir90] K. S. Hirata et al., *Results from one thousand days of real-time, directional solar-neutrino data*, *Phys. Rev. Lett.* **65** (1990) 1297–1300.
- [Hir91] K. S. Hirata et al., *Real-time, directional measurement of B8 solar neutrinos in the Kamiokande II detector*, *Phys. Rev. D* **44** (1991) 2241–2260.
- [Hir04] M. Hirsch et al., *Supersymmetric origin of neutrino mass*, *New Journal of Physics* **6**, 1 (2004) 76.
- [Hän27] H. Hänsel, *Personal communication*, LASEROPTIK GmbH, Garbsen, Germany (2013/06/27).

- [Hän13] H. Hänsel, *Personal communication*, LASEROPTIK GmbH, Garbsen, Germany (2013).
- [Hol92] E. Holzschuh, *Measurement of the neutrino mass from tritium beta-decay*, Rep. Prog. Phys. **55**, 7 (1992) 1035.
- [Hos06] J. Hosaka et al., *Solar neutrino measurements in Super-Kamiokande-I*, Phys. Rev. D **73** (2006) 112001.
- [Hov94] F. E. Hovis et al., *Optical damage at the part per million level: the role of trace contamination in laser-induced optical damage*, Proc. SPIE **2114** (1994) 145–153.
- [Hov95] F. E. Hovis et al., *Mechanisms of contamination-induced optical damage in lasers*, Proc. SPIE **2428** (1995) 72–83.
- [Hov96] F. E. Hovis et al., *Contamination damage in pulsed 1- $\mu$ m lasers*, Proc. SPIE **2714** (1996) 707–716.
- [Hoe12] M. Hötzel, *Simulation and analysis of source-related effects for KATRIN*, Phd thesis, Karlsruhe Institute of Technology (2012).
- [Hub29] E. Hubble, *A relation between distance and radial velocity among extra-galactic nebulae*, Proceedings of the National Academy of Sciences **15**, 3 (1929) 168–173.
- [Jam09] T. M. James, *Cooling upgrade and characterisation of swansea university’s gas raman spectroscopy system, and initial investigations into the raman scattering intensity dependence on laser excitation polarisation.*, Master’s thesis, Swansea University (2009).
- [Jam13a] T. M. James, *Quantitative Raman spectroscopy of gases related to KATRIN*, Phd-thesis, Swansea University (2013).
- [Jam13b] T. M. James et al., *Accurate depolarization ratio measurements for all diatomic hydrogen isotopologues*, Journal of Raman Spectroscopy **44**, 6 (2013) 857–865.
- [Jam13c] T. M. James et al., *Automated Quantitative Spectroscopic Analysis Combining Background Subtraction, Cosmic Ray Removal, and Peak Fitting*, Applied Spectroscopy **67**, 8 (2013) 949–959.
- [Jam14] T. M. James et al., *Trace gas and dynamic process monitoring by Raman spectroscopy in metal-coated hollow glass fibres*, Analyst (2014), submitted.
- [Jen06] L. Jensen et al., *Damage threshold investigations of high-power laser optics under atmospheric and vacuum conditions*, Proc. SPIE **6403** (2006) 64030U–64030U–10.
- [Jon13] S. A. Jones, *Laser Raman Spectroscopy of Hydrogen Isotopologues and Organic/Inorganic Trace Gases*, Master’s thesis, Swansea University (2013).
- [Kam96] Kamiokande Collaboration, *Solar Neutrino Data Covering Solar Cycle 22*, Phys. Rev. Lett. **77**, 9 (1996) 1683–1686.

- [Kam13] KamLAND-Zen Collaboration, *Limit on Neutrinoless  $\beta\beta$  Decay of  $^{136}\text{Xe}$  from the First Phase of KamLAND-Zen and Comparison with the Positive Claim in  $^{76}\text{Ge}$* , Phys. Rev. Lett. **110**, 6 (2013) 062502.
- [Kan72] K. Kanaya et al., *Penetration and energy-loss theory of electrons in solid targets*, Journal of Physics D: Applied Physics **5**, 1 (1972) 43.
- [Kar09] Karlsruhe Institute of Technology, *Transportordnung für den internen Transport radioaktiver Stoffe auf dem Gelände des Forschungszentrums Karlsruhe, Register 13/2, Stand: 01. Juli 2009* (2009).
- [Kas12] F. Kassel, *Weiterentwicklung der Laser-Ramanspektroskopie an gasförmigen Wasserstoffisotopologen zur Prozessüberwachung von Tritiumexperimenten*, Diploma thesis, Karlsruhe Institute of Technology (2012).
- [KAT05] KATRIN Collaboration, *KATRIN Design Report 2004*, volume 7090, FZK - FZKA 7090 (2005).
- [Kaw91] H. Kawakami et al., *New upper bound on the electron anti-neutrino mass*, Physics Letters B **256**, 1 (1991) 105 – 111.
- [KB08] S. Kraft-Bermuth et al., *Development and Characterization of Microcalorimeters for a Next Generation  $^{187}\text{Re}$  Beta-Decay Experiment*, Journal of Low Temperature Physics **151**, 3-4 (2008) 619–622.
- [Kae12] W. Käfer, *Sensitivity studies of the KATRIN experiment*, Phd-thesis, Karlsruhe Institute of Technology (2012).
- [Kib67] T. W. B. Kibble, *Symmetry Breaking in Non-Abelian Gauge Theories*, Phys. Rev. **155**, 5 (1967) 1554–1561.
- [Kim14] Kim, Soo-Bong, *Results on  $\theta_{13}$  Neutrino Oscillations from Reactor Experiments*, EPJ Web of Conferences **66** (2014) 01010.
- [KK01] H. V. Klapdor-Kleingrothaus et al., *Evidence for neutrinoless double beta decay*, Modern Physics Letters A **16**, 37 (2001) 2409–2420.
- [KK04] H. V. Klapdor-Kleingrothaus et al., *Search for neutrinoless double beta decay with enriched  $^{76}\text{Ge}$  in Gran Sasso 1990-2003*, Physics Letters B **586**, 3-4 (2004) 198 – 212.
- [Kla06] H. V. Klapdor-Kleingrothaus et al., *The evidence for the observation of  $0\nu\beta\beta$  decay: The identification of  $0\nu\beta\beta$  events from the full spectra*, Mod. Phys. Lett. A **21**, 20 (2006) 1547–1566.
- [Kle14] M. Kleesiek, *A Data-Analysis and Sensitivity-Optimization Framework for the KATRIN Experiment*, Ph.D. thesis, Karlsruhe Institute of Technology (2014).
- [Kod01] K. Kodama et al., *Observation of Tau Neutrino Interactions*, Physics Letters B **504**, 3 (2001) 218–224.
- [Kol64] W. Kolos et al., *Accurate Adiabatic Treatment of the Ground State of the Hydrogen Molecule*, The Journal of Chemical Physics **41**, 12 (1964) 3663–3673.

- [Kol68] W. Kolos et al., *Improved theoretical ground-state energy of the hydrogen molecule*, J. Chem. Phys. **49**, 1 (1968) 404–410.
- [Kos12] A. Kosmider, *Tritium Retention Techniques in the KATRIN Transport Section and Commissioning of its DPS2-F Cryostat*, Ph.d. thesis, Karlsruhe Institute of Technology (2012).
- [Kra05] C. Kraus et al., *Final results from phase II of the Mainz neutrino mass search in tritium decay*, Eur. Phys. J. C. **40**, 4 (2005) 447–468.
- [Kra13] A. Kramida et al., *NIST Atomic Spectra Database (ver. 5.1)*, Online available. Accessed 2014, March 26 (2013).
- [Kru83] P. Kruit et al., *Magnetic field paralleliser for 2p electron-spectrometer and electron-image magnifier*, J. Phys. E **16**, 4 (1983) 313.
- [Kud11] S. Kudella, *Suche nach Gravitationswellen mittels Laserinterferometrie und Untersuchungen zur Laserstabilität im Rahmen des KATRIN-Raman-Systems*, Bachelor's thesis, Karlsruher Institut für Technologie (2011).
- [Kun00] R. R. Kunz et al., *Experimentation and modeling of organic photocontamination on lithographic optics*, Journal of Vacuum Science & Technology B: Microelectronics and Nanometer Structures **18**, 3 (2000) 1306–1313.
- [Las] Laser Quantum Ltd, *Finesse, Technical data sheet*, Cheshire, SK4 3GL, England.
- [Las08] Laser Quantum Ltd., *Excel - CW 532nm laser, Certificate of Conformity, 08546-96588, 10/03/2008*, Cheshire, SK4 3GL, England (2008).
- [Las10] Laser Quantum Ltd, *Finesse - CW 532nm laser, Certificate of Conformity, 2010/08/11, serial number 120187-970176*, Cheshire, SK4 3GL, England (2010).
- [Las11] Laser Quantum Ltd, *Finesse - CW 532nm laser, Certificate of Conformity, serial 120187-970176, F-0070 Rev 1.2*, Cheshire, SK4 3GL, England (2011).
- [Lei14] B. Leiber, *Investigations of background due to secondary electron emission in the KATRIN-experiment*, Ph.D. thesis, Karlsruhe Institute of Technology (2014).
- [Lew07] R. J. Lewis, *Development of a Raman system for in-line monitoring of tritium at the Karlsruhe Tritium Neutrino (KATRIN) experiment*, Phd-thesis, Swansea University (2007).
- [Li14] Y.-F. Li, *Overview of the Jiangmen Underground Neutrino Observatory (JUNO)*, Int.J.Mod.Phys.Conf.Ser. **31** (2014) 1460300.
- [Lip97] S. G. Lipson et al., *Optik*, Springer-Lehrbuch, Springer, Berlin (1997).
- [Lob99] V. Lobashev et al., *Direct search for mass of neutrino and anomaly in the tritium beta-spectrum*, Physics Letters B **460**, 1-2 (1999) 227 – 235.

- [Lob03] V. M. Lobashev, *The search for the neutrino mass by direct method in the tritium beta-decay and perspectives of study it in the project KATRIN*, Nucl. Phys. A **719** (2003) C153 – C160.
- [Lon83] G. L. Long et al., *Limit of Detection A Closer Look at the IUPAC Definition*, Analytical Chemistry **55**, 7 (1983) 712A–724A.
- [Lon02] D. A. Long, *The Raman Effect: A Unified Treatment of the Theory of Raman Scattering by Molecules*, John Wiley & Sons Ltd (2002).
- [Lor02] T. J. Loredo et al., *Bayesian analysis of neutrinos observed from supernova SN 1987A*, Phys. Rev. D **65**, 6 (2002) 063002.
- [Läs02] R. Lässer et al., *Use of Gas Chromatography in the Tritium Laboratory Karlsruhe*, Fusion Science and Technology **41** (2002) 515–519.
- [Luk12] S. Lukic et al., *Measurement of the gas-flow reduction factor of the KATRIN DPS2-F differential pumping section*, Vacuum **86**, 8 (2012) 1126 – 1133.
- [Mac10] H. A. Macleod, *Thin-film optical filters*, Series in optics and optoelectronics, CRC Press, Boca Raton, 4. ed. edition (2010).
- [Mak62] Z. Maki et al., *Remarks on the Unified Model of Elementary Particles*, Prog. Theor. Phys. **28**, 5 (1962) 870–880.
- [Mal65] I. H. Malitson, *Interspecimen Comparison of the Refractive Index of Fused Silica*, J. Opt. Soc. Am. **55**, 10 (1965) 1205–1208.
- [McM06] R. L. McCreery, *Handbook of Vibrational Spectroscopy*, chapter Photometric Standards for Raman Spectroscopy, John Wiley & Sons, Ltd (2006).
- [Mei30] L. Meitner et al., *Über eine absolute Bestimmung der Energie der primären  $\beta$ -Strahlen von Radium E*, Z. Phys. **60** (1930) 143.
- [Men11] G. Mention et al., *Reactor antineutrino anomaly*, Phys. Rev. D **83** (2011) 073006.
- [Mer12] S. Mertens, *Study of Background Processes in the Electrostatic Spectrometers of the KATRIN experiment*, Phd-thesis, Karlsruhe Institute of Technology (2012).
- [Mic08] D. Michael et al., *The magnetized steel and scintillator calorimeters of the MINOS experiment*, Nuclear Instruments and Methods in Physics Research Section A: Accelerators, Spectrometers, Detectors and Associated Equipment **596**, 2 (2008) 190 – 228.
- [Mik85] S. Mikheev et al., *Resonance Amplification of Oscillations in Matter and Spectroscopy of Solar Neutrinos*, Sov.J.Nucl.Phys. **42** (1985) 913–917.
- [MIN11] MINOS Collaboration, *Improved Search for Muon-Neutrino to Electron-Neutrino Oscillations in MINOS*, Phys. Rev. Lett. **107**, 18 (2011) 181802.
- [Mir11] S. Mirz, *Aufbau und Charakterisierung eines verbesserten Laser-Raman-Systems für das KATRIN-Experiment*, Bachelor's thesis, Karlsruhe Institute of Technology (2011).

- [Mir14] S. Mirz, *Simulation und experimentelle Untersuchung der Kernspinabhängigkeit der Infrarotabsorption flüssiger inaktiver Wasserstoffisotopologe*, Master's thesis, Karlsruhe Institute of Technology (2014).
- [Mül98] H. Müller et al., *Toward spectroscopic accuracy of ab initio calculations of vibrational frequencies and related quantities: A case study of the HF molecule*, Theoretical Chemistry Accounts **100**, 1-4 (1998) 85–102.
- [Mül11] T. A. Müller et al., *Improved predictions of reactor antineutrino spectra*, Phys. Rev. C **83** (2011) 054615.
- [Moh80] R. N. Mohapatra et al., *Neutrino Mass and Spontaneous Parity Nonconservation*, Phys. Rev. Lett. **44**, 14 (1980) 912–915.
- [Moh81] R. N. Mohapatra et al., *Neutrino masses and mixings in gauge models with spontaneous parity violation*, Phys. Rev. D **23** (1981) 165–180.
- [Mon09] B. Monreal et al., *Relativistic cyclotron radiation detection of tritium decay electrons as a new technique for measuring the neutrino mass*, Phys. Rev. D **80** (2009) 051301.
- [Mor29] P. M. Morse, *Diatomic Molecules According to the Wave Mechanics. II. Vibrational Levels*, Phys. Rev. **34** (1929) 57–64.
- [Mur01] D. B. Murphy, *Fundamentals of Light Microscopy and Digital Imaging*, John Wiley & Sons (2001).
- [NEM13] NEMO-3 Collaboration et al., *Search for Neutrinoless Double-Beta Decay of  $^{100}\text{Mo}$  with the NEMO-3 Detector*, ArXiv e-prints (2013) arXiv:1311.5695, to appear in Phys. Rev. D.
- [Ngu11] D. N. Nguyen et al., *Femtosecond pulse damage thresholds of dielectric coatings in vacuum*, Opt. Express **19**, 6 (2011) 5690–5697.
- [NIS08] *Certificate of Analysis (Standard Ref. Mat. 2242)*, NIST, Gaithersburg, MD, USA (2008).
- [Nor74] C. B. Norris et al., *Ionization dilatation effects in fused silica from 2 to 18 keV electron irradiation*, Journal of Applied Physics **45**, 9 (1974) 3876–3882.
- [Ohi92] S. O'hira et al., *On-line tritium process gas analysis by laser Raman spectroscopy at TSTA*, Fusion Technol. **21**, 2 (1992) 465–470.
- [Ohi96] S. O'hira et al., *Development of real-time and remote fuel process gas analysis system using laser Raman spectroscopy*, Fusion Technol. **30**, 3 (1996) 869–873.
- [OPE14] OPERA collaboration, *The fourth transformation of neutrinos*, Press release (2014).
- [Ott08] E. W. Otten et al., *Neutrino mass limit from tritium beta-decay*, Reports on Progress in Physics **71**, 8 (2008) 086201.
- [Par71] W. Parkinson et al., *The use of plastics and elastomers in nuclear radiation*, Nuclear Engineering and Design **17**, 2 (1971) 247 – 280.

- [Pat13] R. Patterson, *The NOvA experiment: status and outlook*, Nuclear Physics B - Proceedings Supplements **235-236**, 0 (2013) 151 – 157.
- [Pau30] W. Pauli, *Offener Brief an die Gruppe der Radioaktiven bei der Gauvereins-Tagung zu Tübingen* (1930), wissenschaftlicher Briefwechsel mit Bohr, Einstein, Heisenberg, u.a: 1930-1939, Springer.
- [PC14a] D. H. Planck Collaboration, *Planck 2013 results. I. Overview of products and scientific results*, Astronomy & Astrophysics (2014) arXiv:1303.5062 [astro-ph.CO], to be published.
- [PC14b] D. H. Planck Collaboration, *Planck 2013 results. XVI. Cosmological parameters*, Astronomy & Astrophysics (2014) arXiv:1303.5076 [astro-ph.CO], to be published.
- [Pen65] A. A. Penzias et al., *A Measurement of Excess Antenna Temperature at 4080 Mc/s.*, Astrophys. J. **142** (1965) 419–421.
- [Per09] D. Perkins, *Particle Astrophysics*, Oxford University Press, 2 edition (2009).
- [Pit86] J. Pitts et al., *Reduction of silica surfaces with particle beams*, Nuclear Instruments and Methods in Physics Research Section B: Beam Interactions with Materials and Atoms **13** (1986) 245 – 249.
- [Pon67] B. Pontecorvo, J. Expl. Theoret. Phys. **53**, 1717 (1967).
- [Pon68] B. Pontecorvo, *Neutrino Experiments and the Problem of Conservation of Leptonic Charge*, Sov. J. Exp. Theo. Phy. **26**, 5 (1968) 984–988.
- [Pri10a] F. Priester, *Systematische Untersuchungen zum Stabilitätsverhalten des KATRIN Tritiumloop*, Diploma thesis, Karlsruhe Institute of Technology (2010).
- [Pri10b] Princeton Instruments, *Grating Efficiency curve 600g/mm with 750 nm blaze* (2010), <http://www.princetoninstruments.com/Uploads/Princeton/Images/Grating%20curves/1-060-750-1120-Sept2010.gif> (2014/03/14).
- [Pri13] F. Priester, *Tritiumtechnologie für die fensterlose Quelle WGTS von KATRIN*, Phd-thesis, Karlsruhe Institute of Technology (2013).
- [Pul99] H. Pulker, *Chapter 6 - Film Formation Methods*, in *Coatings on Glass (Second Edition)*, Elsevier, Amsterdam, second edition edition (1999), pp. 103 – 317.
- [Ram28] C. V. Raman, *A new radiation*, Indian J. Phys. **2** (1928) 387–398.
- [Ram13] S. C. V. Raman, *The Nobel Prize in Physics 1930*, Web (2013).
- [Ran96] J. D. Rancourt, *Optical thin films : user handbook*, SPIE Optical Engineering Press, Bellingham, Wash. (1996).
- [Ran12] P.-O. Ranitzsch et al., *Development of Metallic Magnetic Calorimeters for High Precision Measurements of Calorimetric  $^{187}\text{Re}$  and  $^{163}\text{Ho}$  Spectra*, J. Low Temp. Phys. **167**, 167 (2012) 1004–1014.
- [Rei56] F. Reines et al., *The Neutrino*, Nature **178** (1956) 446–449.

- [Rei59] F. Reines et al., *Free Antineutrino Absorption Cross Section. I. Measurement of the Free Antineutrino Absorption Cross Section by Protons*, Phys. Rev. **113** (1959) 273–279.
- [Rie08] W. Riede et al., *Analysis of the air-vacuum effect in dielectric coatings*, Proc. SPIE **7132** (2008) 71320F–71320F–10.
- [Röl11] M. Röllig, *Studien zu einem Röntgendetektorsystem zur Überwachung der KATRIN Tritiumquelle*, Diploma thesis, Karlsruhe Institute of Technology (2011).
- [Roe12] M. Röllig et al., *Activity monitoring of a gaseous tritium source by beta induced X-ray spectrometry*, Fusion Eng. Des. **88**, 6-8 (2012) 1263–1266.
- [Rob91] R. G. H. Robertson et al., *Limit on  $\bar{\nu}_e$  mass from observation of the beta-decay of molecular tritium*, Phys. Rev. Lett. **67**, 8 (1991) 957–960.
- [Rub13] A. Rubbia, *LAGUNA-LBNO: design of an underground neutrino observatory coupled to long baseline neutrino beams from CERN*, Journal of Physics: Conference Series **408**, 1 (2013) 012006.
- [Rup12] S. Rupp, *Proof of concept of a calibration method for the laser Raman system for KATRIN based on the determination of the system's spectral sensitivity*, Diploma thesis, Karlsruhe Institute of Technology (2012).
- [Rup14] S. Rupp et al., *Enhanced Sensitivity of Raman Spectroscopy For Tritium Gas Analysis Using A Metal-lined Hollow Glass fibre*, Fusion Sci. Technol. **66** (2014), accepted for publication.
- [Rup15] S. Rupp, *PhD thesis in preparation*, Ph.D. thesis, Karlsruhe Institute of Technology (2015).
- [Sae00] A. Saenz et al., *Improved Molecular Final-State Distribution of  $HeT^+$  for the  $\beta$ -Decay Process of  $T_2$* , Phys. Rev. Lett. **84** (2000) 242.
- [SAG02] SAGE Collaboration, *Solar neutrino flux measurements by the Soviet-American gallium experiment (SAGE) for half the 22-year solar cycle*, J. Exp. Theo. Phys. **95**, 2 (2002) 181–193.
- [Sch82] R. W. Schmieder, *Optical emission spectrum of tritium gas*, J. Opt. Soc. Am. **72**, 5 (1982) 593–600.
- [Sch87] C. Schwartz et al., *Nonadiabatic eigenvalues and adiabatic matrix elements for all isotopes of diatomic hydrogen*, J. Mol. Spectrosc. **121**, 2 (1987) 420 – 439.
- [Sch95] P. Schmüser, *Feynman - Graphen und Eichtheorien für Experimentalphysiker*, Springer-Verlag GmbH (1995).
- [Sch97] N. Schmitz, *Neutrino-physik*, Teubner Studienbücher, Teubner B.G. GmbH (1997).
- [Sch09] M. Schlösser, *First Laser Raman measurements with tritium for KATRIN and studies of systematic effects of the LARA-setup*, Diploma thesis, Karlsruhe Institute of Technology (2009).

- [Sch11a] K. K. Schaffer et al., *The First Public Release of South Pole Telescope Data: Maps of a 95 deg<sup>2</sup> Field from 2008 Observations*, *The Astrophysical Journal* **743**, 1 (2011) 90.
- [Sch11c] M. Schlösser et al., *Design Implications for Laser Raman Measurement Systems for Tritium Sample-Analysis, Accountancy or Process-Control Applications*, *Fusion Sci. Technol.* **60**, 3 (2011) 976–981.
- [Sch11d] K. Schönung, *Entwicklung eines Experiments zur Untersuchung optischer Fenster in Tritiumumgebung und Bewertung der ersten Untersuchungen*, Diploma thesis, Karlsruhe Institute of Technology (2011).
- [Sch12a] M. Schlösser et al., *Accuracy of the Laser Raman system for KATRIN*, Proceedings of the International School of Physics "Enrico Fermi", Course CLXXXII "Neutrino Physics and Astrophysics", edited by G. Bellini (2012) 333–336.
- [Sch13f] V. Schäfer, *Charakterisierung des Coating Test Experiments zur Verbesserung der Langzeitstabilität und der Reproduzierbarkeit*, Diploma thesis, Karlsruhe Institute of Technology (2013).
- [Sch13b] M. Schlösser, *Accurate calibration of the Raman system for the Karlsruhe Tritium Neutrino Experiment*, Phd-thesis, Karlsruhe Institute of Technology (2013).
- [Sch13d] M. Schlösser et al., *Accurate calibration of the laser Raman system for the Karlsruhe Tritium Neutrino Experiment*, *J. Mol. Structr.* **1044** (2013) 61–66.
- [Sch13b] M. Schlösser et al., *Evaluation method for Raman depolarization measurements including geometrical effects and polarization aberrations*, *J. Raman Spectrosc.* **44**, 3 (2013) 453–462.
- [Sch13a] M. Schlösser et al., *In-Line Calibration of Raman Systems for Analysis of Gas Mixtures of Hydrogen Isotopologues with Sub-Percent Accuracy*, *Anal. Chem.* **85**, 5 (2013) 2739–2745.
- [Sch14a] M. Schlösser et al., *How to make raman-inactive helium visible in Raman spectra of tritium-helium gas mixtures?*, *Fusion Science and Technology* (2014) accepted for publication.
- [Sch14b] J. Schwarz, *Detector-System Implementation for the KATRIN Experiment*, Ph.D. thesis, Karlsruhe Institute of Technology (2014).
- [Sei11] H. Seitz, *Kalibrierung des KATRIN Laser-Raman-Systems mit katalytisch hergestellten, inaktiven Wasserstoffisotopologen*, Bachelorarbeit, Karlsruher Institut für Technologie (2011).
- [Sem12] Semrock Inc., *532 nm RazorEdge ultrasteep long-pass edge filter (LP03-532RU-25)*, 3625 Buffalo Road, Suite 6 Rochester, New York 14624 USA (2012), [www.Semrock.com/FilterDetails.aspx?id=LP03-532RU-25](http://www.Semrock.com/FilterDetails.aspx?id=LP03-532RU-25) (2014/03/17).
- [Sie13] J. L. Sievers et al., *The Atacama Cosmology Telescope: cosmological parameters from three seasons of data*, *Journal of Cosmology and Astroparticle Physics* **2013**, 10 (2013) 060.

- [Sir13] M. Sirch, *Leak test of LARA cell 23, 13/11/12*, ITEP-TLK, KIT (2013).
- [Sis04] M. Sisti et al., *New limits from the Milano neutrino mass experiment with thermal microcalorimeters*, Nucl. Instrum. Meth. A **520**, 1-3 (2004) 125 – 131.
- [Sle13] M. Slezák et al., *Electron line shape of the KATRIN monitor spectrometer*, Journal of Instrumentation **8**, 12 (2013) T12002.
- [Sme23] A. Smekal, *Zur Quantentheorie der Dispersion*, Naturwissenschaften **11**, 43 (1923) 873–875.
- [SNO01] SNO Collaboration, *Measurement of the Rate of  $\nu_e + d \rightarrow p + p + e^-$  Interactions Produced by  $^8\text{B}$  Solar Neutrinos at the Sudbury Neutrino Observatory*, Phys. Rev. Lett. **87**, 7 (2001) 071301.
- [Ste13] N. Steinbrink et al., *Neutrino mass sensitivity by MAC-E-Filter based time-of-flight spectroscopy with the example of KATRIN*, New Journal of Physics **15**, 11 (2013) 113020.
- [Sto95] W. Stoeffl et al., *Anomalous Structure in the Beta Decay of Gaseous Molecular Tritium*, Phys. Rev. Lett. **75** (1995) 3237–3240.
- [Stu10b] M. Sturm, *Aufbau und Test des Inner-Loop-Systems der Tritiumquelle von KATRIN*, Phd-thesis, Karlsruhe Institute of Technology (2010).
- [Stu10a] M. Sturm et al., *Monitoring of all hydrogen isotopologues at tritium laboratory Karlsruhe using Raman spectroscopy*, Laser Phys. **20**, 2 (2010) 493–507.
- [Sup98b] Super-Kamiokande Collaboration, *Evidence for Oscillation of Atmospheric Neutrinos*, Phys. Rev. Lett. **81**, 8 (1998) 1562–1567.
- [Sup98a] Super-Kamiokande Collaboration, *Measurements of the Solar Neutrino Flux from Super-Kamiokande's First 300 Days*, Phys. Rev. Lett. **81**, 6 (1998) 1158–1162.
- [Tar88] J. D. Targove et al., *Verification of momentum transfer as the dominant densifying mechanism in ion-assisted deposition*, Appl. Opt. **27**, 18 (1988) 3779–3781.
- [Tay01] D. J. Taylor et al., *Enhanced Raman sensitivity using an actively stabilized external resonator*, Rev. Sci. Instrum. **72**, 4 (2001) 1970–1976.
- [Tel13] H. Telle, *LARASoft, Quick guide*, Swansea University (2013).
- [Tho09] Thorlabs Inc., *Glan Taylor Polarizer GT-5, BBAR: 350-700nm CA: 5.0mm, Technical data sheet, 5428-E01*, post box 366 NEWTON NJ (2009).
- [Tho11] Thorlabs Inc., *Optical Isolator IO-5-532-HP, Catalogue V21, page 932*, post box 366 NEWTON NJ (2011).
- [Tho12] Thorlabs Inc., *Optical Isolator IO-5-532-HP, Performance report, TP00623825-1*, post box 366 NEWTON NJ (2012).
- [Tho14a] Thorlabs Inc., *N-BK7 Plano-Convex Lenses (AR Coating: 350 - 700 nm). N-BK7 index of refraction*, post box 366 NEWTON NJ (2014).

- [Tho14b] Thorlabs Inc., *Optical Coatings, AR coatings, web page*, [http://www.thorlabs.de/newgrouppage9.cfm?objectgroup\\_id=5840](http://www.thorlabs.de/newgrouppage9.cfm?objectgroup_id=5840), accessed 2014/04/29, post box 366 NEWTON NJ (2014).
- [Tig08] A. P. Tighe et al., *Growth mechanisms for laser induced contamination on space optics in vacuum*, Proc. SPIE **7132** (2008) 71321L.
- [TLA13] TLK Betriebsbüro, *Technische Liefer- und Abnahmebedingungen des Tritiumlabor Karlsruhe (TLA)*, TLK (2013).
- [Trä07] F. Träger, editor, *Springer handbook of lasers and optics*, Springer, New York, NY (2007).
- [Unf04] Unfallkasse Baden-Württemberg, *Unfallverhütungsvorschrift BGV B 2 (bisherige VBG 93) - Laserstrahlung* (2004).
- [Vac08] R. Vaccarone et al., *The Design of a Frequency Multiplexed Ir-Au TES Array*, Journal of Low Temperature Physics **151**, 3-4 (2008) 921–926.
- [Val09] K. Valerius, *Spectrometer-related background processes and their suppression in the KATRIN experiment*, Ph.D. thesis, Westfälischen Wilhelms-Universität Münster (2009).
- [Val11] K. Valerius et al., *Prototype of an angular-selective photoelectron calibration source for the KATRIN experiment*, J. Instrum. **6**, 01 (2011) P01002.
- [Var09] C. Varlam et al., *Applying direct liquid scintillation counting to low level tritium measurement*, Applied Radiation and Isotopes **67**, 5 (2009) 812 – 816, 5th International Conference on Radionuclide Metrology - Low-Level Radioactivity Measurement Techniques ICRM-LLRMT'08.
- [Veir87] D. Veirs et al., *Raman line positions in molecular hydrogen:  $H_2$ ,  $HD$ ,  $HT$ ,  $D_2$ ,  $DT$ , and  $T_2$* , Journal of Molecular Spectroscopy **121**, 2 (1987) 401–419.
- [Vig85] J. R. Vig, *UV/ozone cleaning of surfaces*, Journal of Vacuum Science & Technology A **3**, 3 (1985) 1027–1034.
- [Wag89] W. Wagner et al., *Concentration profiles of hydrogen in technical oxidic thin films and multilayer systems*, Fresenius' Zeitschrift für analytische Chemie **333**, 4-5 (1989) 478–480.
- [Wan13] N. Wandkowsky, *Study of background and transmission properties of the KATRIN spectrometers*, Ph.D. thesis, Karlsruhe Institute of Technology (2013).
- [Wec14] M. Wecker, *In preparation*, Bachelor's thesis, Karlsruhe Institute of Technology (2014).
- [Wei35] C. Weizsäcker, *Zur Theorie der Kernmassen*, Zeitschrift für Physik **96**, 7-8 (1935) 431–458.
- [Wei99] C. Weinheimer et al., *High precision measurement of the tritium beta-spectrum near its endpoint and upper limit on the neutrino*, Physics Letters B **460**, 1-2 (1999) 219 – 226.

- [Wei03] C. Weinheimer, *Laboratory Limits on Neutrino Masses*, in K. Winter et al., editors, *Neutrino Mass*, volume 190 of *Springer Tracts in Modern Physics*, Springer Berlin Heidelberg (2003), pp. 25–52.
- [Wei13] C. Weinheimer, *Direct neutrino mass measurements*, *Hyperfine Interact.* **215**, 1-3 (2013) 85–93.
- [Wei13b] C. Weinheimer et al., *Neutrino masses*, *Annalen der Physik* **525**, 8-9 (2013) 565–575.
- [Wes87] R. M. West et al., *Astrometry of SN 1987A and Sanduleak-69 202*, *Astronomy and Astrophysics* **177** (1987) L1–L3.
- [Wex69] S. Wexler et al., *Probability of Formation of  $[(^3\text{He})^+]_{4s}$  following Beta Decay of Tritium*, *The Journal of Chemical Physics* **50**, 12 (1969) 5428–5429.
- [Whi12] J. D. White et al., *Compact diffraction grating laser wavemeter with sub-picometer accuracy and picowatt sensitivity using a webcam imaging sensor*, *Review of Scientific Instruments* **83**, 11 (2012) 113104–113104-4.
- [Wil87] J. F. Wilkerson et al., *Limit on  $\nu_e$  Mass from Free-Molecular-Tritium Beta Decay*, *Phys. Rev. Lett.* **58** (1987) 2023–2026.
- [Wol78] L. Wolfenstein, *Neutrino oscillations in matter*, *Phys. Rev. D* **17** (1978) 2369–2374.
- [Woz14] S. Wozniowski, *Relative Kalibrierung der IR Absorptionsspektren gegen die  $\text{H}_2$ -,  $\text{HD}$ - und  $\text{D}_2$ -Konzentrationen*, Bachelor thesis, Karlsruhe Institute of Technology (2014).
- [Yan79] T. Yanagida, *proceedings of the Workshop on Unified Theories and Baryon Number in the Universe, Tsukuba, 1979*, eds. A. Sawada, A. Sugamoto; S. Glashow (1979).
- [Zha08] L. Zhan et al., *Determination of the neutrino mass hierarchy at an intermediate baseline*, *Phys. Rev. D* **78** (2008) 111103.
- [Zha09] L. Zhan et al., *Experimental requirements to determine the neutrino mass hierarchy using reactor neutrinos*, *Phys. Rev. D* **79** (2009) 073007.
- [Zob96] N. F. Zobov et al., *Vibration-rotation levels of water beyond the Born-Oppenheimer approximation*, *Chemical Physics Letters* **260** (1996) 381 – 387.
- [Zub11] K. Zuber, *Neutrino Physics, Second Edition*, Series in High Energy Physics, Cosmology and Gravitation, Taylor & Francis (2011).

# Danksagung

Diese Arbeit wäre ohne die Hilfe und Unterstützung vieler Menschen nicht möglich gewesen, denen ich an dieser Stelle den gebührenden Dank aussprechen möchte.

Ein herzliches Dankeschön gilt meinen Betreuern, die mich durch beständiges Fordern und Fördern, durch viel Freiraum aber auch durch kritisches Nachfragen unterstützt haben. Ich danke Prof. Dr. Guido Drexlin für das beständige Vertrauen, seine Unterstützung und seinen unbändigen Drang immer das Optimum herauszuholen. Prof. Dr. Helmut H. Telle danke ich dafür, dass er beratend zur Seite stand, wenn es mal wieder nicht vorwärts gehen wollte. Es war stets beruhigend zu wissen, dass es im Notfall immer noch den Helmut-Joker gibt. Herzlichen Dank möchte ich Dr. Beate Bornschein aussprechen, die durch ihre klaren Prinzipien und ihre ehrliche Art verlässliche Rahmenbedingungen aber auch ausreichend Entfaltungsspielraum für mich und diese Arbeit geschaffen hat. Ihrem Einsatz für die Ausbildung des wissenschaftlichen Nachwuchses ist es zu verdanken, dass in relativ kurzer Zeit eine schlagkräftige Laser-Raman-Gruppe herangewachsen ist.

Die Laser-Raman-Gruppe in Swansea und Karlsruhe war und ist von konstruktiver Zusammenarbeit, Elan und dem gemeinsamen Ziel des KATRIN Ramansystems geprägt. Ich danke den ehemaligen und aktuellen Mitgliedern, die alle direkt oder indirekt zu dieser Arbeit beigetragen haben: Dr. Ahmed Alshahrie, Alex Bainbridge, Dr. Beate Bornschein, Tim Brunst, Clemens Herkommer, Philipp Herwig, Dr. Tim James, Steven Jones, Florian Kassel, Bennet Krasch, Simon Kudella, Dr. Richard Lewis, Sebastian Mirz, Silvia Napoli, Andreas Off, Simone Rupp, Vera Schäfer, Dr. Magnus Schlösser, Kerstin Schönung, Hendrik Seitz-Moskaliuk, Monika Sirch, Dr. Michael Sturm, Prof. Dr. Helmut Telle und Matthias Wecker. Meinem langjährigen Kollegen Dr. Magnus Schlösser möchte ich für seinen großen persönlichen Einsatz in der Laser-Raman-Gruppe danken. Ich schätze es sehr, dass wir uns gegenseitig anspornen ohne dabei auf Konkurrenzgedanken zu kommen und uns in vielen fachlichen aber auch persönlichen Bereichen ergänzen. Auch wenn es mir wie selbstverständlich erscheint, ist unsere vertrauensvolle und unkomplizierte Zusammenarbeit etwas Besonderes. Ein großes Dankeschön geht an 'meine' Studenten Florian Kassel, Simon Kudella, Sebastian Mirz, Vera Schäfer und Kerstin Schönung, die durch ihren Einsatz maßgeblich zu dieser Arbeit beigetragen haben. Ich hoffe, ich konnte euch etwas beibringen. Ich habe auf jeden Fall viel von und mit euch gelernt. Für die Hilfe beim Umbau und Betrieb von LOOPINO und die stete fachliche wie auch moralische Unterstützung möchte ich mich herzlich bei Dr. Michael Sturm bedanken. I would like to thank Dr. Tim James who has pushed the development of LARASoft and joined forces in Karlsruhe for getting the system up and running.

Ich danke Florian Kassel und Dr. Tim James für die gemeinsame Entwicklung von LARASoft, sowie Robin Größle, Sebastian Mirz, Kevin Richler, Simone Rupp, Dr. Ma-

---

gnus Schlösser, Hendrik Seitz-Moskaliuk und Sebastian Wozniewski, die die unzähligen Bugs in LARASoft gefunden haben.

Kerstin Schönung danke ich für ihren Einsatz beim Aufbau und bei der Durchführung der Experimente zur Untersuchung der optischen Antireflexbeschichtungen. Ich danke dem CAPER Team (Dr. David Demange, Eleonore Fanghänel, Thanh-Long Le und Karl-Heinz Simon) für den wertvollen Platz in ihrer Handschuhbox und die Versorgung mit Tritium. Großer Dank gilt Vera Schäfer, die sich unermüdlich und erfolgreich für die Stabilisierung des Transmissions- und Reflexionsaufbaus eingesetzt hat. Leider war das verbleibende Zeitfenster für eine neue Messreihe vor Abgabe dieser Arbeit zu klein.

Für das Mikroskopieren der mit Tritium beaufschlagten Beschichtungsproben danke ich Manuel Holzer, Dr. Rolf Rolli und Kollegen am Fusionsmateriallabor des KIT.

Ich bedanke mich herzlich bei Martin Ebert und Heiko Hänsel von LASEROPTIK GmbH in Garbsen, die durch die Bereitstellung der Beschichtungsproben und als kompetente Diskussionspartner maßgeblich zum Gelingen dieser Arbeit beigetragen haben.

Ich danke den Mitgliedern der Tritiuminfrastruktur-Gruppe (Hans-Dieter Adami, Dr. Uwe Besserer, Nancy Lohr, Frank Kramer, Stefan Welte), den Kollegen des Betriebsbüros (Sylvia Krieger, Dirk Osenberg, Dr. Jürgen Wendel), sowie den Mitgliedern der Mess- und Regelungsgruppe (Adalbert Braun, Helmut Dittrich, Christin Melzer, Manuel Mungenast, Frank Rehlinghaus und Peter Schäfer) dafür, dass sie stets für einen sicheren und reibungslosen Betrieb des Tritiumlabors sorgen und somit diese Arbeit ermöglichten.

Bernhard Heinle hat mich nicht nur mit wachen Augen bei meinen Experimenten mit Tritium kontrolliert, sondern auch durch viele Tipps und Denkanstöße dazu beigetragen, dass ich heute sicher mit Tritium umgehen kann. Vielen Dank für die Lehrstunden.

Ich bedanke mich bei Hans-Dieter Adami, Thomas Csabo, Helmut Dittrich, Manfred Göckel, Siegfried Horn, Steffen Jokisch, Frank Kramer, Nancy Lohr, Florian Priester, Frank Rehlinghaus und Marco Röllig für die technische Unterstützung.

Ich danke Eva Porter und Sylvia Krieger für die Hilfe bei administrativen Arbeiten sowie allen Kollegen am Tritiumlabor Karlsruhe für die angenehme Arbeitsatmosphäre.

Ich danke Prof. Dr. Mathias Noe für die von ihm vermittelte Wertschätzung und für seinen Einsatz zur Ausbildung und Förderung des wissenschaftlichen Nachwuchts.

Für den gemeinsamen Einsatz, das KATRIN Experiment aufzubauen und für die vielen schönen Momente bedanke ich mich bei allen KATRIN Kollegen.

Ich danke Robin Größle, Dr. Tim James, Judith Nägele, Dr. Diana Parno, Simone Rupp, Dr. Magnus Schlösser und Dr. Michael Sturm für das Korrekturlesen der Arbeit.

Ich danke der Graduiertenschule KSETA und dem Graduiertenkolleg 1694 des KIT.

Ein herzliches Dankeschön möchte ich meinen Eltern und meinem Bruder aussprechen, die mich stets unterstützt haben.

Zuletzt und ganz besonders möchte ich Judith dafür danken, dass sie es mit mir die ganze Zeit über ausgehalten hat aber mir auch immer wieder gezeigt hat, was die wirklich wichtigen Dinge im Leben sind.